A SATELLITE SWARM-BASED APERTURE SYNTHESIS RADIOMETER IN LOW EARTH ORBIT FOR EARTH OBSERVATION APPLICATIONS

Dipl.-Ing. Mark Lützner

Vollständiger Abdruck der von der Fakultät für Luft- und Raumfahrttechnik der Universität der Bundeswehr München zur Erlangung des akademischen Grades eines

Doktor-Ingenieurs (Dr.-Ing.)

genehmigten Dissertation.

Gutachter:

1. Univ.-Prof. Dr.-Ing. Roger Förstner
2. Prof. Dr.-Ing. Alberto Moreira

Die Dissertation wurde am 11.10.2021 bei der Universität der Bundeswehr München eingereicht und durch die Fakultät für Luft- und Raumfahrttechnik am 01.03.2022 angenommen. Die mündliche Prüfung fand am 22.4.2022 statt.

DECLARATION

This dissertation is the result of my own work and includes nothing, which is the outcome of work done in collaboration except where specifically indicated in the text. It has not been previously submitted, in part or whole, to any university of institution for any degree, diploma, or other qualification.

Signed:____

Date:____

Dipl.-Ing. Mark Lützner

Munich

ABSTRACT

Soil moisture and ocean salinity mapping by Earth observation satellites has contributed significantly towards a better understanding of the Earth system, such as its hydrosphere or climate. Nevertheless, an increased spatial resolution below 10 km with a radiometric resolution in the range of 2-3 Kelvin of microwave radiometer data could yield a more complete picture of global hydrological processes and climate change. Operational radiometers, such as SMOS, have already approached prohibitive sizes for spacecraft due to the required large antenna apertures. Therefore, radiometer concepts based on a large number of satellites flying in close proximity (swarms) have been proposed as a possible solution. This thesis investigates the feasibility of placing a satellite swarm-based aperture synthesis radiometer in low Earth orbit for Earth observation applications.

The aperture synthesis antenna array is formed by a large number of individual antennas on autonomously controlled nanosatellites (deputies) and a correlator antenna in Y-configuration, carried by a chief satellite. The proposed design methodology is based on the optimization of satellite positions within a plane and the subsequent translation of coordinates into initial conditions for General Circular Orbits (GCO). This enables a more computationally efficient orbit optimization and ensures the time-invariance of the antenna array response. Based on this methodology, simulations have been performed with swarms consisting of up to 96 satellites. Simulations show the spatial resolution of an aperture synthesis radiometer can be increased to 7,5 km, for applications where the requirements on radiometric sensitivity are more relaxed ($\Delta T \sim 3$ Kelvin).

ZUSAMMENFASSUNG

Die Messung der Bodenfeuchte und des Salzgehalts der Ozeane durch Erdbeobachtungssatelliten hat wesentlich zu einem besseren Verständnis der Hydrosphäre und des Erdklimas beigetragen. Dennoch könnten Mikrowellenradiometerdaten mit einer höheren räumlichen Auflösung von unter 10 km und einer radiometrischen Auflösung im Bereich von 2-3 Kelvin ein vollständigeres Bild der globalen hydrologischen Prozesse und des Klimawandels liefern. Satellitenbasierte Radiometer wie SMOS haben aufgrund der erforderlichen großen Antennenaperturen bereits eine für Raumfahrzeuge unpraktische Größe erreicht. Daher wurden in der Vergangenheit satellitenbasierte Radiometerkonzepte vorgeschlagen, die auf einer großen Anzahl von eng beieinander fliegenden Satelliten (Satellitenschwärmen) basieren. In der vorliegenden Arbeit wird die Machbarkeit eines auf einem Satellitenschwarm basierenden Apertursynthese-Radiometers in einer niedrigen Erdumlaufbahn für Erdbeobachtungsanwendungen untersucht.

Das verteilte Antennenarray des Apertursynthese-Radiometers wird aus einer großen Anzahl von Einzelantennen auf autonom gesteuerten Nanosatelliten („deputies“) und eines zentralen Antennenarray in Y-Konfiguration, das von einem Hauptsatelliten getragen wird, gebildet. Die vorgeschlagene Entwurfsmethodik basiert auf der Optimierung der Satellitenpositionen in einer relativen Orbitalebene und der anschließenden Übersetzung der Koordinaten in Anfangsbedingungen für relative Kreisbahnen („General Circular Orbits“ - GCO). Dies ermöglicht eine recheneffiziente Optimierung der relativen Umlaufbahnen und gewährleistet die Zeitinvarianz der Antennengruppenantwort. Auf der Grundlage dieser Methodik wurden Simulationen mit Schwärmen von bis zu 96 Satelliten durchgeführt. Die Simulationen zeigen, dass die räumliche Auflösung eines Apertursynthese-Radiometers für Anwendungen, bei denen die Anforderungen an die radiometrische Empfindlichkeit geringer sind (ΔT ~3 Kelvin), auf 7,5 km erhöht werden kann.

ACKNOWLEDGEMENTS

I owe a great amount of thanks to Prof. Roger Förstner for agreeing to be my dissertation supervisor. Thank you for taking time to discuss and review my work on a regular basis. Your expertise kept me on track during the course of this work and significantly added to the quality of its outcome.

I am grateful also to all those that have supported me from the DLR Microwaves and Radar Institute. First of all, to Prof. Dr. Alberto Moreira whose guidance and constructive input were important in shaping my work. Thank you for spending time to tutor each one of us PhD students.

I would also like to thank Dr. Thomas Neff, who supported me from the very start and placed trust in the outcome of my work.

Furthermore, I would like to thank the following persons for their generous support and valuable advice: Dr. Ralph Kahle, Dr. Michael Kirschner, Dr. Markus Peichl, Dr. Thomas Jagdhuber and Dr. Jan Eilers.

TABLE OF CONTENTS

1 INTRODUCTION 1

1.1 Why a swarm-based aperture synthesis radiometer? 1
1.2 Applications of L-band satellite-based radiometry 2
1.2.1 Soil moisture 3
1.2.2 Sea surface salinity retrieval 4
1.2.3 Sea ice thickness 4
1.3 A review of state-of-the-art technology 5
1.3.1 Passive microwave remote sensing at L-band 5
1.3.2 Close-proximity formation flight for nanosatellites 9
1.3.3 Satellite swarm-based aperture synthesis radiometry 10
1.4 Research objectives 13
1.5 System concept 16
1.6 Scope and structure 18

2 INTERFEROMETRIC RADIOMETRY 20

2.1 Interferometric radiometry 20
2.1.1 One-dimensional radio interferometry 20
2.1.2 Aperture synthesis in two dimensions 23
2.2 Motion Induced Synthetic Aperture Radiometer (MISAR) 30
2.2.1 MISAR observation model 31
2.2.2 MISAR adjustable delay compensation 32
2.2.3 Radiometric sensitivity 36
2.3 System imperfections 38

3 RELATIVE ORBIT MECHANICS 39

3.1 Orbit mechanics of unperturbed formation flight 39
3.2 Relative orbit design using relative orbit elements 42
3.3 Perturbed satellite motion 46
3.3.1 Earth oblateness 46
3.3.2 Minimizing the $J2$ effects in satellite formations 48
3.3.3 Differential aerodynamic drag 49
3.4 High-fidelity relative motion dynamics model 51

4 SYSTEM SIMULATOR 54

4.1 Simulator overview 54
4.2 Input Module 56
4.3 Orbit Propagation Module 56
  4.3.1 State uncertainties 58
  4.3.2 Corrective impulse control 59
  4.3.3 Thruster error modelling 60
  4.3.4 Orbit propagation 62
4.4 Image Processing Module 64
  4.4.1 PSF generation 64
  4.4.2 Generating spatial frequency coverage 65
  4.4.3 Tapering 66
4.5 System Feasibility Analysis Module 68
  4.5.1 Collision probability determination 68
  4.5.2 Ground-track drift calculation 70

5 SWARM-BASED RADIOMETER DESIGN 73

5.1 Orbit type selection 73
  5.1.1 Influence of orbit type on controller accuracy and fuel consumption 73
  5.1.2 General Circular Orbit 78
5.2 Receiver optimization on the GCO plane 80
  5.2.1 The optimization problem formulation 83
  5.2.2 Optimization algorithm 84
  5.2.3 Translation of optimization frame coordinates 86
  5.2.4 Case study: Optimization of a 16-deputy configuration 86
5.3 Uniform weighting 89
5.4 Effective swath and observation time 91
5.5 Determining inter-deputy distance constraints 93

6 SIMULATION RESULTS 95

6.1 Simulation settings 95
6.2 Case study: Impact of number of deputies 99
  6.2.1 Imaging performance 99
  6.2.2 System implications 107
6.3 Case study: Impact of orbit control system 114
  6.3.1 Impact of control period 114

- 6.3.2 Impact of relative navigation accuracy 117
- 6.4 Case study: Impact of distance constraints 120
  - 6.4.1 Imaging performance 121
  - 6.4.2 System implications 124
- 6.5 Case study: Impact of system orbit height 126
  - 6.5.1 Relationship between revisit time and system spatial resolution 126
  - 6.5.2 Orbit height implications on swarm control 128
- 6.6 Satellite-swarm orbit design method 133

7 SUMMARY, DISCUSSIONS & OUTLOOK 137

- 7.1 Summary 137
- 7.2 Discussion of selected critical system aspects 139
  - 7.2.1 Antenna phase center position determination 139
  - 7.2.2 Data handling 139
  - 7.2.3 Instrument synchronization 141
- 7.3 Outlook 142

8 REFERENCES 144

A 1. ANNEX 156

- A 1.1. Simulator validation 156
- A 1.2. Validation of Image Processing Module 163

LIST OF TABLES

Table 1-1 System parameters of key L-band radiometry missions 9

Table 1-2 Radiometry requirements for various applications [4] 14

Table 5-1 Scenario settings for the investigation of the influence of J_2-variance on the position accuracy and fuel consumption..74

Table 5-2 Algorithm schematic for the numerical optimization of the receiver positions within the optimization frame. 86

Table 5-3 Algorithm for the determination of inter-deputy distance constraints...94

Table 6-1 Orbital elements of chief satellite 95

Table 6-2 Payload parameters for numerical simulations 96

Table 6-3 Spacecraft parameters for numerical simulation of case study 1 98

Table 6-4 σ_G parameter for array optimization. 98

Table 6-5 3dB angular resolution θ_w and radiometric sensitivity ΔT of satellite configurations. 104

Table 6-6 Ground track accuracy L_d and time between semimajor-axis adjustments Ts dependent on magnitude of the adjustment Δa_{GT} [m]................................... 113

Table 6-7 Simulation settings for the investigation of the impact of inter-deputy distance constraints. 121

Table 6-8 System lifetime [days] for different orbit heights [km] and differences in ballistic coefficients.. 131

Table A.1-1 Scenario settings for validation of scenario Eyer [70]. Values denoted with an asterisk are assumed, as they are not explicitly listed in the source. 161

Table A.1-2 Values for the mean fuel consumption in Δv $[ms \cdot orbit]$ and the 3D RMS control accuracy [m] for the scenario settings given in Eyer [70].................... 161

Table A.1-3 Scenario settings for validation of scenario Roth [104]. Values denoted with an asterisk are assumed, as they are not explicitly listed in the source. 162

Table A.1-4 Values for the mean fuel consumption in Δv [$ms \cdot orbit$] and the 3D RMS control accuracy [m] for the scenario settings given in Roth [104]. 162

Table A.1-5 Angular resolution, θ_w and Main Beam Efficiency (MBE) of validation configuration compared with [48] for snapshots tapered by rectangular and Blackman windows. 164

LIST OF FIGURES

Figure 1-1 An artist view of the SMOS satellite [3]. 6

Figure 1-2 An artist's visualization of the proposed satellite concept showing the larger chief satellite with the correlator antenna in Y-configuration and the other Cubesats (deputies) in close proximity........ 17

Figure 1-3 Schematic view of the swarm-based radiometer concept........ 18

Figure 2-1 Geometry of a two-element interferometer with the baseline *D*........ 21

Figure 2-2 Geometric setup of the two-element receiving system observing an extended source of intensity I in the far field. Modified from [43]........ 23

Figure 2-3 Geometric setup of the two-element receiving system observing an extended source with intensity I in the far field with the direction cosines l, m. Modified from [43]. 26

Figure 2-4 Visualization of a single Visibility V and its Hermitian V* in the (u, v) plane. The dashed lines represent the minima and extrema of the spatial frequency spectrum for a point source. 27

Figure 2-5 Receiver path diagram for a single baseline including identical Gaussian filters on both receiver channels. 29

Figure 2-6 Observation scenario for a side-looking MISAR system with the system orbit height H_0, antenna array tilt angle θ_c and the focus point at X_0, Y_0. 32

Figure 2-7 Schematic of a MISAR baseline receiver path........ 33

Figure 2-8 Illustration of the geometric position of the antennas with the focus point at X_0, Y_0 and a signal source at X, Y........ 34

Figure 3-1 Illustration of a chief and deputy satellite in the Hill coordinate system. 40

Figure 3-2 Illustration of the relative inclination angle in the ECI frame. Modified from [40]. 43

Figure 3-3 Definition of the relative eccentricity vector. [40] 44

Figure 3-4 One relative orbit under the conditions $\Delta i = [0,10]^T$ and $\Delta e = [0,10]^T$ (green) and one relative orbit under the condition $\Delta i = [0,10]^T$ and $\Delta e =$

$[0,10]^T$ (yellow) in the Hill frame, taking into account the J_2 perturbations only. 49

Figure 3-5 One relative orbit under the conditions $\Delta i = [0,10]^T$ and $\Delta e = [0,10]^T$ (green) and one relative orbit under the condition $\Delta i = [10,0]^T$ and $\Delta e = [0,10]^T$ (yellow) in the Hill frame, taking into account J_2 perturbations and aerodynamic drag........ 51

Figure 4-1 High-level schematic of the various components and processing steps within the Satellite Swarm-Based Synthetic Aperture Radiometer (SSBSAR) software package. The PSF denotes the Point Spread Function, the IF denotes the Imaging Frame and the LIF the Local Imaging Frame. 55

Figure 4-2 Block diagram for the DLQR-controller for orbit maintenance of deputy satellites. 58

Figure 4-3 Atmospheric density to orbit altitude as a function of the mean solar flux. 63

Figure 4-4 Observation scenario, depicting the Hill frame and the LIF frame........ 65

Figure 4-5 Depiction of the Blackman weighting amplitude over the distance from the (u_λ, v_λ) plane origin. The distance from the origin is given in $q_{j,i}/\rho_{max}$..... 67

Figure 4-6 Cross-section of the probability density function and the carved torus which represents the combined hardbody........ 70

Figure 4-7 Illustration of ground-track drift as a result of aerodynamic drag and periodic maneuvers. Adopted from [76]. 71

Figure 5-1 3D RMS position accuracy for deputies on 500 m pendulum orbits with different degrees of J_2 -variance (Scaling parameter for weighting matrix is Rs=1000). 75

Figure 5-2 3D RMS position accuracy for deputies on 50 m pendulum orbits with different degrees of J_2-variance (Scaling parameter for weighting matrix is Rs=1000). 76

Figure 5-3 Fuel consumption per orbit for deputies on 50 m pendulum orbits with different degrees of J_2-variance (Scaling parameter for weighting matrix is Rs=1000). 76

Figure 5-4 3D RMS position accuracy for deputies on 50 m pendulum orbits with different degrees of J_2-variance (Maneuvers per orbit $F_p = 8$) and different scaling parameters. 77

Figure 5-5 Example of three deputy satellites (red filled circles) flying on GCO around the chief satellite (black circles) in the Hill frame. The optimization frame is spanned by the axes x_{2D}, y_{2D} which lie within the shared GCO orbit plane. The boresight vector specifies the direction of observation and is perpendicular to the optimization frame. 79

Figure 5-6 Illustration of weighting for the objective function by grid cell density $N_{cell,j,i}$. The different colors denote the weight of the sample. A light blue sample signifies a low weight, while a dark blue sample signifies a unity weight. 84

Figure 5-7 Optimized satellite configuration with $N = 16$ deputies in the optimization frame. 87

Figure 5-8 Spatial frequency coverage of optimized satellite configuration as used in the optimization algorithm (assuming constant deputy positions in Hill frame). Blue samples denote chief/deputy baselines, while pink or green samples denote deputy/deputy baselines. 88

Figure 5-9 Spatial frequency coverage of optimized satellite configuration as used in the optimization algorithm (pink) and as a result of a full orbit mechanics simulation (green). 89

Figure 5-10 Illustration of uniform weighting method. Colors signify the weight of the weighted sample depending on the local sample density. 90

Figure 5-11 Uniform weighting of spatial frequency samples by density. The spatial frequency coverage was taken from configuration of case study in 5.2. 91

Figure 5-12 FOV of the swarm-based synthetic aperture radiometer system on ground, including the definitions of the effective swath and the observation region. 92

Figure 6-1. Central array configuration on the chief satellite. The axes x_{2D}, y_{2D} from the optimization frame (see Figure 5-5) 97

Figure 6-2 Illustration of the relationship between the optimized deputy configuration (top row), sampling of the spatial frequency domain (middle row) and the PSF (bottom row) for $N = 16, 24, 32$ (columns) and a minimum intersatellite distance of 3.5 m. On the first row the configurations are shown in the optimization coordinate system. The second row shows the sampled spatial frequencies (blue: chief/deputy baselines, green: deputy/deputy baselines) in the (u_λ, v_λ) plane with the red circle denoting the distance ρ_{max}. Finally, the last row shows contour plots of the PSF respective arrays...........100

Figure 6-3 Illustration of the relationship between the optimized deputy configuration (top row), sampling of the spatial frequency domain (middle row) and the PSF (bottom row) for $N = 40, 48, 56$ (columns) and a minimum intersatellite distance of 3.5 m. On the first row the configurations are shown in the optimization coordinate system. The second row shows the sampled spatial frequencies (blue: chief/deputy baselines, green: deputy/deputy baselines) in the (u_λ, v_λ) plane with the red circle denoting the distance ρ_{max}. Finally, the last row shows contour plots of the PSF respective arrays...........101

Figure 6-4 Illustration of the relationship between the optimized deputy configuration (top row), sampling of the spatial frequency domain (middle row) and the PSF (bottom row) for $N = 80, 88, 96$ (columns) and a minimum intersatellite distance of 3.5 m. On the first row the configurations are shown in the optimization coordinate system. The second row shows the sampled spatial frequencies (blue: chief/deputy baselines, green: Deputy/Deputy baselines) in the (u_λ, v_λ) plane with the red circle denoting the distance ρ_{max}. Finally, the last row shows contour plots of the PSF respective arrays...........102

Figure 6-5 The solid lines denote the actual radial distribution of spatial frequency samples for the optimized configurations. The colors denote the number of satellites used in each configuration (blue for 16 deputies to yellow for 96 deputies). The dashed lines denote a Gaussian distribution of equal standard deviations for each configuration. 103

Figure 6-6 Resolution in km (solid line) and sensitivity in Kelvin (dashed line) for configurations with N deputies and $D_{min,D} = 3.5$ m...105

Figure 6-7 Mean Sidelobe Level in dB (solid line) and MBE in percent (dashed line) for configurations with N deputies and $D_{min,D} = 3.5$ m...106

Figure 6-8 Degree of decorrelation on the largest baselines for configurations with N deputies and $D_{\text{min,D}} = 3.5$ m. 107

Figure 6-9 Configuration of the swarm-based synthetic aperture radiometer with $N = 16$ and $D_{\text{min,D}} = 3.5$ m. 108

Figure 6-10 Configuration of the swarm-based synthetic aperture radiometer with $N = 96$ and $D_{\text{min,D}} = 3.5$ m. 109

Figure 6-11 Deputy position accuracy as 3D root mean square (RMS) error [m] for the formation of $N = 96$ deputies and $D_{\text{min,D}} = 3.5$ m. 109

Figure 6-12 Accumulated collision probability of each satellite per orbit for the formation of $N = 96$ deputies and $D_{\text{min,D}} = 3.5$ m. 110

Figure 6-13 Collision probability of each satellite pair per orbit for the formation of $N = 96$ deputies and $D_{\text{min,D}} = 3.5$ m. 111

Figure 6-14 Average fuel consumption Δv [cm/s] for formation maintenance per orbit for the formation of $N = 96$ deputies and $D_{\text{min,D}} = 3.5$ m. 112

Figure 6-15 Average deputy fuel consumption Δv [cm/s] for formation maintenance per orbit for the formation of $N = 32, 56{,}96$ deputies, $D_{\text{min,D}} = 3.5$ m and different control periods T_{pwm}. 115

Figure 6-16 Average deputy position accuracy 3D RMS [m] for formation maintenance per orbit for the formation of $N = 32, 56, 96$ deputies, $D_{\text{min,D}} = 3.5$ m and different control periodsT_{pwm}. 116

Figure 6-17 Highest probability of collision per orbit of any deputy during formation maintenance for the formation of $N = 32{,}56{,}96$ deputies, $D_{\text{min,D}} = 3.5$ m and different control periods T_{pwm}. 116

Figure 6-18 Position accuracy 3D RMS during formation maintenance for the formation of $N = 56$ deputies and $D_{\text{min,D}} = 3.5$ m over the position knowledge accuracy and velocity knowledge accuracy. 118

Figure 6-19 Highest probability of collision per orbit of any deputy during formation maintenance for the formation of $N = 56$ deputies and $D_{\text{min,D}} = 3.5$ m over the position knowledge accuracy the velocity knowledge accuracy. 119

Figure 6-20 Fuel consumption per orbit and deputy for formation maintenance for the formation of $\mathrm{N} = 56$ deputies and $\mathrm{D_{min,D}} = 3.5\ \mathrm{m}$ over the position knowledge accuracy and the velocity knowledge accuracy....120

Figure 6-21 Illustration of the optimized deputy configuration for $\mathrm{N} = 56$ deputies in the optimization coordinate system. 121

Figure 6-22 The solid lines denote the actual radial distribution of spatial frequency samples for the optimized configurations. The colors denote the number of satellites used in each configuration (blue for the configuration with $\mathrm{Dmin, D} = 2\ \mathrm{m}$ and yellow for the configuration with $\mathrm{D_{min,D}} = 6.5\ \mathrm{m}$. The dashed lines denote a Gaussian distribution of equal standard deviations for each configuration. 122

Figure 6-23 Resolution in km (solid line) and sensitivity in Kelvin (dashed line) for configurations with varying minimum inter-deputy distance constraints $\mathrm{D_{min,D}}$ and $\mathrm{N} = 56$ satellites....123

Figure 6-24 Illustration of an optimized deputy configuration (top row) under various minimum inter-deputy distance constraints, sampling of the spatial frequency domain (middle row) and the PSF (bottom row) for $\mathrm{D_{min,D}} = 2\ \mathrm{m}, 4\ \mathrm{m}, 6.5\ \mathrm{m}$ and $N = 56$ deputies. On the first row the configurations are shown in the optimization coordinate system. The second row shows the sampled spatial frequencies (blue: chief/deputy baselines, green: deputy/deputy baselines) in the $\mathrm{u_\lambda}, \mathrm{v_\lambda}$ plane with the red circle denoting the distance $\mathrm{\rho_{max}}$. Finally, the last row shows contour plots of the PSF respective arrays. 124

Figure 6-25 Average probability of collision per orbit over all deputies (blue line) and maximum probability of collision per orbit of any deputy (red dashed line) for the formation of $\mathrm{N} = 56$ deputies with varying inter-deputy distances. .126

Figure 6-26 Resolution in km (solid line) and the revisit time in days (dashed line) for configurations in varying orbit height and $\mathrm{N} = 56$ satellites....127

Figure 6-27 Average position accuracy for the formation of $\mathrm{N} = 56$ deputies with varying orbit height and difference in ballistic coefficient between deputies and the chief satellite....129

Figure 6-28 Highest probability of collision per orbit over all deputies for the formation of $N = 56$ deputies with varying orbit height and difference in ballistic coefficient between deputies and the chief satellite. 130

Figure 6-29 Average fuel consumption per orbit and deputy for the formation of $N = 56$ deputies with varying orbit height and difference in ballistic coefficient between deputies and the chief satellite. 131

Figure 6-30 Time between semimajor-axis adjustments T_s with varying orbit height and difference in ballistic coefficient between deputies and the chief satellite for a $\Delta a_{GT} = 8$ m semimajor axis orbital adjustment. 132

Figure 6-31 Process diagram for the design method for the orbits of the satellite swarm-based aperture synthesis radiometer. 136

Figure A.1-1 Relative orbital motion of a deputy satellite in the Hill frame, with relative orbital elements set to $\Delta i = [10,0]^T$ and $\Delta e = [10,0]^T$ as given by STK (green) and the SSBSAR (purple)... 157

Figure A.1-2 Discrepancies between the STK and SSBSAR orbital simulations for the relative orbital motion of a deputy satellite, with relative orbital elements set to $\Delta i = [10,0]^T$ and $\Delta e = [10,0]^T$ under J_2 perturbations only. 158

Figure A.1-3 Discrepancies between the STK and SSBSAR orbital simulations for the relative orbital motion of a deputy satellite, with relative orbital elements set at $\Delta i = [0,10]^T$ and $\Delta e = [0,10]^T$ underJ_2 perturbations only. 159

Figure A.1-4 Relative orbital motion of a deputy satellite in the Hill frame, with relative orbital elements set at $\Delta i = [0,10]^T$ and $\Delta e = [0,10]^T$ as given by STK (red) and the SSBSAR (turquoise) under J_2 and aerodynamic perturbations. 159

Figure A.1-5 Discrepancies between the STK and SSBSAR orbital simulations for the relative orbital motion of a deputy satellite, with relative orbital elements set at $\Delta i = [0,10]^T$ and $\Delta e = [0,10]^T$ under J_2 and aerodynamic perturbations. 160

Figure A.1-6 Antenna configuration as investigated by Camps [48]. 163

Figure A.1-7 PSF of antenna configuration investigated by Camps [48] generated with the SSBSAR. 164

LIST OF ACRONYMS

AAReST	Autonomous Assembly Reconfigurable Space Telescope
AMSR	Advanced Microwave Scanning Radiometer
ARU	Antenna Receiver Unit
ATA	Allen Telescope Array
CESBIO	Centre d’Etudes Spatiales de la Biosphère
CIMR	Copernicus Imaging Microwave Radiometer
CNES	Centre National d'Etudes Spatiales
CPOD	CubeSat Proximity Operations Demonstration
CU	Correlation Unit
DARE	Discrete Algebraic Riccati Equation
DFT	Discrete Fourier Transform
DGNSS	Differential Global Navigation Satellite System
DLR	German Aerospace Center
DLQR	Discrete-time Linear Quadratic Regulator
EKF	Extended Kalman Filter
ESA	European Space Agency
FFT	Fast-Fourier Transform
FOV	Field of View
GCO	General Circular Orbit
GNB	Generic Nanosatellite Bus
GNC	Guidance, Navigation and Control
GNSS	Global Navigation Satellite System
GSOC	German Space Operations Center
HCW	Hill-Clohessy-Wiltshire

HPOP	STK High Precision Orbit Propagator
IF	Imaging Frame
JPL	Jet Propulsion Laboratory
LEO	Low Earth Orbit
LIF	Local Imaging Frame
LICEF	Lightweight Cost-Effective Front-end
LQR	Linear Quadratic Regulator
MBE	Main Beam Efficiency
MEMS	Microelectromechanical systems
MIB	Minimum Impulse Bit
MIRAS	Microwave Interferometric Radiometer with Aperture Synthesis
MISAR	Motion Induced Synthetic Aperture Radiometer
MSLL	Mean Sidelobe Level
NASA	National Aeronautics and Space Administration
NIR	Noise Injection Radiometer
OBC	On-Board Computer
OCSD	Optical Communications and Sensors Demonstration
PISAR	Position Induced Synthetic Aperture Radiometer
PSF	Point Spread Function
RAAN	Right Ascension of the Ascending Node
RMS	Root Mean Square
SLL	Sidelobe Level
SMAP	Soil Moisture Active and Passive
SMOS	Soil Moisture and Ocean Salinity
SSBSAR	Satellite Swarm-Based Synthetic Aperture Radiometer
SSO	Sun-Synchronous Orbit

STK	Satellite Tool Kit
VLBI	Very-Long-Baseline Interferometry

LIST OF SYMBOLS (CAPITAL LATIN LETTERS)

$\boldsymbol{A}$	Satellite drag area
A_e	Effective aperture area of antenna
AF_{eq}	Equivalent array factor
B	Bandwidth
B_C	Satellite ballistic coefficient
$B_{1/2}$	Full bandwidth of the signal at half maximum level
$\boldsymbol{B}$	Baseline vector
C	Aerodynamic coefficient of satellite
$\boldsymbol{C_\alpha}$	Rotation matrix for thrust vector error rotation
C_D	Satellite drag coefficient
D	Correlator distance
D_g	Weights for uniform weighting
$D_{min,C}$	Minimum deputy-chief distance for numerical optimization
$D_{min,D}$	Minimum inter-deputy distance for numerical optimization
F	Antenna voltage pattern
F_P	Maneuver frequency
$F_{10.7}$	Mean solar flux over 90 days
$F_{10.7a}$	Solar flux from the previous day
GNC_{Pos}	Accuracy of GNC position
GNC_{Vel}	Accuracy of GNC velocity
H	Frequency response of the passband filter
H_0	Satellite system height above the Earth
$HPBW_{El}$	Half-power beamwidth in elevation
$HPBW_{AZ}$	Half-power beamwidth in azimuth

I	Grey body spectral brightness intensity
I_{SP}	Specific impulse of thrusters
J_2	Zonal harmonic coefficient
$\boldsymbol{K}$	GNC Control Matrix
L	Angular orbit momentum
L_c	Side length of the deputy
L_d	Maximum ground track drift
L_x, L_y	Swath widths in azimuth, elevation
L_{OF}	Area size within optimization frame
M	Orbit mean anomaly
N	Number of deputies in configuration
N_B	Number of baselines
N_k	Total number of possible deputy collision partners
N_S	Total number of samples collected
N_T	Number of timesteps
N_{TR}	Number of ARU
N_{cell}	Number of sample points in grid cell
N_W	Number of samples within weighting radius
P	Total amount of measured power
P_m	Covariance matrix of position uncertainty for deputy m
$P_{C,k}$	Collision probability per orbit for deputy pair k
$P_{C,m}$	Probability of collision for deputy m to any other satellite
$P_{C,Max}$	Maximum permissible collision probability
$\boldsymbol{Q}$	LQR state cost matrix
R	Correlator output
$\boldsymbol{R}$	LQR cost matrix

R_C	Deputy collision radius
R_D	Deputy data rate
R_E	Radius of the Earth
R_S	LQR input cost matrix scaling factor
$\hat{S}$	Flux density estimate
T	Blackbody temperature
$\hat{T}$	Brightness temperature estimate
T_B	Brightness temperature
T_{Black}	Blackman window tapering function
T_{pwm}	Time between GNC control periods
T_{on}	Thruster on time
$T_{on,Min}$	Minimal thruster on time as defined by MIB
T_s	Time between orbit semi-major axis adjustments
T_{sys}	System noise temperature
U_{max}	Maximum thrust per unit mass delivered by the thruster
V	Visibility
$\bar{W}$	Time-averaged Baseline weights
W	Time-dependent baseline weights
X, Y, Z	Imaging Frame coordinates
X_c, Y_c	Point of intersection between antenna boresight axis and ground

LIST OF SYMBOLS (SMALL LATIN LETTERS)

$\boldsymbol{a}$	Orbit semi-major axis
$\boldsymbol{a}$	Acceleration vector
b_e	Magnitude of thrust error

c	Speed of light
d	Distance to origin in optimization frame
e	Orbit eccentricity
$\boldsymbol{e}$	Relative eccentricity vector
f	Measurement frequency
f_c	Center frequency
i	Orbit inclination
$\boldsymbol{i}$	Relative inclination vector
k_B	Boltzmann constant
k_{J2}	J_2-dependent coefficient
l, m	Direction cosines
m_s	Satellite mass
n	Orbital rate
$\boldsymbol{q}$	Spatial frequency vector
$\boldsymbol{r}$	Vector from spacecraft to Earth center
r_W	Weighting radius for uniform weighting
$\boldsymbol{s}$	Vector between antenna and source
t	time
t_{obs}	Duration of observation
t_c	Half the duration of observation
t_s	Sample integration time
v_a	Orbital speed
v_A	Air speed
$\boldsymbol{u}$	Error-free thrust vector
$\boldsymbol{u_\alpha}$	Error-adjusted thrust vector (with error angle only)
$\boldsymbol{u_e}$	Full error-adjusted thrust vector

u_l	Orbit argument of latitude
u_N	Nominal thrust
$u_\lambda, v_\lambda, w_\lambda$	Spatial frequencies normalized to wavelength
x, y, z	Cartesian coordinates

LIST OF SYMBOLS (GREEK LETTERS)

$\boldsymbol{\alpha_0}$	Argument of latitude in optimization frame
α_e	Magnitude of error in thrust angle
γ	J_2-dependent factor
δX_k	Covariance of the distance between a deputy pair
δX_{ref}	Nominal distance between a deputy pair
Δa_{GT}	Magnitude of regular semi-major axis adjustment
$\boldsymbol{\delta\alpha}$	Set of relative orbital elements
$\Delta\lambda$	In-track shift between satellites
$\Delta\tau$	Signal time delay
$\mathbf{\Delta i}$	Relative inclination vector
$\mathbf{\Delta e}$	Relative eccentricity vector
ε_{min}	Stop criterium for numerical optimization of objective function
λ	Wavelength
λ_c	Center wavelength of measurement
η_e	Eccentricity factor
θ	Relative ascending node
θ_c	Chief antenna array cross-track tilt angle
θ_w	Angular resolution of radiometer system
$\varTheta_0$	Off-boresight angle in one dimension

Θ, Φ	Off-boresight angles in two dimensions
μ	Standard gravitational parameter
ν	Orbit true anomaly
φ	Orientation of relative eccentricity vector
Ψ	Degree of J_2-variance
ρ	Atmospheric density
ρ_{max}	Distance from the origin in the spatial frequency domain
σ	Bandwidth factor
σ_G	Gaussian weights for deputy distribution
σ_k	3D RMS position accuracy covariance of satellite pair k
σ_m	3D RMS accuracy of position control for deputy m
σ_S	Standard deviation for Gaussian-fit distribution of (u_λ, v_λ) samples
τ_{eff}	Effective integration time
$\tilde{X}$	Deputy position uncertainty
$\boldsymbol{X}$	Deputy true state in Hill frame
$\boldsymbol{X_{ref}}$	Deputy reference state in Hill frame
$\boldsymbol{X_e}$	Difference between true and reference satellite state in the Hill frame
$\boldsymbol{X_{2D}}$	Position of deputy on the 2D optimization frame
ω	Orbit argument of periapsis
ω_E	Rotation rate of the Earth
ω_x, ω_z	Spacecraft rotation rates around Hill frame axes
Ω	Orbit Right Ascension of the Ascending Node
Ω_A	Antenna solid angle
Ω_m	Main lobe solid angle
Ω_P	Antenna pattern solid angle
$\Omega_{\boldsymbol{s}}$	Solid angle

Ω_{Pix}	Pixel solid angle

1 INTRODUCTION

1.1 Why a swarm-based aperture synthesis radiometer?

Passive microwave remote sensing relies on the measurement of electromagnetic radiation emitted from physical sources in the microwave domain. The characteristics of thermal electromagnetic radiation of physical objects are strongly connected to the object's physical properties, e.g., physical temperature, surface roughness, permittivity and water salinity. Satellite-based passive microwave remote sensing is a technique that has been used to deepen our scientific understanding of hydrological processes on Earth, since the 1970s. The first major satellite carrying a passive-Microwave Radiometer [1] was Nimbus 5, launched in December 1972 by the National Aeronautics and Space Administration (NASA) of the United States. This mission provided imagery on sea ice concentrations at the Earth's poles. Since then, various spacecraft have carried scanning radiometers into orbit, such as the Advanced Microwave Scanning Radiometer (AMSR) on board the NASA Aqua satellite. The AMSR instrument, operating in the range of 6.9 to 89 GHz, is widely recognized as significantly contributing towards a deeper understanding of weather and climate processes and the Earth water and energy cycle. In particular, information on soil moisture and sea surface salinity is critical to high-fidelity numerical climate models. Space-based radiometers operating at a protected frequency band within L-band (1,4 – 1,427 GHz) have the ability of penetrating into the Earth surface, which is required for the measurement of soil moisture. However, the disadvantage of measuring at lower frequency bands lies in the reduced angular resolution.

The Soil Moisture and Ocean Salinity (SMOS) satellite represents a significant milestone in space-based radiometry [2]. It is the first satellite to make use of the aperture synthesis technique. Aperture synthesis enables radiometers to achieve high angular resolutions by the correlation of signals from an array of multiple antennas without mechanical scanning. By using multiple individual antennas with smaller apertures, a larger aperture can be "synthesized". The SMOS satellite operates from a sun-synchronous repeat orbit at 755 km and is capable of scanning the Earth with a spatial ground resolution of up to 35 km [3]. While the SMOS satellite has been able to provide important scientific data at resolutions sufficient for various applications in hydrology and Earth science, a better spatial resolution could offer improvements to existing applications and even enable new ones [4]. In radiometer systems, the spatial ground resolution at a given measurement frequency can only be increased by an increase of the diameter of the synthesized antenna array, which is given by the longest baselines between two individual antennas. The SMOS satellite antenna array with its three folding booms of 4-meter length however, already has approached a prohibitive size for the physical envelope of current launchers. While it is conceivable that larger monolithic array structures may be created with novel in-orbit manufacturing technology, e.g. additive manufacturing [5], [6], large interferometric antennas might also be created by the placement of individual antennas on multiple spacecraft, i.e. on satellite swarms. These satellites would fly in close-proximity to each other in Low Earth Orbit (LEO) and form a giant dynamic antenna array. This idea has been investigated in geostationary orbit [7], in LEO for astronomic purposes [8] and conceptually for Earth observation [9]. A satellite swarm-based aperture synthesis radiometer in low-Earth orbit for Earth observation applications has however never been investigated in-depth to date. In light of advancing technologies in nanosatellite formation flight, nanosatellite propulsion, data handling and inter-satellite links, it is possible a swarm-based radiometric system could help advance Earth science.

1.2 Applications of L-band satellite-based radiometry

Soil moisture and ocean salinity mapping by Earth observation satellites has contributed significantly towards a better understanding of the Earth's climate and hydrosphere. Applications that have directly exploited this data range from weather forecasting to water resource management [10].

Remote sensing of soil moisture and ocean salinity is operationally performed by passive microwave instruments at L-Band frequency. Measurements within a 27 MHz frequency band at 1.4 GHz exhibit both a high sensitivity to salinity and soil moisture [11], [12]. The key advantage of the low frequency band is the high surface penetration depth of up to 5 cm, enabling the derivation of key physical properties from the top surface layer. Furthermore, the 1.4 GHz – 1.427 GHz band is exclusively allocated for radio astronomy and passive microwave Earth sensing and is thus protected from military, commercial and private use. The following sections will provide an overview of the key applications a swarm-based aperture synthesis radiometer could support.

1.2.1 Soil moisture

Soil moisture plays an important role in surface-atmosphere interactive processes. It controls the exchange of water and energy through plant transpiration and evaporation [13] and holds great importance for hydrological and biochemical processes. In general, a more accurate climate model requires the availability of accurate and global data on soil moisture, but some practical applications include:

- The development of weather patterns and precipitation is strongly influenced by soil moisture. Thus, numerical weather prediction models can be significantly improved by information on soil moisture.
- Soil moisture provides information about the filling of the water storage in the soil and therefore about the potential occurrence of floods and droughts.
- Soil moisture data can be used to forecast crop yields, required irrigation and reservoir management.

The retrieval of soil moisture data is based on the estimation of the soil emissivity from the measured brightness temperature. Dual-polarization measurements of the brightness temperature are required due to the fact that two measurements at different polarizations are needed for the soil emissivity model. The volumetric moisture content within the first few centimeters of the soil can be estimated from the soil emissivity using empirical dielectric models. This retrieval process is described in detail in reference [14]. The radiometric sensitivity required for the measurement of soil moisture is relatively modest in the order of three Kelvin [15].

1.2.2 Sea surface salinity retrieval

Sea surface salinity corresponds to the concentration of salt in sea water at the sea surface. It is measured in practical salinity units (psu), which refer to the mass of salt per water volume. Along with soil moisture, sea salinity plays a crucial role in ocean dynamics, global hydrology and the Earth's climate system. Precipitation, evaporation and global water currents affect local levels of salinity in the ocean. Ultimately a better understanding of sea salinity will help model climate change and improve the prediction of weather phenomena.

As opposed to the relatively large penetration depth of soil, the penetration depth of water at L-band is only about one centimeter [14]. Sea surface salinity is best measured with low frequencies to avoid the influence of wind-related factors, such as sea surface roughness. A high radiometric sensitivity ΔT of approx. 0.2 Kelvin is required for the sensing of sea surface salinity.

1.2.3 Sea ice thickness

Information on the global occurrence of sea ice is of crucial importance to improving our understanding of the Earth's climate. Firstly, it represents an important input for climate modelling along with soil moisture and sea surface salinity. Sea ice greatly influences the amount of heat exchanged between the atmosphere and the ocean. Especially, when covered with snow, it strongly reduces the heat transfer capability and increases ocean albedo [16]. Secondly, data on sea ice concentration is essential for the planning of shipping routes at the Earth's poles. Up-to-date maps of sea ice concentration can reduce the risk of hitting icebergs.

Since electromagnetic emissions from sea ice at frequencies of around 1.4 GHz originate in part from the deeper surface layers, they can be measured well using satellite-based L-band radiometry. In 2010, Kaleschke et al. [17] developed a model for SMOS that is capable of retrieving sea-ice thickness based on L-band radiometric measurements. This model first determines the emissivity of the sea ice before deriving the thickness from measured brightness temperatures. Sea ice with a thickness of up to 1.5 m can be detected using this method. While some sources claim that a radiometric sensitivity of around 0.5 Kelvin [4] is needed for sea-ice thickness retrieval, it seems that instruments with lower radiometric sensitivities in the order of a few Kelvin, could be of scientific value as well [17].

1.3 A review of state-of-the-art technology

This section outlines the state-of-the-art technology relevant to this thesis. In particular the areas relevant are satellite-based L-band radiometry, nanosatellite formation flying technology and previous concepts for swarm-based aperture synthesis radiometry. An overview is provided of the important L-band satellite-based radiometric missions and mission concepts that have been proposed for a distributed radiometric system in space.

1.3.1 Passive microwave remote sensing at L-band

1.3.1.1 Soil Moisture and Ocean Salinity (SMOS) mission

The Soil Moisture and Ocean Salinity (SMOS) of the European Space Agency (ESA) was successfully launched on November 2, 2009. It is the second mission of ESA's Earth Explorer Opportunity Programme and the first space mission dedicated to soil moisture and sea surface salinity measurements at L-band (1.4 GHz). It was placed in a 6 AM/6 PM Sun-Synchronous Orbit (SSO) at a height of 750 km with a 98.4° inclination. SMOS is also the first and so far, only mission to carry a two-dimensional interferometric radiometer array. The payload, called the Microwave Interferometric Radiometer with Aperture Synthesis (MIRAS) was jointly developed by the Centre National d'Etudes Spatiales (CNES), Centre d'Etudes Spatiales de la Biosphère (CESBIO) and the Institut de Ciencies del Mar-Consejo Superior de Investigaciones Cientificas. The MIRAS instrument is a foldable correlator array in Y-configuration with three booms carrying a total of 66 Lightweight Cost-Effective Front-end (LICEF) units and 6 Noise Injection Radiometers (NIR) for calibration purposes. Each MIRAS arm has a length of 4 meters and is aligned with 22 LICEF, spaced at 0.875 wavelengths. The brightness temperature map of the imaged radiation distribution is derived by cross-correlating the signals from all LICEF units. The MIRAS correlator array is tilted at a 32.5° angle towards the in-flight direction.

Figure 1-1 An artist view of the SMOS satellite [3].

The instrument takes snapshots over an integration time of 1.2 s at dual polarization, enabling a radiometric snapshot sensitivity of up to 2.5 Kelvin over the ocean [2]. Temporal averaging is applied in post-processing to improve the radiometric sensitivity of the instrument to approx. 0.2 Kelvin. The spatial resolution of SMOS data reaches 35 km in boresight direction.

By 2020, SMOS has lasted a decade in orbit and remains an important source of soil moisture and sea surface salinity data. Not only was SMOS able to demonstrate the critical interferometric radiometer technology, it significantly contributed to the scientific understanding of the global climate and Earth's hydrology [18]. With a revisit time of one to three days, SMOS still provides benchmark data for numerous applications such as drought monitoring, weather forecasting and agricultural management.

1.3.1.2 Aquarius on the SAC-D satellite

The argentine (Satellite de Aplicaciones Cientificas) SAC-D satellite was launched on the 10th of June 2011. It was placed into an SSO at 657 km with an ascending node mean local time of 6 pm, repeating its ground track every seven days. The satellite's primary instrument was Aquarius, a push-broom dual-polarization radiometer built by NASA's Jet Propulsion Laboratory (JPL). Its antenna system consisted of three 50 cm feed horns whose beams were directed at a 2.5-meter reflector antenna. The reflector antenna focused the feed horn beams onto an equilateral triangle around a focus point that was positioned slightly in front of the spacecraft in-track direction. The Aquarius instrument suite offered an especially high radiometric sensitivity (0.1 Kelvin) for the primary mission objective, the measurement of sea surface salinity [19]. A special feature of Aquarius' mission was the correction of the radiometer sea surface salinity measurements by additional surface roughness measurements provided by an S-band scatterometer that was also on-board the Aquarius satellite. While, the native spatial ground resolution of Aquarius reached 76 km, the resulting sea surface salinity maps were made available at a resolution of 150 km. The entire satellite ceased operation in June 2015.

Over its lifetime, Aquarius was successful in providing global sea surface salinity maps with a radiometric sensitivity that outpaced all other historic missions. It succeeded in showing how ocean salinity changes seasonally and regionally and significantly contributed to the validation and improvement of numerical climate models.

1.3.1.3 Soil Moisture Active and Passive (SMAP) mission

The launch of the NASA Soil Moisture Active Passive (SMAP) Mission represented another significant milestone for space-based soil moisture sensing. The particular novelty of SMAP was the possibility of integrating data from a concurrently operating L-band radar and L-band radiometer for combined measurements. The key advantage of conducting coincident radiometer and radar measurements was the possibility of deriving soil moisture estimates at a spatial ground resolution of up to 9 km. This downscaled ground resolution was achieved by refining the native brightness temperatures from the dual-polarization radiometer by using SAR measurements that were available at a spatial resolution of 3 km [20]. The SMAP satellite was launched on the 31 January 2015 into a 6 AM/6 PM SSO at 685 km, enabling global coverage with a revisit time of 2-3 days [21]. The SMAP radiometer operates by conically scanning the Earth, with a 6 m aperture reflector antenna and L-band feed that is shared with the SMAP SAR instrument. The conical scanning delivers a resolution footprint of around 40 km, a 1000 km wide swath and a radiometric sensitivity of 1.3 K. While SMAP does not reach the low sensitivity of the previous Aquarius mission, coarse measurements of sea surface salinity are nevertheless possible.

Despite the cessation of operation by the radar in 2015, SMAP is still delivering global soil moisture information to date. Applications that are using SMAP data include weather and climate forecasting, agricultural management, wildfire containment amongst others.

1.3.1.4 Copernicus Imaging Microwave Radiometer (CIMR)

The CIMR satellite mission is currently being studied by ESA as a candidate mission for the Copernicus series satellites. Its primary mission objective would be to improve the monitoring of the Earth's polar regions and the understanding of the effects of global warming. In particular, the satellite would measure ice thickness, snow coverage, sea surface temperature, wind speeds, sea surface salinity and soil moisture. The CIMR suite of instruments would include an L-band radiometer utilizing a reflector foldable antenna shared with other instruments. The target footprint for the dual-polarization L-band system is 65 km, and the required radiometric sensitivity would be 0.2 K.

The CIMR satellite would provide images of the Earth's poles on a daily basis and data on soil moisture and sea surface salinity on a global scale. The mission is currently in the Phase B of development and will be launched no earlier than 2026 into an SSO at 824 km. [22]

1.3.1.5 Summary

Satellite-based L-band radiometry has been an important source for Earth science since the launch of the SMOS satellite. Soil moisture and sea surface salinity have proven to be important parameters for a large range of environmental applications and there is a consensus among scientists that uninterrupted access to this data will be important. Table 1-1 summarizes the key system parameters of the current and upcoming radiometry missions. While the technical implementations of the radiometric systems vary, research has verified a striking agreement of the soil moisture and sea surface salinity data they generate [23]. The spatial ground resolutions of the existing systems do not reach below 35 km.

Table 1-1 System parameters of key L-band radiometry missions

	SMOS	*Aquarius*	*SMAP*	*CIMR*
Center Frequency	*1413.5 MHz*	*1413 MHz*	*1413.5 MHz*	*1413 MHz*
Bandwidth	*20 MHz*	*27 MHz*	*24 MHz*	*27 MHz*
Swath width	*914 km*	*390 km*	*1000 km*	*>1900 km*
Revisit time	*1-3 days*	*7 days*	*2-3 days*	*Daily for Poles*
Imaging technique	*Push-broom*	*Push-broom*	*Conical scan*	*Push-broom*
Incidence angle	*0°-55°*	*28.7°, 37.8°,45.6°*	*40°*	*TBD*
Orbit	*750 km SSO*	*657 km SSO*	*685 km SSO*	*824 km SSO*
Radiometric Res	*0.2 K*	*0.1 K*	*1.3 K*	*< 0.2 K*
Spatial Res.	*35 km*	*76 km*	*40 km (native)*	*65 km*

1.3.2 Close-proximity formation flight for nanosatellites

A key enabling technology for the satellite swarm-based aperture synthesis radiometer concept is close-proximity formation flying for nanosatellites. Significant progress has been made in the last decade towards enabling an accuracy of formation flight on nanosatellites, that is comparable to that realized with larger satellites.

At time of writing, the benchmark nanosatellite mission for high-accuracy formation flight is CanX-4&5 of the University of Toronto. CanX-4&5 was a technology demonstration mission explicitly aimed at demonstrating sub-meter formation flight of CubeSat-type satellites for low Δv requirements. The two satellites CanX-4 and CanX-5, with a 20 cm cubic form factor were launched in 2014 and succeeded in showing that nanosatellites placed on relative orbits with an inter-satellite distance of 50 m could maintain a relative position accuracy below 1 m for consecutive days [24]. The satellites' Guidance, Navigation and Control (GNC) system was based on the estimation of the satellite state using differential measurements from high-precision Global Navigation Satellite System (GNSS) receivers, an orbit propagation model and a custom low-thrust cold-gas propulsion system.

Since CanX-4&5 two other significant CubeSat proximity formation flying missions have been launched; the TW-1 mission and the Optical Communications and Sensors

Demonstration (OCSD). The TW-1 mission of the Chinese Academy of Sciences was launched 2015 with the objective of conducting experiments on satellite networks. It consisted of one 3U CubeSat and two 2U CubeSats flying at 2.5 km distance. The attained position accuracy for formation flight was given as a relatively coarse 579 m [25]. The OCSD mission involved the two AeroCube OCSD-B/C spacecraft tasked with demonstrating novel inter-satellite optical communication equipment. This mission, launched in 2017, succeeded in attaining a 10 m position accuracy at a 200 m minimum range [26]. While the objectives of these missions were not to demonstrate advances in formation flying itself, they showed that formation flight technology for nanosatellites had matured to a level where it could be employed successfully for scientific purposes.

Currently two missions are in the development pipeline that could exceed the accuracy of formation flight demonstrated with CanX-4&5. These are the NASA CubeSat Proximity Operations Demonstration (CPOD) mission and the Autonomous Assembly Reconfigurable Space Telescope Flight Demonstrator (AArest) mission of the California Institute of Technology. Both missions are set to launch in 2021 and will demonstrate autonomous docking between 3U CubeSats. The position accuracy required for the docking procedure of AArest is given as 5 cm [27]. It can be expected that the CPOD mission will also have to adhere to similar GNC accuracy requirements.

In summary, past nanosatellite missions have not only proven the feasibility of sub-meter CubeSat formation flight over longer timeframes, they have shown that capable GNC systems can be combined with valuable scientific experiments on CubeSats. It is probable that the future CPOD and AArest missions will further mature the technology required for even more precise and miniaturized GNC modules.

1.3.3 Satellite swarm-based aperture synthesis radiometry

Aperture synthesis technology has been used in astronomic applications for almost a century. The most well-known astronomical radio telescopes that use aperture synthesis are the Very Large Array (VLA) and the Atacama Large Millimetre Array (ALMA) telescopes. These telescopes consist of up to 66 parabolic antennas, spread out over large areas. With advances in formation flying and microsatellite technology, some concepts have been proposed that aim to translate the idea of aperture synthesis radio telescopes to space [9], [8], [28]. While all these concepts have in common, that they propose to deploy a larger number of satellites flying in close-proximity formation, their proposed applications differ.

The Formation-Flying Interferometer (FFI) proposal for the Terrestrial Planet Finder mission (TPF) by NASA was the first space-based interferometric radio telescope concept that was seriously investigated. The objective of the proposed mission was to find and characterize Earth-like exoplanets. The concept involved five spacecraft, carrying large parabolic antennas, flying in distances of 8 m to 150 m to each other on a L2 Halo orbit. The spacecrafts would have been operated as one large infrared telescope. Although the mission was finally cancelled in 2011, it prompted studies into enabling technologies for high precision formation flight [29], [30]. A formation flight position control accuracy of 2 cm would have been required for the realization of the FFI concept. A similar study called InfraRed Astronomy Satellite Swarm Interferometry (IRASSI) was conducted in 2019, by the Bundeswehr University Munich. The IRASSI concept would have involved five radio telescopes, equipped with reflectors of 3.5 m diameter in a Halo orbit around the L2 Lagrange point [28].

Another mission, called Orbiting Low Frequency Antennas for Radio Astronomy (OLFAR) was proposed by researchers from the University of Delft in 2009. OLFAR was the first proposal explicitly envisioning a swarm of nanosatellites, operating as a radio telescope. The envisioned frequency band for the OLFAR mission would be between 30 kHz to 30 MHz [31]. OLFAR was proposed to study the interstellar medium and exoplanets from space, to avoid the distortion brought upon the Earth's ionosphere into observations at these wavelengths. As part of OLFAR, a swarm of 50 nanosatellites would form an autonomous sensor-network orbiting Earth's moon. Each nanosatellite would carry its own low frequency receiver forming baselines up to 100 km for a combined radio telescope. Despite a decade having passed since the proposal of OLFAR, renewed interest in low frequency radio astronomy and progress with nanosatellite technology has sustained hopes of eventually funding the mission [32].

Placing spacecraft in a Halo orbit at the L2 Lagrangian point holds the particular advantage that very few orbital perturbations impede on a satellites state. In this environment, larger constellations of satellites can thus be realized without the necessity of high-frequency orbit corrections counteracting external forces. In LEO however the orbital trajectory of a satellite is subject to strong disturbances caused by Earth oblateness, residual aerodynamic drag and other forces. Thus, maintaining a stable and closed swarm formation in LEO requires an approach involving stronger and more frequent thruster impulses, along with more precise orbit-prediction capabilities on-board the spacecraft. In-depth research into satellite swarm-based radio telescope architectures in LEO was conducted by the NASA JPL, resulting in the Swarms of Silicon Wafer Integrated Femtosatellites (SWIFT) approach [8]. SWIFT Swarms would involve a large number (100 s – 1000 s) of 100 g femtosatellites, fully equipped with a 3-axis GNC system (including propulsion), on concentric relative orbits. In this context the JPL developed decentralized satellite-swarm GNC control algorithms for the optimal guidance and reconfiguration of a greater number of satellites [33]. To the author’s knowledge, it also was the first study to investigate the orbit mechanics of a satellite swarm aperture synthesis radiometer in LEO.

The concept of a swarm-based aperture synthesis radiometer in LEO for Earth observation, i.e., for the application to sea surface salinity measurements, was first conceptually explored by Schwartz et al. [9]. Building on the Motion Induced Synthetic Aperture Radiometer (MISAR) concept of Camps [34], Schwartz et al. explored the possibility of extending a central “SMOS-like” array in Y-configuration with receivers on individual satellites, on closed orbits around the central array. Various orbit configurations and their resulting coverages of the spatial frequency domain were explored for up to 108 satellites. This study, however, did not investigate important aspects of the swarm-based aperture synthesis radiometer. These include control strategies for the individual satellites, the feasibility of placing satellites in close proximity from a GNC perspective, the feasibility of ensuring a sufficient system lifetime in light of the large implementation effort due to the system complexity and the actual spatial and radiometric performance of the system. To date an investigation of these aspects has not yet taken place.

1.4 Research objectives

Currently salinity and soil moisture maps are generated by ESA's Soil Moisture Ocean Salinity (SMOS) and NASA's Soil Moisture Active Passive (SMAP) satellites. The two satellites generate data on a global scale with spatial resolutions of 35 km to 50 km [3] [4]. Spatial resolutions within the same magnitude are set as a requirement for the upcoming multi-frequency radiometer mission CIMR of ESA [5]. While L-band radiometer data at these spatial resolutions has proven to be of great value for scientific and societal users [6], an increase in spatial resolution could further improve existing applications and even enable new ones requiring higher-order precision. Hydrological applications ranging from subcatchment-scale water management to agricultural irrigation would benefit from high-resolution soil moisture maps in sub-decakilometer range [7]. A full review of the applications of soil moisture can be found in Dorigo et al. [35]. Furthermore, more spatially detailed damage maps after hydrological extremes, like droughts (e.g., lost crop yield & harvest failure) or floods (e.g. dam bursts & inundated areas) would help provide a more solid basis for appropriate emergency decision making [8], [9]. The former deputy Director of CESBIO Kerr [36] explicitly writes

"…ideally, groundbreaking results could be attained with a 10 km native spatial resolution and possibly a daily revisit for some applications."

CESBIO has been working on a successor mission to SMOS since 2014 and has organized the SMOS-Next working group, tasked with finding a feasible concept for a space-based radiometer with an improved spatial ground resolution. In the context of the working group CESBIO has compiled a list of requirements for the next-generation SMOS mission (see Table 1-2). The CESBIO requirements list highlights many applications that would benefit from an increased spatial resolution. Some of these, e.g., regional hydrology soil moisture, demand high radiometric sensitivities of up to 0.04 K that will be difficult to meet from space. However, applications such as land Numerical Weather Prediction (NWP) soil moisture and coastal areas sea surface salinity would benefit from an increased spatial resolution of 10 km, while requiring only a moderate radiometric sensitivity in the order of 3 K. Therefore, it is these applications that are specifically addressed by the system concept in the present thesis.

Table 1-2 Radiometry requirements for various applications [4]

Application	*Spatial resolution [km]*	*Radiometric Sensitivity [K]*	*Revisit*
Land NWP Soil Moisture	*10*	*3*	*<240 min*
Catchment Hydrology Soil Moisture	*4*	*0.04*	*24 h*
Regional Hydrology Soil Moisture	*10*	*0.04*	*24 h*
Vegetation Water Mangement	*4*	*0.04*	*2 days*
Vegetation Optical Thickness	*4*	*0.5*	*2 days*
Sea Ice	*15*	*0.5*	*2 days*
Coastal Areas Sea Surface Salinity	*3-10*	*1-3*	*2 days*
Open Ocean Sea Surface Salinity	*100*	*0.2*	*Monthly*
Ocean Wind	*50*	*0.2*	*Realtime*

While there is a consensus within the science community that a space-based radiometer is needed capable of delivering higher spatial resolution data, a feasible technical concept for the realization of such a system has not been found to date. An attempt to solve the problem with a “Fourier-Correlation Imaging” concept by researchers at the University of Tübingen and the University of Toulouse seems not to yield an immediate remedy [37]. The key challenge in improving the resolution of a space-based radiometer remains the creation of a large required aperture of the aperture synthesis array. Progress in materials, foldable structures and space-based manufacturing processes could enable the creation of large monolithic structures capable of carrying a sufficiently large antenna array. With progress in satellite formation flying, a distributed approach could however also be feasible. This thesis explores this possibility of conducting numerical simulations on the swarm-based aperture synthesis radiometer. This involves the following steps:

1. Creation of a system simulator

A complete investigation of a swarm-based radiometer concept requires the capability to model the orbit mechanics of a satellite swarm with a great number of satellites and the imaging performance of the resulting interferometric array. On one hand, the orbit mechanical simulator must be capable of considering the dominant perturbations in LEO, such as Earth oblateness and aerodynamic drag. It must be capable of calculating the system lifetime based on the average fuel consumption and the collision risk to the system. This involves the implementation of a suitable satellite swarm control strategy capable of ensuring satellites can maintain a specified position accuracy in orbit. On the other hand, the system simulator shall enable a complete evaluation of imaging performance for a specific configuration of a swarm-based radiometer. Imaging performance can be evaluated by calculating the array response to a point source and deriving common performance metrics, such as the level of side lobes, the radiometric sensitivity and the angular resolution. This requires finding a method for the processing of the irregularly distributed samples in the frequency domain.

2. Derivation of a design methodology

Once a system simulator is available for the evaluation of a specific satellite configuration, various orbit designs for the swarm-based radiometer shall be explored. A numerical optimization method shall be found, that optimizes the orbital parameters of a number of satellites for system imaging performance. The optimization method shall also ensure the feasibility of the system from inter-satellite collision risk and lifetime considerations.

3. Explore the influence of important design parameters on the feasibility of the system concept

Applying the design methodology derived in step two, the influence of important design parameters shall be explored on the feasibility and performance of the system. In particular these are, the number of satellites in formation, the performance of the GNC system, the inter-satellite distances and the system orbit height. In addition to the imaging requirements (spatial and radiometric resolution) a swarm-based radiometer should ideally meet a set of requirements, which are derived from SMOS [32]. These specify that

- the system coverage shall at least comprise the latitudes of 80°N and 80°S.
- the system shall be placed on a repeat-ground-track SSO with a drift of no larger than 25 km.
- the physical size of the system shall be compatible with the Rockot launcher.
- the target system lifetime should be 2 years.

This analysis shall primarily investigate the orbit mechanical feasibility of placing a greater number of smaller satellites in a compact swarm and the resulting imaging performance. The fundamental system concept that was chosen as the primary subject of investigation is presented in the next section.

1.5 System concept

The swarm-based aperture synthesis radiometer proposed in this thesis is composed of the chief satellite and N smaller Cubesat (8U) satellites, (deputies), which orbit the chief satellite in close proximity on fixed circular reference orbits. The interferometric radiometer antenna is formed by a foldable central monolithic array of patch Antenna & Receiver Units (ARU) in Y-configuration, carried by the chief satellite and single ARU on the free-flying deputies. The function of the ARU is to measure the radiation noise power at the receiver, which corresponds to the brightness temperature observed by the antenna. The dual-channel ARU are capable of conducting both measurements in full-polarization and dual-polarization mode. In dual-polarization mode the Horizontal (H) and Vertical (V) polarizations are measured alternatively to yield the Stokes vector. The ARU of the central Y-array and the ARU on-board the deputies are oriented in the same side-looking direction (see Figure 1-2), imaging the same extended target area.

During measurements, all time-synchronized ARU record electromagnetic emission at a center frequency of $f_c = 1.413\ MHz$ with a bandwidth B, generating 2x2-bit digital signals. The digitalized measurements of the deputy ARU are then transferred to the central satellite via an intersatellite-link. There the signals are correlated within a Correlation Unit (CU). Further image processing is conducted on the chief satellite using Interferometric Motion Induced Synthetic Aperture Radiometry (MISAR) algorithms [34]. Processed data are finally downlinked by a wideband communication system from the chief satellite (see Figure 1-3) at the next contact with the ground infrastructure.

All deputies are equipped with low-impulse three-axis propulsion systems, capable of maintaining their position on the relative reference orbits. The relative reference orbits describe a nominal periodic motion around the chief satellite. Relative navigation within the formation is performed on the basis of Differential GNSS (DGNSS) measurements of position and velocity and on-board orbit propagation.

DGNSS is chosen as the main source of position and velocity information due to its flight heritage from many CubeSat missions, its simplicity, accuracy and reliability in orbit. The GNC subsystem on-board each deputy regularly determines the satellite state estimates, compares them with the reference state, which is defined by the deputy nominal orbit, and determines appropriate thruster responses in a leader-follower approach. Three-axis attitude control is conducted by a GNC module, relying on reaction wheels, star trackers and sun sensors. The satellite swarm-based aperture synthesis radiometer will be placed on a circular repeat-orbit at approximately ~750 km altitude. Frequent orbit raising is performed by the entire satellite system to ensure the repeatability of the orbit track.

Figure 1-2 An artist's visualization of the proposed satellite concept showing the larger chief satellite with the correlator antenna in Y-configuration and the other Cubesats (deputies) in close proximity.

In contrast to propulsion systems designed for significant orbit changes, high-precision formation flight requires position and altitude control actuation on small scales, with Minimum Impulse Bits (MIB) below 0.2 mNs [38]. From a system design perspective, it is beneficial to choose a propulsion system that is specifically designed for close-proximity formation flight. Choosing such a system, would entail the simultaneous launch of both the chief and deputy satellites, since conducting larger orbit maneuvers would not be possible. The deputy satellites are launched within a canisterized dispenser module on the chief and ejected into their respective relative orbits by impeding small initial velocity increments.

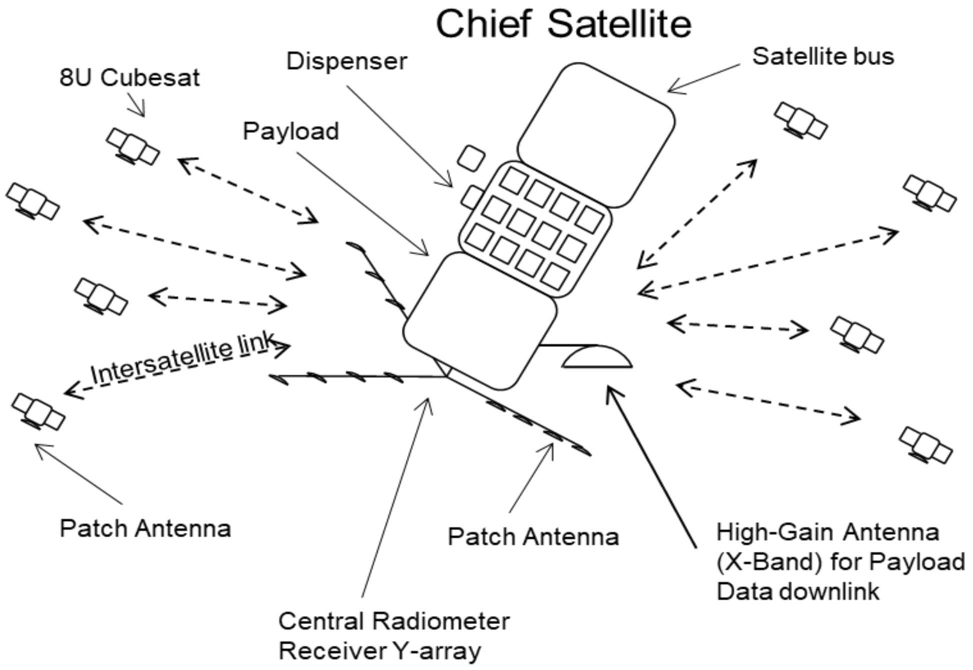

Figure 1-3 Schematic view of the swarm-based radiometer concept

The 8U CubeSat, the Generic Nanosatellite Bus (GNB), format [39] was chosen for the deputy satellites as it should be capable of carrying the ARU payload and the GNC module. Since the CanX-45 mission verified close formation flight in 2014 with a satellite based on the GNB, it is likely a large number of 8U satellites can be manufactured with a similar GNC system and an added payload. The 8U CubeSats would be clad in solar panels, weighing approx. 7 kg with a side length of 20 cm. The ARU patch antenna would occupy a single side of the cube.

1.6 Scope and structure

The main outcome of this thesis has been the proposal and investigation of a satellite swarm-based synthetic aperture radiometer concept for the improvement of the spatial resolution of Earth observing radiometers. These outcomes are described from chapter 4 to chapter 7. Aside from presenting results, this thesis aims to provide the relevant mathematical background for both the orbit mechanics and the radiometry in chapters 2 and 3. In particular the thesis is structured in the following way:

Chapter 2 describes the relevant radiometric background for the swarm-based aperture synthesis radiometer investigated in this study. This includes a treatment of classical aperture synthesis in two dimensions and the introduction of the idealized Motion Induced Synthetic Aperture Radiometer technique. The physical models are presented that are used in the simulation of the swarm-based aperture synthesis radiometer.

Chapter 3 presents the mathematical models for the simulation of the relative orbit mechanics. This chapter addresses both unperturbed and perturbed orbit mechanics and discusses the impact of the individual perturbing forces. Additionally, relative orbital elements [40] are introduced for the design of spacecraft formations in LEO.

Chapter 4 provides an overview of the system simulator for swarm-based aperture synthesis radiometer concepts that was created within the course of this thesis. The chapter highlights the different simulator modules and the simulator logic.

Chapter 5 then focuses on the design methodology for the swarm-based radiometer. It discusses the selection of the orbit type and the influence of the orbit type on the controller accuracy and fuel consumption. Then the position optimization of individual deputy satellites on the relative orbital plane is presented, along with an example configuration containing 16 deputies.

Chapter 6 presents the main thesis results that have been obtained with the simulator presented in chapter 5. Chapter 6 investigates the impact of important system parameters, e.g. number of deputies, orbit control system accuracy, inter-deputy distance and system orbit height on the system performance, e.g., spatial resolution and radiometric sensitivity.

Chapter 7 briefly discusses the important other aspects of the swarm-based aperture synthesis radiometer such as data handling issues and the technical challenges of ensuring instrument synchronization and image reconstruction. It then presents the summary and conclusions.

2 INTERFEROMETRIC RADIOMETRY

This chapter contains the fundamental theory for the radiometric model used in the simulation of the swarm-based aperture radiometer.

2.1 Interferometric radiometry

Radio interferometry has been a critical technique for astronomic observation for almost a century. It is the underlying technology for aperture synthesis, enabling a set of individual radio telescopes to act as one large-aperture observatory. Probably the most prominent modern radio telescope that is based on radio interferometry is the ALMA telescope in Chile, consisting of up to 66 antennas, operating at wavelengths from 0.3 to 9.6 mm and delivering a synthesized aperture of 16 km [41].

2.1.1 One-dimensional radio interferometry

In essence a basic radio interferometer consists of two or more antennas oriented towards a common target and a correlator system that enables the correlation of received signals from individual antennas. The recorded electromagnetic radiation of two antennas is correlated to produce an interferometer fringe function, which is formed by the superposition and cancelling of the time shifted signal due to the time shift between recorded signals. The time shift occurs due to the difference in propagation time from the signal source to receivers at different positions [42]. Figure 2-1 depicts the geometry of a one-dimensional two-element interferometer with the distance D between antennas and a source placed in the far field.

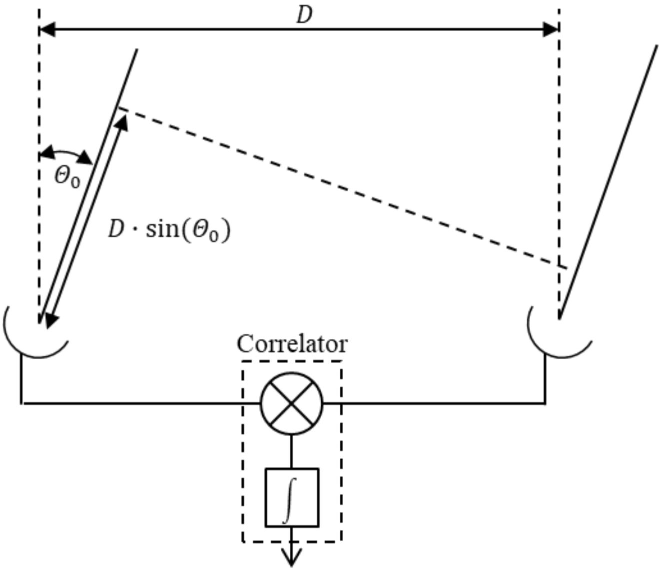

Figure 2-1 Geometry of a two-element interferometer with the baseline *D*.

The output of the correlator R consisting of a multiplier and an integrator, the fringe function, can be stated for a sinusoid and an averaging period of $T \gg 1/f$ as [43]

$$R(\Delta\tau) = \cos(2\pi f \Delta\tau) = \cos\left(\frac{2\pi D l f}{c}\right) \tag{2-1}$$

with $l = \sin(\Theta_0) = \Delta\tau \cdot c/D$, $\Delta\tau$, the signal delay between the two antennas, c, the speed of light in vacuum ($3 \cdot 10^8 m/s$) and f, the frequency. The coordinate l represents the off-boresight angle in radians. For a signal with a finite bandwidth B and a single point source equation (2-1) the correlator output can be extended to

$$R(\Delta\tau) = \int_{-\infty}^{\infty} |H(f)|^2 e^{j2\pi f \Delta\tau} df \tag{2-2}$$

with $|H(f)|^2$ the power spectrum of the input signal at the correlator. Assuming a constant amplitude distribution in frequency domain, $H(f)$ is only determined by the frequency response of the antenna array. A Gaussian passband filter with a center frequency of f_c would yield a power spectrum of

$$|H(f)|^2 = \frac{1}{2\sigma\sqrt{2\pi}}\left(\mathrm{e}^{\left(-\frac{(f-f_c)^2}{2\sigma^2}\right)} + \mathrm{e}^{\left(-\frac{(f+f_c)^2}{2\sigma^2}\right)}\right) \tag{2-3}$$

with the bandwidth factor σ [43]. The bandwidth factor is related to the full bandwidth of the signal at half maximum level with $B_{1/2} = \sqrt{8 \cdot \ln(2)} \cdot \sigma$. Combining equation (2-2) and (2-3) and neglecting the negative frequencies yields an interferometer response to a single point source of

$$R(\Delta\tau) = e^{-2\pi^2\Delta\tau^2\sigma^2}\cos(2\pi f_c\Delta\tau) \tag{2-4}$$

According to [43] equation (2-4) can be expressed as a function of the off-boresight angle Θ_0, as

$$R(\Delta\tau) = \exp\left(-2\left(\frac{\pi D\sigma}{c}\sin(\Theta_0)\right)^2\right)\cdot cos\left(\frac{2\pi f_c D}{c}\sin(\Theta_0)\right) \tag{2-5}$$

The angular resolution of the fringe function is given by the length of the baseline. In radio interferometry the spatial frequency u_λ is commonly introduced to describe the baseline component that is perpendicular to the reference direction. It measures the sinusoidal component of a radiation distribution, i.e., the Fourier component, in the spatial axis direction, which in the one-dimensional case lies in the dimension of the baselines. The spatial frequency, u_λ is measured at the center frequency and normalized by the center wavelength λ_c

$$u_\lambda = \frac{Dcos(\Theta_0)}{\lambda_\mathrm{c}} \tag{2-6}$$

The coverage of the spatial frequency domain by the baselines of an array is crucial for the array response, i.e., the ability to resolve point sources and extended sources. To ensure alias-free sampling of a radiation source at $l_{max} = \sin(\Theta_{max})$ by a one-dimensional array of antennas the Shannon-Nyquist theorem states that the distance between antennas Δu must abide by the criterion

$$\Delta u_\lambda < \frac{1}{2l_{max}} \tag{2-7}$$

If Δu_λ is larger than this factor [44], there will be higher spatial frequencies that fold into the frequency domain representation of the radiation distribution. The angular resolution of a one-dimensional array with a regular sampling interval can be given as

$$\Delta l = \frac{1}{2u_{\lambda,max}} \tag{2-8}$$

with $u_{\lambda,max}$ denoting the maximum sampled spatial frequency. [45]

2.1.2 Aperture synthesis in two dimensions

The one-dimensional interferometer can be extended to the two-dimensional space by adding a second dimension on the spatial frequency domain and the Field Of View (FOV). Figure 2-2 shows the two-element interferometer, consisting of two spatially separated antennas in points A and B. Both antennas are oriented towards a common point in the far field region, which lies at a distance $s_0 \gg D$ from the interferometer. Extended sources of radiation with the intensity distribution $I(\Theta, \Phi)$ are present within the FOV of the interferometer of which a finite element of the source solid angle $d\Omega_s$ is located at the angles Θ and Φ from boresight. The boresight direction of the interferometer is given by the vector pointing from the array center to the source center.

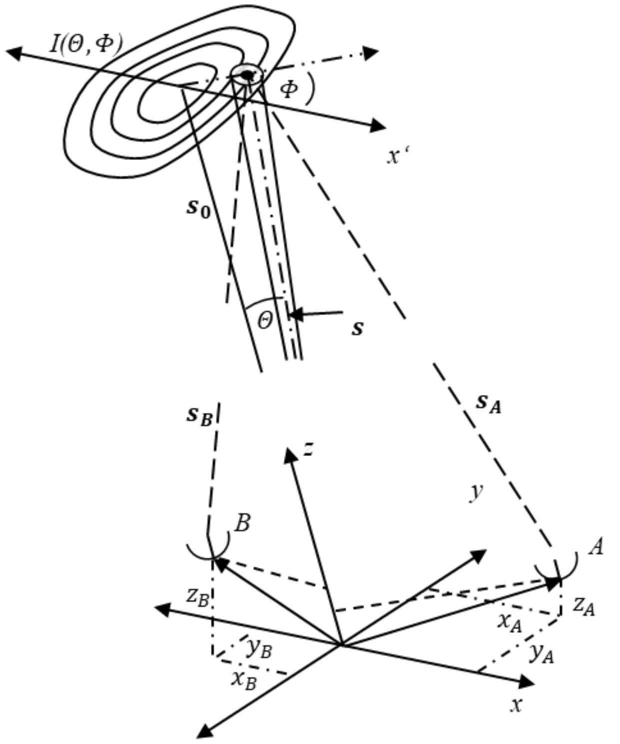

Figure 2-2 Geometric setup of the two-element receiving system observing an extended source of intensity I in the far field. Modified from [43].

The measured spatial frequencies are described in the spatial frequency coordinate system $(u_\lambda, v_\lambda, w_\lambda)$, which shares the same axes as the physical Cartesian coordinate system (x, y, z). Analogous to the one-dimensional case, the baseline components in physical space can directly be associated with the measured spatial frequencies in the $(u_\lambda, v_\lambda, w_\lambda)$ system as

$$u_\lambda = \frac{(x_B - x_A)}{\lambda_c} \qquad v_\lambda = \frac{(y_B - y_A)}{\lambda_c} \qquad w_\lambda = \frac{(z_B - z_A)}{\lambda_c} \tag{2-9}$$

The coherence function as an output of the correlation of the signals at A and B from the source at Θ, Φ can then be given as [44]

$$R(\boldsymbol{s_A}, \boldsymbol{s_B}, \Theta, \Phi) = I(\Theta, \Phi) \cdot \frac{e^{(-j2\pi f_c \cdot \Delta\tau)}}{\|\boldsymbol{s_A}\| \cdot \|\boldsymbol{s_B}\|} \tag{2-10}$$

with $\boldsymbol{s_A}$, $\boldsymbol{s_B}$ the vectors from the antennas at A and B to the source and the resulting time delay $\Delta\tau = (\|\boldsymbol{s_B}\| - \|\boldsymbol{s_A}\|)/c$ of the signal. Due to the far field condition the product $\|\boldsymbol{s_A}\| \cdot \|\boldsymbol{s_B}\|$ can be replaced with $\|\boldsymbol{s}\|^2$, the square of the distance between the antenna array, i.e., interferometer, and the source. The complete coherence function can be derived by integrating over all extended sources S in the FOV of the antennas, using

$$R(\Delta\tau, \|\boldsymbol{s}\|) = \int_S \; I(\Theta, \Phi) \cdot \frac{e^{(-j2\pi f_c \cdot \Delta\tau)}}{\|\boldsymbol{s}\|^2} dS \tag{2-11}$$

with the finite area of the source, dS. The distance $\|\boldsymbol{s_i}\|$ between an antenna i at the coordinate x_i, y_i, z_i and a radiation source at the coordinates x, y, z can be calculated with

$$\|\boldsymbol{s_i}\| \; = \sqrt{(x - x_i)^2 + (y - y_i)^2 + (z - z_i)^2} \tag{2-12}$$

The Cartesian coordinates of the source can be translated into spherical coordinates with

$$\begin{aligned} x &= \|\boldsymbol{s}\| \sin(\Theta) \cos(\Phi) \\ y &= \|\boldsymbol{s}\| \sin(\Theta) \sin(\Phi) \\ z &= \|\boldsymbol{s}\| \cos(\Theta) \end{aligned} \tag{2-13}$$

And for the finite area of the source

$$dS = \|\boldsymbol{s}\|^2 \sin(\Theta) \mathrm{d}\Theta \mathrm{d}\Phi \tag{2-14}$$

With these definitions and a Taylor expansion, the coherence function in equation (2-11) can be expanded [44], [46], [47] and given in spherical coordinates as

$$R(\Delta\tau) = \int_0^{2\pi} \int_{-\pi/2}^{\pi/2} I(\Theta, \Phi) \cdot e^{(-j2\pi f_c \cdot \Delta\tau)} \cdot \sin(\Theta) d\Theta d\Phi \tag{2-15}$$

with

$$\frac{\mathrm{c}}{\lambda_c} \cdot \Delta\tau = \frac{\delta_{AB}}{\lambda_c} + w_\lambda \cos(\Theta) + v_\lambda \sin(\Theta) \sin(\Phi) + u_\lambda \sin(\Theta) \sin(\Phi) \tag{2-16}$$

and

$$\delta_{AB} = \frac{1}{2 \cdot \|\boldsymbol{s}\|} ({z_B}^2 - {z_A}^2 + {y_B}^2 - {y_A}^2 + {x_B}^2 - {x_A}^2) \qquad (2\text{-}17)$$

Equation (2-15) is further simplified by replacing the angles Θ, Φ of the position of the source under observation with direction cosines l and m. The l, m coordinates represent the projection point of the intersection between a hemisphere of unity radius and the vector $\boldsymbol{s}$ onto the x, y plane, as depicted in Figure 2-3. The direction cosines can be expressed from angles Θ, Φ

$$l = sin(\Theta) \cdot cos(\Phi) \qquad m = sin(\Theta) \cdot sin(\Phi) \qquad (2\text{-}18)$$

With these manipulations, equation (2-15) can be stated as [44]

$$R(u_\lambda, v_\lambda, w_\lambda, \delta_{AB}) = e^{\left(-j2\pi\frac{f_c}{c}\delta_{AB}\right)} \cdot \int_{-1}^{1}\int_{-1}^{1} \frac{I(l,m)}{\sqrt{1-l^2-m^2}} \cdot e^{\left(-j2\pi\cdot\left(u_\lambda l+v_\lambda m+w_\lambda\sqrt{1-l^2-m^2}\right)\right)} dldm \qquad (2\text{-}19)$$

The integration limits are set to positive and negative unity because these values mark the limits of the observed hemisphere. If the receivers are placed within a plane ($w_\lambda = 0$), equation (2-19) becomes

$$R(u_\lambda, v_\lambda, \delta_{AB}) = e^{\left(-j2\pi\frac{f_c}{c}\delta_{AB}\right)} \cdot \int_{-1}^{1}\int_{-1}^{1} \frac{I(l,m)}{\sqrt{1-l^2-m^2}} \cdot e^{\left(-j2\pi\cdot\left(u_\lambda l+v_\lambda m\right)\right)} dldm \qquad (2\text{-}20)$$

Equation (2-20) further simplifies if one considers the far field condition $\delta_{AB} \ll \lambda_c$. This condition holds since the denominator of δ_{AB} is devided by the distance to the source $\|\boldsymbol{s}\|$. The expression in front of the integral can thus be removed.

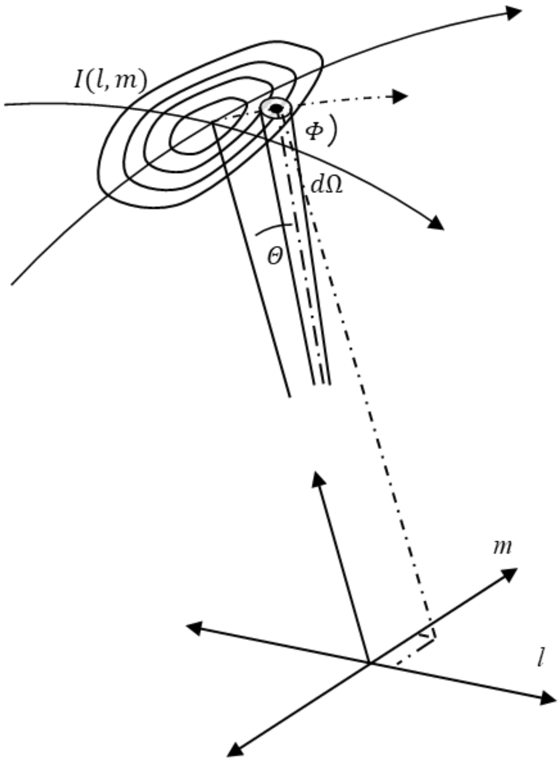

Figure 2-3 Geometric setup of the two-element receiving system observing an extended source of intensity I in the far field with the direction cosines l, m. Modified from [43].

Equation (2-21) finally yields the relationship between the intensity distribution $I(l,m)$ and the measurement, called the visibility $V(u_\lambda, v_\lambda)$, at the spatial frequencies denoted by the two components u_λ and v_λ. This relationship is given by the Visibility Function for a plane receiver array ($w_\lambda = 0$) as

$$V(u_\lambda, v_\lambda) = \int_{-1}^{1}\int_{-1}^{1} \frac{I(l,m)}{\sqrt{1-l^2-m^2}} \cdot e^{(-j2\pi\cdot(u_\lambda l+v_\lambda m))} dldm \qquad \text{(2-21)}$$

It represents a well-known formula in coherence theory, known as the Van Cittert–Zernike theorem [43]. The visibility V is a complex value, which is expressed in dimensions of watt per square meter of antenna area ($W \cdot m^{-2}$). In order to gain a better understanding of the sampled frequencies, the spatial frequency components can be visualized on the (u_λ, v_λ) plane (see Figure 2-4), which lies within the plane of the coplanar receiving array. The spatial frequency vector $\boldsymbol{q} = [u_\lambda, v_\lambda]^T$provides the phase and frequency of the periodic components of the radiation distribution. The u_λ, v_λ axes are usually aligned with the dimensions of a physical reference system, i.e., the x, y axes.

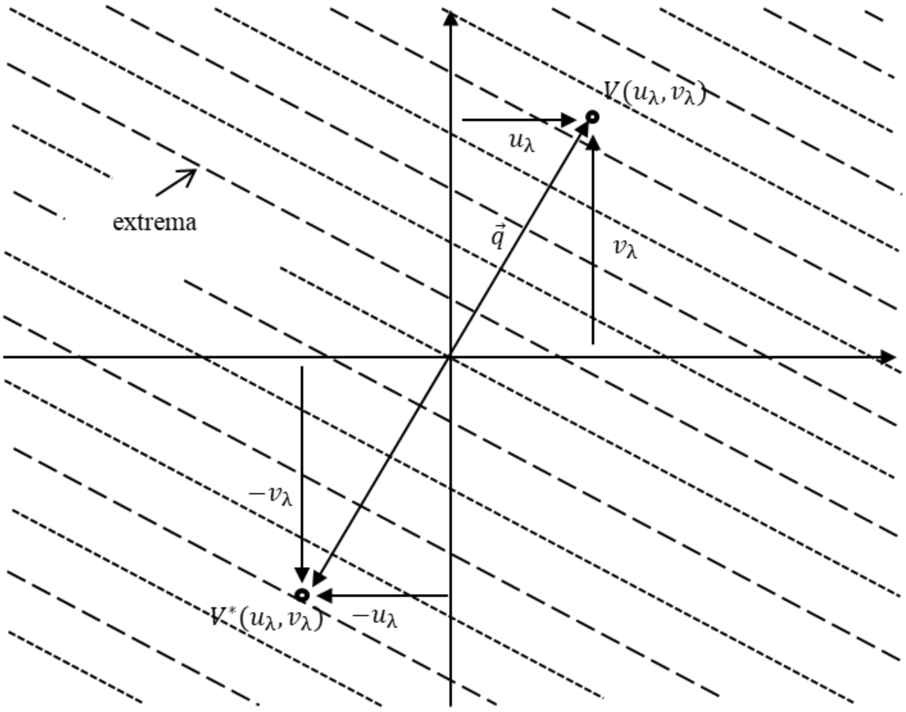

Figure 2-4 Visualization of a single Visibility V and its Hermitian V* in the (u, v) plane. The dashed lines represent the minima and extrema of the spatial frequency spectrum for a point source.

Due to the real values of $I(l, m)$ within the Fourier integral of equation (2-21) the Fourier transform is Hermitian. Thus, each baseline can be associated with two visibilities that are point symmetrical to each other. The following relationships are valid for these visibilities

$$V(-u_\lambda, -v_\lambda) = V^*(u_\lambda, v_\lambda) \qquad V(u_\lambda, -v_\lambda) = V^*(-u_\lambda, v_\lambda) \qquad (2\text{-}22)$$

A single baseline always generates a complex conjugate pair of visibilities. The obliquity factor $1/\sqrt{1 - l^2 - m^2}$ in equation (2-21) accounts for larger angles between antenna boresight and source. This factor is sometimes included in the antenna beam patterns $F(l, m)$ and therefore not explicitly stated. If the beam patterns for both antennas are included, equation (2-21) yields

$$V(u_\lambda, v_\lambda) = A_e \cdot \int_{-1}^{1}\int_{-1}^{1} \frac{F(l, m) \cdot I(l, m)}{\sqrt{1 - l^2 - m^2}} \cdot e^{(-j2\pi \cdot (u_\lambda l + v_\lambda m))} dldm \qquad (2\text{-}23)$$

which assumes that the patterns of both antennas are identical. To receive the Visibility value in Watt at the correlator output, the effective area of an individual antenna A_e has also been multiplied with equation (2-21). Inserting the definition of the brightness temperature T_b [48] into equation (2-23) yields

$$V(u_\lambda, v_\lambda) = \frac{A_e k_B B}{{\lambda_c}^2} \cdot \int_{-1}^{1}\int_{-1}^{1} \frac{F(l,m) \cdot T_B(l,m)}{\sqrt{1-l^2-m^2}} \cdot e^{(-j2\pi\cdot(u_\lambda l + v_\lambda m))} dldm \qquad (2\text{-}24)$$

with k_B, the Boltzmann constant ($1.38 \cdot 10^{-23} J/K$) [48]. The terms A_e and ${\lambda_c}^2$ can be replaced with the antenna solid angle Ω_A and the obliquity factor with the pixel solid angle Ω_{Pix}

$$V(u_\lambda, v_\lambda) = \frac{\Omega_{Pix} k_B B}{\Omega_A} \cdot \int_{-1}^{1}\int_{-1}^{1} F(l,m) \cdot T_B(l,m) \cdot e^{(-j2\pi\cdot(u_\lambda l + v_\lambda m))} dldm \qquad (2\text{-}25)$$

An expression for the brightness intensity can be derived from equation (2-25) with an inverse transform. With this expression the brightness intensity can be calculated from the combined visibilities measured by all baselines with

$$T_B(l,m) = \frac{\Omega_A}{\Omega_{Pix} k_B B} \frac{1}{F(l,m)} \cdot \int_{-\infty}^{\infty}\int_{-\infty}^{\infty} V(u_\lambda, v_\lambda) \cdot e^{(j2\pi\cdot(u_\lambda l + v_\lambda m))} dudv \qquad (2\text{-}26)$$

Conveniently the integral of the equation (2-26) represents a two-dimensional Fourier Transform. This enables the use of the Fast-Fourier Transform (FFT) algorithm allowing efficient computation of a great quantity of data. The usage of the FFT however requires the availability of $V(u_\lambda, v_\lambda)$ values on a regular grid. Irregular sampled visibilities must first be transformed into regular grid, before an FFT can be applied.

The expression for the visibility in equation (2-25) is valid for narrow-bandwidth measurements. Measurement bandwidths that are required for Earth observation radiometry however are wide enough for significant spatial decorrelation to occur. Spatial decorrelation is a result of a lack of correlation in superimposed wideband signals that are received at spatially distant positions. The reception of a wideband signal at spatially distant locations will introduce a time-delay that will lead to phase-differences of varying magnitudes for the signal components. These varying phase differences ultimately lead to decorrelation if they become too large.

Spatial decorrelation needs to be taken into account in the definition of the visibility by adding an additional factor, often called the “fringe-wash” function in literature. The fringe-wash function effectively reduces the contribution of baselines where large signal time-delays occur due to a large baseline length or large off-boresight angle. The function can be derived from the receiver frequency response, which can be modelled as a Gaussian filter [34]

$$H(f) = e^{\left(\frac{-\pi(f-f_c)^2}{2B^2}\right)} \tag{2-27}$$

The Gaussian filter is assumed to be identical in both receiver paths and can be modelled as a further component in both receiver channels as depicted in Figure 2-5.

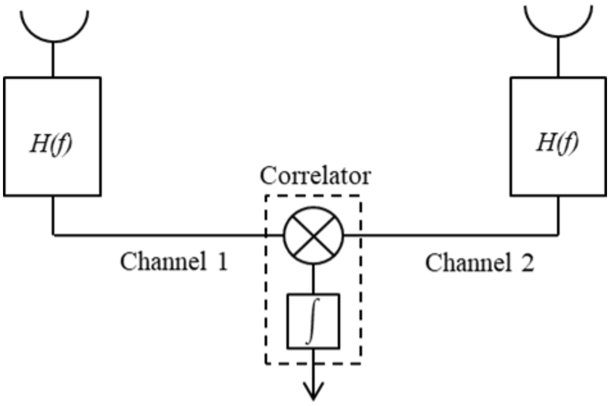

Figure 2-5 Receiver path diagram for a single baseline including identical Gaussian filters on both receiver channels.

With the receiver frequency response, the fringe-wash function can be calculated with equation (2-2) to

$$\tilde{r}(\Delta\tau) = e^{(-\pi B^2 \Delta\tau^2)} \tag{2-28}$$

Inserting the fringe-wash function into the equation (2-26), the visibility function for wideband signals is obtained [34]

$$V(u_\lambda, v_\lambda) = \frac{\Omega_{Pix} k_B B}{\Omega_A} \cdot \int_{-1}^{1}\int_{-1}^{1} F(l,m) \cdot T_B(l,m) \cdot \tilde{r}\left(-\frac{u_\lambda l + v_\lambda m}{f_c}\right) \cdot e^{(-j2\pi\cdot(u_\lambda l + v_\lambda m))} dl dm \tag{2-29}$$

The fringe-wash function controls for the spatial decorrelation effects by down-weighting the responses from long baselines. This leads to a decreased spatial resolution at large off-boresight angles, since these result in an increased time-delay between the reception of signals at two spatially distant receivers of a baseline. Therefore, the large baseline components are increasingly neglected in the image, leaving only the smaller baseline components. This in turn is equivalent to an array with a smaller diameter.

The design of an interferometer usually sets a minimum for the acceptable coherence of signals at baselines. The information loss at the edge of the FOV of SMOS was approximately 60%, i.e., a fringe-wash function value of 0.4 [48]. This leads to a reduced spatial resolution at the SMOS array edges of 3.6 %.

2.2 Motion Induced Synthetic Aperture Radiometer (MISAR)

Two-dimensional synthetic aperture radiometry that was introduced in the last section can also be referred to as Position Induced Synthetic Aperture Radiometry (PISAR) [49], [50]. The PISAR technique can be employed from a single instrument position for the imaging of static radiation sources. The basic technique is thus a method based on spatial synthesis alone. In practice, various forms of temporal aperture synthesis have emerged over the recent years with the aim of improving the radiometric sensitivity or frequency coverage of radiometric systems. In temporal aperture synthesis the motion of baselines is used to gather temporally shifted measurements of a target. Measurements taken at different times by a moving baseline yield a series of visibility samples associated with different spatial frequency vectors. Astronomy was the first discipline to employ a form of temporal aperture synthesis, called rotational synthesis. Rotational synthesis is a key enabling technology for Very-Long-Baseline Interferometry (VLBI) allowing aperture synthesis radio telescopes to gain a more complete coverage of the sky [43], [51]. VLBI uses the rotational motion of the Earth over time to enable measurements with different baseline geometries, achieving a better coverage of the spatial frequency domain.

In Earth observation the only form of temporal aperture synthesis used to date is the technique of temporally averaging radiometric data in post-processing. The SMOS Earth observation satellite uses a snapshot averaging technique for the improvement of the radiometric sensitivity. By continuously taking snapshots over a target area during overflight, SMOS is capable of lowering its radiometric sensitivity to under 0.3 K [52]. Effectively this is akin to a lengthening of the system integration time.

The first analysis of a true temporal aperture synthesis radiometer concept for Earth observation was performed by Camps et al. [34] in 2001. The described concept, called the “2-D Doppler-Radiometer”, involves a three-antenna radiometer with the capability of imaging a radiation distribution by continuously recording signals during overflight. The key difference to a traditional radiometer is the addition of instrumental delays in the antenna receiver paths. This technique is also called Motion Induced Synthetic Aperture Radiometry (MISAR). MISAR is crucial in enabling a swarm-based aperture synthesis radiometer system, as the distance between individual antennas can effectively be increased, without decreasing sampling density. Park et al. [53] extended the 2-D Doppler Radiometer concept to more complex antenna arrays and provided an expression for the radiometric sensitivity. With minor modifications the following derivation of the MISAR equations are taken from the expressions presented in [53].

2.2.1 MISAR observation model

A simplified observation scenario for a side-looking, Earth observing MISAR system is depicted in Figure 2-6. The satellite system is situated in a quasi-circular orbit at height H_0 continuously scanning a swath along the flight path (X-axis) with an antenna array tilt angle θ_c in cross-track direction (Y-axis). The coordinate system (X, Y, Z) will be referred to as the Imaging Frame (IF). Assuming a rectangular footprint, each point source within the swath (Width: $2 \cdot L_y$) is observed from $t = -t_c$ to $t = t_c$ for a duration of $t_{obs} = 2 \cdot t_c = 2 \cdot L_x \cdot v_a$, with a half footprint in flight direction, L_x, and the orbital speed, v_a.

The point X_c, Y_c is the point on ground at which the antenna boresight is oriented and the point X_0, Y_0 is the focused pixel. The focus point is the point for which the propagation delays will be compensated with a matched filtering technique. In principle a MISAR satellite system can also be forward-looking, but for reasons that will become apparent in chapter 5 a purely side-looking system has been chosen for the system concept presented within this thesis.

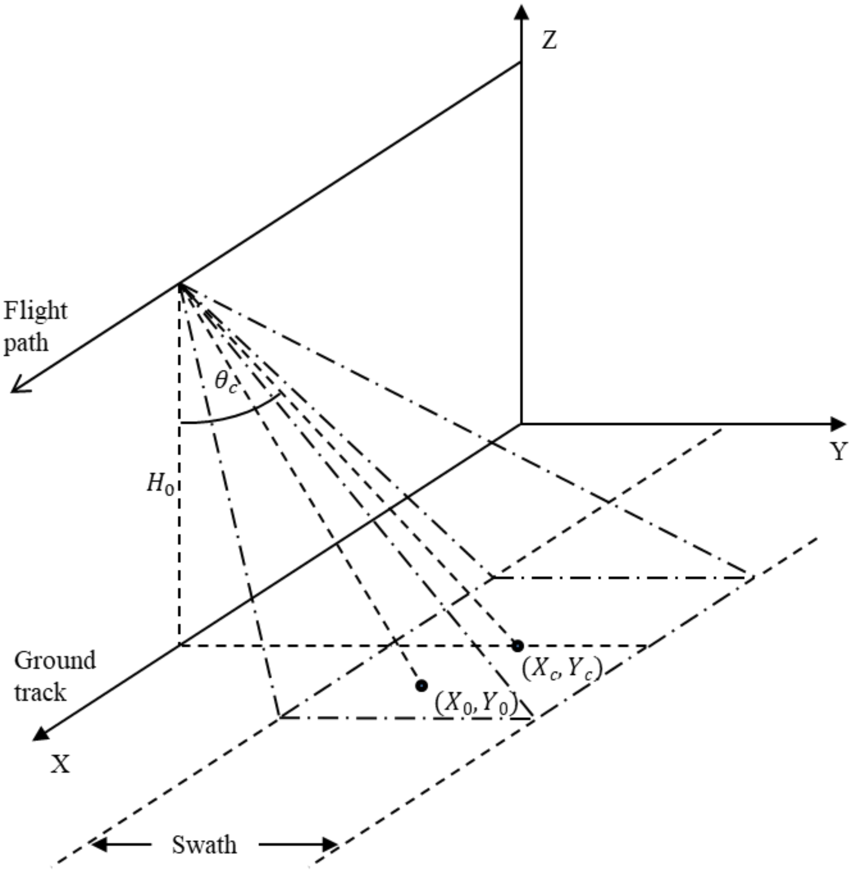

Figure 2-6 Observation scenario for a side-looking MISAR system with the system orbit height H_0, antenna array tilt angle θ_C and the focus point at X_0, Y_0.

2.2.2 MISAR adjustable delay compensation

The basic idea underlying MISAR is to use adjustable delays, i.e., matched filters, in the baseline receiver paths to compensate for the delay in propagation. This allows for a “focusing” of the received correlated energy onto a single focus point during the entire flyover of a target area. Figure 2-7 shows the modified receiver path of a baseline for a MISAR instrument. It adds two time-adjustable delays, $\tau_1(t)$ and $\tau_2(t)$ in the two baseline receiver channels.

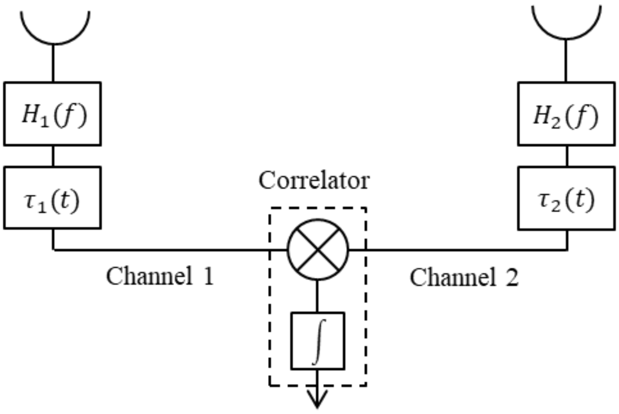

Figure 2-7 Schematic of a MISAR baseline receiver path.

The adjustable delays are varied in time to exactly compensate for the evolution of the propagation delay during the change of geometry while flying over the target area. These time delays represent the propagation time from the antennas to the focused pixel at X_0, Y_0. The time delays can be given as

$$\tilde{\tau}_1(t) = \frac{\|\tilde{\boldsymbol{s}}_1(t,\mathrm{X}_0,\mathrm{Y}_0)\|}{c} \qquad \tilde{\tau}_2(t) = \frac{\|\tilde{\boldsymbol{s}}_2(t,\mathrm{X}_0,\mathrm{Y}_0)\|}{c} \tag{2-30}$$

The signal delay resulting from an arbitrary signal source at the position *X, Y* is given as a function of the distance from antennas to the source by

$$\tau_1(t) = \frac{\|\boldsymbol{s}_1(t,\mathrm{X},\mathrm{Y})\|}{c} \qquad \tau_2(t) = \frac{\|\boldsymbol{s}_2(t,\mathrm{X},\mathrm{Y})\|}{c} \tag{2-31}$$

The geometric relationship is shown in Figure 2-8 for an exemplary two-dimensional case. The variables $\tilde{\boldsymbol{s}}_1$ and $\tilde{\boldsymbol{s}}_2$ denote the vectors between the antennas and the focused pixel and the variables $\boldsymbol{s}_1$ and $\boldsymbol{s}_2$ denote the vectors between the antennas and the signal source. With the definition of the time delays, the total delay error of a signal source, i.e., non-focused pixel can be stated as

$$\Delta\tau(t) = \frac{\|\boldsymbol{s}_1(t,\mathrm{X},\mathrm{Y})\| - \|\tilde{\boldsymbol{s}}_1(t,\mathrm{X}_0,\mathrm{Y}_0)\| - \|\boldsymbol{s}_2(t,\mathrm{X},\mathrm{Y})\| + \|\tilde{\boldsymbol{s}}_2(t,\mathrm{X}_0,\mathrm{Y}_0)\|}{c} \tag{2-32}$$

This time delay represents the shift at which the signals from the two antennas are correlated.

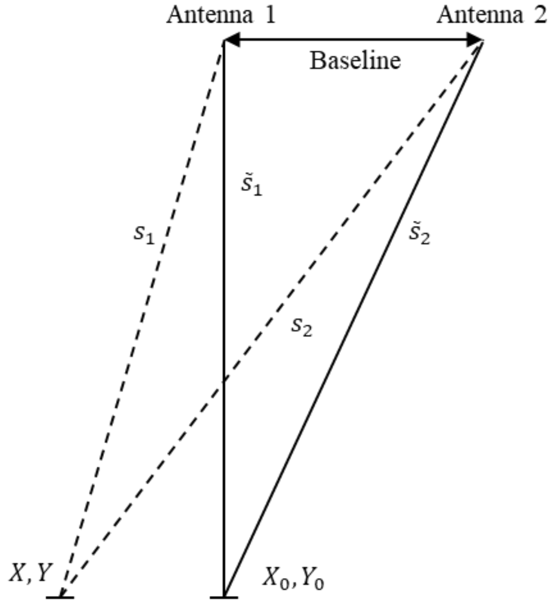

Figure 2-8 Illustration of the geometric position of the antennas with the focus point at X_0, Y_0 and a signal source at X, Y.

With the above statements, the MISAR visibility function V_{12} for a single baseline can be obtained by integrating the equation (2-26) in time over the entire observation duration. The equation as a function of the Cartesian coordinates of the source (X, Y) and the focussed pixel (X_0, Y_0) can then be rewritten as

$$V_{12}(X_0, Y_0) = \frac{\Omega_{Pix} k_B B}{\Omega_A} \cdot \frac{1}{2t_c} \cdot$$

$$\int_{-t_c}^{t_c} \int_{y_c-L_y}^{y_c+L_y} \int_{-\mathrm{v_a} t_c - L_x}^{\mathrm{v_a} t_c + L_x} F(X, Y) \cdot T_B(X, Y) \cdot \tilde{r}(\Delta\tau) \cdot e^{(-j2\pi f_c \cdot \Delta\tau)} dX dY dt \tag{2-33}$$

The inclusion of the time delay enables the continuous accumulation of the signal power from one source over time. The integration limits are chosen to encompass the entire square FOV.

According to [53] equation (2-33) can also be expressed in terms of the equivalent array factor AF_{eq}. The equivalent array factor can be seen as the array response to a point source. In literature it is sometimes also referred to as the Point Spread Function (PSF). The PSF represents a key characteristic of the antenna array that can be used to assess the quality of the interferometric configuration. To get AF_{eq} the equation (2-33) can be expressed as

$$V_{12}(X_0, Y_0) = \int_{Y_c-L_y}^{Y_c+L_y} \int_{-\mathrm{v_a} t_c - L_x}^{\mathrm{v_a} t_c + L_x} T_B(X, Y) AF_{12}(X_0 - \mathrm{X}, Y_0 - \mathrm{Y})\, dX dY \tag{2-34}$$

Where

$$AF_{12}(X_0 - \mathrm{X}, Y_0 - \mathrm{Y}) = \frac{\Omega_{Pix} k_B B}{\Omega_A} \cdot \frac{1}{2t_c} \cdot \int_{-t_c}^{t_c} F(X,Y) \cdot \tilde{r}(\Delta\tau) \cdot e^{(-j2\pi f_c \cdot \Delta\tau)} dt \tag{2-35}$$

The baseline equivalent array function AF_{12} represents the point source response for a single baseline only. In the following investigation the antenna beam pattern will be assumed Gaussian, which can be expressed as

$$F(X,Y) = e^{-\frac{(Y-Y_c)^2}{2{L_y}^2}} e^{-\frac{(X-v_a t)^2}{2{L_x}^2}} \tag{2-36}$$

According to Park et al. [53] the MISAR visibility is equivalent to a weighting of the measured brightness temperatures from all baselines. Therefore, one can equate the result of equation (2-34) with an estimation of the brightness temperature from the single baseline 1-2.

$$\hat{T}_{12}(X_0, Y_0) = V_{12}(X_0, Y_0) \tag{2-37}$$

with $\hat{T}_{12}(X_0, Y_0)$ representing the brightness temperature estimate at the focused pixel at (X_0, Y_0). The brightness temperature from all baselines can then be expressed as

$$\hat{T}(X_0, Y_o) = \frac{\sum_j \bar{W}_j \cdot \hat{T}_j(X_0, Y_0)}{\sum_j \bar{W}_j} \tag{2-38}$$

where $\bar{W}_j$ is the weight of the j-th baseline response. Weighting is an important part of image processing, as it enables the homogenization of the spatial frequency domain sampling and sidelobe suppression. The selection of appropriate baseline weights will be described in more detailed in chapter 4. With the above expressions the estimation of the brightness temperature can be expressed with the equivalent array function

$$\hat{T}(X_0, Y_0) = \int_{Y_c - L_y}^{Y_c + L_y} \int_{-\mathrm{v_a} t_c - L_x}^{\mathrm{v_a} t_c + L_x} T_B(X,Y) AF_{eq}(X_0 - \mathrm{X}, Y_0 - \mathrm{Y})\, dX dY \tag{2-39}$$

Where

$$AF_{eq}(X_0 - \mathrm{X}, Y_0 - \mathrm{Y}) = \frac{\sum_j \bar{W}_j AF_j(x_0 - x, y_0 - y)}{\sum_j \bar{W}_j} \tag{2-40}$$

with AF_j denoting the baseline equivalent array function of the j-th baseline and AF_{eq} denoting the equivalent array function, which is the point source response or PSF. The PSF is a three-dimensional function that describes the response of the aperture synthesis array to impeding radiation as a function of the direction cosines.

2.2.3 Radiometric sensitivity

Along with the spatial resolution, the radiometric resolution is one of the key performance metrics of an aperture synthesis array used for radiometric purposes. The radiometric sensitivity can be determined using the general derivation given by Wrobel et al. [54] for a synthesis image of a radio interferometer. This derivation was chosen as it considers the density weighting technique applied within the present study. The estimated brightness temperature $\hat{T}(X_0, Y_o)$ given in equation (2-39) may also be stated as the weighted sum of the individual baseline measurements

$$\hat{T}(X_0, Y_o) = \frac{\sum_j \bar{W}_j \cdot \hat{T}_j(X_0, Y_0)}{\sum_j \bar{W}_j} \tag{2-41}$$

To calculate the system radiometric sensitivity, only the point at the origin $X_0 = 0$ and $Y_0 = 0$ is considered. The associated variance $\Delta\hat{T}^2(0,0)$ in brightness temperature is the sum of the squared variances of each temperature measurement $\Delta\hat{T}_j(0,0)$ of baseline j. The square root of $\Delta\hat{T}^2(0,0)$ is then

$$\Delta\hat{T}(0,0) = \frac{1}{\sum_j \bar{W}_j} \sqrt{\sum_j \bar{W}_j^{\,2} \cdot \Delta\hat{T}_j^{\,2}(0,0)} \tag{2-42}$$

Assuming equal sensitivity of each ARU, one can assume equal $\Delta\hat{T}_j$ for all baselines. The fluctuation of brightness temperature for each baseline can be given as a function of the estimated flux density fluctuations $\Delta\hat{S}_j$ using the Rayleigh-Jeans relation

$$\Delta\hat{T}_j = \frac{\lambda^2}{2k} \cdot \frac{1}{\Omega_{Pix}} \cdot \Delta\hat{S}_j \tag{2-43}$$

According to Wrobel et al. [54] the flux density fluctuations $\Delta\hat{S}_j$ for a single sideband receiver and a Gaussian predetection filter can be given as

$$\Delta\hat{S}_j = \frac{2k}{A_e}\cdot\frac{T_{sys}}{\sqrt{B\tau_{eff}}}\cdot\frac{1}{\sqrt[4]{2}} \tag{2-44}$$

Combining equations (2-42), (2-43) and (2-44) with $\Omega_A = \lambda^2/A_e$ yields the radiometric sensitivity for the system at boresight

$$\Delta T = \frac{\Omega_A}{\Omega_{pix}}\cdot\frac{T_{sys}}{\sqrt[4]{2}\cdot\sqrt{B\tau_{eff}}}\frac{\sqrt{\sum_j \bar{W}_j^{\,2}}}{\sum_j \bar{W}_j} \tag{2-45}$$

With T_{sys} the system noise temperature, Ω_A the solid angles of an individual antenna, Ω_{pix} the solid angle of a resolved pixel, i.e., the array resolution, τ_{eff} the effective integration time. Equation (2-45) assumes a single sideband receiver and a Gaussian pre-detection filter. The effective integration time τ_{eff} can be calculated by $\tau_{eff} = \frac{t_{obs}}{1.14}$. This assumes a dual-channel receiver, the usage of 2x2-bit digital correlators with a sampling rate of four times the bandwidth. It is assumed that the entire overflight time is used for observation [48]. From equation (2-45) it can be seen that the introduction of weighting will always lead to a lower radiometric sensitivity. Weighting however is necessary for the homogenization of the sampling plane and thus a prerequisite for achieving low sidelobes.

According to Park et al. [55] , there is a physical relationship between the angular resolution and the radiometric sensitivity of the aperture synthesis radiometer. It is called the “radiometric uncertainty principle”. This principle shows that the product of radiometric sensitivity and angular resolution is a constant

$$\theta_w \cdot \Delta T \approx constant$$

This constant is dependent on the system noise temperature, the bandwidth, the integration time and the solid angle of the individual antenna and the selection of baseline weights. According to the uncertainty principle the radiometric system design must always trade-off the radiometric and spatial resolution. The constant is only a function of the bandwidth, the system noise temperature and the integration time.

2.3 System imperfections

The derivation of the theoretical MISAR model in this section was done without considering imperfections in the system hardware. In general system imperfections that affect system performance are similar to the ones affecting monolithic aperture synthesis radiometers. In his analysis of the MIRAS instrument, Camps [48] conducted a detailed investigation of hardware errors with possible implications for the final measurements. The findings show that while hardware errors do have a non-negligible impact on the system, they do not radically change the overall system performance, in terms of spatial resolution or radiometric sensitivity. Thus, an in-depth investigation will not be performed in this thesis, because its aim is to prove the fundamental feasibility of the swarm-based synthetic aperture radiometer for the first time.

3 RELATIVE ORBIT MECHANICS

An evaluation of the swarm-based aperture synthesis radiometer concept necessitates a detailed look at the formation-flight dynamics, due to the interdependencies between the imaging performance and satellite orbits. On one hand it is necessary to ensure formation flight can be conducted in a safe and reliable manner with a large number of nanosatellites, while on the other hand a satellite orbit configuration must be found that enables a suitable sampling of the spatial frequency plane. This chapter presents the theoretical background for the orbit mechanics and the autonomous control algorithm implemented for the simulation of the swarm-based aperture synthesis radiometer.

3.1 Orbit mechanics of unperturbed formation flight

In orbit mechanics unperturbed motion refers to the motion of satellites or celestial objects in an idealized gravitational space environment. It is sometimes referred to as motion that can be described by the solution of the Kepler problem, where natural or artificial objects in space are simplified as point masses onto which only mutual gravitational forces act. The Kepler problem, which is a special case of the two-body problem, is commonly used in orbit mechanics to predict the approximate motion of artificial satellites around the Earth. Its orbit description neglects the gravitational forces of any other celestial objects, e.g., moon, planets, along with other acting forces such as solar pressure or aerodynamic drag. Based on these assumptions, the relative motion of two spacecraft in circular orbits around a central body can be described by the well-known Hill-Clohessy-Wiltshire (HCW) equations [56]

$$\begin{aligned}\ddot{x} &= 3n^2x + 2n\dot{y}\\ \ddot{y} &= -2n\dot{x}\\ \ddot{z} &= -n^2z\end{aligned} \tag{3-1}$$

with the x-axis, denoting the radial vector, pointing from the Earth center to the chief spacecraft, the z-axis oriented along the angular momentum vector and the y-axis completing the right-hand system. The parameter n is the orbit rate which is defined as

$$n = \sqrt{\frac{\mu}{a^3}} \tag{3-2}$$

with $a \approx R_E + H_0$ the Chief semi-major axis of the circular orbit and $\mu = 3.986 \cdot 10^{14}\ m^3/s^2$ the standard gravitational parameter. $R_E = 6371\ km$ is assumed as the mean radius of the Earth. Furthermore equation (3-1) is only valid for small relative positions between the two spacecraft. According to this definition the y-axis points in the along-track direction. Figure 3-1 illustrates the described coordinate system that is often also referred to as the "Hill frame" in literature.

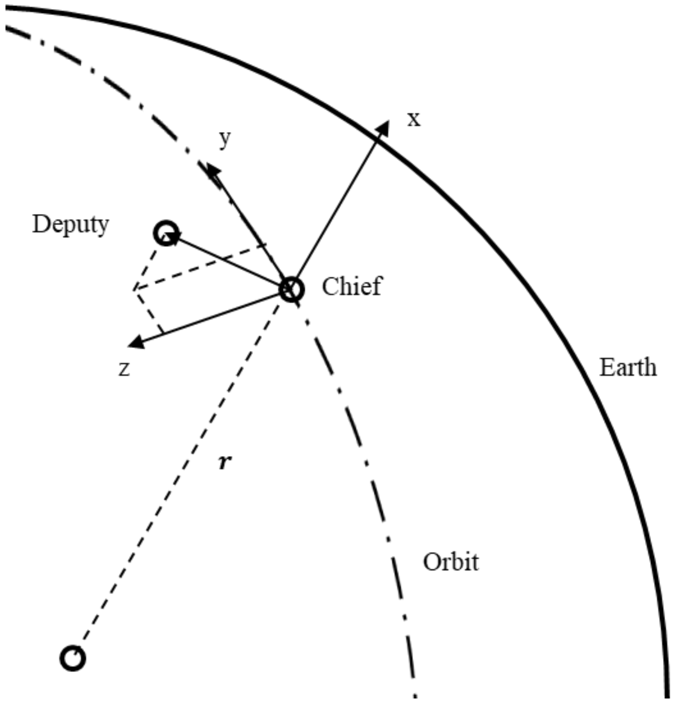

Figure 3-1 Illustration of a chief and deputy satellite in the Hill coordinate system.

The HCW equations describe the orbit as a set of differential equations for which a closed-form solution can be given by [57]

$$\boldsymbol{X}(\boldsymbol{t}) = \begin{bmatrix} \big(4-3cos(nt)\big)x_0 + \frac{sin(nt)}{n}\dot{x}_0 + \frac{2}{n}(1-cos(nt))\dot{y}_0 \\ 6(sin(nt)-nt)x_0 + y_0 - \frac{2}{n}\big(1-cos(nt)\big)\dot{x}_0 + \frac{4sin(nt)-3nt}{n}\dot{y}_0 \\ z_0 cos(nt) + \frac{\dot{z}_0}{n} sin(nt) \\ 3nsin(nt)\cdot x_0 + cos(nt)\cdot\dot{x}_0 + 2\sin(nt)\cdot\dot{y}_0 \\ -6n(1-\cos(nt))x_0 - 2\sin(nt)\cdot\dot{x}_0 + (4\cos(nt)-3)\cdot\dot{y}_0 \\ -nsin(nt)\cdot z_0 + \cos(nt)\cdot\dot{z}_0 \end{bmatrix} \tag{3-3}$$

using the deputy state vector

$$\boldsymbol{X}(\boldsymbol{t}) = \begin{bmatrix} x(t) \\ y(t) \\ z(t) \\ \dot{x}(t) \\ \dot{y}(t) \\ \dot{z}(t) \end{bmatrix} \tag{3-4}$$

where coordinates carrying the subscript “0” denote the initial conditions. These equations explicitly state the position of a deputy spacecraft relative to the chief with initial conditions of position and velocity given in Cartesian coordinates. From these equations it is difficult to systematically design bounded periodic relative orbits, as required for close-proximity formation flight. A more convenient first-order form for near-circular orbits can be given in terms of the classical orbit elements [58]

$$\begin{bmatrix} x(t) \\ y(t) \\ z(t) \end{bmatrix} \approx \begin{bmatrix} \Delta a - a\Delta ecos(\nu) + ae\Delta Msin(\nu) \\ a\Delta u_l + a\Delta\Omega\cos(i) + 2a\Delta esin(\nu) + 2ae\Delta Mcos(\nu) \\ a\sin(\nu+\omega)\,\Delta i - a\cos(\nu+\omega)\Delta\Omega\sin(i) \end{bmatrix} \tag{3-5}$$

with $\Delta(\cdot)$ denoting the arithmetic difference between orbital elements of the chief and the deputy. The classical elements, given in the Earth-Centered-Inertial (ECI) reference frame are the semi-major axis a, the eccentricity e, the true anomaly ν, the mean anomaly M, the Right Ascension of the Ascending Node (RAAN) Ω, the argument of periapsis ω and the inclination i (orbital elements without subscript denote the elements of the chief satellite). The quantity Δu_l denotes the difference in the mean argument of latitude, with $u_l = M + \omega$. The equations in (3-5) are only valid for inter-satellite distances up to 1000 m and small arithmetic differences between elements.

This form already allows one to draw conclusions about the relative orbit from the classical elements. For example, if there is no difference in the semimajor-axis between the chief and the deputy satellite $(\Delta a = 0)$ a closed-form periodic relative orbit will result, with harmonically varying components in all three Cartesian directions. Differences in eccentricity will impact the motion of the satellite in the orbit plane, while differences in inclination or RAAN will result in a motion perpendicular to the orbit plane.

3.2 Relative orbit design using relative orbit elements

While the given form of the HCW in equations (3-5) allow an explicit description of the relative orbit with classical orbit elements, it provides no immediate insight into the actual form of the relative orbit. To further simplify the design of relative orbits the German Space Operations Center (GSOC) of the German Aerospace Center (DLR) began to adopt the concept of relative eccentricity and inclination vectors for the description of relative satellite orbits in LEO. The concept of using relative eccentricity and inclination vectors, originally developed for satellites in geostationary orbit, allows for immediate insight on the relative orbit geometry.

The parameter δi is defined by the angle enclosed by the orbital planes of two satellites at the argument of latitude at which the orbital planes intersect in ascending direction (Figure 3-2). According to D'Amico [40], the relative inclination vector can be expressed as

$$\Delta \boldsymbol{i} = \begin{bmatrix} \Delta i_x \\ \Delta i_y \end{bmatrix} = \sin(\delta i) \begin{bmatrix} \cos(\theta) \\ \sin(\theta) \end{bmatrix} \tag{3-6}$$

with the relative ascending node θ. Assuming small angles for δi along with small differences in the orbital elements and considering trigonometric laws, this definition can be simplified to

$$\Delta \boldsymbol{i} \approx \begin{bmatrix} \Delta i \\ \Delta \Omega \cdot \sin(i) \end{bmatrix} \tag{3-7}$$

The first component of $\Delta \boldsymbol{i}$ denotes the arithmetic difference of the inclinations of the two orbital planes and the second component denotes the difference in RAAN, adjusted for the inclination of the chief orbit. The relative inclination vector is a measure of out-of-plane motion of the deputy satellite. A first-order approximation of the relative motion for a chief-centered orbit can be given as

$$z(t) = \left(-\Delta i_y cos\left(u_l(t)\right) + \Delta i_x sin\left(u_l(t)\right)\right) \cdot a \tag{3-8}$$

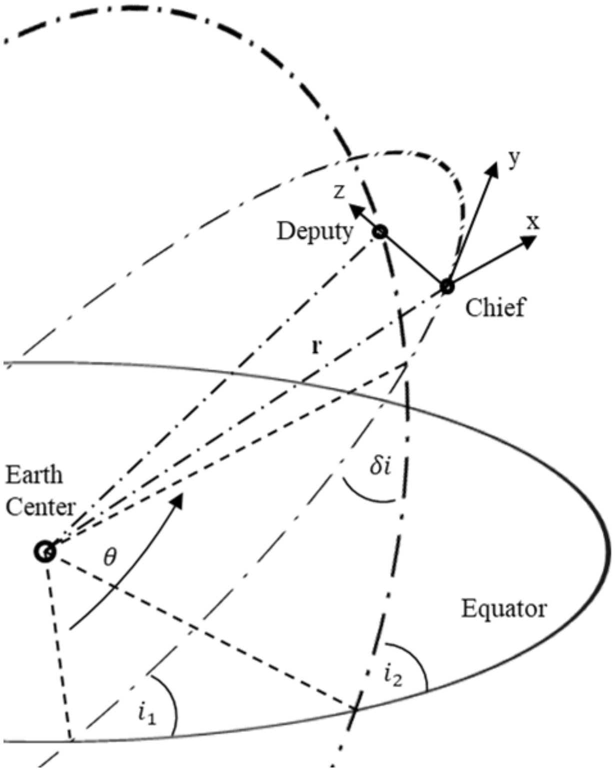

Figure 3-2 Illustration of the relative inclination angle in the ECI frame. Modified from [40].

The relative eccentricity vector provides information on the in-plane motion of the deputy satellite relative to the chief satellite. It can be expressed as the difference of the eccentricity vectors, which are defined as

$$\boldsymbol{e} = \begin{bmatrix} e_x \\ e_y \end{bmatrix} = e \cdot \begin{bmatrix} cos(\omega) \\ \sin(\omega) \end{bmatrix} \tag{3-9}$$

With the eccentricity vectors of the chief and deputy satellites the in-plane motion of the deputy satellite can be described with the relative eccentricity vector

$$\Delta\boldsymbol{e} = \begin{bmatrix} \Delta e_x \\ \Delta e_y \end{bmatrix} = \delta e \cdot \begin{bmatrix} cos(\varphi) \\ \sin(\varphi) \end{bmatrix} \tag{3-10}$$

with the angle φ denoting the orientation and δe denoting the magnitude of the relative eccentricity vector as shown in Figure 3-3. It is important not to confuse the relative eccentricity ($\Delta\boldsymbol{e}$) and inclination ($\Delta\boldsymbol{i}$) vectors with the differences in the eccentricity (Δe) and inclination (Δi). With the definition of the relative eccentricity vector the in-plane motion can be given for a chief-centered orbit as

$$x(t) = \left(-\Delta e_x cos\left(u_l(t)\right) - \Delta e_y sin\left(u_l(t)\right)\right) \cdot a \tag{3-11}$$

These simplified representations of the relative orbital mechanics can be used to derive a comprehensive model of the oscillating motion of the deputy satellite around the chief. This model can be used to easily design relative orbits, as the orbital elements have a clear geometric relationship with the orbital shape.

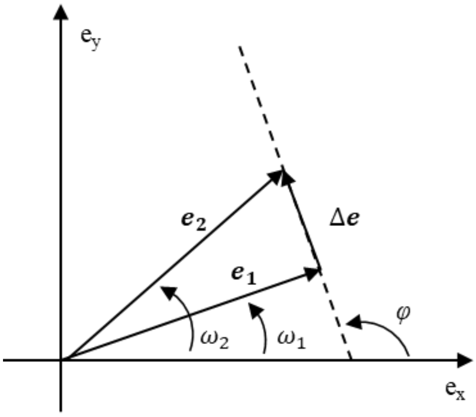

Figure 3-3 Definition of the relative eccentricity vector. [40]

Using the definition of the relative eccentricity and inclination vectors the complete linearized equations of motion of the deputy can be given as

$$\boldsymbol{X} = \begin{bmatrix} \Delta a & 0 & -\Delta e_x a & -\Delta e_y a \\ \Delta\lambda \cdot a & -3\Delta a/2 & -2\Delta e_y a & 2\Delta e_x a \\ 0 & 0 & -\Delta i_y a & \Delta i_x a \\ 0 & 0 & -\Delta e_y v_a & \Delta e_x v_a \\ -3\Delta a \cdot v_a/2a & 0 & 2\Delta e_x v_a & 2\Delta e_y v_a \\ 0 & 0 & \Delta i_x v_a & \Delta i_y v_a \end{bmatrix} \times \begin{bmatrix} 1 \\ u_l - u_{l,0} \\ \cos(u_l) \\ \sin(u_l) \end{bmatrix} \tag{3-12}$$

With $\Delta\lambda = \left(u_{l,d} - u_l\right) + (\Omega_d - \Omega) \cdot \cos(i)$, the in-track shift of the deputy. Using the linearized equations, the state of the deputy satellite can be determined with the chief mean argument of latitude and the relative elements $\Delta\lambda, \Delta a$, $\Delta\boldsymbol{e}$, $\Delta\boldsymbol{i}$. The element u_0 denotes the mean argument of latitude at the epoch t_0. For equal semi-major axes ($\Delta a = 0$) and centered relative orbits ($\Delta\lambda = 0$), the geometrical form of the relative orbit becomes apparent when expressed as a function of the angle φ and the relative ascending node θ as given in [40]

$$\begin{gathered} x(t) = -\delta e \cdot \cos(u_l - \varphi) \cdot a \\ y(t) = 2\delta e \cdot \sin(u_l - \varphi) \cdot a \\ z(t) = \delta i \cdot sin(u_l - \theta) \cdot a \end{gathered} \tag{3-13}$$

The relative eccentricity and inclination vector formulation is especially practical for the design of relative orbits. Depending on the relative orientation of the relative eccentricity and inclination vectors to each other, different geometric orbit shapes can be realized.

As stated above the main advantage of using the relative eccentricity and inclination vector formulation is the simple design of bounded, chief-centered relative orbits. This formulation leaves four parameters $\left(\Delta e_x,\ \Delta e_y,\ \Delta i_x,\ \Delta i_y\right)$ which have a direct geometric relationship with the relative orbit shape. Along with the in-track shift $\Delta\lambda$ and the difference in semi-major axis Δa the relative orbit can be parameterized by the following set of relative orbital elements

$$\boldsymbol{\delta\alpha} = \begin{bmatrix} \Delta a \\ \Delta\lambda \\ \Delta e_x \\ \Delta e_y \\ \Delta i_x \\ \Delta i_y \end{bmatrix} \tag{3-14}$$

3.3 Perturbed satellite motion

So far, the relative motion of two satellites has been given for the two-body, i.e., Keplerian case only. In the idealized Keplerian case the deputy satellites could remain on fixed orbits indefinitely. In a real-life scenario however, the orbital dynamics of satellites are governed by a range of perturbations that stem from various sources. Deviations from the Keplerian orbit model are mainly caused by

- the non-spherical shape of the Earth, i.e., Earth oblateness. Differential accelerations of up to $10^{-6} m/s^2$ may act on satellites in close-proximity flight depending on the inter-satellite distance. [58]
- aerodynamic drag from the residual atmosphere. The magnitude of the differential accelerations between satellites in close-proximity flight are strongly dependent on the differences in ballistic coefficients.
- solar radiation pressure, originating from the momentum of photons impinging onto surfaces. Differential accelerations up to $10^{-16} m/s^2$ may act on the satellites. [58]

The dominant perturbations for LEO satellites are represented by the Earth oblateness perturbation and the residual aerodynamic drag.

3.3.1 Earth oblateness

In the last section, the Keplerian formulation of orbital mechanics, assumed a spherical central gravitational body. The real shape of the Earth, however, significantly deviates from an ideal sphere and is more akin to an oblate spheroid, which is flattened at the poles. The measure which characterizes the degree to which Earth is flattened is called Earth flattening or Earth oblateness. The difference between the Earth semi-major and semi-minor axis is approx. 21,385 km. The non-spherical shape of the Earth has implications for its geopotential model that describes the gravitational field. In orbit mechanics, perturbing forces resulting from deviations from the spherical gravitational model are described as a function of the zonal coefficients. Zonal coefficients of different order are associated with the spherical harmonics of the Earth's surface. The primary perturbing forces to satellites in LEO are associated with the J_2 zonal coefficient. The J_2 forces lead to short-periodic, long-periodic and secular perturbations of the relative satellite motion during formation flight. An analytical expression has been derived for the first-order secular variations of the classical orbital elements by Brouwer [59]. These are given by

$$\frac{d}{dt}\begin{bmatrix} a \\ e \\ i \\ \Omega \\ \omega \\ M \end{bmatrix} = \begin{bmatrix} 0 \\ 0 \\ 0 \\ -3\gamma n cos(i) \\ \frac{3}{2}\gamma n(5 \cdot cos^2(i) - 1) \\ \frac{3}{2}\gamma n \eta_e (3 \cdot cos^2(i) - 1) \end{bmatrix} \tag{3-15}$$

with

$$\gamma = \frac{J_2}{2}\left(\frac{R_E}{a}\right)^2 \frac{1}{{\eta_e}^4} \tag{3-16}$$

and the eccentricity factor $\eta_e = \sqrt{1 - e^2}$. Equation (3-15) shows that the J_2 perturbations lead to a gradual shift of the RAAN, the argument of perigee and the mean anomaly. Neglecting second-order terms and assuming close near-circular orbits, D'Amico [58] derived an expression for the variation of the relative orbital elements of the deputy satellite circumventing a chief satellite. For close-proximity formation flight, the variation of the relative orbital elements under J_2 perturbations can be expressed as

$$\boldsymbol{\delta\alpha(t)} = \begin{bmatrix} \Delta a \\ \Delta\lambda - \frac{21}{2}(\gamma sin(2i)\Delta i_x + \frac{\Delta a}{7a})(u_l(t) - u_{l,0}) \\ \delta e cos(\varphi + \varphi'(u_l(t) - u_{l,0})) \\ \delta e sin(\varphi + \varphi'(u_l(t) - u_{l,0})) \\ \Delta i_x \\ \Delta i_y + 3\gamma sin^2(i)\Delta i_x(u_l(t) - u_{l,0})) \end{bmatrix} \tag{3-17}$$

Where

$$\varphi' = \frac{d\varphi}{du_l} = \frac{3}{2}\gamma(5 \cdot cos^2(i) - 1) \tag{3-18}$$

It can be seen from expression (3-17) that the J_2 forces lead to a circular shift of the relative eccentricity vector, a change of Δi_y and a growing in-track distance.

3.3.2 Minimizing the J_2 effects in satellite formations

The swarm-based aperture synthesis radiometer will require a large number of satellites orbiting a chief satellite for longer period of time. Equation (3-17) shows that the magnitude of secular variations of a relative orbit is strongly dependent on the selection of the relative orbit elements. Freely choosing relative orbit elements would likely lead to a strong drift of the relative orbit over time. In a satellite swarm containing a large number of deputies on slightly different relative orbits this would lead to a disintegration of the swarm within hours or days. While a certain drift from a reference orbit cannot be totally prevented due to the non-linear effects, which have been neglected in equation (3-17) and other perturbing forces, it is possible to minimize the first-order J_2 effects by a convenient choice of relative orbital elements. Since any internal drift in the satellite swarm must be corrected by the orbit control system under the consumption of precious fuel, it seems reasonable to attempt to minimize fuel consumption by choosing relative orbits that are “supported” by physics. From equation (3-17) it can be seen that the conditions for a minimal drift orbit are

$$\Delta i_x = \Delta i = 0 \qquad \Delta a = 0 \tag{3-19}$$

In the case of equal chief and deputy orbit inclination the in-track drift $\Delta\lambda$ and the drift of the second component of the relative inclination vector Δi_y are zero. Despite equal inclinations a cross-track offset of the satellites can be achieved by choosing different RAAN ($\Delta\Omega \neq 0$) leading to a maximum cross-track distance at the Earth’s poles. This concept has been successfully used for the Helix orbit of the TanDEM-X mission [60], [61], where the distance between the satellites is kept between 120 and 500 m.

Figure 3-4 shows the motion of two deputy satellites on different relative orbits in the Hill frame for over 40 orbits under the influence of J_2 perturbations. The first satellite is placed on a relative orbit (green) with relative orbital elements set to $\Delta\boldsymbol{i} = [0,10]^T$ and $\Delta\boldsymbol{e} = [0,10]^T$. This orbit adheres to the condition given in equation (3-19). The small orbital variations that remain can be attributed to non-linear effects in the orbit mechanics. The second satellite is placed on a relative orbit (yellow) with relative orbital elements set at $\Delta\boldsymbol{i} = [10,0]^T$ and $\Delta\boldsymbol{e} = [0,10]^T$. In comparison to the green orbit the orbital drift is significantly larger, which is due to a shift of the relative inclination vector as described in equation (3-17). When designing a satellite formation, it is thus generally beneficial to choose reference orbits that are supported by orbital mechanics in order to minimize satellite drift and the need for corrections from the satellite orbit control system.

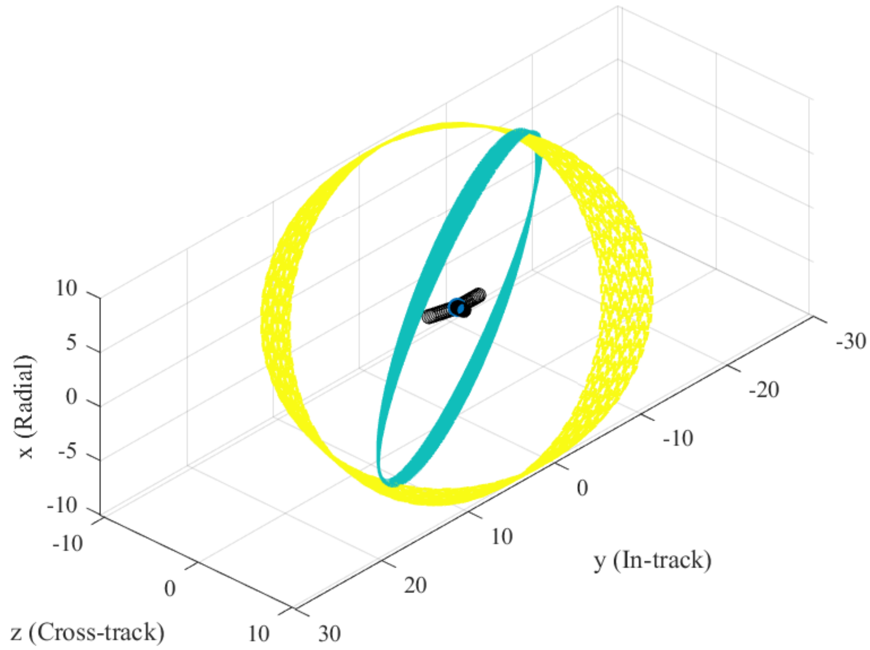

Figure 3-4 One relative orbit under the conditions $\Delta i = [0,10]^T$ and $\Delta e = [0,10]^T$ (green) and one relative orbit under the condition $\Delta i = [10,0]^T$ and $\Delta e = [0,10]^T$ (yellow) in the Hill frame, taking into account J_2 perturbations only.

3.3.3 Differential aerodynamic drag

Satellites in LEO experience significant aerodynamic drag due to the interaction with the residual atmosphere. Aerodynamic drag manifests itself as a constant deceleration of the satellite against the direction of flight. The aerodynamic forces acting on a single satellite can be described as [58]

$$\ddot{y} = -\frac{1}{2}\rho {v_A}^2 C_D \frac{A}{m_s} \tag{3-20}$$

with the density of the atmosphere ρ, the velocity with respect to the atmosphere v_A, the aerodynamic drag coefficient C_D and the ratio of satellite cross-section area A to the satellite mass m_s. The aerodynamic drag coefficient which is related to the shape of the satellite is difficult to determine in practice. In the exosphere the molecular density is so low that formulas used to calculate the drag coefficients for airplanes cannot be applied. In high altitudes free molecular flow dominates the fluid dynamics of gasses around a satellite. Sentman [62] investigated satellite drag in the early 1960s and found drag coefficient values of $C_D = 2.2$ to $C_D = 2.6$. In literature [58] the ballistic coefficient

$$B_C = C_D \frac{A}{m_s} \tag{3-21}$$

is also often used to aggregate all influences of the satellite on the aerodynamic drag into one parameter. Neglecting density variations in close-proximity formation flight the relative along-track shift due to aerodynamic drag can be given as

$$y(t) = \frac{3}{4n^2} \Delta B_C \rho {v_A}^2 (u_l(t) - u_{l,0})^2 \tag{3-22}$$

The decelerating effect of aerodynamic drag also results in a relative change of semi-major axis [58]

$$x(t) = -\frac{1}{n^2} \Delta B_C \rho {v_A}^2 (u_l(t) - u_{l,0}) \tag{3-23}$$

Figure 3-5 shows the relative orbits from Figure 3-4 with added aerodynamic drag (only 5 orbits shown). The in-track shift grows exponentially due to the direct deceleration because of aerodynamic drag and the resulting decrease of the satellite orbit height.

Differential drag in the swarm-based aperture synthesis radiometer arises due to differences in the ballistic coefficient between the chief and the deputy satellites. It will need to be compensated by the orbit control system and thus effectively increases fuel consumption. The aerodynamic drag is a significant factor impacting the selection of the orbit height for the radiometer system under study.

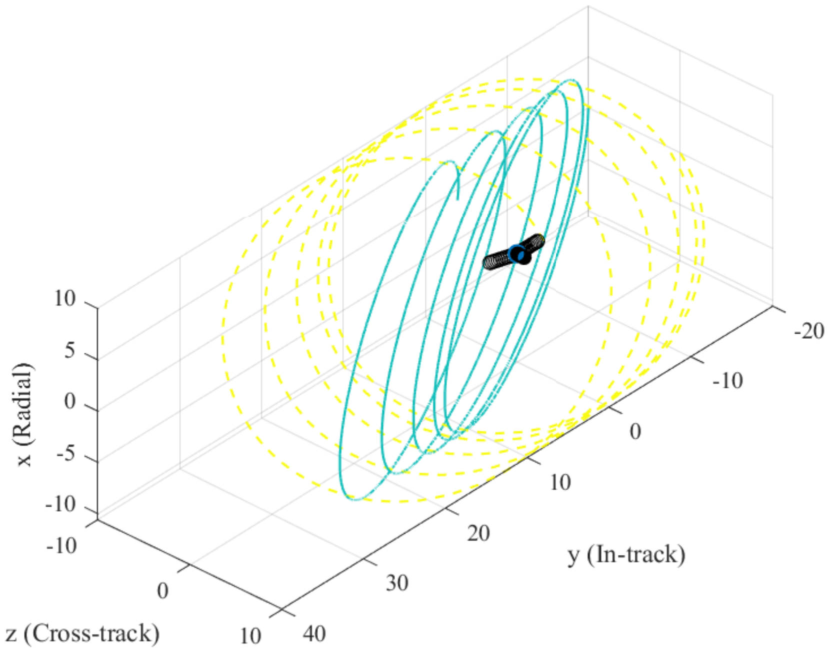

Figure 3-5 One relative orbit under the conditions $\Delta i = [0,10]^T$ and $\Delta e = [0,10]^T$ (green) and one relative orbit under the condition $\Delta i = [10,0]^T$ and $\Delta e = [0,10]^T$ (yellow) in the Hill frame, taking into account J_2 perturbations and aerodynamic drag.

3.4 High-fidelity relative motion dynamics model

The previous chapter provided an overview of relative orbital elements and on how orbit perturbations affect the relative trajectory of a deputy satellite. The relative orbital element formulation is convenient for the conceptual design of relative orbits, since they enable a direct intuitive understanding of orbit geometry. However, for simulations of high-precision close-proximity flight (<100 m) a model of the orbit mechanics is required, that includes the higher order J_2 terms as well. For orbit propagation of satellite formations both closed-form analytical and numerical models can be used. The closed-form analytical models hold the distinctive advantage in computational efficiency and are thus employed where computational resources are sparse, e.g., satellite On-Board Computers (OBC) or large timeframes are to be simulated. The accuracy of such models over a 24-hour simulation period lies below 200 m [63] for a close-proximity satellite formation in LEO when compared to a full-force high-fidelity numerical model.

For the simulations conducted in this thesis, high-fidelity numerical models are chosen to ensure high accuracy orbit propagation. A range of nonlinear models have been proposed for the relative motion of satellites in LEO under perturbing forces.

While some of these models neglect the perturbation of the chief orbit [64] others are complex in their inclusion of the higher-order J_2 perturbations [65]. A model that has recently seen adoption [66] is the model devised by Xu and Wang [67]. This model uses a set of differential equations to derive an exact nonlinear model of the relative motion of a deputy satellite. It expresses the chief orbit in terms of reference satellite variables and uses Lagrangian mechanics to obtain first-order differential equations. The model has the advantage of accurately taking into account the perturbation of the chief orbit, while still maintaining a simple form.

Considering aerodynamic drag and the J_2 perturbations, the equations of motion for the chief orbit can be described by

$$\frac{d}{dt}\begin{bmatrix} r \\ \dot{r} \\ L \\ \Omega \\ i \\ u_l \end{bmatrix} = \begin{bmatrix} \dot{r} \\ -\frac{\mu}{r^2}+\frac{L^2}{r^3}-\frac{k_{J2}}{r^4}\left(1-3sin^2(i)sin^2(u_l)\right)-C\|v_A\|\dot{r} \\ -\frac{k_{J2}sin(2u_l)sin^2(i)}{r^3}+C\|v_A\|(L-\omega_E r^2 cos(i)) \\ -\frac{2k_{J2}cos(i)sin^2(u_l)}{Lr^3}+\frac{C\|v_A\|\omega_E r^2 sin(2u_l)}{2L} \\ -\frac{k_{J2}sin(2i)sin(2u_l)}{2Lr^3}+\frac{C\|v_A\|\omega_E r^2 sin(i)cos^2(u_l)}{L} \\ \frac{L}{r^2}+\frac{2k_{J2}cos^2(i)sin^2(u_l)}{Lr^3}+\frac{C\|v_A\|\omega_E r^2 cos(i)sin(2u_l)}{2L} \end{bmatrix} \tag{3-24}$$

with the geocentric distance r (see Figure 3-1), the angular orbit momentum $L = r \times \dot{r}$, the RAAN Ω, the inclination i, the argument of latitude u_l and the rotation of the Earth $\omega_E = 7.2921 \cdot 10^{-5}\ rad/s$. The parameter k_{J2} is defined as

$$k_{J2} = \frac{3}{2} J_2 \mu {R_E}^2 \tag{3-25}$$

The second terms in equations (3-24) include the velocity of the chief with respect to the atmosphere $v_A \approx v_a$, and the aerodynamic coefficient C, defined by

$$C = \frac{1}{2} C_D \frac{A}{m_s} \rho \tag{3-26}$$

With the definition of the chief satellite motion, the deputy motion can be described in the Hill frame by

$$\begin{bmatrix}\ddot{x}\\ \ddot{y}\\ \ddot{z}\end{bmatrix} = \begin{bmatrix} 2\dot{y}\omega_z - x({\eta_d}^2 - {\omega_z}^2) + y\alpha_z - z\omega_x\omega_z \\ -2\dot{x}\omega_z + 2\dot{z}\omega_x - x\alpha_z - y({\eta_d}^2 - {\omega_z}^2 - {\omega_x}^2) + z\alpha_x \\ -2\dot{y}\omega_x - x\omega_x\omega_z - y\alpha_x - z({\eta_d}^2 - {\omega_x}^2) \end{bmatrix} + \begin{bmatrix} -(\xi_d - \xi)sin(i)sin(u_l) - r({\eta_d}^2 - \eta^2) \\ -(\xi_d - \xi)sin(i)\cos(u_l) \\ -(\xi_d - \xi)cos(i) \end{bmatrix} + a_A \tag{3-27}$$

With the aerodynamic forces acting on the deputy satellite

$$a_A = \begin{bmatrix} -C_d\left\|v_{A,d}\right\|(\dot{x} - y\omega_z) - (C_d\left\|v_{A,d}\right\| - C\|v_A\|)\dot{r} \\ -C_d\left\|v_{A,d}\right\|(\dot{y} + x\omega_z - z\omega_x) - (C_d\left\|v_{A,d}\right\| - C\|v_A\|)(\frac{L}{r} - \omega_E r cos(i)) \\ -C_d\left\|v_{A,d}\right\|(\dot{z} + y\omega_x) - (C_d\left\|v_{A,d}\right\| - C\|v_A\|)\omega_E r cos(u_l)\sin(i) \end{bmatrix} \tag{3-28}$$

The quantities $C, v_A, \xi, \eta, L, r, i, u_l$ without a subscript refer to quantities of the chief satellite. The terms ξ, η have been introduced for simplicity and are defined as

$$\xi = \frac{2k_{J2}sin(i)sin(u_l)}{r^4} \qquad \xi_d = \frac{2k_{J2}r_{d,Z}}{{r_d}^5} \tag{3-29}$$

And

$$\eta^2 = \frac{\mu}{r^3} + \frac{k_{J2}}{r^5} - \frac{5k_{J2}sin^2(i)sin^2(u_l)}{r^5} \qquad {\eta_d}^2 = \frac{\mu}{{r_d}^3} + \frac{k_{J2}}{{r_d}^5} - \frac{5k_{J2}{r_{d,Z}}^2}{{r_d}^7} \tag{3-30}$$

Along with

$$r_d = \sqrt{(r + x)^2 + y^2 + z^2} \tag{3-31}$$

And

$$r_{d,Z} = (r + x)sin(i)sin(u_l) + ysin(i)cos(u_l) + zcos(i) \tag{3-32}$$

A complete derivation of the model is given in [67]. It is convenient because it can easily be extended with further forces acting on the deputy or chief, e.g., thruster inputs. With a set of initial conditions for the chief and deputy the above equations result in a system of nine ordinary differential equations that can be solved using standard numerical solvers.

4 SYSTEM SIMULATOR

4.1 Simulator overview

As outlined in section 1.4 an investigation of the feasibility of the satellite swarm-based synthetic aperture radiometer requires a system simulator that is capable of analyzing both the orbit mechanical aspects and the interferometric imaging simultaneously. For this purpose, the Satellite Swarm-Based Synthetic Aperture Radiometer (SSBSAR) software package has been created. It represents the main tool for the analysis of specified satellite configurations in regard to the feasibility of the orbit mechanics and the imaging performance.

Figure 4-1 shows a high-level schematic of the various components of the system simulator. The system simulator can be broadly divided into the Input Module, an Orbit Propagation module, an Image Processing Module and a System Feasibility Analysis Module. The Input Module enables the user to define the key parameters that define the satellite orbit configuration and the spacecraft bus and payload capabilities. After calculating basic orbital properties for the chief and Cartesian initial conditions in the Hill frame, the state of the satellites is propagated for a number of orbits that can be specified by the user. The orbit propagation considers the impulsive forces originating from the active orbit control systems on board of the deputy satellites.

The propagation returns an array with the Cartesian coordinates of the deputies in the Hill frame over the propagated timeframe with a timestep that is user defined. The coordinates for the deputy motions are then handed over to the Image Processing Module and the System Feasibility Analysis Module. The Image Processing Module effectively generates the array PSF of the synthesized antenna that is formed by the deputy ARU and the ARU on the central receiver array. The output of the Image Processing Module includes the ground spatial resolution, the sidelobe levels and the Main Beam Efficiency (MBE) of the PSF. The System Feasibility Analysis Module requires the propagated relative deputy states as an input. It determines the amount of fuel expended per orbit by the formation-keeping maneuvers, the collision probability with other deputies in proximity and the ground-track drift. Finally, a Visualization Module (which is not shown in the diagram) gives the user various options in visualizing the simulator output.

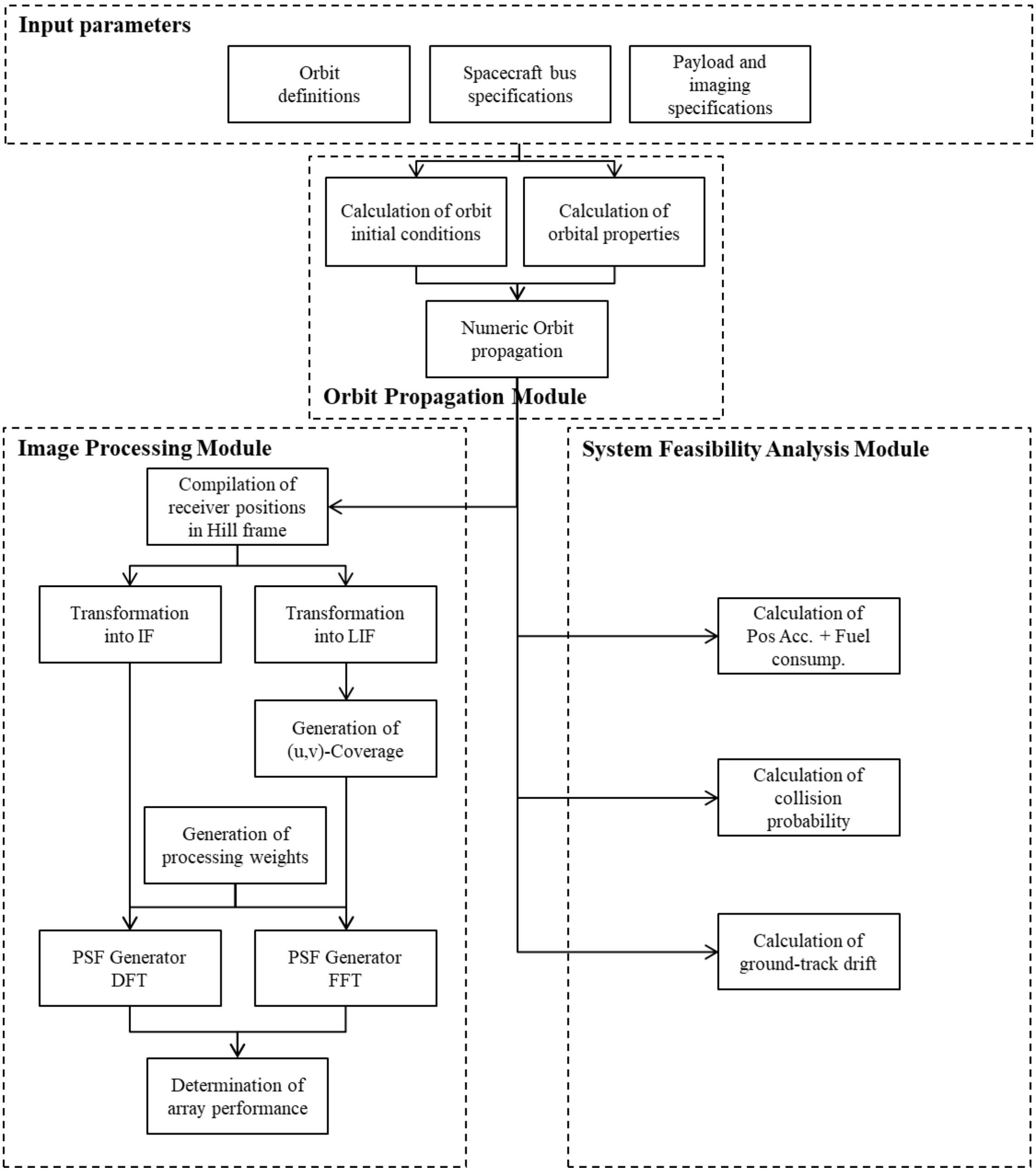

Figure 4-1 High-level schematic of the various components and processing steps within the Satellite Swarm-Based Synthetic Aperture Radiometer (SSBSAR) software package. The PSF denotes the Point Spread Function, the IF denotes the Imaging Frame and the LIF the Local Imaging Frame.

The following sections discuss the implementation of the system simulator in detail. They provide an overview of each modules' functionality and describe the core system simulator validation steps.

4.2 Input Module

As described above, the Input Module enables the user to define all parameters that are relevant for setting a specific simulation scenario. The chief orbit definition is given by classical orbit elements, while the definition of the deputy satellite orbits is given by a set of relative orbit elements. An initial argument of latitude is used as a starting point for the propagation of the system. The spacecraft bus definition requires the specification of the main spacecraft physical parameters and the on-board GNC system.

All input parameters used in the system simulator are given in SI-units. The spacecraft parameters include the spacecraft mass, the spacecraft area, the drag coefficient C_D among others. Propulsion parameters that need to be specified are the nominal thrust of the thrusters on-board the deputy satellite, the thruster I_{SP} in [s] and the carried propellant mass. In addition, the thruster inaccuracies have to be defined along with the accuracy of the position and velocity delivered by the GNC system. Settings for the orbit feedback-controller also need to be made, as explained in the next section. Finally, satellite payload and imaging parameters must be defined. These parameters include the basic information on the observation geometry, including the observation angles, payload characteristics (frequency, bandwidth etc.), as well as inputs for the image processing and the central array configuration.

4.3 Orbit Propagation Module

In order to keep the deputy satellites on a predefined reference orbit regarding the chief satellite, each deputy must be capable of correcting for orbital perturbations with an impulsive orbit control system. Keeping the deputy on a specific relative orbit for longer periods of time, called "station-keeping" requires a closed-loop control method that periodically compares the current state and the reference state in orbit and triggers corrective thrust impulses. There are different centralized and decentralized schemes for the control of satellite swarms. Centralized approaches are “leader-follower” approaches that require differential navigation measurements of all deputies to one single satellite “leader” or “chief”. In decentralized approaches differential measurements to other deputy satellites in proximity are also required [68]. The decentralized approach is often preferred when a “single-point of failure” is to be avoided. However, since the chief satellite represents a single-point of failure for the swarm-based radiometer system anyway (as it carries the data processing and downlink capabilities), centralized approaches are sufficient for the current study. The predominant centralized approach for close-proximity formation flying is the Linear Quadratic Regulator (LQR) approach. It has been successfully validated by a number of small satellite missions, most notably the CanX-45 mission [24]. The LQR approach represents a control method that is capable of enabling high-precision orbit control while optimizing fuel consumption. It is based on weighting the state error according to a control matrix, which is determined by solving a cost function.

The discrete-time Linear Quadratic Regulator (DLQR) control method is a discrete formulation of the LQR method. It enables the implementation of an impulsive formation control that is stable also with less frequent control maneuvers [69]. Additionally, it can be easily implemented on small satellite hardware due to its computational efficiency. A block diagram of the DLQR controller that is employed to simulate orbit control within the swarm-based aperture radiometer system is depicted in Figure 4-2.

At the start of the simulation the state $\boldsymbol{X_0}$ needs to be determined from the initial conditions set by the user. In the system simulator the initial conditions are set by choosing a reference orbit through defining the relative orbital element vector as given in equation (3-14). The relative orbital element vector is then translated into a set of Cartesian coordinates in the Hill frame, which uses the linear mapping in equation (3-12). To avoid significant non-linear effects, satellite distances should not exceed 1000 m for the system simulator. With the initial conditions the relative deputy positions can be propagated for a specified timeframe, assuming the model presented in section 3.4.

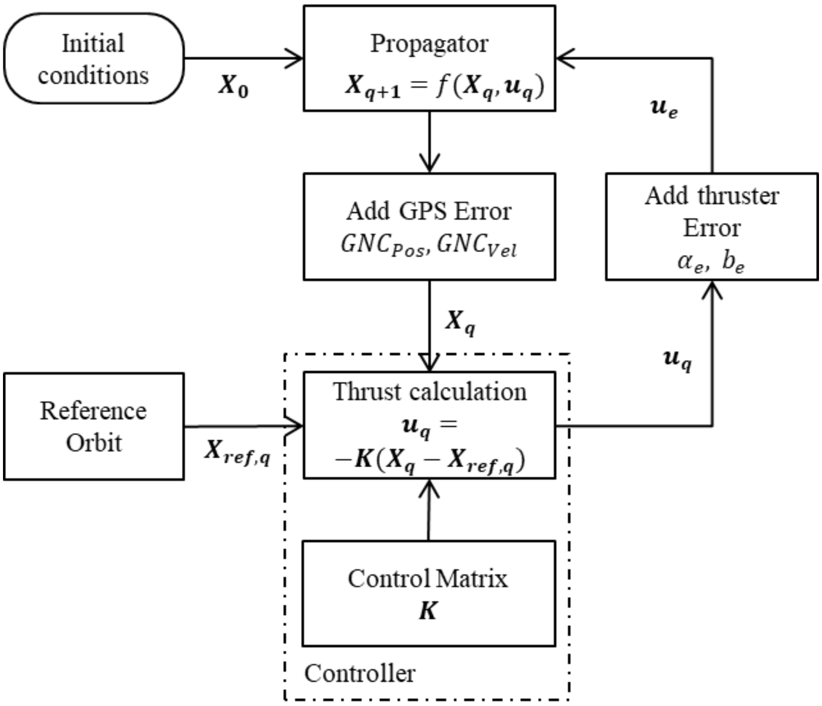

Figure 4-2 Block diagram for the DLQR-controller for orbit maintenance of deputy satellites.

4.3.1 State uncertainties

In the real-world implementation, the relative position and velocity estimates are based on Carrier Phase Differential GNSS (DGNSS) measurements and on-board orbit propagation data [70]. The state estimates from orbit propagation and DGNSS measurements are both subject to errors. Due to the limited computational power, on-board, orbit propagation in nanosatellites is conducted using analytical models, which neglect higher-order orbit perturbations. State estimates from DGNSS will be subject to errors as well, such as clock-related errors, signal propagation errors and other system errors. The state-of-the art method to generate single state measurements from multiple sources is by employing an Extended Kalman Filter (EKF) [69]. Since previous missions, e.g. PRISMA [71], have shown that the output of the EKF filter has an approximately Gaussian characteristic, the simulation model used within this thesis can be greatly simplified by assuming Gaussian velocity and position errors directly. While this simplification will still enable modelling of the spacecraft trajectory and control inputs with sufficient accuracy, it alleviates one of the need to perform complex GNSS satellite modelling and the implementation of an EKF. The simulations conducted within this thesis thus model the satellite state errors directly by randomly choosing a deviation from the ideal propagated position according to a Gaussian distribution. GPS-blackouts are not taken into account and thus it is assumed that the statistical nature of the GNSS error is time-independent.

4.3.2 Corrective impulse control

After determining the state estimate at control period q, the corrective impulsive control thrust u_q in N/kg can be calculated by a linear state-feedback control law

$$\boldsymbol{u_q} = -\boldsymbol{K}(\boldsymbol{X_q} - \boldsymbol{X_{ref,q}}) \tag{4-1}$$

with the tracking error $\boldsymbol{X_{e,q}} = (\boldsymbol{X_q} - \boldsymbol{X_{ref,q}})$, the reference state $\boldsymbol{X_{ref,q}}$ and the current state $\boldsymbol{X_q}$ at control period q and the control matrix $\boldsymbol{K}$. The discrete control matrix represents the gain of the feedback controller and is determined by solving the Discrete Algebraic Riccati Equation (DARE), using the state space representation of the Keplerian dynamics and weighting matrices.

The calculation of the discrete constant gain matrix $\boldsymbol{K}$ for the autonomous control of the deputy satellites is based on the HCW formulation given in equation (3-1). The continuous relative equations can be written in the discretized matrix form as

$$\dot{\boldsymbol{X}}_{\boldsymbol{e,q}} = \Phi \boldsymbol{X_{e,q}} + \boldsymbol{B_d}\boldsymbol{u_q} \tag{4-2}$$

where $\boldsymbol{B_d}$ is defined as

$$\boldsymbol{B_d} = \left(\int_0^{T_{pwm}} e^{\boldsymbol{A}\tau}\, d\tau\right)\boldsymbol{B} \tag{4-3}$$

and

$$\Phi = e^{\boldsymbol{A}\cdot T_{pwm}} \tag{4-4}$$

With the time between control periods, T_{pwm}. The state space representation of the HCW dynamics can be described by

$$\boldsymbol{A} = \begin{bmatrix} 0 & 0 & 0 & 1 & 0 & 0 \\ 0 & 0 & 0 & 0 & 1 & 0 \\ 0 & 0 & 0 & 0 & 0 & 1 \\ 3n^2 & 0 & 0 & 0 & 2n & 0 \\ 0 & 0 & 0 & -2n & 0 & 0 \\ 0 & 0 & -n^2 & 0 & 0 & 0 \end{bmatrix} \tag{4-5}$$

and

$$\boldsymbol{B} = \begin{bmatrix} 0_{3x3} \\ I_{3x3} \end{bmatrix} \tag{4-6}$$

Using these definitions, a discrete quadratic cost function can be defined as

$$J = \frac{1}{2}\sum_{k=0}^{\infty}\left(\boldsymbol{X_{e,q}}^{\boldsymbol{T}}\boldsymbol{Q}\boldsymbol{X_{e,q}} + \boldsymbol{u_q}^{\boldsymbol{T}}\boldsymbol{R}\boldsymbol{u_q}\right) \tag{4-7}$$

with $\boldsymbol{Q}$ and $\boldsymbol{R}$ denoting the weighting matrices. When minimizing the cost function for equation (4-1), the discrete constant gain matrix $\boldsymbol{K}$ is found to be

$$\boldsymbol{K} = \left(\boldsymbol{B_d}^{\boldsymbol{T}}\boldsymbol{\overline{P}}\boldsymbol{B_d} + \boldsymbol{R}\right)^{-1}\boldsymbol{B_d}^{\boldsymbol{T}}\boldsymbol{\overline{P}}\Phi \tag{4-8}$$

The matrix $\boldsymbol{\overline{P}}$ can be determined by numerically solving the DARE equation given by

$$\Phi^{\boldsymbol{T}}\boldsymbol{\overline{P}}\Phi - \boldsymbol{\overline{P}} - \Phi^{\boldsymbol{T}}\boldsymbol{\overline{P}}\boldsymbol{B_d}\left(\boldsymbol{B_d}^{\boldsymbol{T}}\boldsymbol{\overline{P}}\boldsymbol{B_d} + \boldsymbol{R}\right)^{-1}\boldsymbol{B_d}^{\boldsymbol{T}}\boldsymbol{\overline{P}}\Phi + \boldsymbol{Q} = 0 \tag{4-9}$$

The weighting matrices used for the calculation of the control matrices for the autonomous orbital control of the deputy satellites are adopted from the ones used in the CanX-45 mission. This mission was chosen as a reference since its high-precision formation flying demonstration with 8U CubeSats represents a similar scenario to the one presented within the context of this thesis. The weighting matrices used in the system simulator are thus given by

$$\boldsymbol{R} = R_S\frac{1.4}{n^2}\begin{bmatrix}1 & 0 & 0\\ 0 & 1 & 0\\ 0 & 0 & 1\end{bmatrix} \tag{4-10}$$

with R_S, a scaling parameter, and

$$\mathbf{Q} = \begin{bmatrix}1.1n^2 & 0 & 0 & 0 & 0 & 0\\ 0 & 1.1n^2 & 0 & 0 & 0 & 0\\ 0 & 0 & 1.1n^2 & 0 & 0 & 0\\ 0 & 0 & 0 & 0.78 & 0 & 0\\ 0 & 0 & 0 & 0 & 0.78 & 0\\ 0 & 0 & 0 & 0 & 0 & 0.78\end{bmatrix} \tag{4-11}$$

The DARE equation is solved in the system simulator using the method laid out using Schur-decomposition type solvers [72]. A more elaborate description of the optimization of control matrices and a trade-off between the LQR and the DLQR method can be found in [70].

4.3.3 Thruster error modelling

Once the DARE equation is solved, the resulting control matrix can be used to calculate the desired thruster response $\boldsymbol{u_q}$ with equation (4-1). The desired thruster response cannot be implemented perfectly in an actual satellite system. Inaccuracies with the alignment of the thruster, the nozzle, slight changes of the spacecraft center of gravity and irregularities in thruster burns lead to a deviation of the implemented thruster response, which causes the spacecraft to deviate from the ideal trajectory. These inaccuracies need to be included in the simulation model separately. According to simulations conducted for the CanX-45 mission [70], the thrust direction errors and thrust magnitude errors are the dominant error sources that need be taken into account when simulating close-proximity formation flight in nanosatellites.

The thrust direction error is modelled by generating random angles within a user-specified maximum error angle α_e that are then used to rotate the ideal thrust vector. According to [70] the equation used to generate the random angles α_k can be defined as

$$\alpha_k = \alpha_e[(Rand - 0.5) \cdot 2] \cdot \frac{\pi}{180}, \quad k = 1,2,3 \tag{4-12}$$

with a random variable, $Rand$, drawn from a discrete uniform distribution over the set $\{-\alpha_e, \dots, +\alpha_e\}$. With these angles the ideal thrust vector can then be rotated using the rotation matrix

$$\boldsymbol{C_\alpha} = \begin{bmatrix} c(\alpha_2)c(\alpha_3) & c(\alpha_2)s(\alpha_3) & -s(\alpha_2) \\ s(\alpha_1)s(\alpha_2)s(\alpha_3) - c(\alpha_1)s(\alpha_3) & 0 & 0 \\ c(\alpha_1)s(\alpha_2)c(\alpha_3) - s(\alpha_1)s(\alpha_3) & 0 & 0 \end{bmatrix} + \begin{bmatrix} 0 & 0 & 0 \\ 0 & s(\alpha_1)s(\alpha_2)s(\alpha_3) - c(\alpha_1)c(\alpha_3) & s(\alpha_1)c(\alpha_2) \\ 0 & c(\alpha_1)s(\alpha_2)s(\alpha_3) - s(\alpha_1)c(\alpha_3) & c(\alpha_1)c(\alpha_2) \end{bmatrix} \tag{4-13}$$

With “s” and “c” denoting the sine and cosine functions. The resulting thrust vector can thus be calculated as

$$\boldsymbol{u_\alpha} = \boldsymbol{C_\alpha u_q} \tag{4-14}$$

The thrust magnitude error can be calculated by changing the magnitude of the thrust by a user-specified value b_e. This value is applied to the error-adjusted thrust vector with

$$\boldsymbol{u_e} = b_e \left[u_{\alpha,1} \left\| \frac{u_{\alpha,1}}{\|\boldsymbol{u_\alpha}\|} \right\| \quad u_{\alpha,2} \left\| \frac{u_{\alpha,2}}{\|\boldsymbol{u_\alpha}\|} \right\| \quad u_{\alpha,3} \left\| \frac{u_{\alpha,3}}{\|\boldsymbol{u_\alpha}\|} \right\| \right]^T + \boldsymbol{u_\alpha} \tag{4-15}$$

to receive the final thrust vector $\boldsymbol{u_e}$, which is used to conduct orbit propagation until the next control period.

4.3.4 Orbit propagation

The acceleration vector $\boldsymbol{a}$ acting on the spacecraft as a result of the activated thruster can be calculated with

$$\boldsymbol{a} = \frac{\boldsymbol{u_e}}{\|\boldsymbol{u_e}\|} U_{max} \tag{4-16}$$

U_{max} is the maximum thrust per unit mass delivered by the thruster. Formation-keeping thrusts are implemented in a Pulse Width Modulation (PWM) method, where the duration of thrust pulses in a control period determines the thrust magnitude. The orbit propagation up to the next control period is then conducted in two steps.

In the first step, the thrust acceleration vector $\boldsymbol{a}$ is included in the right side of the equation (3-27) and the deputy trajectory is propagated for the time the thruster is activated T_{on}, which is given by

$$T_{on} = \frac{\|\boldsymbol{u_e}\|}{U_{max}} T_{pwm} \tag{4-17}$$

Both the state of the chief and the deputy are propagated by solving the system of differential equations presented in chapter 3.4 using the standard built-in MATLAB ODE solver. Before the propagation of the thruster phase, the value of T_{on} is checked to ensure it does not lead to a thruster impulse that is smaller than the time $T_{on,Min}$, which is the time that would lead to a violation of the Minimum Impulse Bit (MIB) of the defined thruster. This condition can be stated as

$$T_{on} > T_{on,Min} \tag{4-18}$$

The second step is the propagation of the “unpowered” flight for the rest of the control period. This step is conducted using the unaltered nonlinear relative orbit model of Xu et al. [67] (as presented in the previous section) considering J_2 perturbations and aerodynamic forces. The magnitude of aerodynamic forces is strongly dependent on the density of the atmosphere. The system simulator calculates the atmospheric density in a separate function using the Mass-Spectrometer-Incoherent-Scatter 86 (MSIS-86) model. This model requires as inputs the mean solar flux over 90 days $F_{10.7}$, the solar flux from the previous day $F_{10.7a}$ and the local solar time.

Figure 4-3 shows the atmospheric density as a function of orbit altitude and mean solar flux. From the image it becomes apparent that the atmospheric density is strongly impacted by the solar flux. Differences can range up to an order of magnitude.

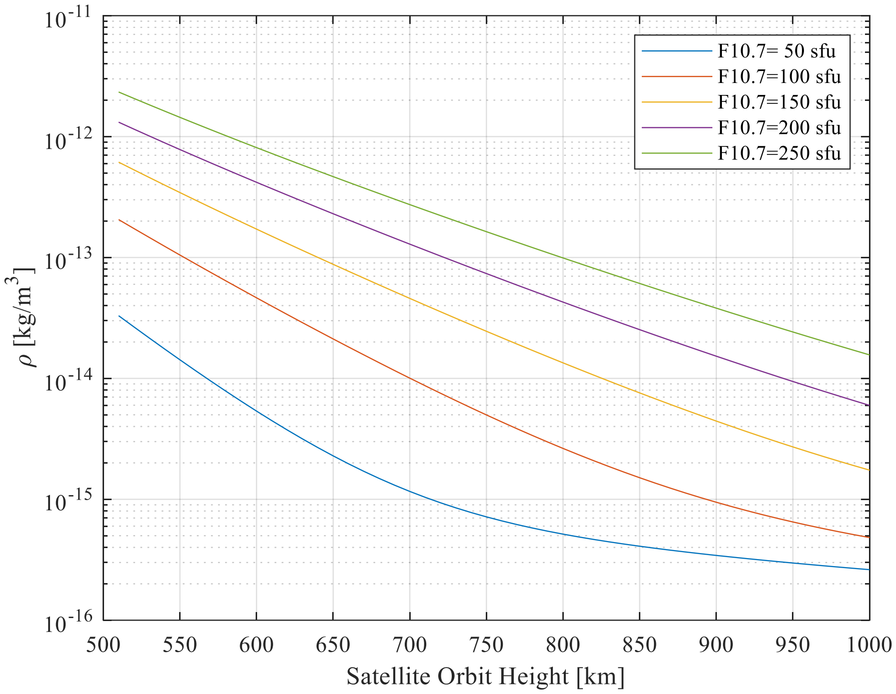

Figure 4-3 Atmospheric density to orbit altitude as a function of the mean solar flux.

Within this thesis the values for the solar flux are assumed to be 150 solar flux units (sfu) [73]. With the local solar time of 6:40 the atmospheric density reaches approximately $2.1 \times 10^{-14}\ kg/m^3$ at an orbit height of 755 km. This value was validated with the Satellite Tool Kit (STK).

The orbit propagation will result in the actual new deputy and chief satellite state at the next control period. GNC state estimation errors are then applied to the actual deputy satellite state by generating random inaccuracies from a normal distribution with the variances given by the user-defined relative GNC position and velocity accuracies. The resulting state estimate is then used to determine the position error to the reference orbit and the necessary thruster activation.

4.4 Image Processing Module

The Image Processing Module takes the inputs from the Orbit Propagation Module and the payload and imaging specifications from the user and calculates the (u_λ, v_λ) coverage and the PSF. Array performance parameters, i.e. the spatial and radiometric resolution, the sidelobe levels and the MBE are calculated from the PSF. Specific array configurations can be easily compared and evaluated using these parameters.

4.4.1 PSF generation

The Image Processing Module first compiles an array of receiver positions from the central antenna receivers and the deputy positions in the Hill frame over the entire overflight time of a target area. The Image Processing Module gives the user two options in calculating the PSF. The first option calculates the PSF, based on the coverage of the spatial frequency domain and a gridding algorithm followed by a Fast Fourier Transform. The second approach simply applies the Discrete Fourier Transform (DFT) to the signal delays by calculating the PSF directly using equation (2-40). While both approaches are not entirely equivalent, they yield PSF that are very similar. The first approach has the advantage that it is computationally efficient since it used the FFT algorithm to process data points. Its drawback however is that the FFT algorithm is based on the (u_λ, v_λ) coverage, which is calculated with respect to the point at the center of the target area defined by the user. For non-center pixels the PSF response will deviate from the DFT-solution, since the response at non-center pixels is also calculated with the (u_λ, v_λ) coverage that was generated with respect to the center pixel. Thus, the calculation of the PSF with the FFT method is only used for a first, rough evaluation of an array response within this thesis. The FFT approach however is useful for a fast evaluation of array configurations during the design process.

Due to the irregular motion of the receiver-carrying deputy satellites as part of the interferometric array, the sampling of the (u_λ, v_λ) domain is also irregular. In order to apply the FFT algorithm to irregularly sampled data, the data must be regridded. Regridding is the process of resampling the visibilities on a regular grid for subsequent use of the FFT. For this purpose, the system simulator implements the

Gaussian-gridding based Non-Uniform FFT (NUFFT) [74]. This approach relies on the interpolation of visibility sampled on a regularized grid.

4.4.2 Generating spatial frequency coverage

The calculation of the (u_λ, v_λ) coverage and the PSF neglects the curvature of the Earth and assumes that the satellite swarm is flying over a plane as depicted in Figure 2-6. According to the observation scenario, the (u_λ, v_λ) coverage is calculated by first transforming the receiver positions from the Hill frame into the Local Imaging Frame (LIF) by two consecutive rotations.

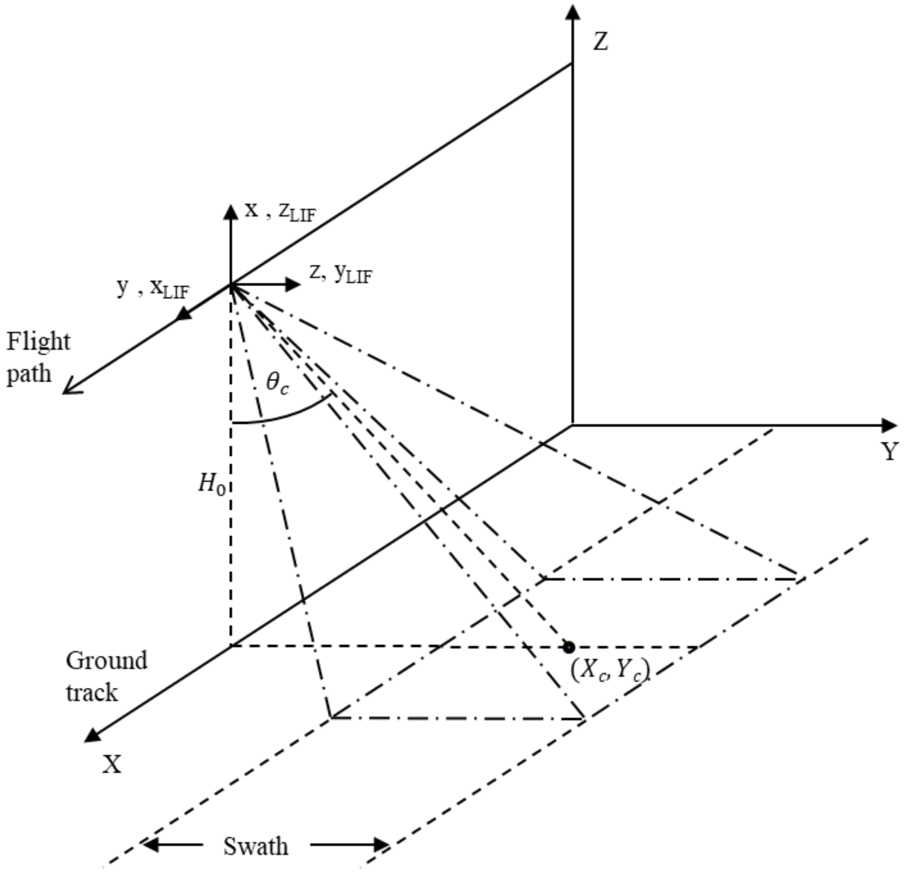

Figure 4-4 Observation scenario, depicting the Hill frame and the LIF frame

Each spatial frequency sampled by the baseline $j \in \{0, \dots N_B\}$ at the discrete time step $i \in \{0, \dots N_T\}$ (at times $t_i \in \{-t_c, -t_c + \Delta t \cdot i, \dots t_c\}$) can be expressed in a vector notation $\boldsymbol{q_{j,i}} = \left[u_{\lambda,j,i}, v_{\lambda,j,i}\right]^T$ in the (u_λ, v_λ) plane. With the baseline vector $\boldsymbol{B_{j,i}} = [\Delta x_{LIF}, \Delta y_{LIF}, \Delta z_{LIF}]^T$ and the position of the chief $X_{C,i}$ at time t_i the spatial frequencies for all baselines can be calculated by

$$\boldsymbol{q}_{j,i} = \Upsilon \cdot \begin{bmatrix} \left({Y_c}^2 + {H_0}^2\right) \cdot \Delta x_{LIF} + Y_c \cdot \Delta y_{LIF} - H_0 \cdot X_{C,i} \cdot \Delta z_{LIF} \\ X_{C,i} \cdot \Delta x_{LIF} \cdot Y_c + \left({X_{C,i}}^2 + {H_0}^2\right) \cdot \Delta y_{LIF} + H_0 \cdot Y_c \cdot \Delta z_{LIF} \end{bmatrix} \tag{4-19}$$

With

$$\Upsilon = \frac{\sqrt{\left({Y_c}^2 + {H_0}^2\right)}}{\lambda_c \cdot ({X_{C,i}}^2 + {Y_c}^2 + {H_0}^2)^{3/2}} \tag{4-20}$$

The generation of the spatial frequency vectors is not necessary if the PSF is generated directly with the DFT. In this case the signal time delays seen by each baseline are directly calculated with equation (2-32) after transforming the deputy positions into the IF. The PSF can then calculated with equation (2-40).

4.4.3 Tapering

As described in chapter 2, a weighting function can be applied to the spatial frequency samples. A weighting technique is used to reduce the sidelobes of the PSF. In windowing, weights are applied to the individual baseline samples that downweight (u_λ, v_λ) samples far from the origin, i.e., those stemming from long baselines. The "Blackman" window function (sometimes also called "tapering function" or "taper") was chosen for the tapering of the PSF in this thesis, since it has been extensively used with SMOS and in interferometric radiometry in general. It is defined by the function

$$T_{Black,j,i} = 0.42 + 0.5 \cdot cos\left(\pi \cdot \frac{\left\|\boldsymbol{q}_{j,i}\right\|}{\rho_{max}}\right) + 0.08 \cdot cos\left(2\pi \cdot \frac{\left\|\boldsymbol{q}_{j,i}\right\|}{\rho_{max}}\right) \tag{4-21}$$

where $\left\|\boldsymbol{q}_{j,i}\right\|$ is the length of the spatial frequency vector for baseline j and time step i. The parameter ρ_{max} denotes the distance from the origin of the spatial frequency domain at which the values of the taper function fall to a minimum of 0.42. Due to the irregular nature of the aggregated antenna, ρ_{max} cannot be determined by simply taking the length of the longest baselines present in the (u_λ, v_λ) plane. Depending on the aggregated antenna, this could lead to (u_λ, v_λ) samples that are abnormal outliers in the frequency domain determining the maximum weighting of samples. Samples that are still on the relative outer rim of the area covered in the (u_λ, v_λ) plane would be down-weighted extensively, yielding an array response with an artificially degraded resolution. To address this problem a heuristic was developed that ignores the samples on the outer rim of the spatial frequency domain. The value ρ_{max} is chosen to be the radius at which a uniform Gaussian distribution with the same standard deviation as the actual sample distribution takes a value of 5%. This is done by

$$\rho_{max} = \sqrt{-\sigma_S{}^2 \cdot 2 \cdot log(0.05)} \tag{4-22}$$

where σ_S is the standard deviation of the actual (u_λ, v_λ) sample distribution. Figure 4-5 shows the value of the Blackman weights over the relative distance to the origin in the (u_λ, v_λ) plane.

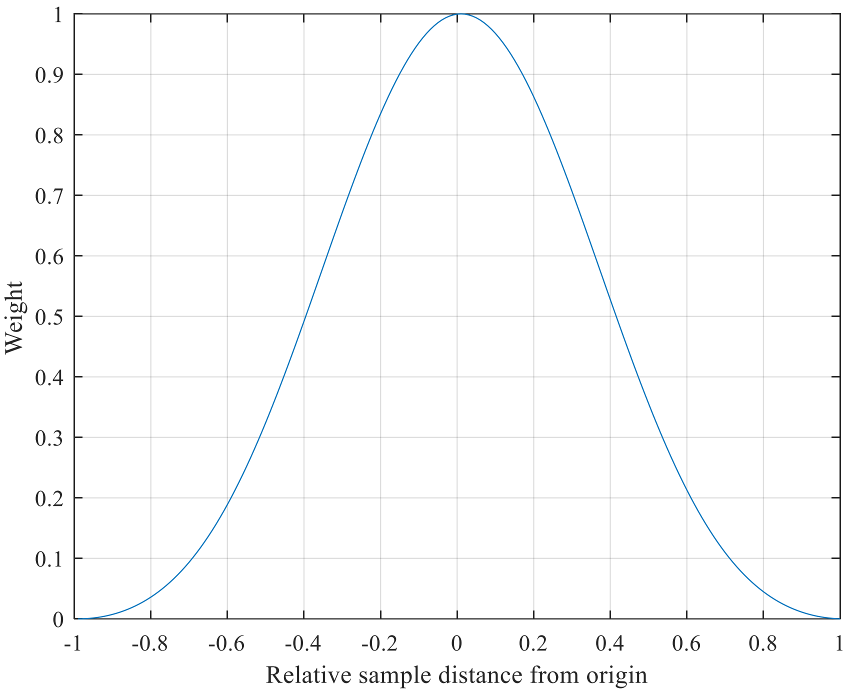

Figure 4-5 Depiction of the Blackman weighting amplitude over the distance from the (u_λ, v_λ) plane origin. The distance from the origin is given in $\|\boldsymbol{q}_{j,i}\|/\rho_{max}$.

Since baseline geometries and lengths change during overflight of the target area, the weighting of each baseline is actually time-dependent. Therefore, the time dependency needs to be reflected in the calculation of the PSF and the radiometric sensitivity. The definition of the PSF, i.e., the equivalent array function in equation (2-40), can be extended by talking into account time-dependent weights with

$$AF_{eq}(X_0 - \mathrm{X}, Y_0 - \mathrm{Y}) = \frac{\sum_{j,i} W_{j,i} AF_{j,i}(x_0 - x, y_0 - y)}{\sum_{j,i} W_{j,i}} \tag{4-23}$$

where the time-independent weights $\overline{W}_j$ have simply been replaced with the time-dependent weights $W_{j,i}$ that may vary for each time step i. The radiometric sensitivity in equation (2-45) also needs to be extended accordingly by

$$\Delta T = \frac{\Omega_A}{\Omega_{pix}} \cdot \frac{T_{sys}}{\sqrt[4]{2} \cdot \sqrt{B\tau_{eff}}} \frac{\sqrt{\sum_{j,i} {W_{j,i}}^2}}{\sum_{j,i} W_{j,i}} \tag{4-24}$$

4.5 System Feasibility Analysis Module

The System Feasibility Analysis Module enables the user to check for the important orbit mechanical aspects of system feasibility. In particular, it enables the calculation of fuel consumption, deputy collision probability and ground-track drift. These factors are directly tied to the selection of the satellite orbits and must thus be investigated before settling on a specific orbit design.

4.5.1 Collision probability determination

The accuracy of the orbit control for deputies can be directly determined by the swarm-based aperture synthesis radiometer simulator. The control accuracy is given as the 3D RMS deviation from the Keplerian reference trajectory. In a satellite swarm involving dozens of satellites on various reference orbits, the orbit control accuracy varies significantly, depending on relative orbit form and particularly the distance to the chief. In order to gauge which satellites are placed too close to each other, it is necessary to determine the collision probability of satellites with each other. The collision probability is mainly a function of the control accuracy and the nominal distance between satellites. Collision probability information is crucial for the orbit design process, as it helps determine which kind of control accuracy and thus hardware is needed, and/or if satellites nominal positions need to be adjusted.

A number of methods have been developed over the last two decades for the calculation of the collision probability P_C between two satellites. Generally, one distinguishes between methods that are capable of calculating the collision probability for short-term conjunctions, e.g. risk from space debris, and methods that are capable of calculating the collision probability for long-term conjunctions, e.g. formation-flying objects. The determination of the collision probability for long-term conjunctions is more complex as it requires considering the non-linear long-term relative motion. It requires numerical integration of a volume which is carved out by the combined bodies (hardbody) of the two encountering spacecraft in three-dimensional space. For long-term conjunctions Patera [75] presented a method that is capable of calculating the collision probability based on the transformation of the problem into a scaled frame in which the error covariance matrix is symmetric in three dimensions. A computationally efficient analytical solution can be found for relative satellite motions that are circular.

In order to quantify the long-term risk of collision within the present system simulator, the method of Patera [75] is applied. The position uncertainty $\tilde{X}_m$ of a deputy satellite m, can be described by a Gaussian distribution $\tilde{X}_m = N(0, P_m)$. The covariance matrix P_m can be approximated by the mean 3D RMS accuracy σ_m of position control. P_m is assumed to be time-invariant and isotropic. The covariance of the distance δX_k between two deputies, i.e., pair k, can then be calculated as the sum of the position accuracy covariance of both satellites $\sigma_k = \sigma_m + \sigma_{m+1}$. With the combined covariance σ_k, the probability density function of δX_k [75] is given as

$$pdf(\delta X_k) = 1/(\sqrt[3]{2\pi}{\sigma_k}^3) \cdot e^{(-\frac{1 {\delta X_k}^2}{2\ {\sigma_k}^2})} \tag{4-25}$$

This function represents the instantaneous probability of collision that occurs between satellites of pair k as a function of the distance to each other. An estimate of the accumulated probability of collision, $P_{C,k}$, between pair k during one entire orbit can be calculated by integrating equation (4-25) over the volume that is carved out by the collision region R_C, during the trajectory around the chief satellite. If each deputy pair circumvents each other at a nominal distance of $\delta X_{ref,k}$ on a circular trajectory, the integration region resembles a torus with a minor radius of R_C and a major radius of δX_k. The collision probability per orbit $P_{C,k}$ for pair k is given as

$$P_{C,k} = \frac{1}{\sigma_k}\sqrt{\frac{2}{\pi}}\, e^{\left(-\frac{({\delta X_{ref,k}}^2 + {R_C}^2)}{2{\sigma_k}^2}\right)} \int_{-R_{Coll}}^{R_{Coll}} \sinh\left(\frac{\delta X_{ref,k}\sqrt{{R_C}^2 - z^2}}{{\sigma_k}^2}\right) dz \tag{4-26}$$

The collision region can be assumed to be the combined maximum dimension of the two cubic deputy satellites, i.e., $R_C = \sqrt{3}L_c$, with L_c the side length of the deputy. The total collision probability per orbit for a single deputy is then given as the sum of the probabilities of collision with any other deputy

$$P_{C,m} = \sum_{1}^{N-1} P_{C,k} \tag{4-27}$$

for all possible collision partners k for satellite m. The probability of collision $P_{C,m}$ for a satellite during on orbit period can be used to estimate the frequency of required collision avoidance manoeuvres.

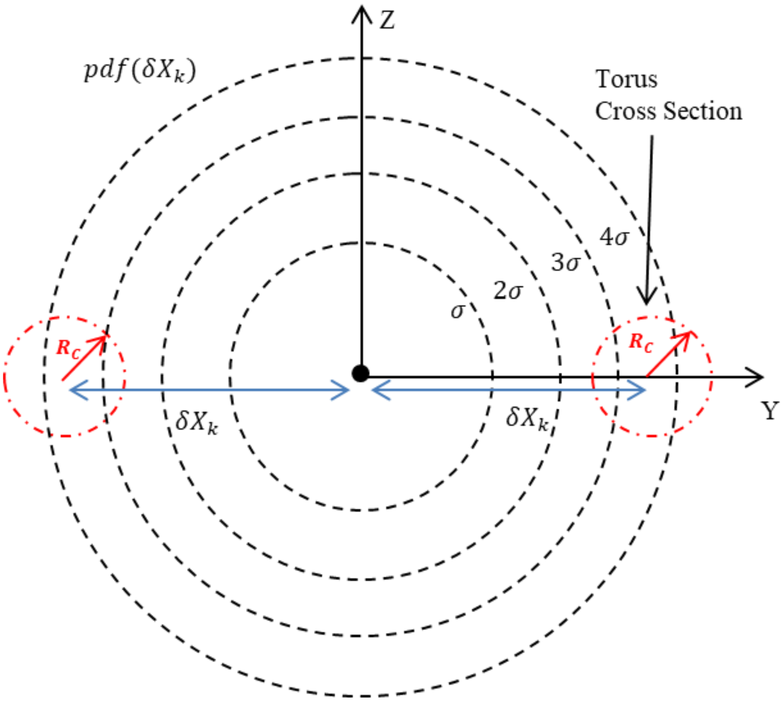

Figure 4-6 Cross-section of the probability density function and the carved torus which represents the combined hardbody.

4.5.2 Ground-track drift calculation

Residual aerodynamic drag acting on the system will result in a slow orbital decay of the radiometer system. Loss of orbit altitude will in turn result in changes in the sampling pattern and repeat interval. This is a problem, since observations at different times of the day will result in different physical temperatures of the target area. Thus, it is paramount that radiometric satellite systems adhere to requirements concerning the drift of the ground track. For SMOS the required repeat ground track accuracy was 25 km [32]. This requirement will also be used for the present investigation of the satellite swarm-based synthetic aperture radiometer.

Keeping the orbit height within certain boundaries necessitates the periodic raising of the orbit height. Figure 4-7 illustrates the ground-track drift that occurs due to aerodynamic drag and the periodic orbit correction.

Given a required ground-track accuracy, the required magnitude of orbit correction is a function of the frequency of orbit correction. He et al. [76] derived an analytical method with which the magnitude of required orbit correction and the correction frequency can be calculated for repeat-ground track station keeping of satellites on sun-synchronous orbits. Due to its simplicity this method has been implemented into the system simulator.

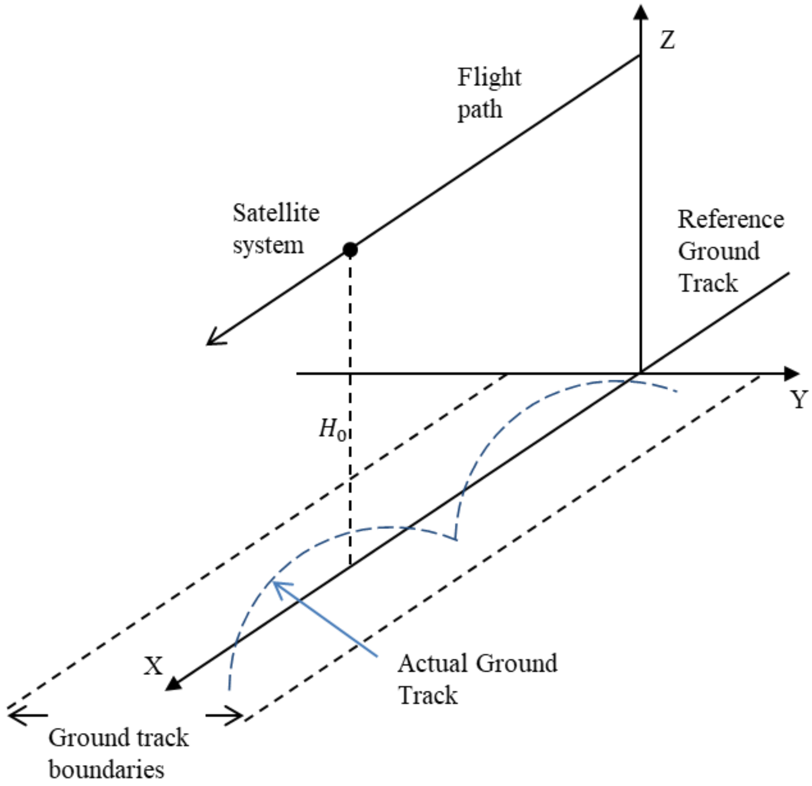

Figure 4-7 Illustration of ground-track drift as a result of aerodynamic drag and periodic maneuvers. Adopted from [76].

According to He et al. [76] the first-order equation for the necessary semimajor axis adjustment Δa_{GT} for ground track station keeping within a maximum drift threshold L_d can be given as

$$\Delta a_{GT} = \frac{1}{2}\sqrt{\frac{4a\dot{a}L_d}{3(\omega_e - \dot{\Omega})R_E}} \tag{4-28}$$

with the semi-major axis decay $\dot{a}$ and the drift rate of the RAAN $\dot{\Omega}$ of the chief. The semi-major axis decay of the system (or chief satellite) as a result of aerodynamic drag can be given as

$$\dot{a} = -B\rho\sqrt{a \cdot \mu} \tag{4-29}$$

The drift rate of the RAAN $\dot{\Omega}$ can be given as

$$\dot{\Omega} = -3\gamma n cos(i) \tag{4-30}$$

With these definitions the frequency of maneuvers can be derived by calculating the time between maneuvers T_s with

$$T_s = \sqrt{\frac{16aL_d}{3(\omega_e - \dot{\Omega})R_E\dot{a}}} \tag{4-31}$$

The given strategy represents an ideal scenario, where there are no errors in the state estimate of the system and the execution of the maneuvers. A more realistic approach will lead to more frequent maneuvers and larger semi-major axis adjustments. However, the deviations from the given idealization are small and not relevant for a feasibility assessment as conducted within this thesis. Assuming the absolute position of the chief can be determined with an accuracy of 0.5 m, the error of T_s due to errors in the determination of the satellite state should stay below 5%.

5 SWARM-BASED RADIOMETER DESIGN

Chapter 4 outlined the system simulator that is capable of investigating one specific satellite configuration for performance and feasibility. Chapter 5 describes a proposed design process for the attainment of an optimal antenna configuration and orbit design for the swarm-based aperture synthesis radiometer in low-Earth orbit. The first section 5.1 investigates the impact of the orbit design on the feasibility of the system and proposes a fundamental orbit type, the General Circular Orbit (GCO), for the configuration of deputy satellites. Section 5.2 describes the numerical optimization process which is used to distribute satellites on the GCO. Section 5.3 describes the adapted sample weighting process extending the visibility weighting scheme described in section 2.2. Section 5.4 presents the effective swath and integration time and finally 5.5 discusses the determination of the inter-satellite distance constraints for numerical optimization.

5.1 Orbit type selection

5.1.1 Influence of orbit type on controller accuracy and fuel consumption

In order to investigate the feasibility of the system concept it is important to understand the relationship between the choice of relative orbit, position control accuracy and fuel consumption of the deputies. Ultimately this enables the design of an aperture synthesis antenna array to the lifetime and imaging performance requirements of specified applications. In order to investigate the impact of the relative orbit elements on the position control accuracy and the fuel consumption of deputies, simulations have been conducted for deputies on relative orbits with varying “degree of J_2-invariance”. The degree of J_2-variance is defined by the degree to which inclination is used within the relative inclination vector to achieve a cross-track motion. In particular the degree of J_2-variance is defined as

$$\Psi = \frac{2}{\pi} atan\left(\frac{\Delta i_x}{\Delta i_y}\right) \tag{5-1}$$

According to this definition and equation (3-17) relative orbits with a low degree of J_2-variance ($\Psi \approx 0$) are less subject to drift from J_2 perturbations.

Figure 5-1 shows the 3D RMS position accuracy for deputies on 500 m relative pendulum orbits with different degrees of J_2-variance, simulated over 50 orbits. A pendulum orbit [77] is a sole cross-track motion brought about by an inclination or a difference in RAAN. This means that only the relative inclination vector is varied, i.e., the ratio between Δi_x and Δi_y with $||\Delta \boldsymbol{i}|| = 500/a$. All other elements of the relative orbit vector are set to zero. The orbit control system settings are given in Table 5-1.

Table 5-1 Scenario settings for the investigation of the influence of J_2-variance on the position accuracy and fuel consumption.

Simulation setting	*Values*
Chief orbit	$a = 7121\ km, i = 97.6°, e = 0.025, \omega = 0°, \Omega = 0°, M = 0°$
Deputy orbit	$\Delta \boldsymbol{e} = [0,0]^T, \Delta \boldsymbol{i} = [\Delta i_x, \Delta i_y]^T$
Nominal thrust (Deputy)	$u_N = 25\ mN$
GNC Accuracies (Deputy)	$GNC_{Pos} = 5\ cm$, $GNC_{Vel} = 0.21\ mm/s$
Thrust errors (Deputy)	$\alpha_e = 2°$, $b_e = 0.05$ (5%)
Spacecraft masses	$m_{s,d} = 6.85\ kg$

The green dashed line in Figure 5-1 represents Ψ, the degree of J_2-variance of a particular deputy orbit. The manoeuvre frequency F_P represents the frequency at which orbit control manoeuvres are performed per orbit.

Generally speaking, there is a clear correlation between the position control accuracy and Ψ. As expected, an orbit with a higher degree of J_2-variance will result in a lower position accuracy. The position accuracy of a satellite on an orbit with no J_2-variance will result in an approx. 25 % lower position accuracy. This suggest that at distances of 500 m the J_2 perturbations do have a significant effect on the position accuracy which should be considers when designing satellite swarm orbits at this distance. Furthermore, more frequent maneuvers yield a higher accuracy in the position control.

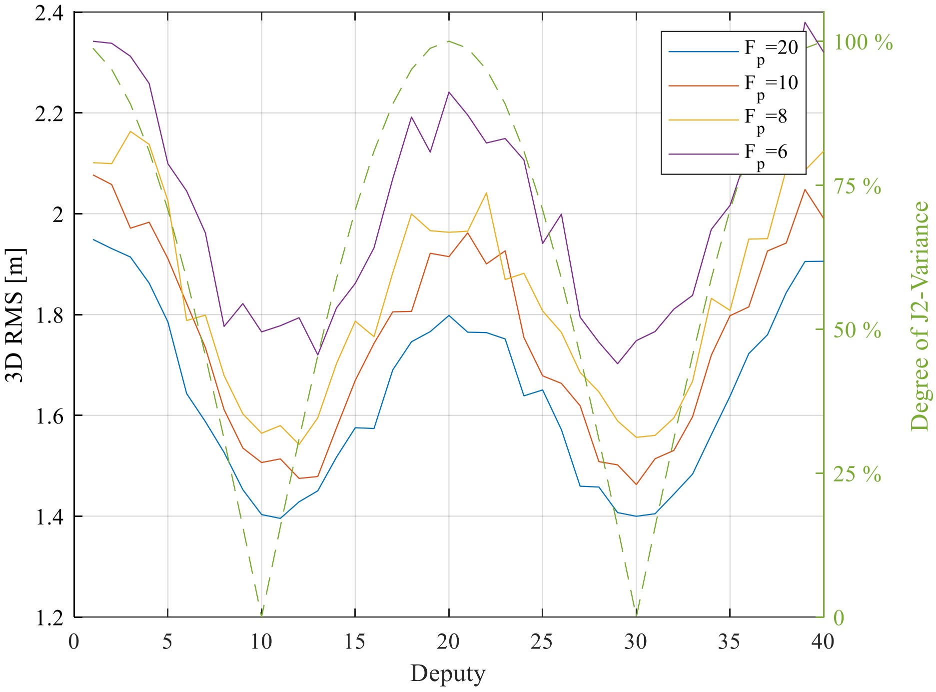

Figure 5-1 3D RMS position accuracy for deputies on 500 m pendulum orbits with different degrees of J_2-variance (Scaling parameter for weighting matrix is R_s=1000).

Figure 5-2 shows the RMS position accuracy for deputies on 50 m pendulum orbits. The closer distance of the satellites to each other, decreases the differential J_2 perturbations and thus the impact of the degree of J_2-variance. This means that the position inaccuracy is mainly driven by the inaccuracy in the thrust implementation and the inaccuracy in position and velocity state estimation. Independent of maneuver frequency F_P no clear correlation between the relative orbit and the position accuracy can be discerned. Overall, the position accuracy improves when compared to the accuracy for deputies on 500 m pendulum orbits due to the lower differential J_2 perturbations between satellites.

The fuel consumption behaves analogous to the position accuracy. Figure 5-3 shows the fuel consumption per orbit for deputies on 50 m pendulum orbits. A higher maneuver frequency F_P will result in a lower fuel consumption, due to the shortened drift time and the shorter thrust impulses between orbit control maneuvers [70]. The degree of J_2-variance is irrelevant to the fuel consumption because the position inaccuracies are driven by the state estimation and not by the differential J_2 perturbations which are very small between deputies.

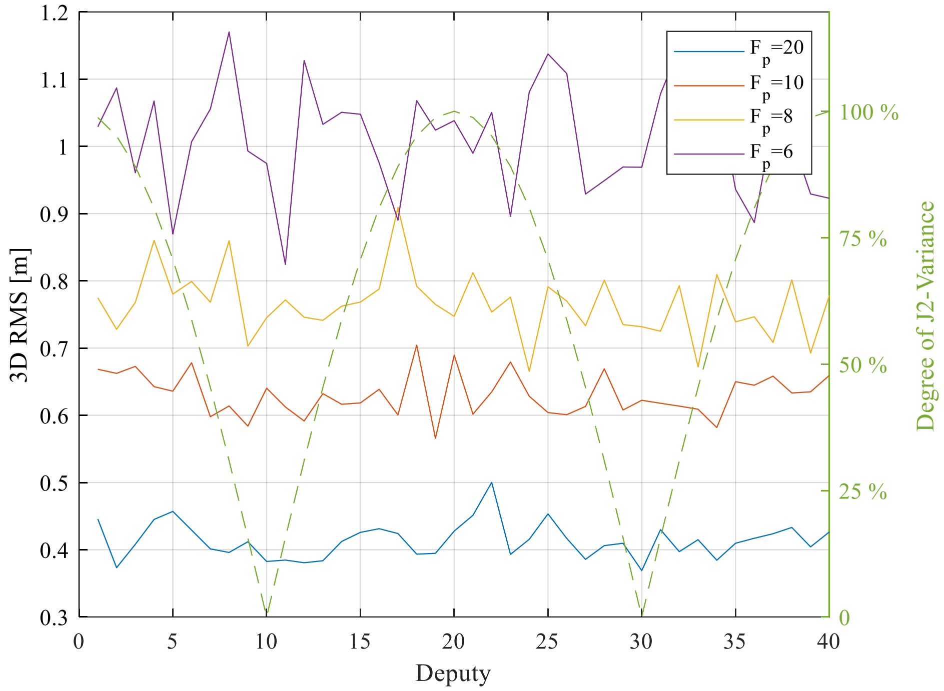

Figure 5-2 3D RMS position accuracy for deputies on 50 m pendulum orbits with different degrees of J_2-variance (Scaling parameter for weighting matrix is R_s=1000).

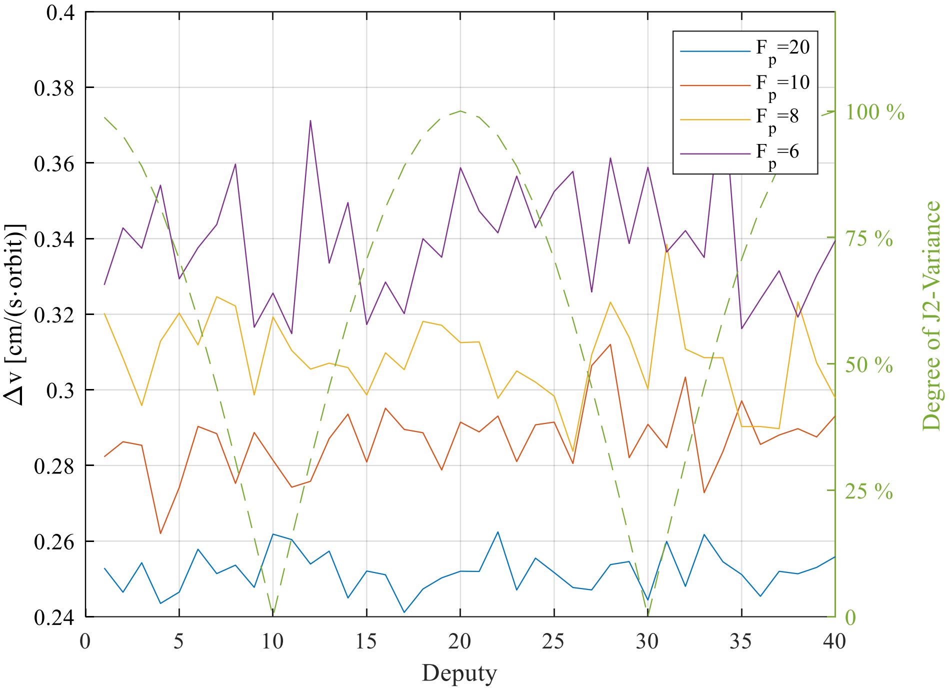

Figure 5-3 Fuel consumption per orbit for deputies on 50 m pendulum orbits with different degrees of J_2-variance (Scaling parameter for weighting matrix is R_s=1000).

The LQR control algorithm behavior is also strongly dependent on the scaling of the LQR cost matrix $\boldsymbol{R}$. Figure 5-4 shows the impact of the scaling parameter R_s onto the position accuracy of the orbit control system. In general, a larger scaling factor will result in a less responsive control system and larger position inaccuracies. Conversely, the fuel consumption behaves contrary to the position accuracy. A larger scaling parameter will result in lower average fuel consumption, since a less responsive controller can tolerate larger position inaccuracies. Interestingly, a low scaling parameter ($R_s = 100$) can result in a converse relationship with the degree of J_2 -variance at larger deputy distances. This is likely due to a gross overcompensation of position inaccuracies by the position control algorithm. Furthermore, the RMS position accuracy only provides average deviations from the reference position. In reality, deviations from the reference position will be larger along-track than across-track.

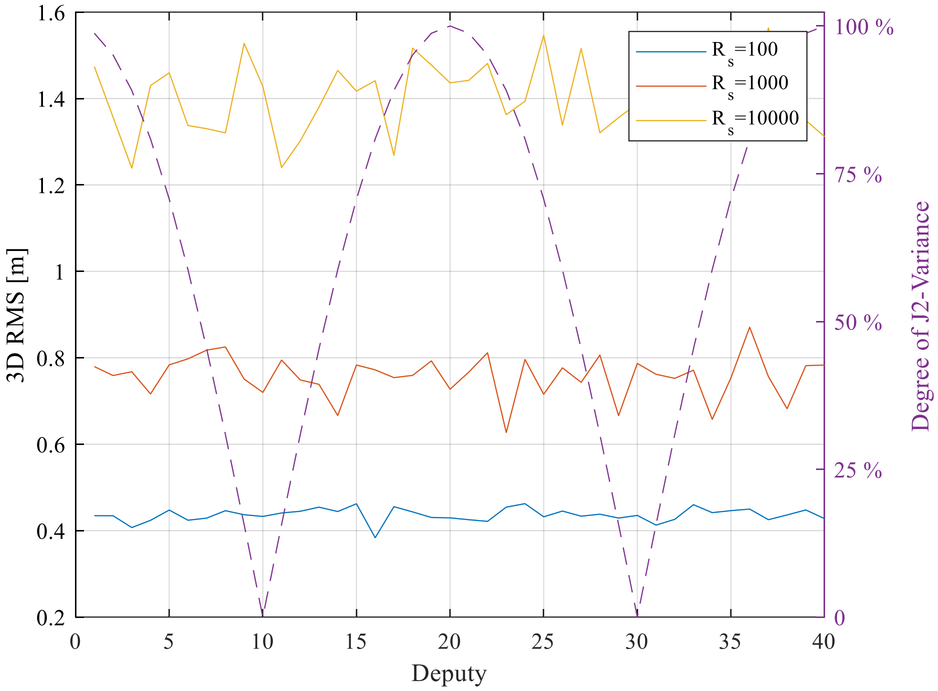

Figure 5-4 3D RMS position accuracy for deputies on 50 m pendulum orbits with different degrees of J_2-variance (Maneuvers per orbit F_p =8) and different scaling parameters.

In summary, for short close-proximity formation flight (~50 m distance), the dominating disturbances can be attributed to the inaccuracies of the control state estimation and the thrust vector implementation. The degree of J_2-variance of a relative orbit only influences the average deputy fuel consumption and position control accuracy at larger distances. For the swarm-based aperture synthesis radiometer, where inter-satellite distances remain below 100 m, relative orbits can be chosen independent of degree of J_2-variance. Only the chief-deputy distance seems to have a significant impact on the average deputy fuel consumption and position control accuracy. The orbit design can thus focus on choosing relative orbits that aim to optimize the imaging performance of the system.

5.1.2 General Circular Orbit

A regular sampling pattern of the spatial frequency domain is not possible when each antenna of an array is mounted on its own free-flying satellite (deputy). In this case, the receiver configuration is thus linked intrinsically to the relative orbits of the deputy around the chief. The choice of satellite orbits for a swarm-based aperture synthesis radiometer must consider the imaging performance requirements and the system feasibility requirements, i.e., collision avoidance, fuel consumption. On one hand, receivers are most effectively placed within a plane facing the center of the target area [43]. This maximizes the longest baselines with respect to the target. On the other hand, the deputy relative orbits should not intersect to avoid collisions. These two requirements strongly favor the satellite arrangement on relative GCO [78]. An idealized, Keplerian formulation of the GCO can be given in the Hill frame by

$$X_{ref} = \begin{bmatrix} x \\ y \\ z \\ \dot{x} \\ \dot{y} \\ \dot{z} \end{bmatrix} = \begin{bmatrix} 0.5 \cdot d \cdot \cos\,(n \cdot t + \alpha_0) \\ -d \cdot \sin(n \cdot t + \alpha_0) \\ 0.5 \cdot \sqrt{3} \cdot d \cdot \cos(n \cdot t + \alpha_0) \\ -0.5 \cdot d \cdot n \cdot \sin(n \cdot t + \alpha_0) \\ -d \cdot n \cdot \cos(n \cdot t + \alpha_0) \\ -0.5 \cdot \sqrt{3} \cdot d \cdot n \cdot \sin(n \cdot t + \alpha_0) \end{bmatrix} \tag{5-2}$$

with, d, the distance to the satellite center, n, the orbital rate, α_0, the argument of latitude and t, time [69]. As an example, Figure 5-5 depicts three satellites on GCO centered on the chief. The GCO relative orbits represent circles that lie in a common plane whose normal vector is tilted by 30° in cross-track direction from the z-axis. By varying the distance d and angle α_0 of individual satellites the recreation of any 2D receiver pattern can be realized within the relative GCO orbit plane. The deputies will then rotate around the chief satellite over the course of one orbit, while maintaining their distances and thus relative position amongst each other. This satellite configuration has two advantages. First, a fixed receiver configuration over all latitudes is preserved, enabling comparability of acquired radiometric imagery, independent of which location is imaged on Earth. The comparability is achieved because an aperture synthesis antenna array with a rotational symmetric response function will be indifferent to rotations around boresight.

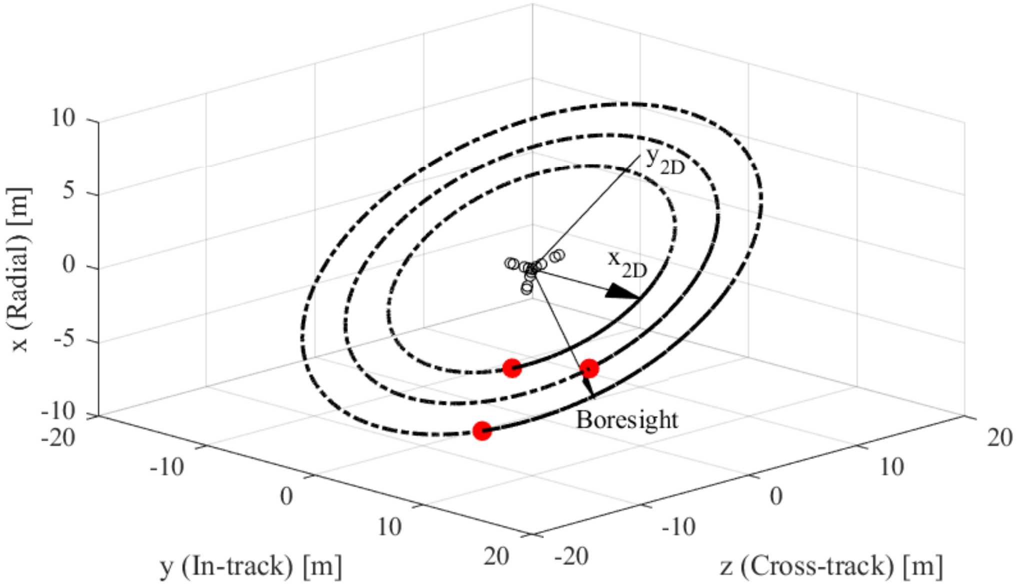

Figure 5-5 Example of three deputy satellites (red filled circles) flying on GCO around the chief satellite (black circles) in the Hill frame. The optimization frame is spanned by the axes x_{2D}, y_{2D} which lie within the shared GCO orbit plane. The boresight vector specifies the direction of observation and is perpendicular to the optimization frame.

Second, as will be shown in section 5.2, placing all satellites on a plane enables the optimization of receiver, i.e., deputy configuration, within a 2D-plane, with two Cartesian coordinates per deputy instead of three for a configuration spread in three-dimensional space. This greatly simplifies the numerical optimization of the deputy orbital configuration and thus the definition of the individual orbit parameters. The coordinate system spanned by the axes x_{2D}, y_{2D} in Figure 5-5 will be called the optimization frame in which the numerical optimization of receiver positions is performed.

Equation (5-2) enables the formulation of initial conditions for each deputy satellite that is placed on a GCO. Due to orbital perturbations, notably from Earth oblateness and aerodynamic drag, a satellite will drift from the idealized reference orbit [79]. Close proximity formation flight, as required for a dense swarm-based aperture synthesis antenna array, necessitate fully autonomous control of each deputy.

5.2 Receiver optimization on the GCO plane

The placement of satellites on GCO allows the creation of an aggregated rotating, side-looking planar receiver array. Within the shared planar relative orbit plane, called the optimization frame, the initial relative position of a deputy m may be described by two Cartesian coordinates $\boldsymbol{X_{2D,m}} = \left[x_{2D,m}, y_{2D,m}\right]^T$. This coordinate system lies within the GCO plane with the chief satellite as its origin. The x_{2D}-axis is oriented along the flight direction and the y_{2D}-axis is oriented towards space (see Figure 5-5). In case of a rotational symmetric PSF, the rotation of the array will not change the array response significantly. The positions of the deputies within this plane are to be optimized for imaging performance of the swarm-based radiometer. The relevant metrics for imaging performance of an aperture synthesis antenna array are spatial resolution, radiometric sensitivity the magnitude of the sidelobes and the Main Beam Efficiency (MBE) [48]. MBE is defined as

$$MBE = \frac{\Omega_m}{\Omega_P} \tag{5-3}$$

With the antenna pattern solid angle

$$\Omega_P = \iint_{sidelobe} PSF(\Theta, \Phi) \mathrm{d}\Omega_s \tag{5-4}$$

With the main lobe solid angle

$$\Omega_m = \iint_{mainlobe} PSF(\Theta, \Phi) \mathrm{d}\Omega_s \tag{5-5}$$

The challenge of distributing a defined number of receivers on a 2D-plane has been investigated in radio astronomy for many decades and is sometimes denoted the “configuration problem” [80]. The objective of the configuration problem is to define the positions of individual receivers of an interferometric array in such a way that the response of the imaging system (PSF) matches the imaging requirements.

Requirements usually define the level of permissible sidelobes and the resolution of the system. Much research has been performed on various methods for configuration design.

Early interferometric telescopes were simply based on specific geometrical patterns (Reuleaux Triangle, Circle) that were known to yield a homogenous or Gaussian distribution of baseline vectors, i.e. (u_λ, v_λ) samples. More sophisticated numerical optimization methods were employed for the design of modern radio telescopes, such as ALMA and the Allen Telescope Array (ATA). Many of these methods seek to optimize a distribution of samples in the spatial frequency domain rather than optimizing for the requirements directly. Some well-known methods of this type, are the methods proposed by Keto [81], Boone [80] and Su et al. [82]. Other methods, e.g., by Jang et al. [83].

Keto's method is based on using the known geometrical patterns (e.g., Reuleaux Triangle) as an initial condition and the perturbation of single receivers away from the perfect shape to yield a more homogenous or Gaussian (u_λ, v_λ) sampling [81]. The method developed by Boone [80] is based on the computation of pressure forces, making it possible to emulate a specified Gaussian distribution of (u_λ, v_λ) samples from an initial random distribution. Su et al. [82] proposed a "sieving approach" that used weighting functions for (u_λ, v_λ) samples to choose an optimal antenna configuration from a large set of candidates with the objective of achieving a specified distribution of samples in the spatial frequency domain.

A study with pseudorandom arrays conducted by Woody [84] for radio telescopes revealed that ideally a dense homogenous Gaussian distribution of samples in radial direction yields the lowest sidelobes on interferometric arrays. Any optimization must thus recreate a sample distribution in the (u_λ, v_λ) plane that is homogenous in azimuth and of Gaussian form in the radial direction from the origin. Woody [84] showed that a denser sample distribution with a given number of receivers will lower side lobes, but will decrease the spatial resolution. The Gaussian distribution must thus be iteratively found by setting a target for the sidelobe levels or the resolution.

Some methods for the solution of the configuration problem have been developed with the objective of directly optimizing the antenna sidelobes. These involve the identification of the largest sidelobes and the subsequent minimization by shifting the position of individual antennas according to an objective function [85], [86], [87].

The key difference between the design of an astronomical interferometer and the design of an antenna configuration for the swarm-based radiometer, is the need for large inter-antenna distances on the part of the satellite swarm. The distances required for the swarm-based radiometer are ultimately governed by the accuracy of the position control system. While the aperture of the ARU patch antenna on the deputy satellites is approximately 20 cm, the position control will only deliver accuracies in the order of one meter. Thus, the distance δX_k between deputies of a deputy pair k, will likely be larger than five times the diameter of the antenna. In contrast, the inter-antenna distance constraint for a terrestrial astronomic radio interferometer lies more in the order of a single antenna diameter [87]. To ensure no collision takes place with the sensitive solar panels or the central payload antenna of the chief satellite, extra-large distances will need to be adhered to between the deputy and the chief satellite as well.

The stringent minimum inter-satellite constraints make it difficult to impose a specific Gaussian distribution for the spatial frequency samples a priori, as required in the method by Boone. In this case, imposition of a specific sample distribution together with large inter-satellite distances and few satellites will lead to poor configuration results. The method by Su et al. [82] is more suited for the present applications, since it does not fix a predefined sample distribution, but simply weights each sample by its distance to the spatial frequency domain origin. It thus is capable of “pulling” samples towards the center achieving a Gaussian distribution with standard deviation which is as small as possible. For a sparse array, as is subject in this thesis, the method of Su et al. is principally applicable, but requires the selection of candidate positions a priori and will thus not provide an absolute global optimum. Nevertheless, the objective function used in this method can be adapted for the use with other optimization algorithms and will thus serve as a basis for the method presented in this thesis. In principle any method optimizing the (u_λ, v_λ) sample distribution can be combined with a method aimed at the subsequent reduction of sidelobes. However, since there are no distinct sidelobes in the swarm-based radiometer due to the irregular sampling of the frequency domain, this step would not lead to radical improvements of the antenna configuration. The antenna optimization performed in this study is thus only based on an optimization of the (u_λ, v_λ) samples in the spatial frequency domain. The following method numerically optimizes the initial positions $\boldsymbol{X_{2D,m}}$ of N deputies in the optimization frame (see Figure 5-5).

5.2.1 The optimization problem formulation

In mathematical optimization an objective function is minimized by the systematic selection of appropriate values from an allowed set as input values and the calculation of the function value. The numerical objective function f must thus be defined to ensure a dense Gaussian sampling of the spatial frequency domain in radial direction and a uniform sampling in azimuthal direction.

Each spatial frequency vector $\boldsymbol{q_{j,i}}$ for sample j and step i on the (u, v) plane is weighted according to the distance from the origin, $\|\boldsymbol{q_{j,i}}\|$ and the number of sample points $N_{cell,j,i}$ within the same grid cell. The objective function is similar to the one used in the “Sieving algorithm” by Su et al. [82]. It is defined as

$$f(x) = \sum_{j}^{2N_B} \sum_{i}^{N_T} {N_{cell,j,i}}^{-1} \cdot e^{-\frac{1}{2}\cdot\left(\frac{\|\boldsymbol{q_{j,i}}\|}{\sigma_G}\right)^2} \tag{5-6}$$

with σ_G, a parameter with which the density of the samples can be controlled and N_T the number of time steps. Because the complex conjugate samples are included, the integration is conducted over double the number of physical baselines. This definition of the objective function ensures that samples that are farther away from the origin and those in dense regions of the (u_λ, v_λ) plane are down-weighted. For the simulations in chapter 6, the resolution of the Cartesian grid on the (u_λ, v_λ) plane was set to a single wavelength. Figure 5-6 illustrates the down-weighting of individual samples after a grid is applied. The objective function ensures the homogenous and dense sampling of the spatial frequency plane.

The optimization must also consider a minimum distance between the deputies $D_{min,D}$ and a minimum distance to the chief satellite $D_{min,C}$. With these conditions the optimization problem can be defined as

$$\begin{aligned} &\underset{x}{\text{minimize}} && f(x) && \\ &\textit{subject to} && D_{min,D} \le \delta X_k, && k = 1, \dots, N_k \end{aligned} \tag{5-7}$$

$$D_{min,C} \leq \left\|\boldsymbol{X}_{\boldsymbol{2D,m}}\right\|, \quad m = 1, \dots, N$$

with N_k, the number of possible deputy collision partners. Where the variable δX_k is the length of the inter-satellite distance between deputies of deputy pair k and $\left\|\boldsymbol{X}_{\boldsymbol{2D,m}}\right\|$ is effectively the distance between deputy m and the center of the chief satellite.

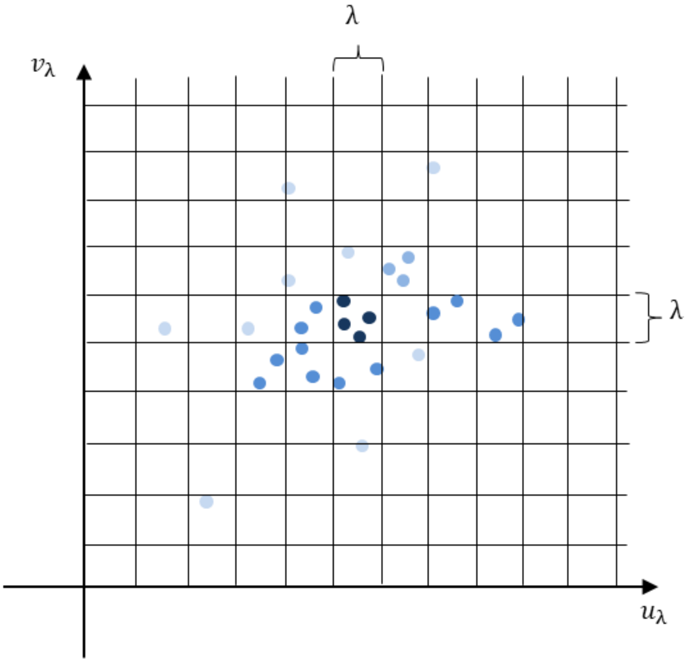

Figure 5-6 Illustration of weighting for the objective function by grid cell density $N_{cell,j,i}$. The different colors denote the weight of the sample. A light blue sample signifies a low weight, while a dark blue sample signifies a unity weight.

5.2.2 Optimization algorithm

The optimization problem can be solved using standard algorithms that are capable of finding global solutions for non-smooth functions subject to non-linear boundary conditions [88], [89]. Within the course of this thesis both the pattern search and genetic algorithm of the MATLAB global optimization toolbox were investigated as potential solvers. Both numerical solvers consistently converged towards similar solutions. Since the pattern search algorithm converged slightly faster, it was finally chosen as the main optimization algorithm for the simulations. The pattern search is based on the well-known Augmented Lagrangian Pattern Search (ALPS) algorithm [28]. The ALPS algorithm for nonlinearly constrained optimization is not reliant on gradients or higher derivatives but is based on calculating solutions for a constructed mesh. Initial conditions are generated by randomly selecting receiver coordinates.

Table 5-2 outlines the step-by-step schematic for the numerical optimization of the deputy receiver configuration. The algorithm inputs are the chief antenna configuration, the number of deputies N, the inter-satellite distance constraints $D_{min,D}$, $D_{min,C}$. At first, the algorithm generates random deputy receiver positions around the chief satellite. The area within the optimization frame that the deputy receivers can be placed on, is limited by the user, through the parameter L_{OF}. This parameter has to be chosen by the user iteratively, as a too large value can result in deputies being placed at the edges of the area. After refactoring the deputy position coordinates, the antenna positions on the chief payload array are added to the deputy receiver positions. Necessary system parameters, such as the footprint area and the center point X_c, Y_c are then calculated. As a last step before the optimization iteration commences, the minimum distance constraints are defined in a separate function.

The optimization iteration begins with the processing step in line 7. The optimization steps (steps 7 – 12) are then repeated until the difference in the output of the objective function Δf is smaller than a predefined tolerance ε_{min}. The first processing step within the iteration is the generation of the spatial frequency vectors $\boldsymbol{q}_{j,i}$ for each baseline j and timestep i. This is done by using the functions outlined in 4.4.2. To avoid the need to propagate each individual deputy, the deputy positions are assumed to be static within the optimization frame. Following the generation of the frequency vectors, the density weights are calculated for each sample within the spatial frequency domain. These weights are then multiplied with the Gaussian weights. The Gaussian weights are calculated using the σ_G parameter, that is predefined by the user. Finally, the value of the objective function is calculated by summing up all weights. New deputy positions are then generated according to the logic of the pattern search algorithm. The output of the algorithm represents the final optimized configuration.

It can be necessary to run the algorithm multiple times with different σ_G parameters. If this parameter is too large the algorithm will place deputies on the outer rim of the user-defined area of the optimization frame. If it is too small the deputies will be distributed only according to density and any “pull” of the deputies towards the chief satellite will not happen. In summary both σ_G and L_{OF} must be determined iteratively.

Table 5-2 Algorithm schematic for the numerical optimization of the receiver positions within the optimization frame.

```
Input: Orbital scenario, Chief antenna configuration, $N$, $D_{min,D}$, $D_{min,C}$, $\sigma_G$, $L_{OF}$
Output: Optimized configuration $\boldsymbol{X_{2D,m}}$,   $m = 1, \dots, N$
Generate random deputy (receiver) positions as initial condition $\boldsymbol{X_{2D,m}}$,   $m = 1, \dots, N$
Refactor initial deputy positions to single column vector
Add the chief antenna receiver positions to the deputy receiver positions
Calculate system footprint, center point $X_c, Y_c$ and swarm center position for target overflight
Input minimum distance constraints ($D_{min,D}$, $D_{min,C}$)
While $\varepsilon = |\Delta f| > \varepsilon_{min}$
    Generate the spatial frequency vectors for each baseline $j$ and timestep $i$, $\boldsymbol{q_{j,i}}$
    Generate density weights ${N_{cell,j,i}}^{-1}$ for each sample in the $(u_\lambda, v_\lambda)$ plane
    Generate Gaussian weights $exp(-\frac{1}{2} \cdot (\frac{\|q_{j,i}\|}{\sigma_G})^2)$ for each sample in the $(u_\lambda, v_\lambda)$ plane
    Calculate fitness value from objective function of current configuration: $f$
    Shift deputy positions $\boldsymbol{X_{2D,m}}$ according to pattern search algorithm
```

5.2.3 Translation of optimization frame coordinates

The translation of the deputy positions from the optimization frame to initial conditions within the Hill frame is performed by calculating the distance d from the chief center and the angle between the flight vector and the chief/deputy vector α_0 with

$$d = \|\boldsymbol{X_{2D}}\| \qquad \alpha_0 = arctan2\left(\frac{x_{2D}}{y_{2D}}\right) + \frac{\pi}{2} \tag{5-8}$$

for each deputy. These parameters are then inserted into equation (5-2) to obtain the initial Cartesian conditions for the GCO. The initial conditions are then used to define the reference orbit for the autonomous control of the deputy satellites.

5.2.4 Case study: Optimization of a 16-deputy configuration

To validate the optimization algorithm a configuration of 16 deputies was optimized with a chief orbit identical to the one chosen for section 5.1. The inter-satellite distance constraints have been set to $D_{min,D} = 3.5\ m$ and $D_{min,C} = 10\ m$, as first reasonable estimates for the inter-satellite distances required to avoid collision with state-of-the-art GNC systems. The parameters σ_G and L_{OF} have been set to 40 and 65 m respectively. Figure 5-7 shows the optimized satellite configuration with $N = 16$ deputies in the optimization frame. The optimized result shows that the optimizer distributes the individual deputies around the chief satellite in a form that resembles a circle. Some deputies are placed in a "second row" outside of the inner deputy circle. The configuration result is an indicator that configurations with stringent distance requirements can look significantly different to configurations used for astronomic interferometers where there are less restrictions on the placement of antennas. When the inter-antenna distances are in the order of a single antenna aperture, ring-like formations are beneficial, since short baselines can be formed by neighboring antennas. Long enforced inter-satellite distances however would not enable ring-like formations without neglecting short baselines. Short baseline can only be formed by placing individual deputies outside of a perfect circle, even though voids are left.

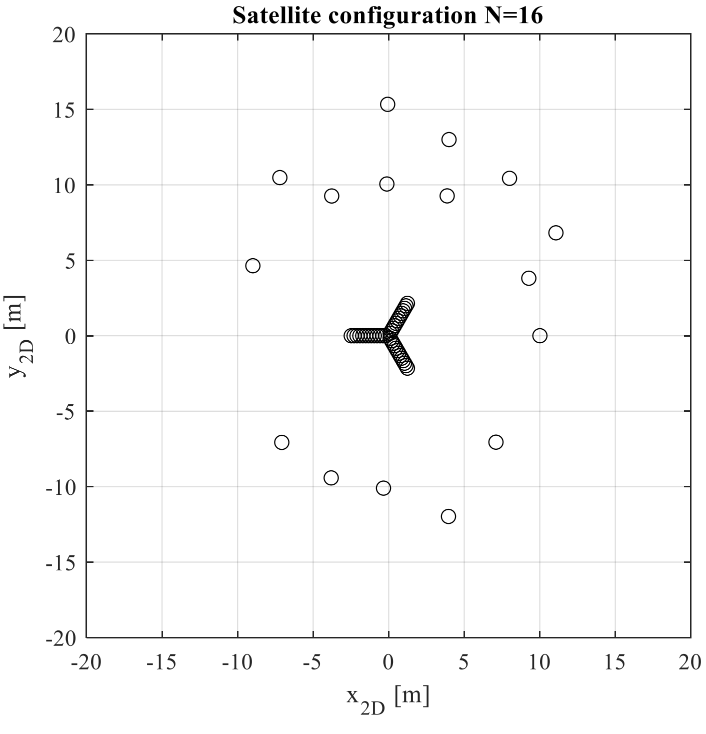

Figure 5-7 Optimized satellite configuration with $N = 16$ deputies in the optimization frame.

Figure 5-8 shows the resulting spatial frequency coverage of the optimized satellite configuration. The image shows the spatial frequency coverage that results from the swarm-based radiometer during overflight of the target area without considering changes in deputy positions due to relative orbit mechanics. In other words, the deputy positions in the Hill frame are assumed to be constant, as the rotation of the deputies around the chief during flyover of one target area is rather small (below 6° for a swarm of 50 m radius). This is advantageous since any need to propagate relative orbital positions at each optimization step is avoided. The blue samples that are distributed around the origin result from the baselines between the chief satellite payload and the individual deputy antennas. The pink samples, representing the samples from baselines between deputies, are placed in a relatively regular and circular fashion around the chief satellite as well. To limit computational load, the overflight time is discretized to only four timesteps. Thus, only four samples are obtained per baseline which together coarsely represent curved formations in Figure 5-8. Validation experiments have shown that for optimization purposes a relatively coarse approximation of the spatial frequency sampling is sufficient.

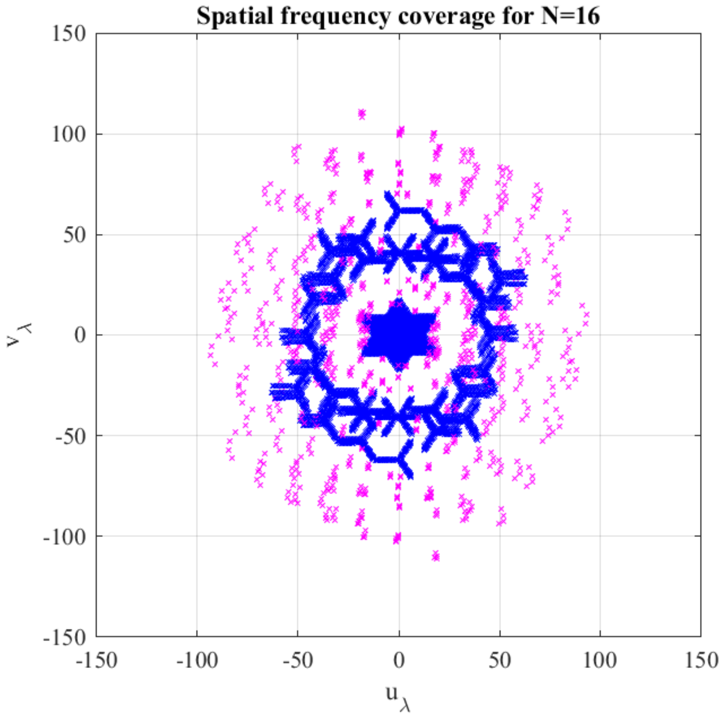

Figure 5-8 Spatial frequency coverage of optimized satellite configuration as used in the optimization algorithm (assuming constant deputy positions in Hill frame). Blue samples denote chief/deputy baselines, while pink or green samples denote deputy/deputy baselines.

The optimized configuration can be used as an initial condition for the simulation of the full swarm-based aperture synthesis radiometer, as described in chapter 4. Figure 5-9 shows the spatial frequency coverage from the SSBSAR overlaid with the approximated spatial frequency coverage of the optimizer. It is apparent that both spatial frequency coverages are not identical. The optimization result differs from the simulator result in that the outer spatial frequency samples are circularly shifted in clockwise direction. This is due to the rotation of the deputies in the orbital plane that had been neglected during optimization. Since the angular shift is constant for all deputies during overflight of the target area, position changes of deputies in the Hill frame on the outer rim of the configuration are larger because of the larger distance to the rotation center. The stronger rotation with larger deputy distances can explain the larger deviations between the spatial coverage used for optimization and spatial coverage derived with the full orbit mechanics simulation. Despite shifts in the spatial frequency sampling, the optimization correctly reproduces the approximate nature of the spatial frequency sample distribution. The approximations greatly improve the efficiency of the optimization.

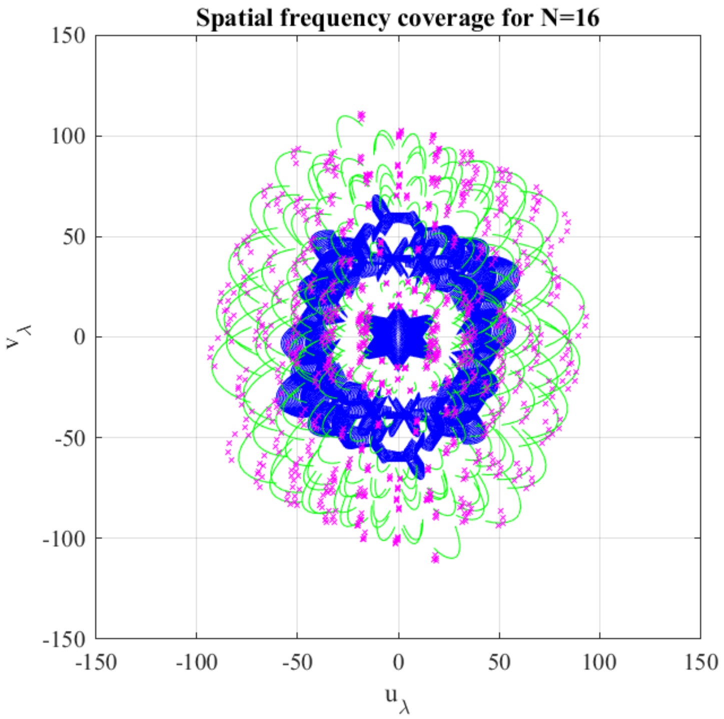

Figure 5-9 Spatial frequency coverage of optimized satellite configuration as used in the optimization algorithm (pink) and as a result of a full orbit mechanics simulation (green).

5.3 Uniform weighting

Due to the constraints, the chief antenna and the limited number of deputies, the optimization process will yield an irregular sampling pattern within the (u_λ, v_λ) plane. There will inevitable be local areas within the (u_λ, v_λ) plane that will be sampled denser than others. Without corrective weighting this would ultimately result in a distortion of the final brightness temperature image, as given by equation

(2-39). In order to correct for inhomogeneities, a gridless weighting scheme is applied to the spatial frequency samples. This method has been applied in VLBI [90]. It weights each spatial frequency sample according to the number of spatial frequency samples in its proximity on the (u_λ, v_λ) plane. The weights $D_{g,j,i}$ are defined as

$$D_{g,j,i} = \frac{1}{N_{W,j,i}} \tag{5-9}$$

with $N_{W,j,i}$ denoting the number of samples within the radius r_W from the sample of baseline j at time step i in the (u_λ, v_λ) plane. For the simulations within this thesis a value of $r_W = 3\lambda$ yielded the best results. The total composite weight for baseline j at time step i are thus given as

$$W_{j,i} = D_{g,j,i} \cdot T_{Black,j,i} \tag{5-10}$$

Figure 5-10 illustrates the uniform weighting technique. The simulator first detects the samples that are in the proximity of a selected spatial frequency sample. Each sample weight is defined as the reciprocal of the number of samples in its proximity.

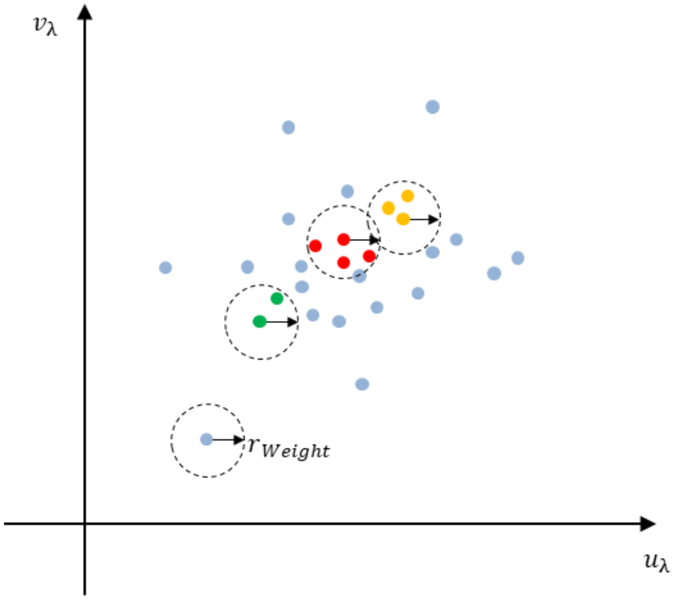

Figure 5-10 Illustration of uniform weighting method. Samples of the same color are used for the determination of the local sample density for the weighting of the center sample.

A visualization of the resulting spatial frequency weights is given in Figure 5-11. The image shows the samples in the spatial frequency domain along with their associated weight by color. It is apparent that the uniform weighting technique down-weights all samples in the densely sampled region (blue) that is formed by the baselines between deputy antennas and central chief antenna, as well as the baselines between antennas on the central array itself. With exceptions, samples on the outer rim almost all carry the unity weight, since the samples are distributed farther apart. The uniform weighting technique ultimately prevents the overrepresentation of spatial frequency regions in the resulting PSF. It has two effects. First, it introduces a form of "smoothing" to the array response. This means that high frequency oscillations introduced by the irregular sampling are damped out. Second, uniform weighting decreases the signal response outside of the PSF main beam area, leading to a significantly higher main beam efficiency.

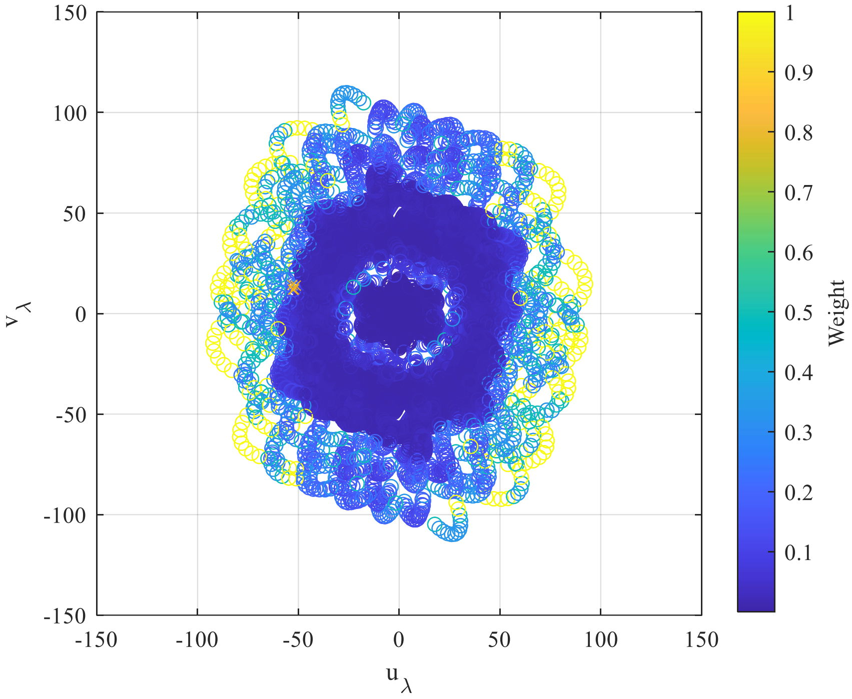

Figure 5-11 Uniform weighting of spatial frequency samples by density. The spatial frequency coverage was taken from configuration of case study in 5.2.

5.4 Effective swath and observation time

In order to evaluate the system revisit time and the imaging performance it is crucial to understand both the effective swath width and the time that is available for observation during flyover. The observation time influences both the coverage of the (u_λ, v_λ) domain and the radiometric sensitivity.

The FOV of the swarm-based synthetic aperture radiometer system is defined by the FOV of the individual antenna, i.e., their half-power beamwidth. Assuming the conical beam of a patch antenna, the FOV will appear as an ellipse on the ground as the antennas are tilted by 30° in cross-track direction to match the orientation of the GCO planes (see Figure 5-12). The duration of time each point remains in the observation region, defines the integration time that is used for the subsequent calculations of the (u_λ, v_λ) coverage and the radiometric sensitivity. In practise, the edges of the FOV are used as well for the observation, but to enable a conservative estimate of radiometric sensitivity and array response and to simplify the calculation, the same observation time is used for all sources within the swath width. As a result, the assumed swath width does not include the outer edges of the FOV, because sources in this region remain within the FOV for a duration that is shorter than the observation time t_{obs}.

As opposed to SMOS, the swarm-based synthetic aperture radiometer system investigated within this thesis does not have an aliasing region, since aliasing effects are spread throughout the array response because of the irregular sampling. Thus, aliasing does not decrease the swath, but degrades the main beam efficiency and the sidelobe levels.

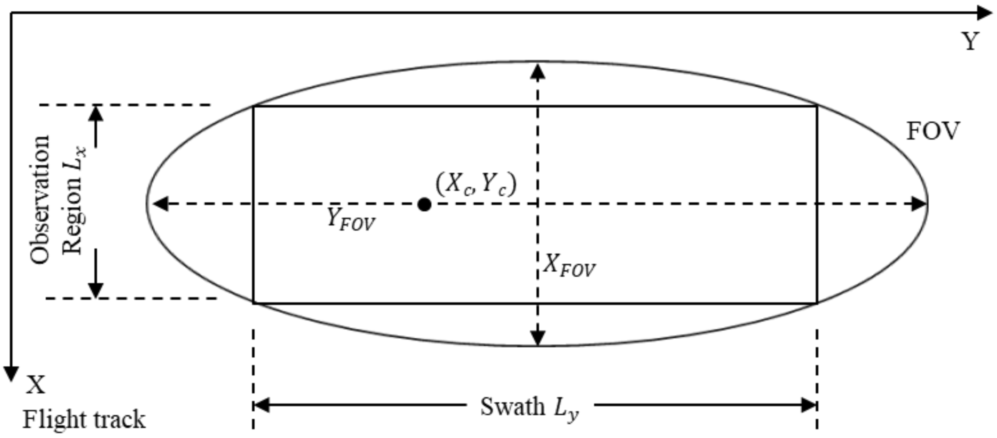

Figure 5-12 FOV of the swarm-based synthetic aperture radiometer system on ground, including the definitions of the effective swath and the observation region.

To enable an assessment of the entire system as a whole, the dimensions L_x and L_y are defined by the largest possible rectangle within the system FOV. Thus L_x and L_y can be defined as

$$L_x = 2 \cdot \sqrt{\left({H_0}^2 + {Y_c}^2\right)} \cdot tan\left(\frac{HPBW_{AZ}}{2}\right) \cdot \frac{\sqrt{2}}{2} \qquad (5\text{-}11)$$

and

$$L_y = H_0 \cdot \left(tan\left(\theta_c + \frac{HPBW_{El}}{2}\right) - tan\left(\theta_c - \frac{HPBW_{El}}{2}\right)\right) \cdot \frac{\sqrt{2}}{2} \tag{5-12}$$

with the half-power beamwidths of the individual antennas in azimuth $HPBW_{AZ}$ and elevation $HPBW_{El}$. The total time of observation can thus be calculated as

$$t_{obs} = \frac{L_x}{v_a} \tag{5-13}$$

5.5 Determining inter-deputy distance constraints

The previous sections have described the optimization of deputy positions on GCO orbits, given boundary conditions of minimal distance between chief and the deputies. The question remains as to how the distance constraints $D_{min,D}$ and $D_{min,\mathrm{C}}$ might be determined without a priori knowledge of the collision probability. The solution to this problem can only be found in an iterative approach.

Table 5-3 summarizes the approach for the determination of the inter-deputy distance constraints. As an input, the user must specify a maximum permissible collision probability $P_{C,Max}$. With a specified number of deputies N and an initial arbitrary but realistic setting for $D_{min,D}$ and $D_{min,C}$ a configuration can be optimized with the approach described in section 5.2. A full system simulation is performed of the resulting deputy configuration by the SSBSAR, yielding the collision probability $P_{C,k}$ for each satellite pair k. The resulting collision probabilities are then compared to the maximum permissible collision probability $P_{C,Max}$. If the condition is breached there are two options. First, the user can increase the distance constraints $D_{min,D}$ and $D_{min,\mathrm{C}}$ for all deputy satellites. However, this will result in a generally sparser interferometric array and thus higher sidelobes. Second, the individual deputy pairs that are responsible for the breach of the collision probability condition can be repositioned manually. This is an efficient way of reducing the collision probability of individual satellite pairs, without significantly changing the quality of the imaging. The previous steps are repeated until the collision probabilities of all deputy satellites meet the constraint condition.

Table 5-3 Algorithm for the determination of inter-deputy distance constraints.

```
Input: Orbital scenario, Chief antenna configuration, Deputy orbit control system parameters, $N$, $\sigma_G$, $L_{OF}$, $D_{min,D}$, $D_{min,C}$, $P_{C,Max}$
Output: Optimized configuration $\boldsymbol{X_{2D,m}}, \quad m = 1, \dots, N$ subject to $P_{C,Max} > P_{C,k}, \quad k = 1, \dots, N_k$
While $P_{C,Max} < P_{C,k}, \quad k = 1, \dots, N_k$
    Optimize the configuration using algorithm described in Table 5-2, yielding $\boldsymbol{X_{2D,m}}, \quad m = 1, \dots, N$
    Perform a simulation with SSBSAR using $\boldsymbol{X_{2D,m}}, \quad m = 1, \dots, N$ as initial conditions
    Increase $D_{min,D}$ and $D_{min,C}$ or manually shift individual deputy position $\boldsymbol{X_{2D}}$ that violates the condition
```

6 SIMULATION RESULTS

This chapter presents the simulation results of the swarm-based aperture synthesis radiometer and investigates the impact of key system parameters on the system performance and feasibility. The configuration optimizations have been conducted with the method outlined in the previous chapter, while all system simulations were conducted using the SSBSAR software outlined in chapter 4.

6.1 Simulation settings

Numerical simulations have been conducted on an exemplary mission scenario in order to demonstrate the design methodology described in chapter 5.

The chief satellite orbital elements have been modelled after those of the SMOS satellite to ensure that the system simulation is representative in meeting the science orbit requirements and the system is thus comparable to SMOS. The chief satellite is set to a sun-synchronous circular orbit at an orbit height of 755 km.

Table 6-1 Orbital elements of chief satellite

Orbit elements	*a [km]*	*i [°]*	*e*	*Ω [°]*	*ω [°]*	*M*
Values	7126	*97.53*	*0*	*54.95*	*0*	*0*

Table 6-2 summarizes the parameters assumed for the individual ARU on the chief and deputy satellites and the chief antenna array configuration. The center frequency of 1.4 GHz at L-band represents the frequency band that is protected for Earth science and astronomical observations, as used for measurements by SMOS (ESA) and SMAP (NASA). The receiver noise bandwidth is set to 7 MHz as a trade-off between spatial decorrelation effects and radiometric sensitivity. The half-power beamwidths in azimuth and elevation have been set to the values given for the individual MIRAS antennas in [91]. The system temperature has been chosen as the mean system temperature given for MIRAS the reference system in [91].

Table 6-2 Payload parameters for numerical simulations

Antenna Parameters	*Values*
Center frequency	$f_c = 1.4\ GHz$
Receiver noise bandwidth	$B = 7\ MHz$
System Temperature	$T_{sys} = 280\ K$
Half-power beamwidth in elevation	$HPBW_{El} = 62°$
Half-power beamwidth in azimuth	$HPBW_{Az} = 62°$
Chief antenna array	*Uniform Y-Shaped array*
Number of antennas per arm	*13*
Chief antenna tilt angle	$\Theta_c = 30°$

The ARU on the central array (chief payload) are placed in a Y-configuration (Figure 6-1). The individual receivers on the Y-antenna of the chief are placed at a distance that is equal to 0.89 wavelengths, which is equal to the value of MIRAS as well. There are a total of 13 ARU placed on each beam. The chief array is tilted 30° in cross-track direction to form a single side-looking receiver plane with the deputies that are placed on GCO.

Table 6-3 summarizes the spacecraft parameters used for the numerical simulation. It is assumed that the deputy satellites are each equipped with a non-toxic R134a propulsion system [92] designed for close-proximity operations. The propulsion system provides 25 mN of nominal thrust with a specific impulse of 40 s. The thrust magnitude and vector error are based on the values assumed for the CanX-45 mission [70]. The relative position and velocity knowledge accuracies are assumed to be identical to the values determined for the PRISMA mission [71].

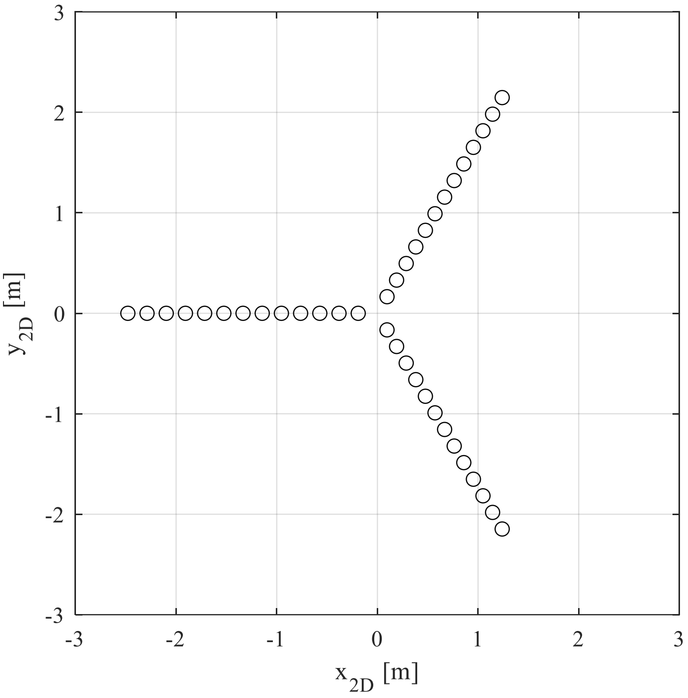

Figure 6-1. Central array configuration on the chief satellite. The axes x_{2D}, y_{2D} from the optimization frame (see Figure 5-5).

The spacecraft control period is set to 15 min to enable sufficient time for primary science operation between maneuvers. The mass of the chief satellite is selected to be equal to the SMOS satellite [52], while the mass of the deputy satellite is selected to be equal to that of the 8U CanX-45 satellites [70]. The areas of the SMOS satellite and the CanX-45 satellites are adopted for the calculation of the aerodynamic drag for the chief and deputy satellite in the current simulation as well. The deputy spacecraft drag coefficient is set to that of a cube $C_{D,d} = 2.2$. To account for the probable difference in drag coefficient between deputies and chief, the unknown drag coefficient of the chief satellite is assumed to be $C_{D,c} = 2.4$.

The minimal safety distance between deputy and chief of $D_{min,C} = 10\ m$ is assumed for the optimization of the receiver configuration. The σ_G parameter, given in Table 6-4 is set to accommodate the increasing number of satellites. Due to the non-linearity of the optimization problem, σ_G has to be determined empirically for each number of deputies.

Table 6-3 Spacecraft parameters for numerical simulation of case study 1

Antenna Parameters	*Values*
Nominal thrust (Deputy)	$u_N = 25\ mN$
Minimum Impulse Bit (Deputy)	$u_{min} = 0.2\ mNs$
Specific Impulse (Deputy)	$I_{SP} = 40\ s$
Propellant Mass (Deputy)	$m_p = 300\ g$
GNC Position Accuracy (Deputy)	$GNC_{Pos} = 5\ cm$
GNC Velocity Accuracy (Deputy)	$GNC_{Vel} = 0.21\ mm/s$
Thrust vector error (Deputy)	$\alpha_e = 2\ °$
Thrust magnitude error (Deputy)	$b_e = 5\%$
Control period (Deputy)	$T_{pwm} = 900\ s$
Chief Spacecraft mass	$m_{s,c} = 1163\ kg$
Chief Spacecraft aerodynamic area	$A_c = 9.05\ m^2$
Chief Spacecraft drag coefficient	$C_{D,c} = 2.4$
Deputy Spacecraft mass	$m_{s,d} = 6.85\ kg$
Deputy Spacecraft aerodynamic area	$A_d = 0.12\ m^2$
Deputy Spacecraft drag coefficient	$C_{D,d} = 2.2$

Table 6-4 σ_G parameter for array optimization.

N Deputies	*16*	*24*	*32*	*40*	*48*	*56*
$\boldsymbol{\sigma_G}$	*40*	*60*	*80*	*100*	*120*	*126*
N Deputies	*64*	*72*	*80*	*88*	*96*	
$\boldsymbol{\sigma_G}$	*144*	*180*	*200*	*220*	*240*	

To limit the computational cost of the simulation, the overflight time is discretized into eight steps for the imaging algorithm. Thus, eight visibility samples are generated from each baseline, which simulations show to be a reasonable approximation of the continuous sampling in the current case. Both uniform weighting and tapering functions are applied to the visibility samples as described in sections 5.4 and 4.3.

6.2 Case study: Impact of number of deputies

The purpose of this case study is to investigate the impact of the number of deputy satellites on the system performance and feasibility. In this context configurations with 16 to 96 deputies have been investigated and optimized.

6.2.1 Imaging performance

Figure 6-2 shows the results of the array optimization simulations for $N = 16, 24, 32$ deputies and a minimum intersatellite distance of $D_{min,D} = 3.5\ m$. The first row of images illustrates the deputy configuration in the relative GCO plane. It can be seen that deputies are placed on a dense formation around the chief satellite. Multiple simulations have shown that there is some dependence on the initial conditions which involve deputy positions that are chosen randomly within a distance of the chief. On other simulation runs, the deputies are indeed set in a more cluster-like formation. However, different simulations have shown that, while the distribution around the chief satellite might change, the overall system performance remains very comparable.

The spatial frequency coverage of the aggregated array is depicted in the second row of Figure 6-2. Each line represents the coverage of a single baseline during overflight of a target area. The images from left to right show an increasingly homogeneous and dense sampling of the spatial frequencies, due to the addition of deputies. The green lines visualize the frequency coverage of the inter-deputy baselines, while the blue lines visualize the baselines between the ARU on the chief array and the deputy satellites. The color distinction highlights the importance of the chief array, which greatly increases the density coverage of the spatial frequency plane. The red circle denotes the distance ρ_{max}.

The last row in Figure 6-2 shows the resulting PSF. Two effects are clearly visible: First, it can be seen that an increase in the number of deputies will lead to a tighter main lobe and thus a higher spatial resolution ($\theta_w = 1.15°$ for $N = 16$ to $\theta_w = 0.71°$ for $N = 32$). This is a direct result of a larger diameter of the spatial frequency coverage. Second, a reduction of the sidelobe levels can be observed with an increase in the number of deputies. This is attributable to the denser coverage of the spatial frequencies.

In contrast to the PSF of correlation arrays with regular antenna distances, the PSF in Figure 6-2 shows no dominant sidelobes. Instead, the entire region around the main beam is more akin to an elevated plateau. A plateau outside of the main beam in the PSF leads to a response from sources outside of the focused pixel and thus to a blurring of the final image. The plateau is caused by an over- and under-sampling of regions within the spatial frequency plane. To quantify the level of the plateau the Mean Sidelobe Level (MSLL) is defined, denoting the mean PSF response outside of the main beam. The MSLL is calculated as the average of all maxima from the generated PSF. In Figure 6-2 MSLL can be seen to decline from $MSLL = -12.7\ dB$ at $N = 16$ to $MSLL = -19.2\ dB$ at $N = 32$.

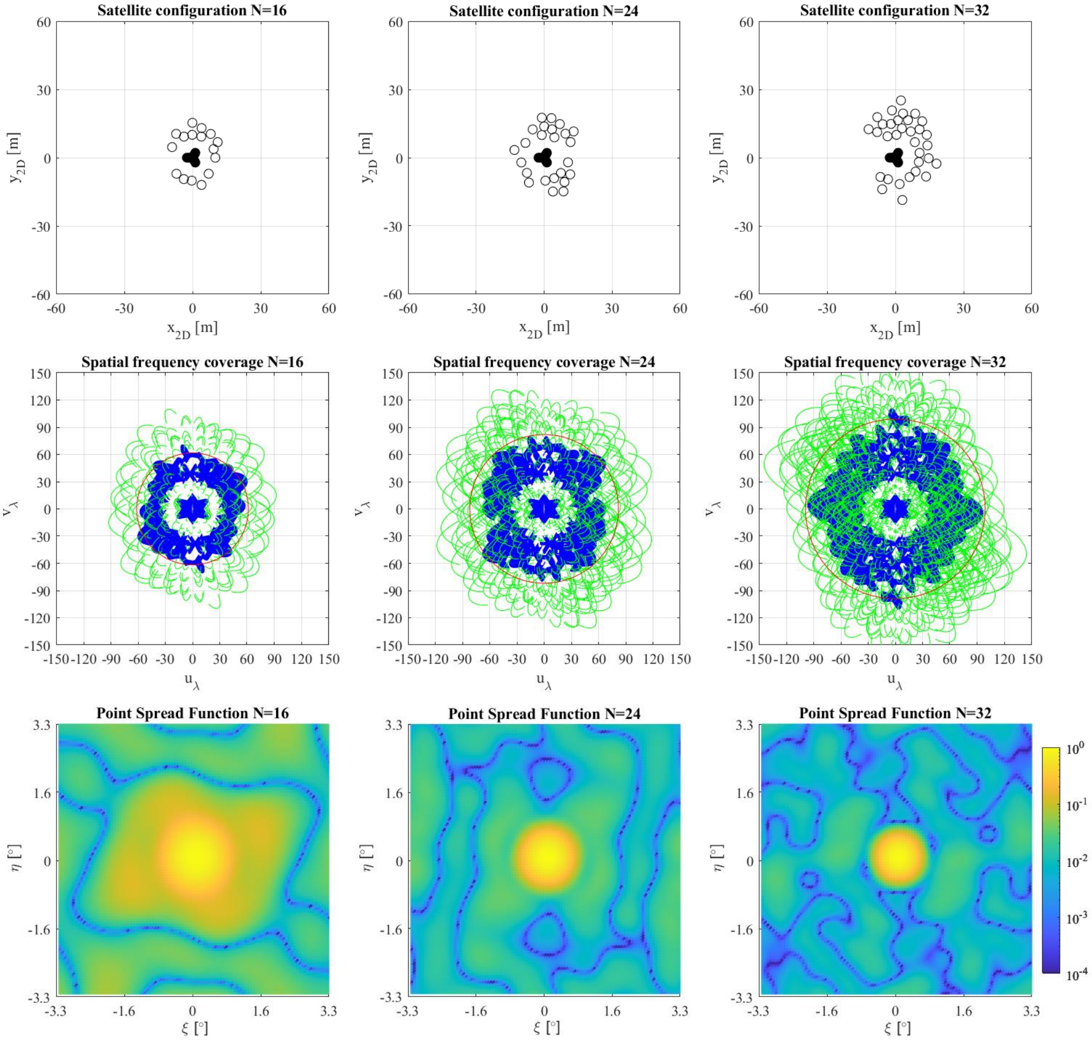

Figure 6-2 Illustration of the relationship between the optimized deputy configuration (top row), sampling of the spatial frequency domain (middle row) and the PSF (bottom row) for $N = 16, 24, 32$ (columns) and a minimum intersatellite distance of 3.5 m. On the first row the configurations are shown in the optimization coordinate system. The second row shows the sampled spatial frequencies (blue: chief/deputy baselines, green: deputy/deputy baselines) in the (u_λ, v_λ) plane with the red

circle denoting the distance ρ_{max}. Finally, the last row shows contour plots of the PSF respective arrays.

Figure 6-3 depicts the optimized configurations for satellite swarms including $N = 40, 48, 56$ deputies. As can be seen in the first row, the optimization algorithm places deputies consistently around the chief satellite improving the sampling of the spatial frequency domain. As a result of the improved sampling of the spatial frequency plane by more baselines, the MSLL declines from $MSLL = -21\ dB$ at $N = 40$ to $MSLL = -23.5\ dB$ at $N = 56$.

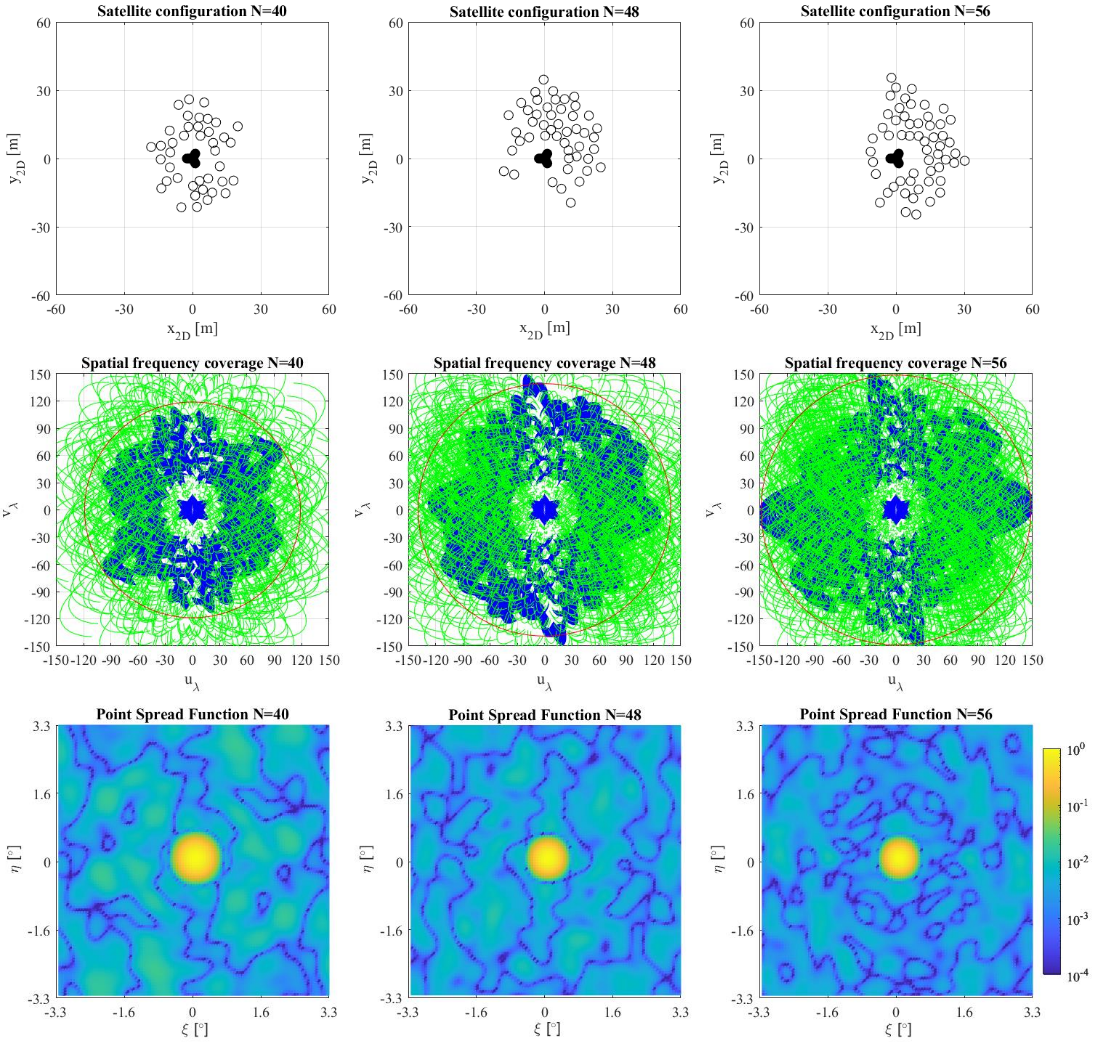

Figure 6-3 Illustration of the relationship between the optimized deputy configuration (top row), sampling of the spatial frequency domain (middle row) and the PSF (bottom row) for $N = 40, 48, 56$ (columns) and a minimum intersatellite distance of 3.5 m. On the first row the configurations are shown in the optimization coordinate system. The second row shows the sampled spatial frequencies (blue: chief/deputy baselines, green: deputy/deputy baselines) in the (u_λ, v_λ) plane with the red circle denoting the distance ρ_{max}. Finally, the last row shows contour plots of the PSF respective arrays.

The results of the optimized configurations with $N = 80, 88, 96$ deputies are shown in Figure 6-4. The deputies are placed in a distance to the chief of up to 60 m and are clustered in a similar way as the configurations with less deputies. A total of 9045 baselines in the case of $N = 96$ enable the dense circular sampling of the spatial frequency domain. The dense sampling and the large coverage of the spatial frequency domain results in a generally lower sidelobe level and a more concentrated main beam.

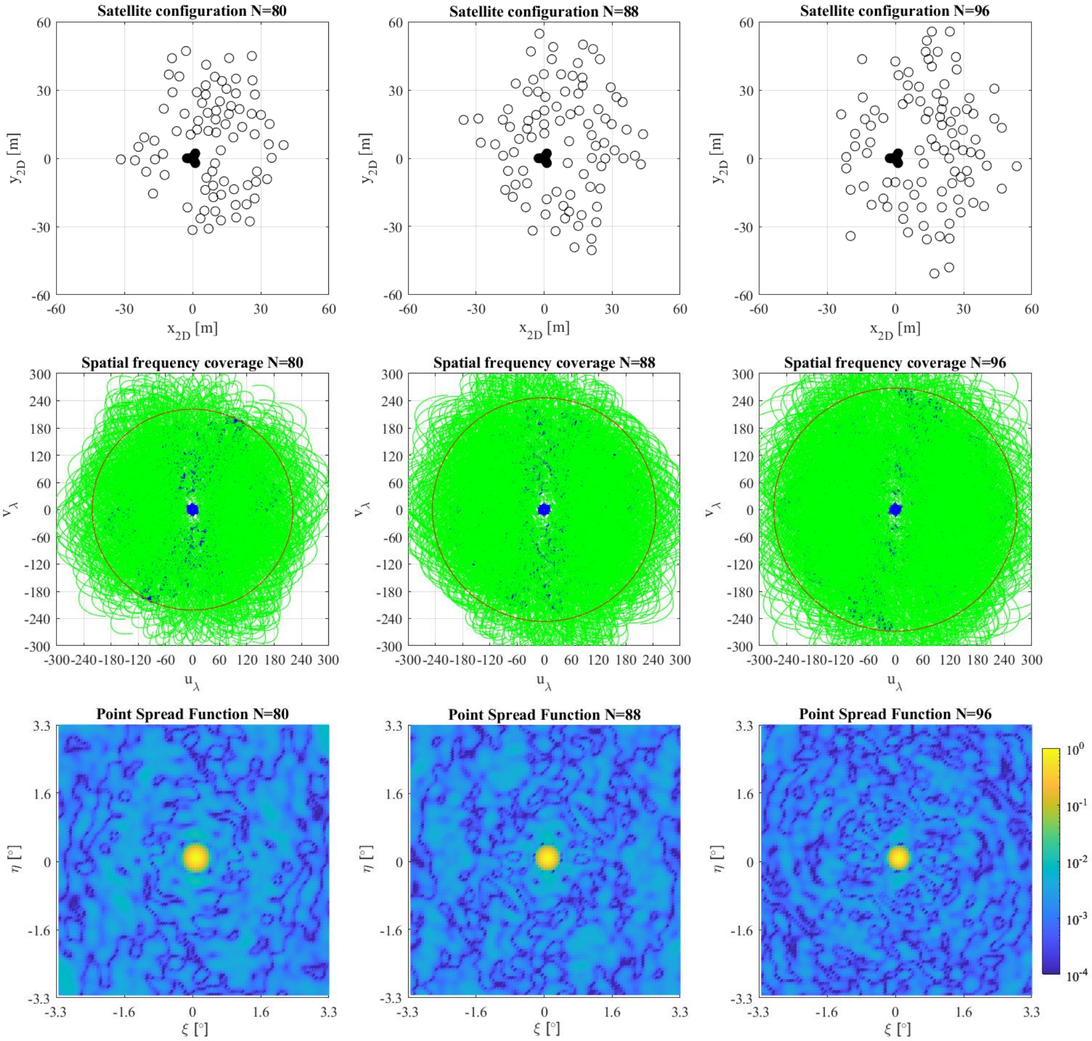

Figure 6-4 Illustration of the relationship between the optimized deputy configuration (top row), sampling of the spatial frequency domain (middle row) and the PSF (bottom row) for $N = 80, 88, 96$ (columns) and a minimum intersatellite distance of 3.5 m. On the first row the configurations are shown in the optimization coordinate system. The second row shows the sampled spatial frequencies (blue: chief/deputy baselines, green: deputy/deputy baselines) in the (u_λ, v_λ) plane with the red circle denoting the distance ρ_{max}. Finally, the last row shows contour plots of the PSF respective arrays.

For the observation of extended sources, a Gaussian distribution of samples [84] was shown to lead to lower sidelobes in interferometric arrays. Thus, the degree to which the radial distribution of samples resembles a Gaussian distribution can be used as a quality measure of the optimized configuration.

Figure 6-5 illustrates the radial distribution of samples in the (u_λ, v_λ) plane for configurations of different numbers of deputies and $D_{min,D} = 3.5\ m$ (solid line). In all cases the sample distribution exhibits clear deviations from the Gaussian distribution of equal standard deviation (dashed line). This is due to the two constraints on satellite distances, i.e., the necessity to keep safety distances to avoid collision. Less stringent constraints on the inter-deputy distances will result in more Gaussian distribution of the samples in the spatial frequency plane. The safety distance to the chief satellite $D_{min,C}$ is responsible for the large drop in sample density at approx. 30 wavelengths from the origin. The large drop is more pronounced with configurations with few deputies. In general, the addition of deputies can be seen to lead to a better recreation of the Gaussian distribution and denser (u_λ, v_λ) plane coverage.

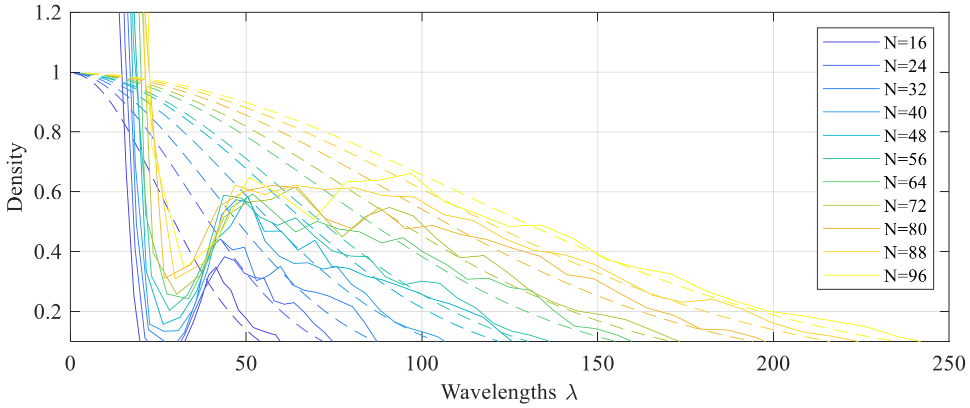

Figure 6-5 The solid lines denote the actual radial distribution of spatial frequency samples for the optimized configurations. The colors denote the number of satellites used in each configuration (blue for 16 deputies to yellow for 96 deputies). The dashed lines denote a Gaussian distribution of equal standard deviations for each configuration.

The spatial ground resolution and the sensitivity of aggregated arrays for configurations with up to 96 deputies are given in Figure 6-6. As a result of the increasing diameter of the array, the spatial ground resolution increases asymptotically to a minimum of 4 km for 96 deputies. Any further improvement of the resolution becomes costlier in terms of required deputies, since an additional percentage change in diameter requires more covered area in the spatial frequency domain. The radiometric sensitivity of the system deteriorates from 1.84 K with 16 deputies to 5.10 K at configurations with 96 deputies. The sensitivity of the system deteriorates due to the increasing number of baselines within the aggregated array and an improvement of spatial resolution.

The increase in the number of baselines leads to a larger weighting term in equation (5-10), while the increase in resolution leads to an increase of the beam filling factor Ω_A/Ω_{pix}. According to the radiometric uncertainty principle [55], the product of the angular resolution and the radiometric sensitivity should be a constant. Table 6-5 confirms this principle for the swam-based aperture synthesis radiometer as well. The deviations of $\Delta T \cdot \theta_w$ (from a constant) can be attributed to the different degrees of required density weighting. Some configurations require a stronger density weighting to compensate for an inferior optimization solution. Independent of the number of satellites used, the sensitivity stays significantly below that of current systems such as SMOS (0.33 K for cold backgrounds) [52].

Table 6-5 3dB angular resolution θ_w and radiometric sensitivity ΔT of satellite configurations.

N Deputies	*16*	*24*	*32*	*40*	*48*	*56*
$\boldsymbol{\theta_w}$ *[°]*	*1.15*	*0.86*	*0.71*	*0.59*	*0.51*	*0.48*
$\boldsymbol{\Delta T}$ $[\boldsymbol{K}]$	*1.84*	*2.03*	*2.52*	*2.51*	*2.85*	*2.53*
$\boldsymbol{\Delta T \cdot \theta_w}$ *[°K]*	*2.14*	*1.74*	*1.79*	*1.49*	*1.45*	*1.21*
N Deputies	*64*	*72*	*80*	*88*	*96*	
$\boldsymbol{\theta_w}$ *[°]*	*0.40*	*0.37*	*0.32*	*0.29*	*0.27*	
$\boldsymbol{\Delta T}$ $[\boldsymbol{K}]$	*3.27*	*3.52*	*4.11*	*4.74*	*5.10*	
$\boldsymbol{\Delta T \cdot \theta_w}$ *[°K]*	*1.32*	*1.29*	*1.33*	*1.38*	*1.36*	

Figure 6-7 shows the influence of the number of deputies on the MSLL and the MBE for the aperture synthesis radiometer. Especially for configurations with higher numbers of deputies, the PSF shows a relatively homogenous residual response in the areas outside the main side lobe. There are no distinct "largest" sidelobes at all. The MSLL shows a continuous decline from -12.72 to -26.54 dB for an increasing number of deputy satellites. The decline can be attributed to the denser and increasingly Gaussian distribution of the spatial frequency samples in the (u_λ, v_λ)

plane. With efficiencies of around 60% the MBE reaches levels comparable to monolithic arrays and sufficient for imaging extended sources. The MBE stays relatively constant across the different configurations. This is because the improvement in spatial resolution is compensated by the effect of a declining level of MSLL. While a decline of MSLL in the non-main lobe region of the PSF increases the energy concentrated in the main beam, a tighter main beam, enlarges the side lobe region.

The irregularity of the curves in Figure 6-6 and Figure 6-7 again indicates that the solution of the numerical optimization can differ between optimization runs. When designing the actual swarm-based radiometer system it is advisable to conduct multiple optimization cycles, choosing the best optimization result.

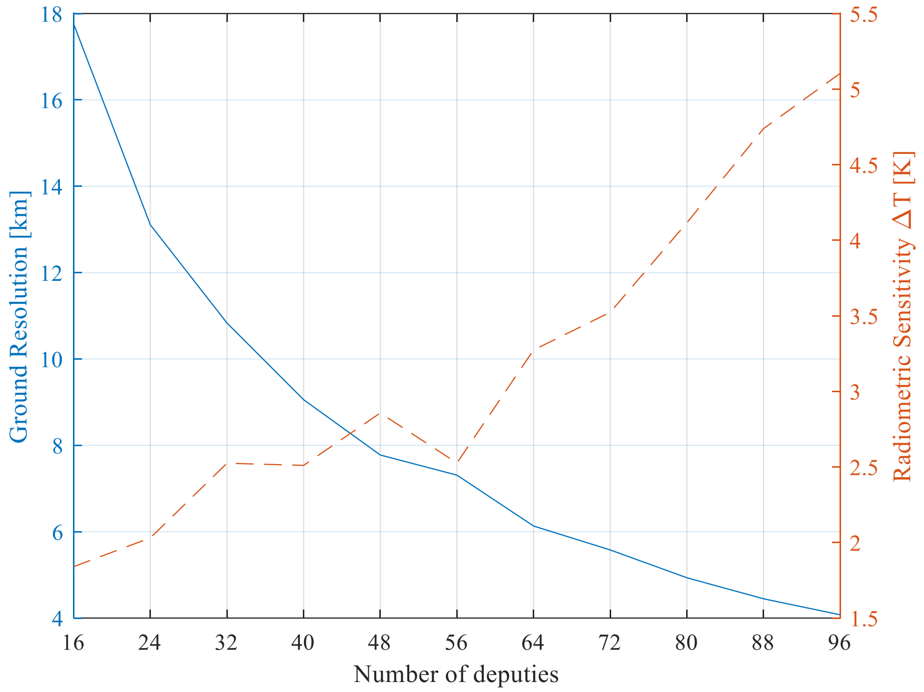

Figure 6-6 Resolution in km (solid line) and sensitivity in Kelvin (dashed line) for configurations with N deputies and $D_{min,D} = 3.5\ m$.

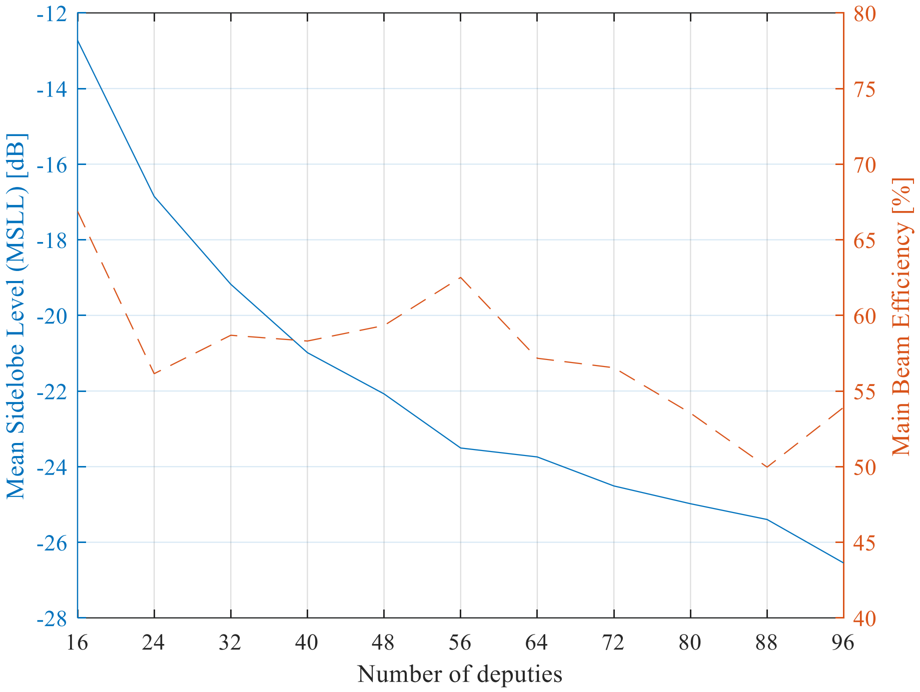

Figure 6-7 Mean Sidelobe Level in dB (solid line) and MBE in percent (dashed line) for configurations with N deputies and $D_{min,D} = 3.5\ m$.

Spatial decorrelation occurs in interferometric systems due to the loss of coherence in wideband signals that are recorded at spatially distant points. The difference in autocorrelation due to the phase shifts that are measurable when recording a narrow-band signal at varying points in space, decreases with an increase in bandwidth. This relationship is given mathematically with the fringe-wash term in equation (2-28). It enables the calculation of the degree of decorrelation. The longer the baseline, the more decorrelation effects become a problem. Figure 6-8 shows the degree of decorrelation on the largest baseline as a relationship of the number of deputies in a swarm configuration. As expected, configurations with a larger number of deputies involve longer baselines, which in turn increase the spatial decorrelation of measurements at that particular baseline. Configurations including over 56 deputies yield decorrelation effects that exceed 50%. This means a significant decrease in radiometric sensitivity towards the edges of the useful field at approx. 30° off-boresight angle.

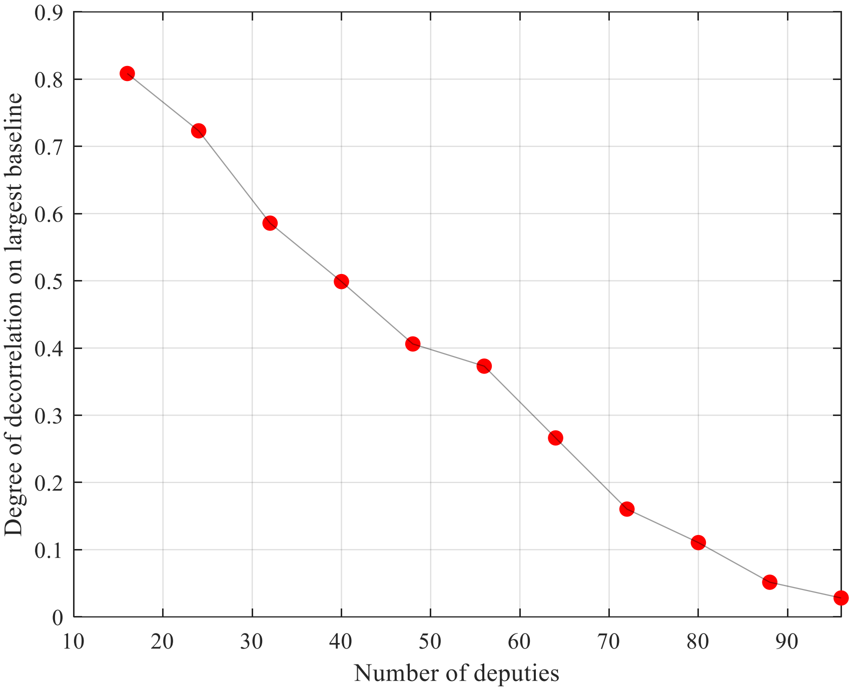

Figure 6-8 Degree of decorrelation on the largest baselines for configurations with N deputies and $\mathrm{D}_{\mathrm{min,D}} = 3.5$ m.

6.2.2 System implications

The optimization of deputies on the optimization frame (GCO plane) yields a dense formation of deputies circumventing the chief satellite. The last section investigated the imaging performance that could be expected from a distributed radiometer modelled after the optimized orbital configurations. This section investigates the system feasibility, with a focus on the collision probability and the fuel consumption of the individual deputies. Figure 6-9 shows the optimized swarm configuration for $N = 16$ deputies in three-dimensional space. The deputies are placed in distances that barely adhere to the minimum distance requirements set in the optimization algorithm. Deputies roughly form an inner ring which is augmented by individual deputies on a second ring and a single deputy further away from the chief.

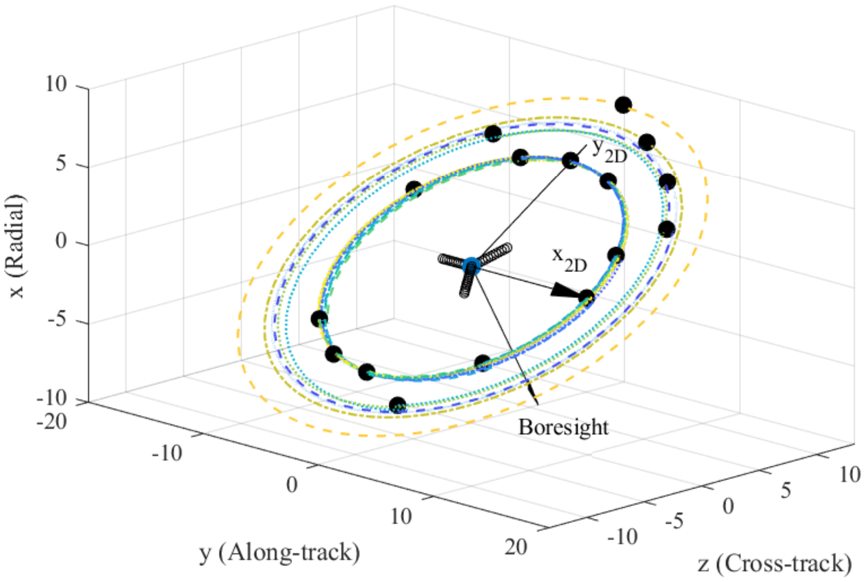

Figure 6-9 Configuration of the swarm-based synthetic aperture radiometer with $N = 16$ and $\mathrm{D}_{\mathrm{min,D}} = 3.5$ m.

Figure 6-10 shows the optimized swarm configuration for $N = 96$ deputies. The swarm of deputies circles the chief satellites in distances up to 65 m. To understand the risk from collision in this dense swarm, the position accuracy and collision probability are plotted on graphs for the $N = 96$ configuration which serves as a representative example.

Figure 6-11 illustrates the mean 3D RMS position accuracy of the autonomous controller for each satellite within the $N = 96$ configuration, ordered by distance to the chief. The position accuracy of the deputies exhibits a Gaussian distribution around a slightly decreasing mean value, staying within 0.76 m. Within short distances between the chief and the deputy satellites, the randomness introduced to the position and velocity of the individual deputies dominates any physical effects that would be introduced by physics. The variations around the mean are thus caused by the Gaussian nature of the imposed navigation errors, i.e., the GNC position, GNC velocity error and the thruster errors. The exact position of a deputy on a GCO at a given distance seems to have no significant impact on fuel consumption, aside from the orbiting distance to the chief. A systematic relationship between the deputy-chief distance or the degree of J_2-invariance could not be observed at these short inter-satellite distances.

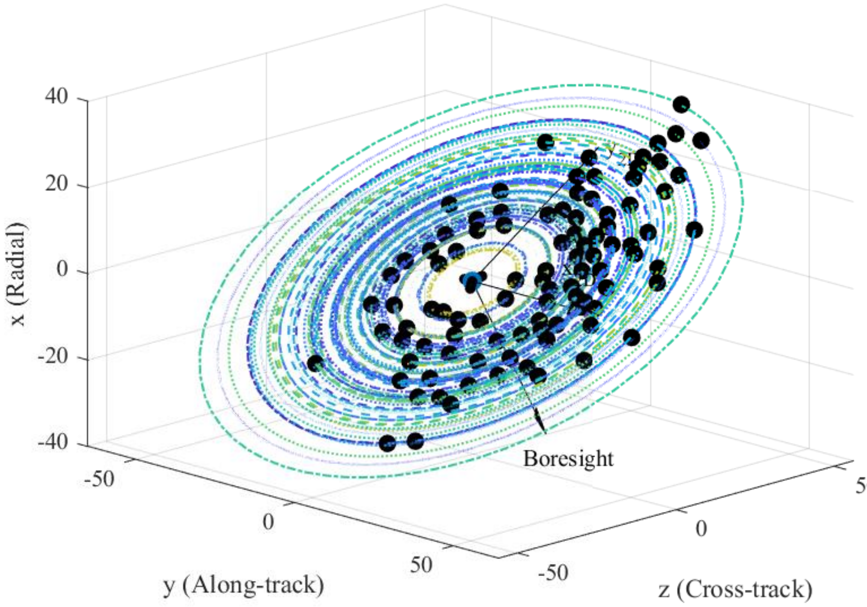

Figure 6-10 Configuration of the swarm-based synthetic aperture radiometer with $N = 96$ and $D_{min,D} = 3.5\ m$.

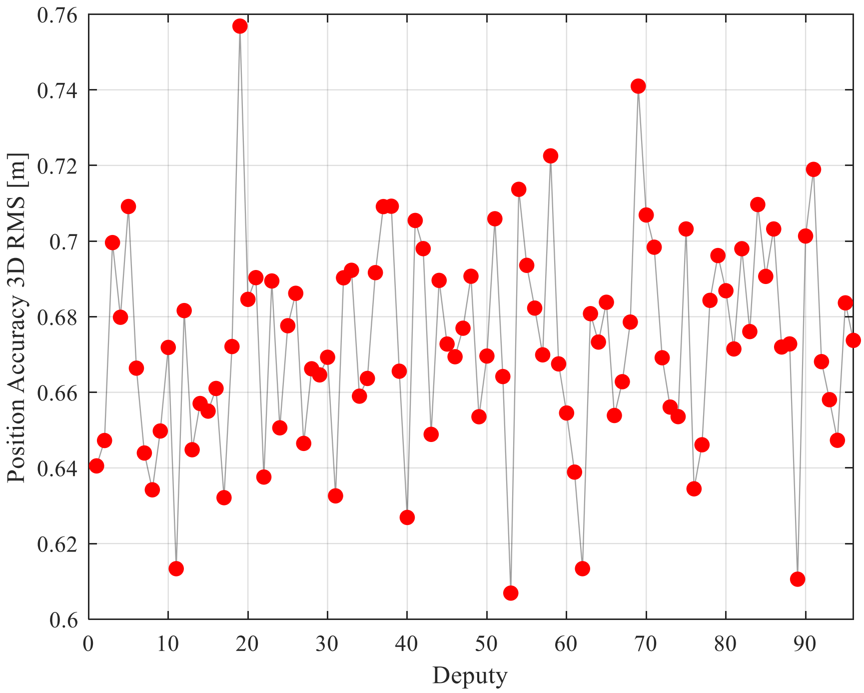

Figure 6-11 Deputy position accuracy as 3D root mean square (RMS) error [m] for the formation of $N = 96$ deputies and $D_{min,D} = 3.5\ m$.

Figure 6-12 shows the accumulated probability of collision per orbit for the same configuration. The probability for deputy satellite m is calculated by summing up the collision probabilities of deputy m with all other deputies as given in equation (4-27).

The total collision probability does not exceed $1.5 \cdot 10^{-2}$ per orbit for any deputy. A higher collision probability is caused by a closer reference distance to any other satellite or a lower position accuracy. For this most extreme case, a satellite collision would occur approximately every 67 orbits. Thus, while collision avoidance maneuvers will still be necessary at least every 67 orbits, it can be assumed that the fuel budget is dominated by the periodic orbit maintenance maneuvers. Of course, the introduction of additional inter-deputy safety distances, that could be necessary due to the reaction time of the orbit and attitude control system could further increase the required frequency of collision avoidance maneuvers. This however is dependent on the implementation of the orbit and attitude control system and the overall acceptable mission risk.

As mentioned in the previous chapter, overall collision risk can be further lowered either by increasing the minimum distance constraint for all deputies $D_{min,D}$ or by iteratively repositioning single satellites.

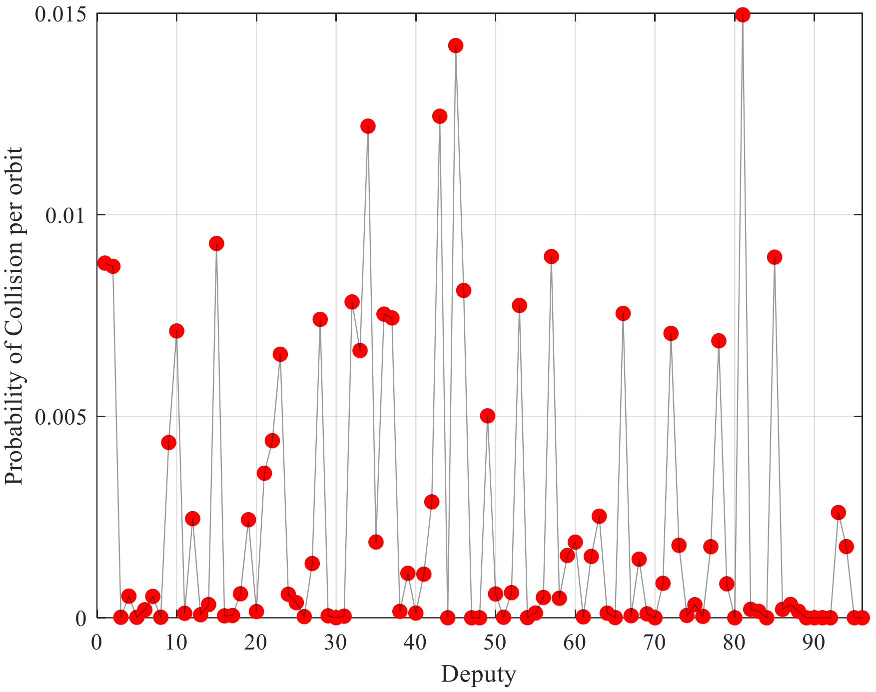

Figure 6-12 Accumulated collision probability of each satellite per orbit for the formation of $\mathrm{N} = 96$ deputies and $\mathrm{D}_{\mathrm{min,D}} = 3.5$ m.

A histogram of the collision probability per deputy pair and orbit is shown in Figure 6-13. The histogram only counts pairs that have a probability of collision larger than 10^{-4}. There are a total of 49 deputy pairs of a total of 4560 possible deputy pairs that fall into that category. The largest collision probability per orbit for a single pair is $8.7 \cdot 10^{-3}$. Only 25 pairs have a probability of collision that is above 10^{-3} per orbit. This would mean that a collision event would occur up to every 7th day for these critical pairs. It is very likely the positions of the deputies with critical collision probabilities could be rearranged to greatly lower the overall risk to the satellite swarm without significantly affecting imaging performance. This analysis shows that while the collision risk is theoretically low for most of the deputies, it is not negligible for others. Thus, the implementation of an active collision avoidance system is a prerequisite for a seamless operation of the system.

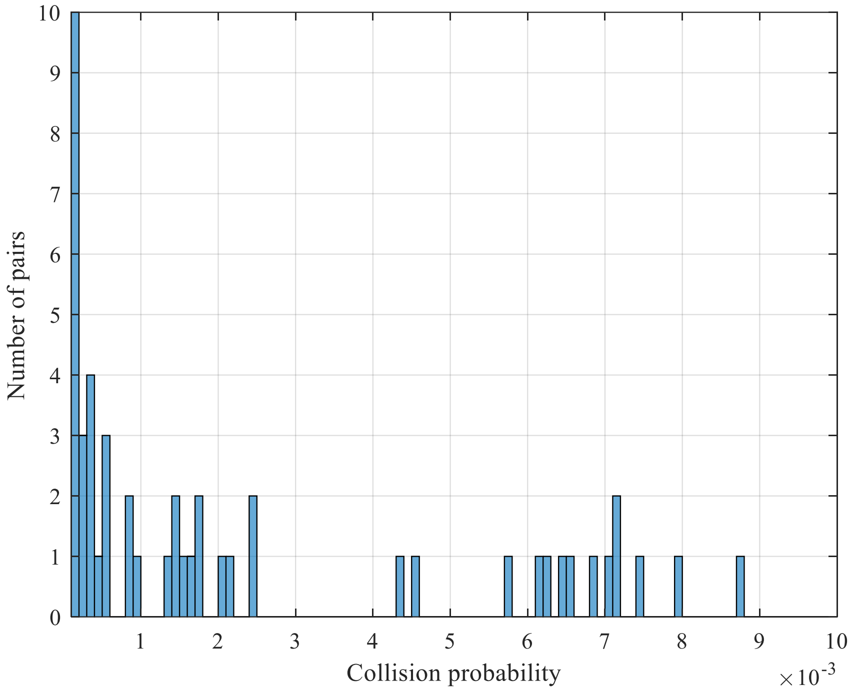

Figure 6-13 Collision probability of each satellite pair per orbit for the formation of $N = 96$ deputies and $D_{min,D} = 3.5$ m.

Figure 6-14 shows the mean fuel consumption Δv per satellite and orbit required for periodic formation maintenance manoeuvres. Fuel consumption per deputy stays below 0.9 cm/s per orbit, even for the deputies on the outer rim of the aperture synthesis antenna array. Assuming that fuel consumption is largely defined by the periodic formation maintenance maneuvers, this leads to a swarm lifetime of 156 days. Naturally this represents a lower bound for the fuel consumption as maneuvers such as deployment and occasional collision avoidance or reconfiguration maneuvers will add to the total fuel consumption.

Generally, the fuel consumption behaves analogously to the position accuracy, meaning that a lower fuel consumption equates to a better position accuracy of the deputy orbit control system. This seems intuitive, since larger displacements will also mean that more fuel needs to be spent for formation maintenance. As with the position accuracy, no systematic significant relationships could be found between the fuel consumption and the chief-deputy distance or the degree of J_2-variance within the close-proximity domain. The fuel consumption also seems to be influenced mostly by the randomized error of the orbit control system.

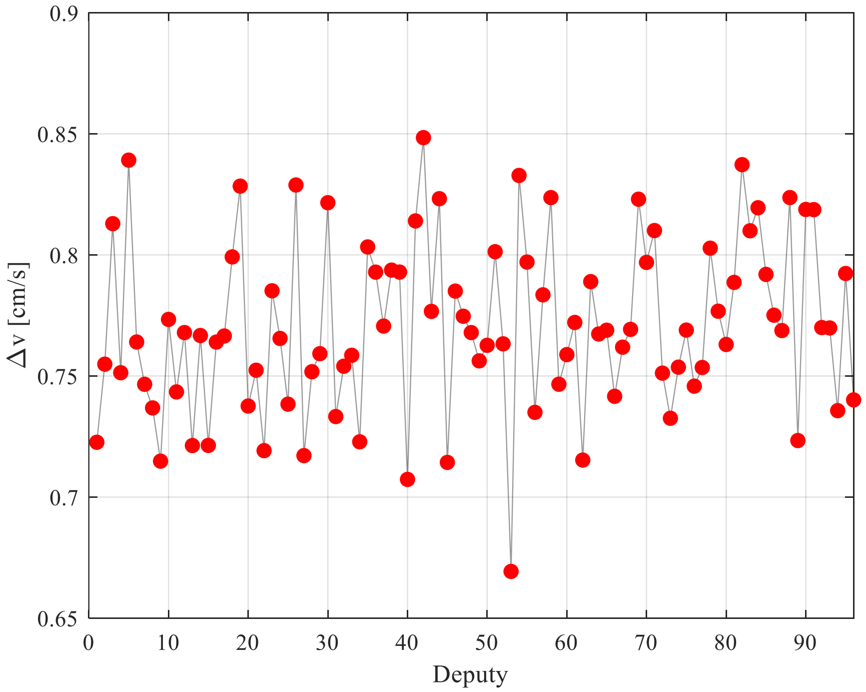

Figure 6-14 Average fuel consumption Δv [cm/s] for formation maintenance per orbit for the formation of $N = 96$ deputies and $D_{min,D} = 3.5\ m.$

The overall simulation results show that a minimum inter-deputy distance of 3.5 m with the orbit control configurations given in Table 6-3 will still result in a dense satellite swarm that requires occasional collision avoidance maneuvers. As outlined in the previous chapter the specific inter-deputy distance of the system to be implemented needs to be adjusted to the specific application and the performance of the GNC.

While the aerodynamic drag in an altitude of 755 km is low, it will still cause a drift of the ground track over time. Using the method described in section 4.5.2, the ground-track drift was calculated for a system which orbit's semimajor-axis is periodically adjusted by Δa_{GT}. The ground track accuracy L_d [m] and the required maneuver frequency T_s [s], calculated with equations (4-31) and (4-28), are given in Table 6-6 for different values of the semimajor-axis adjustment Δa_{GT} [m]. Two requirements need to be considered when choosing the frequency of semimajor-axis adjustment. Firstly, the maximum ground track drift of 25 km, that was adopted from the SMOS requirements. This requirement effectively necessitates an adjustment of semimajor-axis at least every 36 days, as a larger adjustment would violate the requirement directly. Secondly, the capability of the distributed system to actually implement the semimajor-axis adjustment without instabilities within the system. Any semimajor-axis adjustment will necessarily have to be performed by all satellites simultaneously, i.e., all deputies and the chief satellite. In any case, this will be a challenge for the control of the satellite swarm, as the nominal distances between satellites are very small.

Table 6-6 Ground track accuracy L_d and time between semimajor-axis adjustments T_s dependent on magnitude of the adjustment Δa_{GT} [m].

$\Delta\boldsymbol{a}_{GT}$ *[m]*	*1*	*2*	*4*	*8*	*16*	*32*	*64*	*128*
$\boldsymbol{L}_d$ *[m]*	*2.4*	*9.6*	*38.4*	*153.6*	*614.4*	*2457.4*	*9829.7*	*39218.8*
$\boldsymbol{T}_s$ *[days]*	*1.1*	*2.3*	*4.6*	*9.1*	*18.2*	*36.4*	*72.9*	*145.8*

The method described in section 4.5.2 assumes that the semimajor-axis adjustment takes place in a Hohmann-transfer type impulsive maneuver. In this case the chief would perform an impulsive maneuver while the autonomous orbit control of the deputies would follow the chief. Thus, it is necessary to ensure that the frequency of the orbit deputy maneuvers for relative orbit maintenance is sufficient to prevent significant drift from the nominal positions during orbit adjustments. While this aspect will require more analysis in the future, it is reasonable to assume that semimajor-axis adjustments would need to be very small (perhaps below 10 m) if a control period in the order of $T_{pwm} = 15\ min$ (approx. 6 maneuvers per orbit) is used for the autonomous control of the deputies. Assuming a semimajor-axis adjustment of 8 m, the frequency of required semimajor-axis adjustments would be 9.1 days. The requirement for the ground track accuracy could be easily kept in that case. Thus, for a distributed swarm-based synthetic aperture radiometer, the ability of the deputy orbit control to follow any semimajor-axis adjustments by the chief is the driving requirement governing the frequency of orbit adjustments.

6.3 Case study: Impact of orbit control system

6.3.1 Impact of control period

The investigation within the previous section showed a rather short lifetime of the system with the orbit control settings given in Table 6-3. A key parameter defining the position accuracy and the fuel consumption of the system is the control period T_{pwm}, which was set to 15 minutes for the investigation in the last chapter. In order to perform science measurements with the satellite swarm-based aperture synthesis radiometer, the deputy satellites ARU will need to be directed towards the common center point X_c, Y_c of the target area during the entire flyover. While this brings with it many challenges in attitude control, it limits the time in which orbit control maneuvers can be performed as orbit control and measurements cannot be performed simultaneously. Thus, assuming that an orbit maneuver will take around one minute [70], measurements will have to be interrupted every 14 minutes. Therefore, from the measurement aspect, it is beneficial to prolong the time between maneuvers to maximize actual operation time of the payload. On the other hand, longer control periods will increase the collision probability of the satellites and thus the need for larger inter-deputy distances. To investigate the relationship between the control period T_{pwm}, the fuel consumption and the deputy position accuracy, the mission scenario presented in section 6.1 was simulated with different control periods. Control period varied between 300 and 1100 s.

The impact of the control period on the average deputy fuel consumption can be seen in Figure 6-15. There is a clear positive correlation between the value for Δv per orbit and the control period. A longer control period will thus mean an increase in fuel consumption. This relationship can be explained by the larger accumulated drift of the deputies from their reference orbit, if no corrections occur for a longer period of time. The larger drift is a result of the larger relative J_2 perturbations between the chief and the deputy. The increase in average deputy fuel consumption does not differ significantly between configurations, which confirms the findings of the previous section, that in inter-satellite distances below 50 m, the inaccuracy of the satellite orbit control dominates over inaccuracies stemming from physical perturbations.

An analogous relationship between the average deputy fuel consumption and the control period can be observed in Figure 6-16. As expected longer drifts from the ideal reference orbit will result in a degradation of position accuracy. It can be seen that the degradation of position accuracy is more pronounced as the increase in fuel consumption. Performing maneuvers every 1100 s instead of 900 s will result in a degradation of the position accuracy by the factor of two.

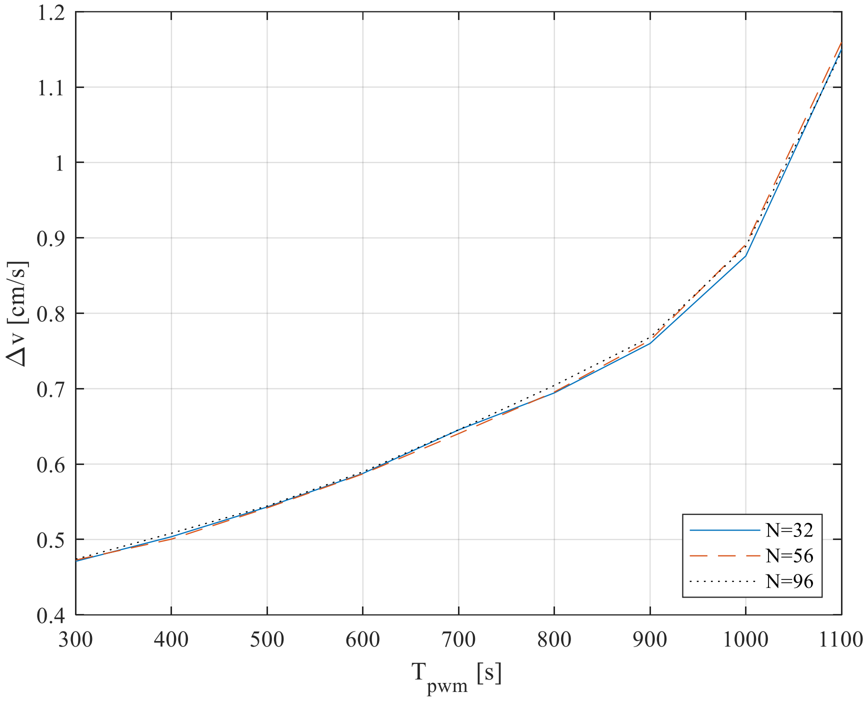

Figure 6-15 Average deputy fuel consumption Δv [cm/s] for formation maintenance per orbit for the formation of $N = 32, 56, 96$ deputies, $D_{min,D} = 3.5\ m$ and different control periods T_{pwm}.

The impact of the control period on the probability of collision for configurations with different number of deputies is displayed in Figure 6-17. The largest accumulated probability of collision for any deputy increases steadily with an increase in the control period. Large control periods such as $T_{pwm} = 1100\ s$ lead to high probability of collision per orbit of approximately every 20th orbit. The higher probability of collision is a result of a decreased frequency of orbit control maneuvers, allowing larger drifts from the reference orbit. There seems to be little difference in the probability of collision between the configurations with $N = 32$ and $N = 56$ deputies, independent of control period.

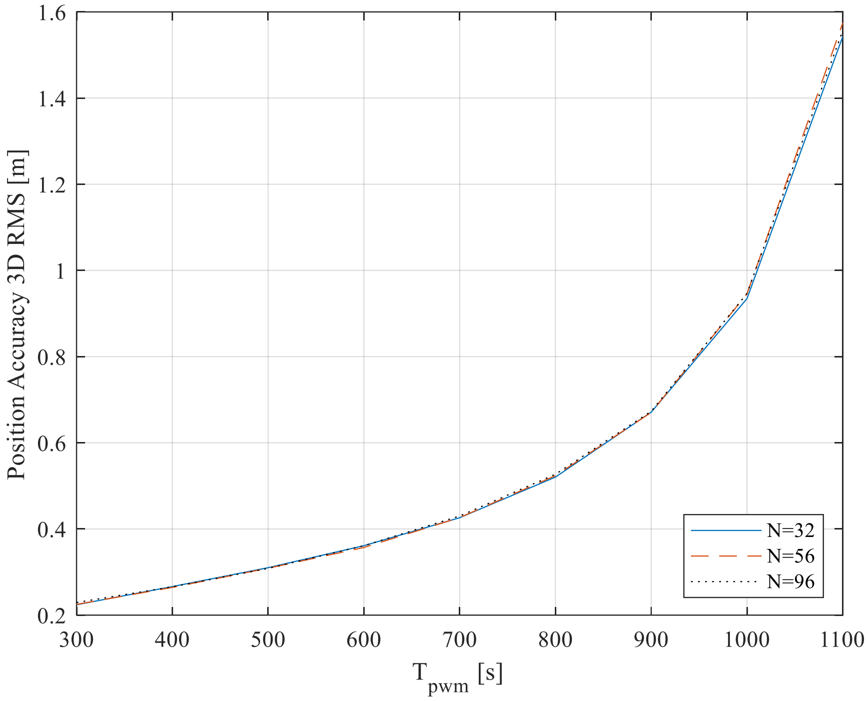

Figure 6-16 Average deputy position accuracy 3D RMS [m] for formation maintenance per orbit for the formation of $N = 32, 56, 96$ deputies, $D_{min,D} = 3.5\ m$ and different control periods T_{pwm}.

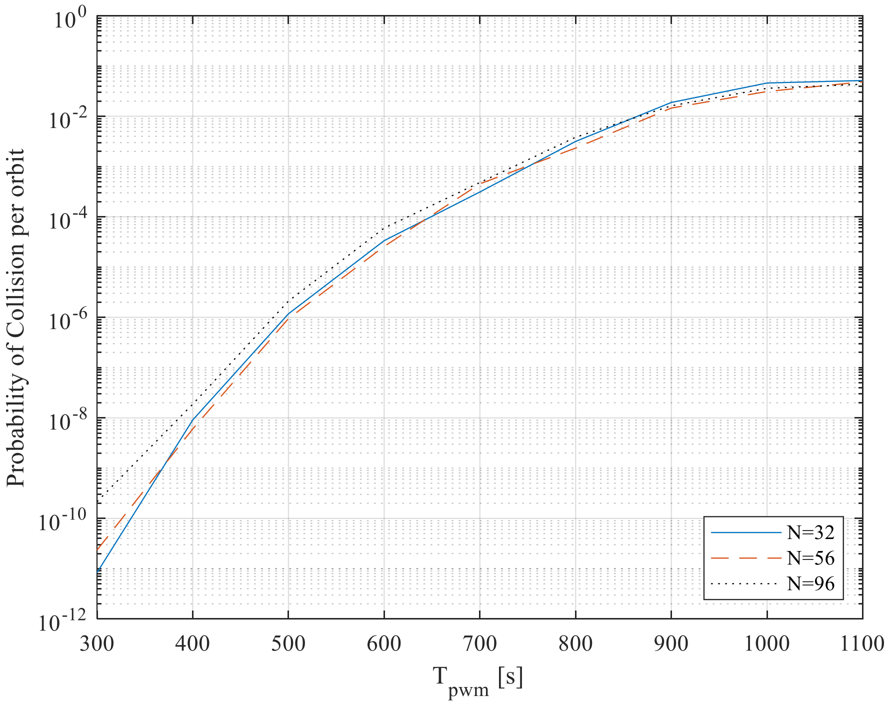

Figure 6-17 Highest probability of collision per orbit of any deputy during formation maintenance for the formation of $N = 32,56,96$ deputies, $D_{min,D} = 3.5\ m$ and different control periods T_{pwm}.

To summarize, the selection of the control period T_{pwm} impacts both the collision probability and the fuel consumption. Longer control periods will lead to a higher consumption of fuel per orbit and a high probability of collision, due to longer drifts from the reference orbits between maneuvers. The selection of shorter control periods however has the significant disadvantage of leaving less time for science measurements between maneuvers. This is because each maneuver requires the satellite to perform a sequence of tasks. These involve the reorientation of the deputy attitude in accordance with the required thrust orientation, the firing of the thruster and the subsequent reorientation of the deputy antenna to the side-looking position for measurements. A detailed simulation would have to be conducted for a precise determination of the required time for the maneuvers themselves.

6.3.2 Impact of relative navigation accuracy

Aside from the control period, the accuracy of the GNC deputy state estimate (position and velocity) is critical to the feasibility of the swarm-based aperture synthesis radiometer. The accuracy of the position and velocity estimates that can be provided by on-board GNC systems has improved significantly over the last decades, due to the evolution of the GNSS receiver hardware, the emergence of new processing algorithms and the usage of multi-GNSS receivers [93]. To shed light on the impact of the position and velocity knowledge, simulations have been conducted of the formation with $\mathrm{N} = 56$ deputies with various GNC accuracies. The simulation scenario is identical to the simulation scenario used in section 6.1. The results of these simulations can be seen in Figure 6-18, Figure 6-19 and Figure 6-20.

The mean position accuracy of the deputy orbit control system over the mean position and velocity knowledge of the deputy GNC system is shown in Figure 6-18. The GNC position and velocity knowledge was varied as a multiple of the values used for the reference simulation in section 6.1, i.e. $GNC_{Pos} = 5\,cm$ and $GNC_{Vel} = 0.21\,mm/s$. The results clearly underscore the importance of the GNC velocity knowledge accuracy for the position accuracy of the deputy orbit control. A decrease in velocity knowledge accuracy by just 50 % results in a decrease of the position accuracy by almost two (see yellow and blue curve in Figure 6-18). The strong impact of the velocity state estimation accuracy highlights the importance of fusing orbit propagation data, with GNSS measurement data. Without this step the velocity estimates would be an order of magnitude worse, making the implementation of the swarm-based aperture synthesis radiometer impossible. The importance of the accuracy of position estimates is less pronounced. A degradation of the GNC position by the factor of two, leads to a control accuracy degradation of 10 – 20 cm only.

Since the position and velocity accuracy impacts the position accuracy of the orbit control system, the probability of collision will be impacted as well. Figure 6-19 shows the highest probability of collision per orbit for the deputies as a function of the GNC performance. As expected, the probability of collision rises with a deterioration of GNC velocity estimate. For a velocity estimate accuracy of $1.5 \cdot GNC_{Vel}$, the highest collision probability for any deputy rises to 4 %, which likely would lead to an instability of the entire deputy swarm. It also becomes evident, that systems with higher accuracy velocity estimates are influenced more by degradations of the position estimate. A degradation of the position knowledge by a factor of two leads to a significant rise of the probability of collision between deputies in particular for the case with higher accuracy of the reference GNC velocity estimate ($0.5 \cdot GNC_{Vel}$).

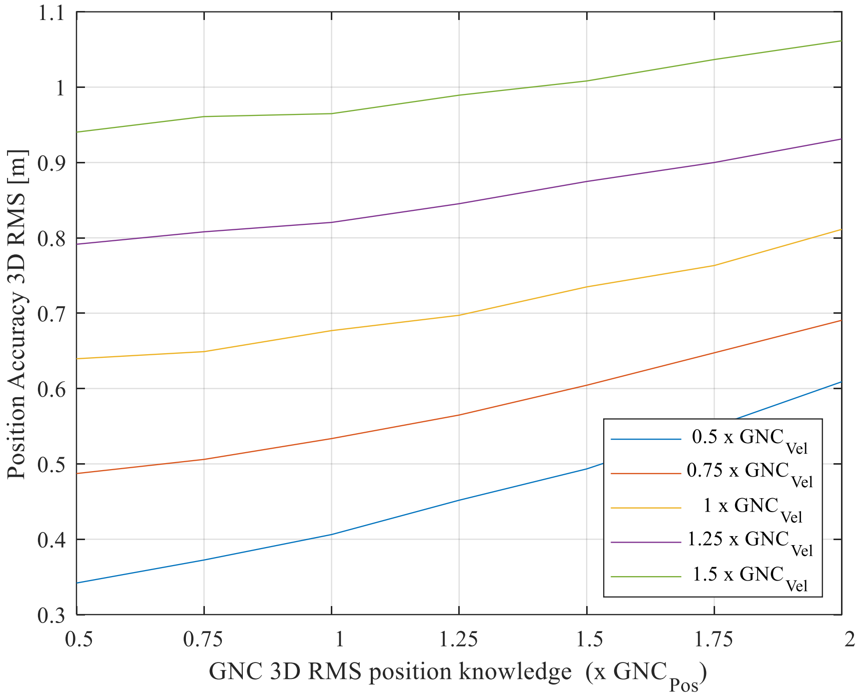

Figure 6-18 Position accuracy 3D RMS during formation maintenance for the formation of $N = 56$ deputies and $D_{min,D} = 3.5\ m$ over the position knowledge accuracy and velocity knowledge accuracy.

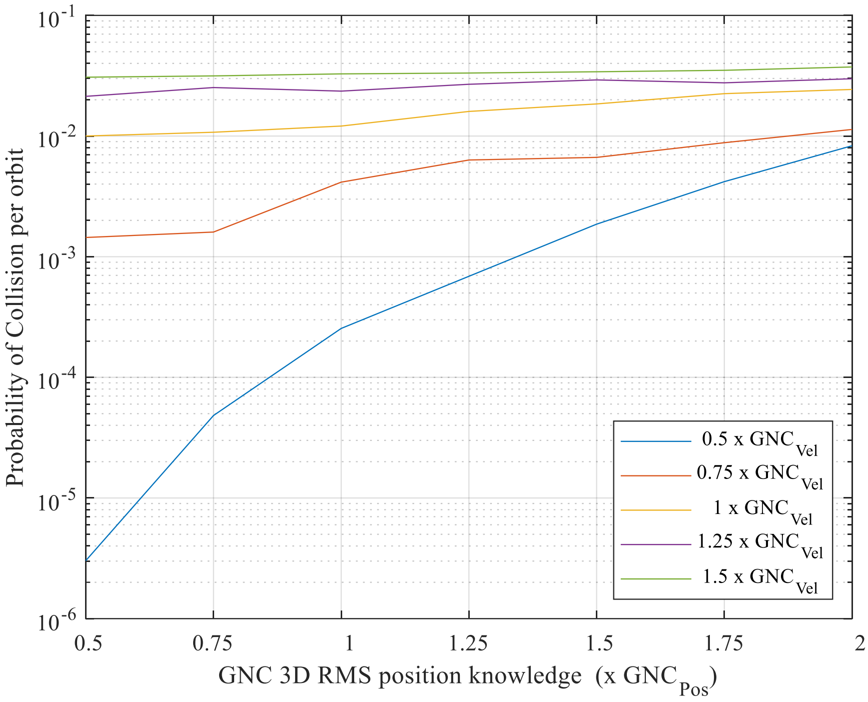

Figure 6-19 Highest probability of collision per orbit of any deputy during formation maintenance for the formation of $N = 56$ deputies and $D_{min,D} = 3.5\ m$ over the position knowledge accuracy the velocity knowledge accuracy.

Nevertheless, the figure again highlights the key importance of accurate GNC state estimates for the feasibility of the system. Since the fuel consumption (see Figure 6-20) behaves analogously to the position accuracy, a better GNC system will decrease fuel consumption and thus increase the lifetime of the system. It must be noted additionally that a high probability of collision will lead to a high frequency of collision avoidance maneuvers. While this issue is not explored quantitatively in this study, a high frequency of collision avoidance maneuvers might be unfeasible for a densely distributed system as the one proposed.

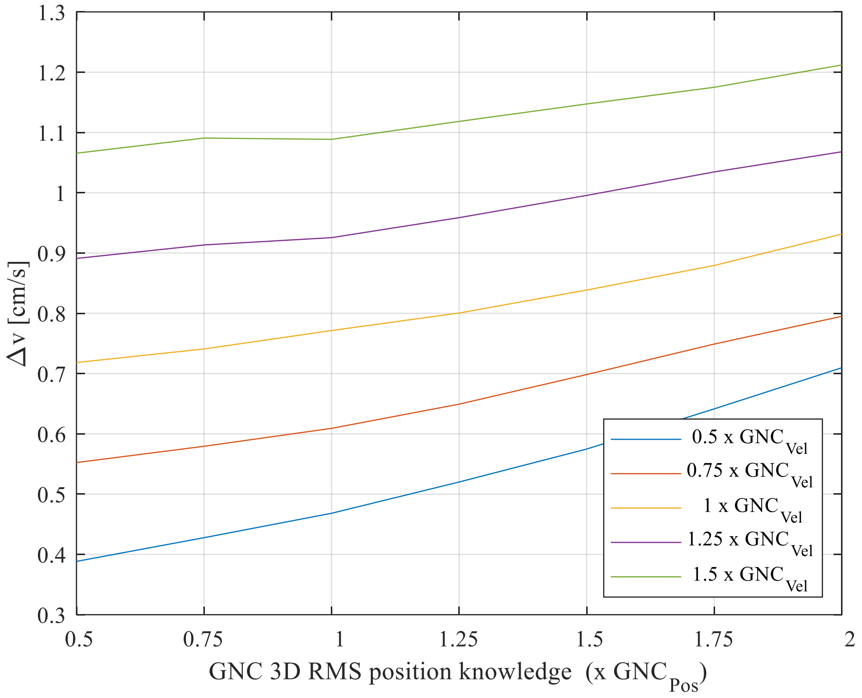

Figure 6-20 Fuel consumption per orbit and deputy for formation maintenance for the formation of $N = 56$ deputies and $D_{min,D} = 3.5\,m$ over the position knowledge accuracy and the velocity knowledge accuracy.

6.4 Case study: Impact of distance constraints

After having investigated the impact of the number of satellites and the accuracy of the GNC system on the feasibility and performance of the system, more attention needs to be put on the selection of the constraint parameters during the numerical optimization of the configuration itself. Choosing the minimum inter-satellite distances impacts both the collision probability, the deputy fuel consumptions, i.e., the system lifetime and the density of the spatial frequency coverage. The purpose of this section is to shed light on the system impact of different inter-satellite distance constraints and ultimately to provide an indication for their selection in the system design.

To investigate the impact of the distance constraints, simulations were performed with varying minimum inter-deputy distances $D_{min,D}$. Aside from the minimum inter-deputy distance constraints, the basic system scenario was not changed from the one given in section 6.1. The settings for the minimum inter-deputy distance constraint are given in Table 6-7. The number of deputies were set at $N = 56$ for all simulations.

Table 6-7 Simulation settings for the investigation of the impact of inter-deputy distance constraints.

Simulation run	*1*	*2*	*3*	*4*	*5*	*6*	*7*	*8*	*9*	*10*
$\boldsymbol{D_{min,D}}$ *[m]*	*2*	*2.5*	*3*	*3.5*	*4*	*4.5*	*5*	*5.5*	*6*	*6.5*

6.4.1 Imaging performance

The optimized configurations in the optimization frame for different settings of the minimum inter-deputy distance constraints can be seen in Figure 6-21. The configurations seem to become more regular with an increasing inter-deputy distance.

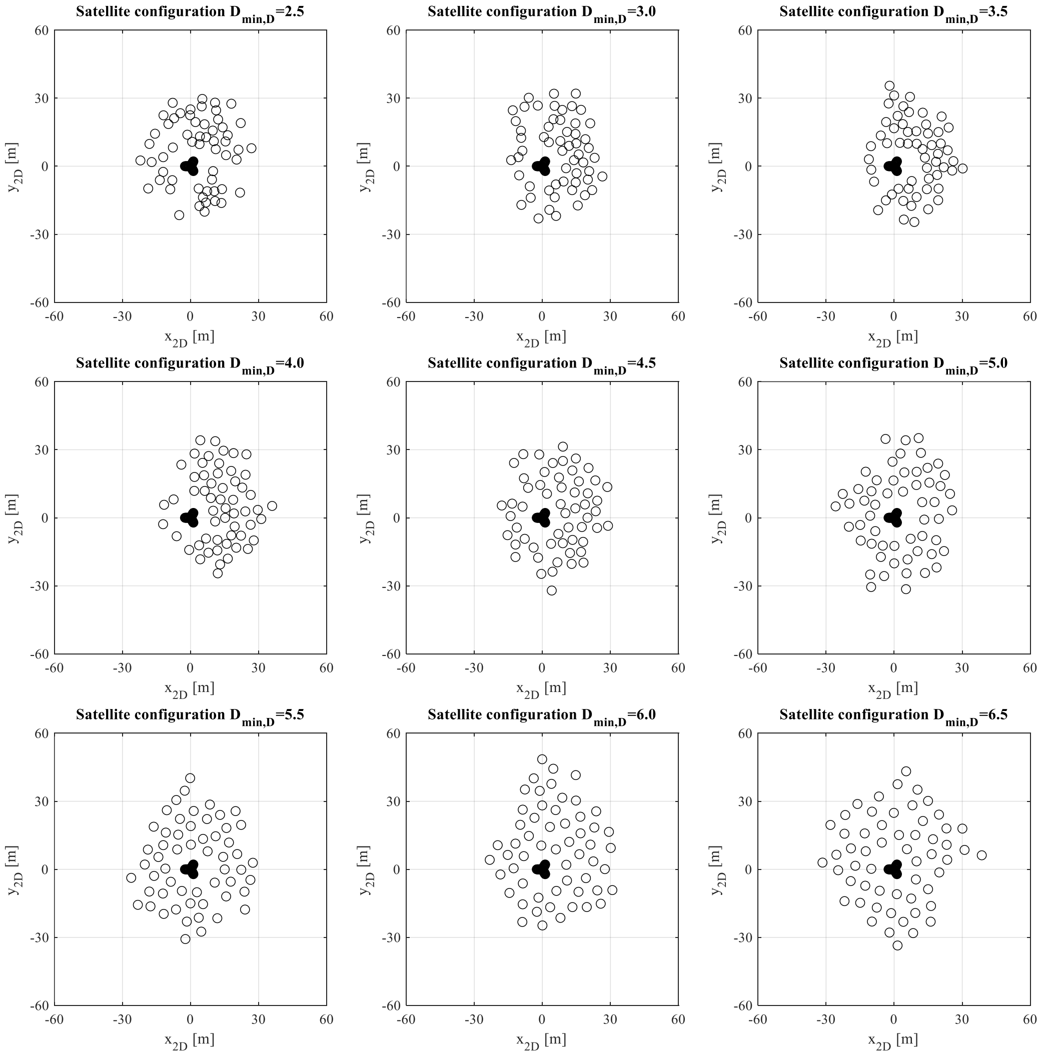

Figure 6-21 Illustration of the optimized deputy configuration for $N = 56$ deputies in the optimization coordinate system.

In general, a larger inter-deputy distance will inevitably lead to a more spread out configuration and thus a larger aperture. Plotting the radial distribution of the spatial frequency samples in the (u, v) plane (Figure 6-22) provides an indication on how the optimization algorithm optimizes the satellite system with varying numbers of deputy satellites. Independent of inter-deputy distance the optimization algorithm remains uncapable of filling the large gap in sample density at 20 to 50 signal wavelengths distance to the chief satellite. A less strict minimum inter-deputy distance (e.g., $D_{min,D} = 2\ m$) does however allow the simulator to recreate a profile that more closely resembles a Gaussian density profile. Large minimum inter-deputy satellite distances will thus lead to a less dense sampling in the (u_λ, v_λ) plane.

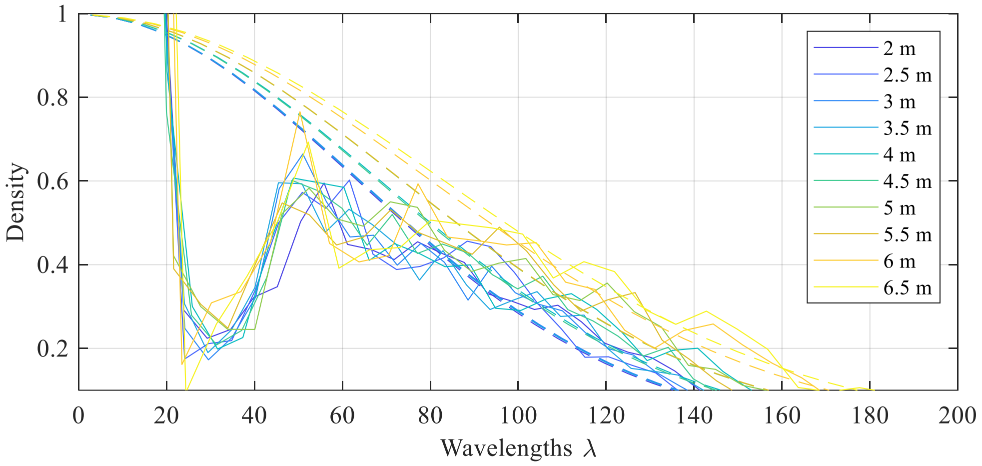

Figure 6-22 The solid lines denote the actual radial distribution of spatial frequency samples for the optimized configurations. The colors denote the number of satellites used in each configuration (blue for the configuration with $D_{min,D} = 2\ m$ and yellow for the configuration with $D_{min,D} = 6.5\ m$. The dashed lines denote a Gaussian distribution of equal standard deviations for each configuration.

In order the evaluate the impact of the inter-deputy distance on the system imaging performance, it is plotted against the radiometric sensitivity and ground resolution (Figure 6-23). Due to the larger array diameter with stricter minimum inter-deputy constraints, an improvement of the ground resolution to up to 5.5 km can be observed. Regarding the radiometric sensitivity, the image confirms the known relationship given in section 6.2.1 that the radiometric sensitivity and the ground resolution behave in an opposite way.

Interestingly, the simulations show that a decrease of minimum-satellite distance to 3.5 m seems to have little impact on the resolution or radiometric sensitivity of the optimized array system. Significant changes of the spatial resolution and the radiometric sensitivity can only be observed after the minimum inter-deputy distance is increased beyond $D_{min,D} = 3.5\ m$. A likely explanation for this phenomenon, is that the optimization algorithm is capable of finding configurations that are more evenly spread out on both sides of the chief satellite, as soon as the "protected" zone around the chief satellite becomes less important to the configuration with a larger minimum inter-deputy distance. The diameter of the array only significantly grows after the deputies can be positioned around the chief satellite, without leaving out short baselines. This effectively results in longer average baselines, as can be seen Figure 6-21. From Figure 6-23 it can also be observed that the decline in spatial resolution is irregular and rough. This can likely be attributed to the quality of the optimized array configurations, which varies slightly as part of the numerical optimization.

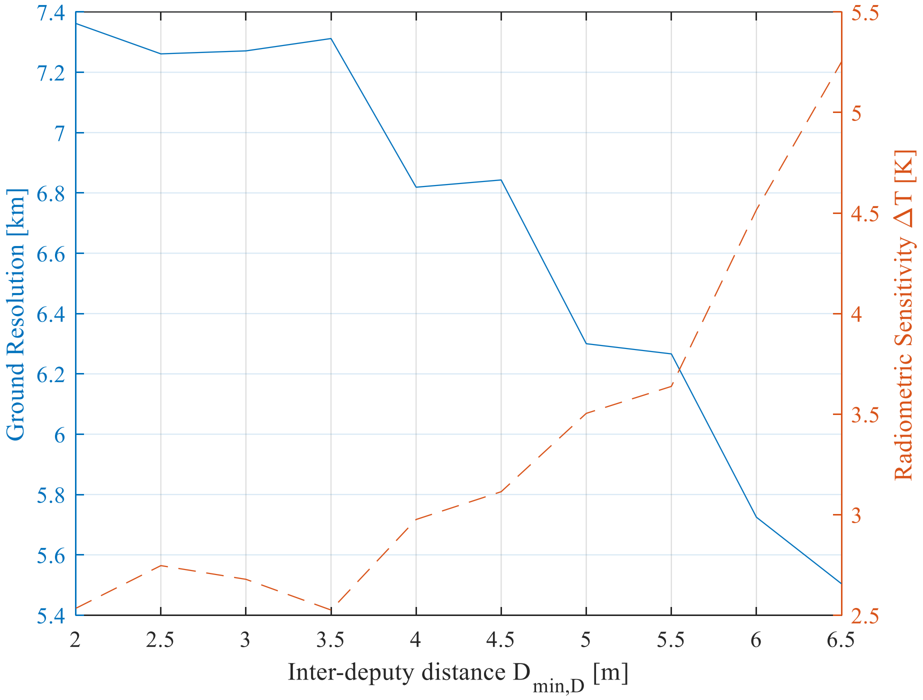

Figure 6-23 Resolution in km (solid line) and sensitivity in Kelvin (dashed line) for configurations with varying minimum inter-deputy distance constraints $D_{min,D}$ and $N = 56$ satellites.

The impact of the minimum inter-deputy distance on the configuration and the PSF can be seen in Figure 6-24. The figure shows that the deputies within the GCO plane are more regularly distributed with an increasing minimum inter-deputy distance. With an increasing $D_{min,D}$ the optimization algorithm is capable of placing the deputies around the chief satellite regularly because a homogenous distribution of baselines is achievable despite the center void space caused by the minimal distance of deputies to the chief satellite. While the configuration is similar for $D_{min,D} = 2\ m$ and $D_{min,D} = 4\ m$, the configuration for $D_{min,D} = 6.5\ m$ shows a circular distribution around the chief.

With larger inter-deputy distances the system is capable of covering a larger area of the spatial frequency. While this results in a tighter main beam (see PSF with $D_{min,D} = 6.5\ m$), it also yields slightly higher sidelobe levels.

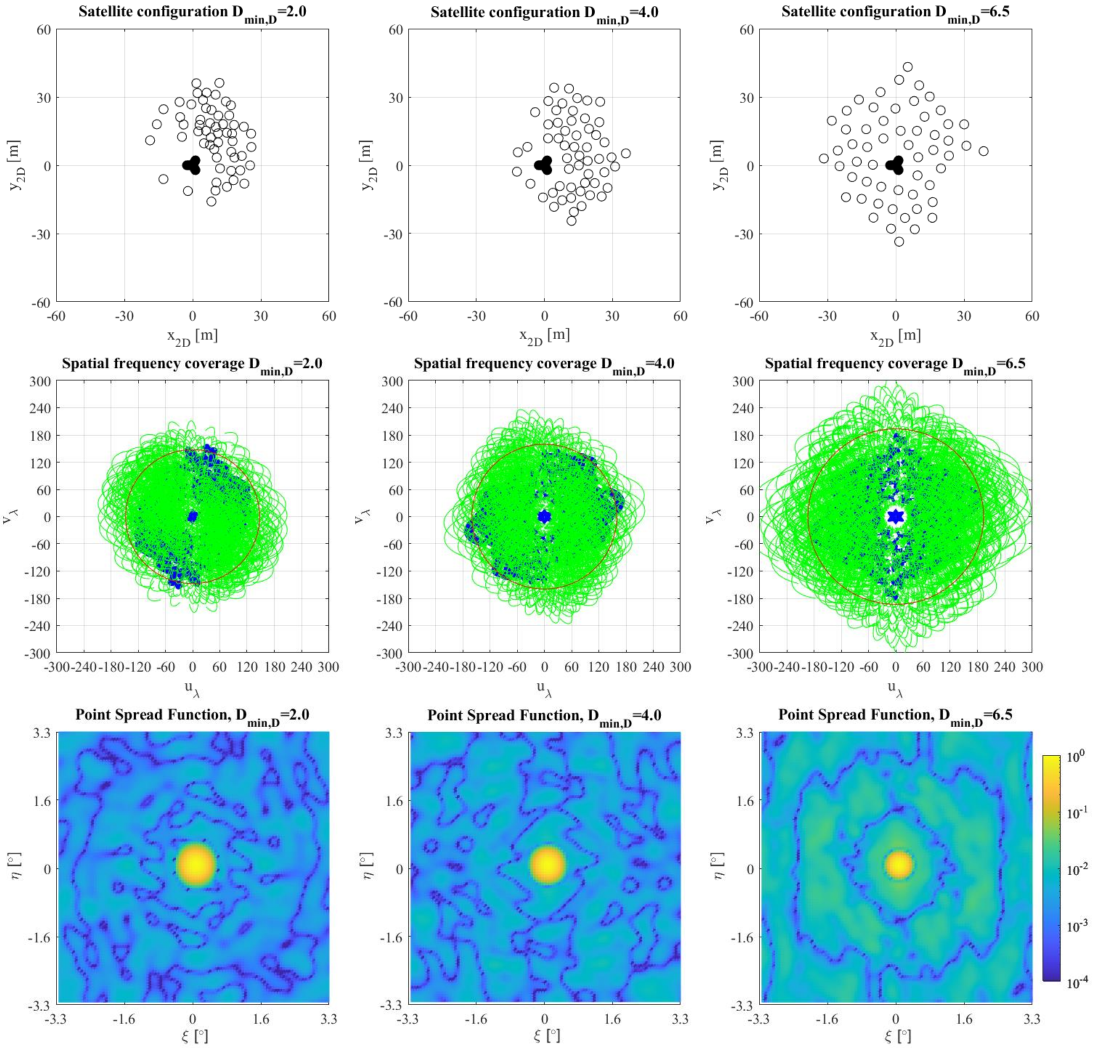

Figure 6-24 Illustration of an optimized deputy configuration (top row) under various minimum inter-deputy distance constraints, sampling of the spatial frequency domain (middle row) and the PSF (bottom row) for $D_{min,D} = 2\ m, 4\ m, 6.5\ m$ and $N = 56$ deputies. On the first row the configurations are shown in the optimization coordinate system. The second row shows the sampled spatial frequencies (blue: chief/deputy baselines, green: deputy/deputy baselines) in the (u_λ, v_λ) plane with the red circle denoting the distance ρ_{max}. Finally, the last row shows contour plots of the PSF respective arrays.

6.4.2 System implications

The constraints on the minimum distances between deputies not only impact the imaging performance but also the probability of collision between deputies. Figure 6-25 shows the relationship between the average probability of collision per orbit over all deputies with the inter-deputy distance (blue line) for the configuration of

$N = 56$ deputies. The average probability of collision decreases from $1.5 \cdot 10^{-2}$ per orbit for a minimum inter-deputy distance of $D_{min,D} = 2\,m$ to a probability of collision of $2.5 \cdot 10^{-6}$ per orbit for $D_{min,D} = 6.5\,m$. The maximum collision probability per orbit of any deputy (red dashed line) behaves largely analogous to the average collision probability. In general, the change of deputy collision probability is entirely due to the more closely packed deputies, as the position accuracy of the deputy orbit control systems stays approximately constant. The difference between maximum and average collision probabilities also grows slightly with a greater minimum inter-deputy distance, although this is likely not a systematic effect, but simply a result of the specific optimized configuration used within this analysis.

By comparing Figure 6-23 and Figure 6-25 with each other it becomes apparent that a significant reduction in collision probability can only be achieved by implementing stricter inter-deputy distance constraints, which in turn lead to higher spatial resolution but also a lower quality of array, i.e. sidelobe levels. While collision avoidance maneuvers as an addition to the regular orbit maintenance maneuvers for deputies are unavoidable, their frequency will determine the stability of the greater satellite swarm. More detailed analysis of the swarm orbit control will need to take place, to determine the exact value of the permissible collision probability. Charting the inter-deputy distance over the probability of collision per orbit, as seen in Figure 6-25 and comparing collision probabilities with the system imaging performance can however be key to making the trade-off between collision risk and system performance.

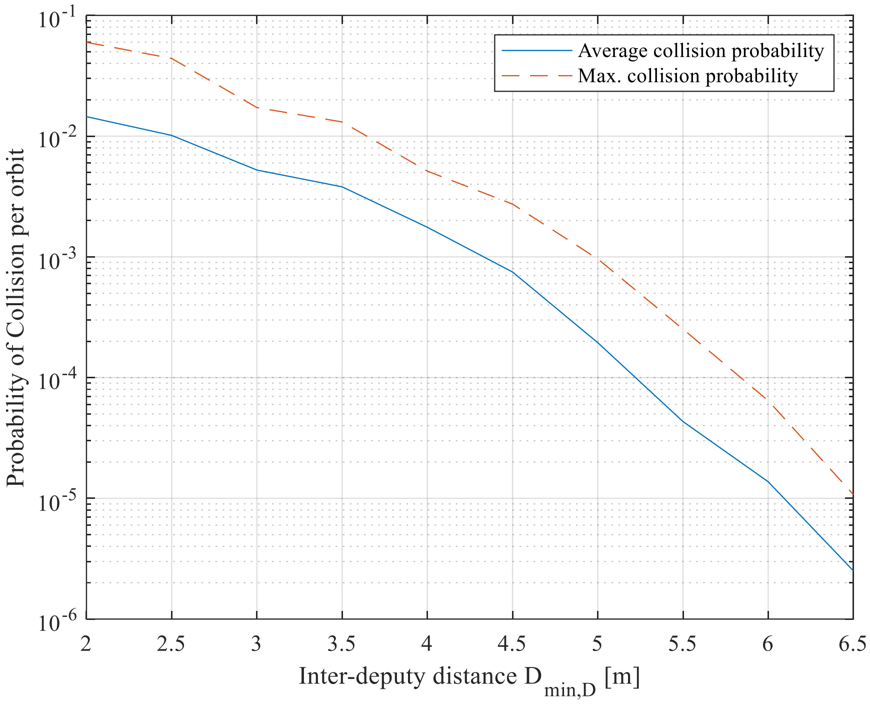

Figure 6-25 Average probability of collision per orbit over all deputies (blue line) and maximum probability of collision per orbit of any deputy (red dashed line) for the formation of $N = 56$ deputies with varying inter-deputy distances.

6.5 Case study: Impact of system orbit height

In the previous investigation the system orbit height was set to the orbit height of the SMOS system at 755 km. However, it is conceivable that a subsequent system could deviate from this, if trade-offs can be made between the revisit time and the spatial resolution. This section discusses the relationship between revisit time and system spatial resolution as well as the implications for the formation keeping.

6.5.1 Relationship between revisit time and system spatial resolution

STK was used for the investigation of the revisit time on satellite systems placed in various orbit heights. Figure 6-26 shows the relationship between the spatial ground resolution and the average revisit time. The swath width, that underlies the revisit time calculation has been determined by equation (5-12). Since the revisit time is calculated by discretizing the entire globe into finite areas and counting the number of observed areas within a timeframe, the unsteadiness in the revisit time curve is not physical but an attribute of the numerical calculation. Nevertheless, the evolution of the revisit time with increasing orbit height provides a good estimate of the interrelationship between both quantities. The asymptotic behavior of the revisit time can be attributed to the smaller percentual change in the swath width with increasing orbit height.

The revisit time is largely a function of the latitude, so the average revisit times are much shorter at the poles. While the spatial resolution of the system can reach 4.9 km for 500 km, the revisit time decreases to 2.1 days at the equator. This revisit time thus satisfies the 2-day requirement set for the vegetation optical thickness, sea ice and coastal areas sea surface salinity applications (see Table 1-2) for all heights except at 500 km. Since the swath width is only a function of the beamwidths of the individual ARU, the revisit time would remain the same also for configurations with a different number of deputies. Therefore, from a system perspective it seems like lower orbit heights would be beneficial, as they would entail an improvement in spatial resolution and a sufficient revisit time. Before considering an orbit height however, the impact of orbit height on the ability of the deputy control systems to keep a stable formation must be analyzed.

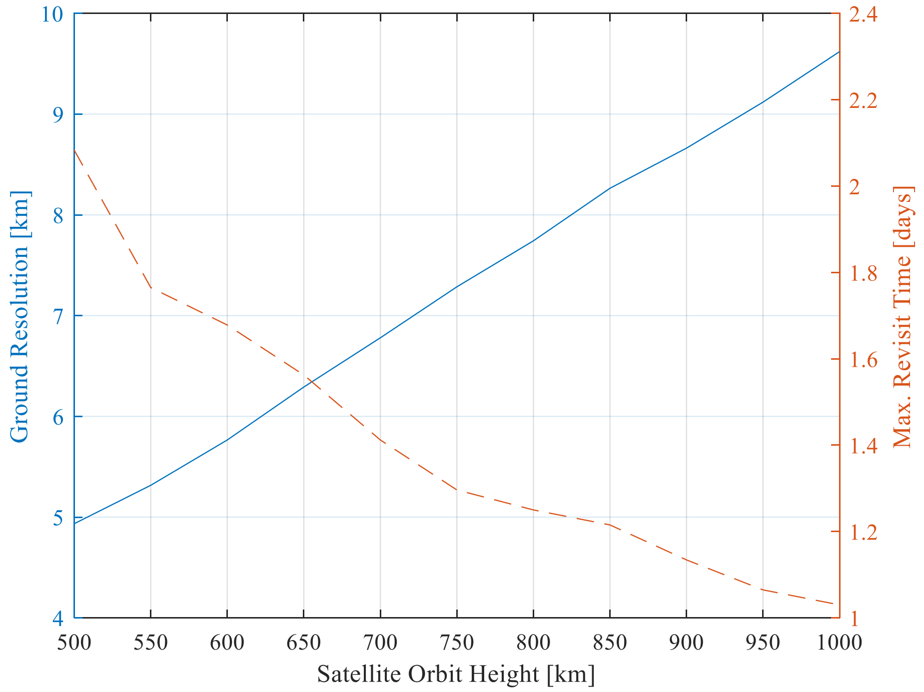

Figure 6-26 Resolution in km (solid line) and the revisit time in days (dashed line) for configurations in varying orbit height and $N = 56$ satellites.

6.5.2 Orbit height implications on swarm control

As mentioned previously, the dissimilarity between the deputy and the chief satellites leads to differences in ballistic coefficients. Due to these differences, the swarm-based synthetic aperture radiometer will be subject to differential aerodynamic forces. Ultimately the deputy orbit control system will need to compensate the differential accelerations together with the forces from differential J_2 perturbations. Since the orbit height strongly influences the atmospheric density that the system is subject to, an orbit height must be chosen that represents a trade-off between the spatial resolution and the stability and lifetime of the system.

Figure 6-27 shows the influence of the system orbit height on the position accuracy of the deputy orbit control in relationship to the difference in ballistic coefficients between deputy and chief satellite. The red curve represents the relationship, assuming a difference in ballistic coefficient of $\Delta B_C = 1.99 \cdot 10^{-2}$. This value was derived directly from the satellite masses, the effective satellite aerodynamic areas and coefficients given in Table 6-3. The other curves in Figure 6-27 represent the position accuracy when differences in ballistic coefficients ΔB_C are 1.5 (blue) or 0.05 (yellow) multiples of the value used for the reference simulation (red).

The position accuracy attainable by the orbit control system improves with an increase in orbit height because of the diminishing effects of the residual atmosphere and differential J_2 perturbations. Above the altitude of 650 km, the differences in ballistic coefficient seem to have no effect on the attainable position accuracy. At these altitudes, the atmospheric density is so low that differences in the satellite mass, the satellite area or the aerodynamic coefficients do not affect the relative satellite trajectory significantly if periodic corrections are performed for formation keeping. In this case the displacements due to atmospheric effects are just compensated by the routine formation keeping maneuvers every 15 min. If a small ΔB_C is assumed, then the linear relationship between position accuracy and orbit height is continued even below 650 km. This is logical, since the linear relationship is determined by the decreasing influence of the J_2 perturbations.

In contrast to the linear increase of the orbit control position accuracy for orbit heights above 650 km, the control position accuracy decreases exponentially below the orbit height of 650 km. The decrease of position accuracy below an orbit height of 650 km is exacerbated by an increase in the difference of the ballistic coefficients.

For a large difference in ballistic coefficients ($1.5 \cdot \Delta B_C$) the position accuracy is almost doubled from its value at an orbit height of 750 km.

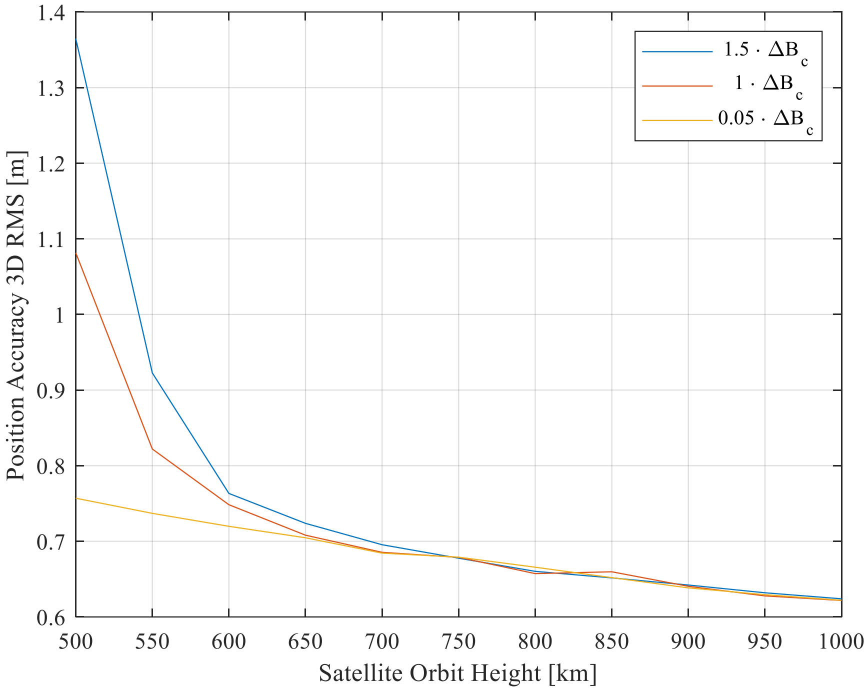

Figure 6-27 Average position accuracy for the formation of $N = 56$ deputies with varying orbit height and difference in ballistic coefficient between deputies and the chief satellite.

The attainable position accuracy of the deputy orbital control system has an impact on the probability of collision between deputies (see Figure 6-28). Along with the degradation of orbit control accuracy, the largest probability of collision rises to almost 4.5 % per orbit for low orbit heights and large differences in ballistic coefficients. For systems placed in an orbit above 650 km, the probability of collision rises mostly linearly with an increase of orbit height in accordance with the linear relationship of the position accuracy.

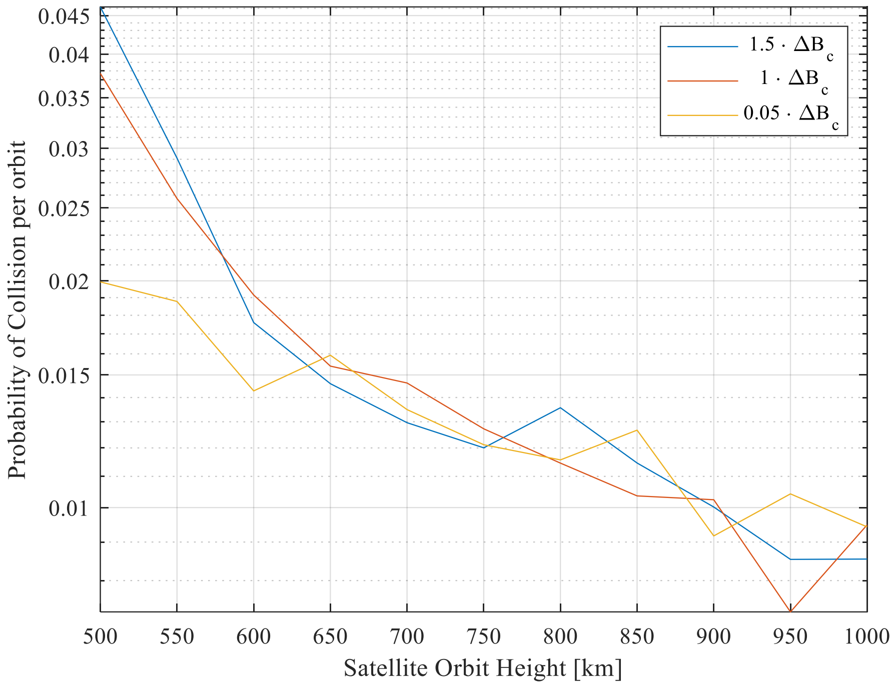

Figure 6-28 Highest probability of collision per orbit over all deputies for the formation of $N = 56$ deputies with varying orbit height and difference in ballistic coefficient between deputies and the chief satellite.

The fuel consumption per orbit and deputy as a function of system orbit height and difference in ballistic coefficient is shown in Figure 6-29. Analogous to the evolution of the position accuracy, the fuel consumption rises with decreasing system altitudes because of the increased orbital perturbations from Earth oblateness and aerodynamic forces. Differences in ballistic coefficients between chief and deputy satellites will especially impact the performance of the deputy orbital control system under an altitude of 650 km. The slight differences in fuel consumption for systems in orbit heights above 650 km can be attributed again to a degree of randomness in the generation of the optimized system configuration and the numerical simulation.

The impact of the increased fuel consumption in different orbit heights on the system lifetime is given in Table 6-8. Assuming classical cold-gas propulsion systems, the system lifetime stays under 180 days. While this seems short, it is based on a conservative assumption of 40 s of specific impulse. It is likely, improved propulsion systems with specific impulses over 100 s [94] may extend the lifetime of the system in the future. The small differences in lifetimes for systems placed in orbits above 750 km can be disregarded as a relic of the random nature of the modelled disturbances. For systems placed in orbits below 750 km a divergence of the fuel consumption can be observed for systems with different differential ballistic coefficients. At these orbit heights differential aerodynamic drag causes a noticeable increase of the fuel consumption.

Table 6-8 System lifetime [days] for different orbit heights [km] and differences in ballistic coefficients.

Orbit alt.	*500*	*550*	*600*	*650*	*700*	*750*	*800*	*850*	*900*	*950*	*1000*
$0.05 \cdot \Delta B_c$	*128.5*	*140.2*	*147.0*	*150.3*	*155.3*	*157.6*	*161.2*	*164.2*	*169.1*	*173.2*	*176.6*
$1 \cdot \Delta B_c$	*133.1*	*140.1*	*147.6*	*151.9*	*154.7*	*157.9*	*162.6*	*167.1*	*169.1*	*173.1*	*176.3*
$1.5 \cdot \Delta B_c$	*140.2*	*143.1*	*148.2*	*150.9*	*153.4*	*158.6*	*164.2*	*164.2*	*168.7*	*172.7*	*176.2*

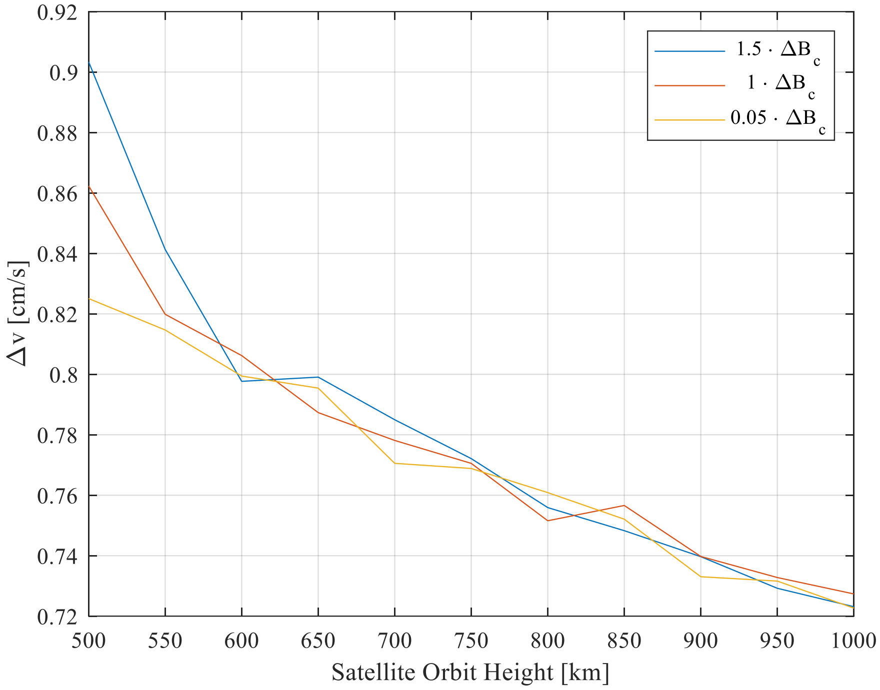

Figure 6-29 Average fuel consumption per orbit and deputy for the formation of $N = 56$ deputies with varying orbit height and difference in ballistic coefficient between deputies and the chief satellite.

Besides having an influence on the deputy orbital control system, the orbit height influences the need for periodic orbital raising of the system in order to prevent a drift of the ground track over time. Though this aspect has to be considered when selecting an orbit height for the satellite swarm-based aperture synthesis radiometer. Figure 6-30 shows the required frequency of semimajor-axis adjustments T_s as a relationship of the system orbit height and the difference in satellite ballistic coefficients. The results in the figure assume a semimajor axis orbital adjustment of $\Delta a_{GT} = 8\ m$ within a single orbit. T_s rises from every 4.8 hours for an orbit height of 500 km to 113 days for an orbit height of 1000 km. Since time required for orbit adjustment will not be available for science measurements it is important to maximize the time between necessary adjustments. A reasonable requirement could be minimizing the number of orbits used for orbital adjustments of the system to less than 1 % of total orbits. In this case the frequency of orbital adjustments should not exceed 7.28 days. Assuming the difference in ballistic coefficients is equal to the difference assumed in section 6.1, i.e. $1 \cdot \Delta B_C$, this would mean that the system would need to be placed in an altitude above 730 km.

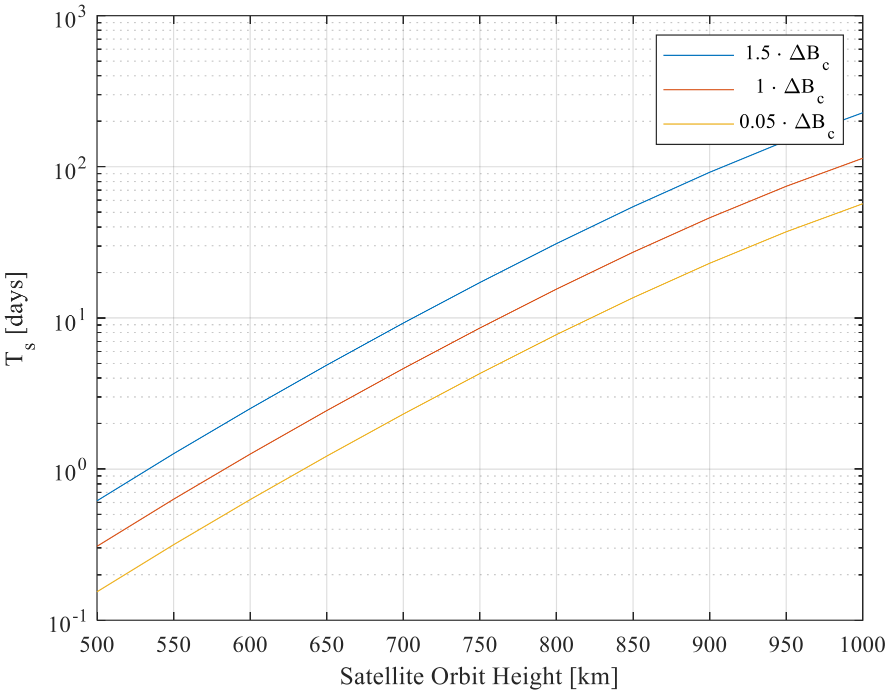

Figure 6-30 Time between semimajor-axis adjustments T_s with varying orbit height and difference in ballistic coefficient between deputies and the chief satellite for a $\Delta a_{GT} = 8\,m$ semimajor axis orbital adjustment.

The orbit height influences the system spatial resolution, the revisit time, the system lifetime, the stability of the satellite swarm and the time that needs to be allocated for the period orbit corrections of the system. In general, it is beneficial to choose an orbit height that is as low as possible, as long as the requirements concerning the other system aspects can be met. From the given simulations it can also be concluded that the differences in ballistic coefficients play a secondary role for system orbit heights above 750 km. In these heights the aerodynamic drag is very low and the differential drag between chief and deputy satellites has no impact on orbit control performance. To decrease the uncertainty involved with the determination of the differential aerodynamic drag (which is dependent on parameters, e.g., the orientation of the two satellites, that are difficult to determine precisely) it seems beneficial to use an orbit height of 750 km as a lower limit for system orbit height.

6.6 Satellite-swarm orbit design method

The previous sections shed light on the influences of different design decisions on the performance and feasibility of the system. In this section a general design methodology is discussed for the design of the satellite swarm-based aperture synthesis radiometer system based on the previous analyses.

The objective of the orbit design is to specify key design parameters in a way that respects both the system imaging requirements and the limitations set by the orbital control hardware specifications. The four key design parameters are:

- Control period, T_{pwm}
- System orbit height, H_0
- Number of deputies in formation, N
- Minimum inter-deputy distance constraints, $D_{min,D}$

These parameters all strongly influence the performance and feasibility of the system and have to be determined in an iterative approach. The proposed approach is based on sequentially finding the relationships between the key design parameters, the required orbit control system specifications, and the overall system imaging performance.

A schematic of the proposed approach is displayed in Figure 6-31. As a prerequisite, the system requirements have to be defined, which include imaging requirements (i.e., spatial ground resolution, sidelobe level or MBE and radiometric sensitivity) that are derived from the intended application and requirements regarding the system lifetime, collision risk and the percentage of total operation time that can be allocated to system orbit maintenance (i.e., the time used for formation maintenance and control of system orbit height). Additionally, initial conditions must be determined that serve as a basis for performing simulations that can be used to give insight into the influence of the key design parameters. In particular, initial conditions must be defined for the orbit height, the number of deputies in the formation and the minimum inter-deputy distance constraints. The initial conditions should lie within the center of the parameter space, e.g. for orbit height an initial assumption of 875 km could be used since it lies between the lower limit for satellites of 750 km and a reasonable upper limit of 1000 km. Together with the definition of the spacecraft and payload parameters (see Table 6-2 and Table 6-3), these initial assumptions are then used to analyze the influence of each key parameter separately.

After defining the spacecraft and payload parameters and the initial conditions for the key design parameters, the first step should be to specify the control period. While a shorter deputy control period leads to smaller orbital deviations from the reference orbit and a lower fuel consumption, it also shortens the time that can be used for the primary science operation. Therefore, it is advisable to choose a control period that is as long as possible while adhering to the requirements for the system lifetime and the collision risk.

After specifying the orbit control period, the impact of the orbit height can be analyzed as shown in section 6.5. From the perspective of imaging performance, a low orbit height will yield a better spatial resolution. On the other hand, a lower system height will increase the influence of differential drag and J_2 perturbations on the performance of the deputy orbit control system and increase the frequency or magnitude of the required system orbit correction. A minimum orbit height can be defined directly from the time that can be attributed to the periodic raising of the system orbit and the capability of the deputy GNC system to follow the chief during those maneuvers. While more frequent system orbit maintenance means a smaller necessary change in semimajor axis and thus less stringent requirements on the deputy GNC, it requires time that cannot be used for science operation. After defining a minimum permissible orbit height, a trade-off needs to be made between imaging performance and the collision risk. While a lower orbit height will provide a better spatial resolution, it entails a lower deputy position accuracy and a higher fuel consumption. As long as the collision risk is manageable it is advisable to choose an orbit height along the lower limit.

The primary influence on the system imaging performance is the number of deputies. A larger number of deputies will enable a higher spatial resolution, but entail a lower radiometric sensitivity. Thus, the number of deputy satellites is directly dependent on the system imaging requirements which is specific to the envisioned science application. Other system requirements, such as chief satellite size, mass, data storage and processing capacity can also provide upper limits to the feasible number of deputies. The third step in the design process should therefore be the generation of multiple system configurations, containing different numbers of deputies. These simulations shed light on the relationship between the number of deputies and the spatial resolution, the attainable MBE and radiometric sensitivity. A reasonable initial value should be chosen for the inter-deputy distance constraint.

Having chosen a control period, a system orbit height and a number of deputies, the final step involves the definition of the minimum inter-deputy distance constraints. By increasing the inter-deputy distance constraints, it is possible to increase the spatial resolution of the system and decrease the risk of collision between deputies. The drawback, however, will lie in a decrease of the radiometric sensitivity of the system and a lower MBE (higher MSLL). Changing the inter-deputy distance constraints (see section 5.5) can be used to tweak the system configuration to the system imaging requirements or to ensure the distances between the deputies are manageable.

After specifying an inter-deputy distance, the first iteration is complete. The resulting configuration can then be compared with the system requirements and the capabilities of the deputy GNC system. If the collision risk between deputies is too high, individual deputies can be repositioned to lower the collision risk between critical pairs. In case the system requirements are not met at the end of the iteration, previous design decisions can be revisited by updating models and redoing the previous steps.

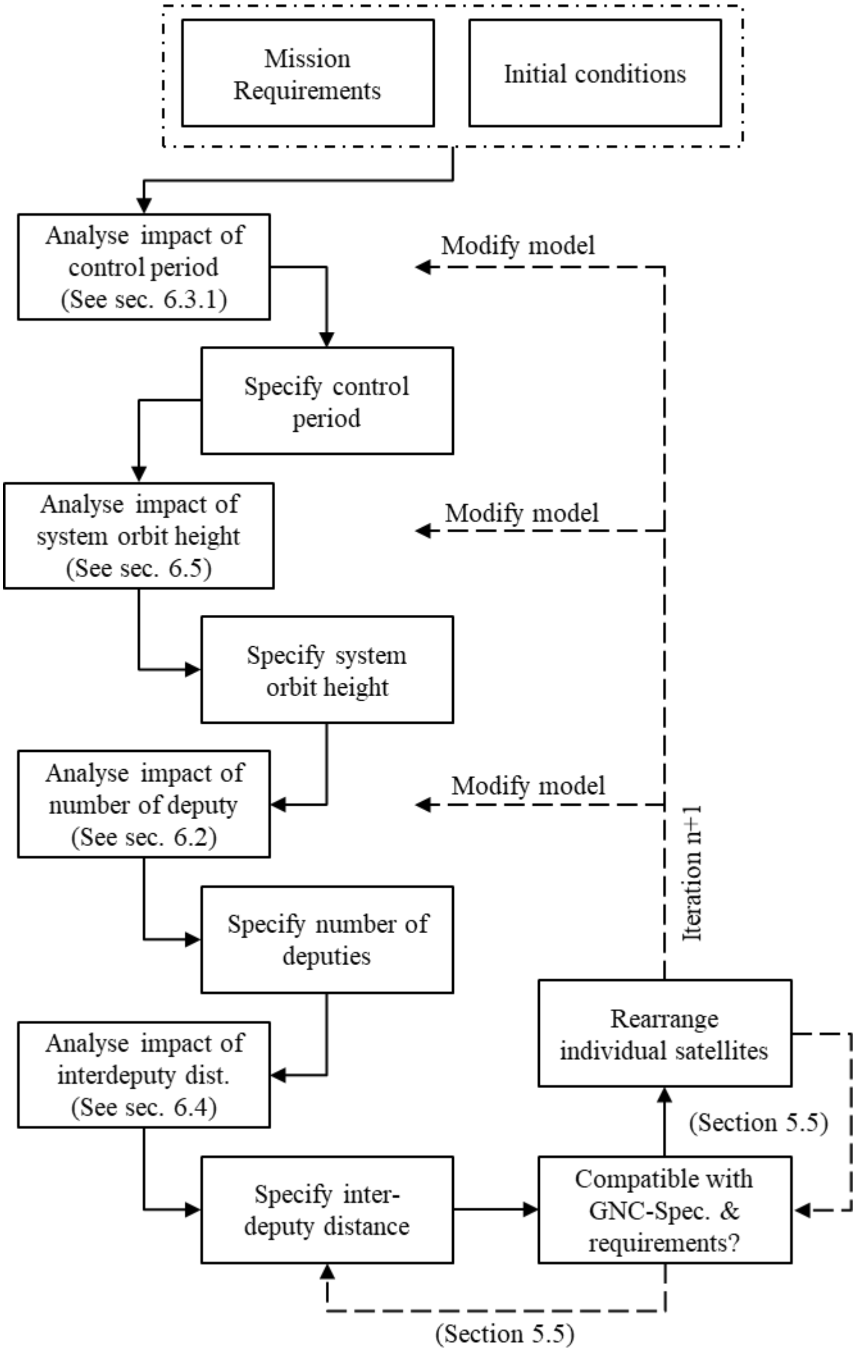

Figure 6-31 Process diagram for the design method for the orbits of the satellite swarm-based aperture synthesis radiometer.

7 SUMMARY, DISCUSSIONS & OUTLOOK

7.1 Summary

In this thesis, the imaging performance and orbit mechanics were explored for the definition and development of an Earth-observing satellite-swarm-based radiometer mission scenario. A design and simulation tool, the Satellite Swarm-Based Synthetic Aperture Radiometer (SSBSAR) software package, was developed for the design of such a system and demonstrated by simulating configurations with varying numbers of deputy satellites, orbit controller settings, inter-satellite distances and orbit heights. Simulation results show that the placement of deputy satellites on GCO in optimized formations around the chief satellite enable the creation of an aperture synthesis antenna array capable of reaching main beam efficiencies that approach, albeit not reach, the efficiencies of sensors based on established monolithic space-based arrays, like ESA's SMOS sensor. It was shown that angular resolutions θ_w can reach 0.27 degrees (4 km) for configurations with 96 deputies. This represents an approximate ninefold improvement over the spatial resolution reported for the SMOS instrument [3]. While radiometric sensitivities of the simulated configurations do not reach the values of previous systems, e.g., SMOS with 0.33 Kelvin, sensitivities could be sufficient to add value to science applications. Especially the configurations with 56 deputies seem to represent a good trade-off between spatial (7.5 km) and radiometric resolution (2.53 K). This approaches the requirements set for soil moisture monitoring and sea surface salinity at coastal areas [4].

Simulations show that state-of-the-art nanosatellite orbit control systems are capable of positioning satellites on close-proximity GCO orbits with a relative position accuracy below 1 m RMS. The largest collision risk for any satellite placed in reference positions not closer than 3.5 meters to each other, does not exceed $1.5 \cdot 10^{-2}$ per orbit for the optimized configurations. The given concept will thus still require periodic orbital collision avoidance maneuvers. These will be rather infrequent in comparison with the regular orbit maintenance maneuvers and will not have a strong impact on the fuel budget (<5%). Relative velocities between deputies are in the order of a few cm/s. Nevertheless, the implementation of a capable swarm control concept represents one major challenge to be addressed for the realization of the proposed concept.

Furthermore, it was shown that fuel consumption for deputies on GCO stays below 0.9 cm/s per orbit. Assuming state-of-the-art cold gas propulsion systems the lifetime of the system could be up to 156 days. With the utilization of next generation MEMS-based propulsion, e.g. water micro-resistojets [94], it is plausible the lifetime can be extended to significantly longer durations with specific impulses in the order of 100 s. which will be needed for Earth observation missions including missions focused on larger-period (multi-year) hydrologic and climatologic phenomena.

Investigations of the impact of system orbit height uncovered the sensitivity to differences in deputy/chief ballistic coefficients below orbit heights of 750 km. For large differences in ballistic coefficients, a strong increase in fuel consumption and a significant decrease in position accuracy can be observed below 750 km. The frequency of necessary semi-major-axis adjustments to the system is also strongly impacted by its orbit height. Assuming the necessary impulsive semimajor axis orbital adjustments should not exceed 8 m, the time between orbit adjustments rises from 7.28 days at an altitude of 730 km to 113 days at an orbit altitude of 1000 km.

In summary, the innovative contributions of this thesis are:

1. The proposal of a satellite swarm-based synthetic aperture radiometer concept for the improvement of the spatial resolution of Earth observing radiometers.
2. The confirmation that a satellite swarm-based synthetic aperture radiometer based on large numbers of satellites is feasible in LEO from an orbit

mechanical perspective considering both constraints, from orbit mechanics, satellite orbit control and relevant array performance parameters.

3. The development of an iterative design method for the requirement-driven design of a satellite swarm-based synthetic aperture radiometer. This includes the optimization of the satellite swarm-based synthetic aperture radiometer design in terms of user requirements, relative orbits, number of deputies, radiometric sensitivity, spatial resolution, collision risk and fuel consumption.
4. Investigation of the impact of important system parameters, e.g., orbit height, satellite number and satellite density on system performance.

7.2 Discussion of selected critical system aspects

7.2.1 Antenna phase center position determination

While relative navigation is critical to the operation of large satellite swarms, it also provides position knowledge that is critical to the correct processing of the science data. In order to ensure measurements can be attributed to the correct spatial frequencies the phase centers of the ARU antennas must be known with very high accuracy. A lack of ARU position knowledge is a significant source of error for the determination of the PSF. Errors in the PSF will in turn result in errors in the measured radiometric distribution. For example, the RMS of the antenna phase center positioning error is estimated to be around 0.6 mm at the center measurement frequency of 1.4 GHz for a 1° maximum phase error. To ensure a reasonable radiometric accuracy for soil moisture retrieval, the positions of the ARU phase centers must be known to millimeter-level accuracy [48]. Current GNC positioning solutions for CubeSats are not capable of delivering this accuracy. It is conceivable a pulse-based proximity navigation system might be capable of delivering the required position knowledge [60]. This navigation system could possibly be based on the required inter-satellite communication infrastructure.

7.2.2 Data handling

An interferometric radiometer performing measurements using the MISAR technique will generate large amounts of data. This data needs to be quantized within the ARU unit, transferred to the main processing unit on the chief satellite (by inter-satellite link in case it is recorded by a deputy ARU), processed and transmitted to the facility on the ground.

For a dual-channel instrument, the number of visibility samples during overflight can be determined by

$$N_S = \frac{t_{obs}}{t_S} \cdot N_B \cdot 4 \tag{7-1}$$

Assuming a satellite swarm of 56 deputies, each carrying a single ARU and a chief satellite with a central array of 39 ARU, the number of total receivers would be 95. This would yield a total of $N_B = 4465$ baselines. The sample integration time t_S must be chosen to ensure that the relative movements between deputies do not exceed the permissible position accuracy during measurement. Assuming a permissible maximum measurement phase error of 1° and a maximum inter-deputy distance of 50 m (resulting in approx. 5.25 cm/s of relative velocity), a sample integration time of $t_S = 10\ ms$ would be sufficient to ensure measurements can be performed without a relative displacement of 0.6 mm.

In combination with the system orbit described in Table 6-1 and the payload parameters in Table 6-2, a total number of $176.8 \cdot 10^6$ visibility samples would be obtained within an overflight of an observation region L_x, lasting $t_{obs} = 99$ s. If a 10-bit quantization was used a total data volume generated by one observation region would amount to 1.77 Gbit of data. If the system was to continuously observe the Earth for a complete orbit, the total amount of data would generate a total of 106.9 Gbit of data. This is a moderately large amount of data, considering the data storage capacity of state-of-the-art Earth observation satellites lies in the order of a few Tbit (e.g., 3.2 Tbit for the Worldview-4 launched in 2016). Considering the ongoing development of more capable storage technologies however it seems very likely that these data volumes can be accommodated.

The raw measurements can either be correlated and processed on-board or transmitted to ground unprocessed. In light of the high raw data rate (21.3 Gbit/s) that is generated by the measurements alone the latter option seems unfeasible even with future optical data links. Therefore, the only realistic option is the cross-correlation of data on-board the satellite. This however would require high-performance correlator units that are capable of correlating the in-phase and quadrature data streams. The correlated data of the satellite swarm-based aperture synthesis radiometer would amount to 1.54 Tbit per day. This data would need to be downlinked by a data downlink system. While this data volume is demanding for today's optical communication systems, it is very plausible future X-band, Ka-band systems or optical data downlinks could handle the challenge. For example, with a 1 Gbit/s downlink system and a ground station network of 3 stations, at Kiruna, Inuvik and O' Higgins, the study by Henninger et al. [95] found that a total data volume of 24.5 Tbit a day could be downloaded. Thus, it is very reasonable a common X-band with a throughput of 520 Mbit/s [96], such as the one used on Sentinel-1 could easily handle the amount of data involved.

A distributed interferometric radiometer that is composed of spatially distant receiver units must transfer the individual ARU measurement via inter-satellite links to the chief satellite for processing. Camps et al. [34] briefly discussed the estimation of the data volume for a MISAR. Assuming a precision of 1% is sufficient for the measurements of the signal amplitude, sampling can take place with a resolution of $\Delta t = 1/(4 \cdot B)$ [97]. This would yield a sampling period of 36 ns for the bandwidth of 7 MHz, assumed for the system investigated within this thesis. For a 2x2 bit quantization and a dual channel instrument, the data rate per second generated by an individual deputy can then be calculated by

$$R_D = \frac{1}{\Delta t} \cdot 2 \cdot 2 \cdot 2 \tag{7-2}$$

This is because the number of samples per second is multiplied by two because both I and Q are sampled for two channels with a four-level, i.e., two-bit, quantization method. Each ARU on a deputy satellite generates a 224 Mbit/s data stream during measurement. CubeSat X-band transmitters are likely capable of coping with data rates of up to 1 Gbit/s [98]. However, for higher number of CubeSats an X-band system would be insufficient to accommodate all CubeSats in an FDMA approach. It is likely communication systems operating in higher frequency bands such as Ka-band would need to be used.

7.2.3 Instrument synchronization

Accurately measuring the signal phases will require a synchronization accuracy in the order of magnitude of 2 ps (assuming a 1° permissible phase error) over a single measurement sampling time of 10 ms. The short measurement period ensures signal phases can be measured with the required phase error of 1°. Space-qualified Oven-Controlled Crystal Oscillators (OCXO) with Allan variances in the order of $\sigma_{\mathrm{y}} = 10^{-12}$ [99], [100], [101] are capable of delivering the required short-term stability. These would be placed on individual satellites. A two-way microwave Phase-Locked Loop (PLL) could keep OCXO oscillators on deputies synchronized with the master oscillator on the chief once calibrated [102]. The practical implementation of this synchronization scheme on a CubeSat swarm has not been performed so far.

7.3 Outlook

The thesis shows the basic feasibility of a swarm-based aperture synthesis radiometer with one chief and many deputies from an orbit mechanical perspective. Further research must be conducted on other issues surrounding the implementation of such a system. These aspects include a deeper investigation of

- In-depth quantitative analysis of the impact of error sources: The current thesis, investigates an ideal system. A further in-depth study of the impact of error sources on the radiometric performance must be carried out. In particular these refer to investigations of antenna errors, (e.g. antenna position errors, antenna pattern phase and gain ripples, antenna pointing errors, errors in the antenna coupling and the cross polarization), channel errors and baseline errors [48].
- The MBE for the swarm-based aperture synthesis radiometer still stays below those of monolithic arrays. Further techniques should be explored that enable an improvement of the MBE.
- Timing synchronization errors: Accurately measuring the signal phases will require a synchronization accuracy in the order of magnitude of two ps. The application of high-accuracy PLL to a CubeSat swarm needs to be studied in detail.
- Deputy deployment: Research is required on the sequence of deployment, the design of the dispenser module and requirements for chief attitude control.

- Inter-satellite links: Close proximity, high bandwidth communication systems need more research to enable low-power solutions for CubeSats [103].
- Implementation of satellite swarm control algorithms: The control of large amounts of spacecraft presents its own challenge. Algorithms must be investigated that allow operation with minimal risk.
- Risk-reduction for contingency events: A strategy needs to be developed to ensure defunct deputies are safely removed from the swarm without endangering any other satellites. A slight reorientation of the deputy relative orbital planes to achieve a degree of cross-track separation could enable the removal of defunct deputies by aerodynamic drag. While this would also cause the relative orbits to become elliptical, it is likely a trade-off can be reached between safety concerns and imaging performance.

Even though this thesis showed that swarm-based systems can improve the spatial resolution of space-based radiometers, it also showed their inherently reduced radiometric sensitivity and MBE. It is therefore unlikely, that such systems could be used for applications which demand high radiometric sensitivities, such as open sea surface salinity. Nevertheless, with further progress in proximity positioning systems, CubeSat propulsion, satellite-swarm control, and miniaturization of spacecraft electronics, it is reasonable to believe a swarm-based aperture synthesis radiometer could be a feasible way of improving and enabling applications that do not demand a high radiometric sensitivity. However, future studies must also specifically focus on how to further improve the MBE of swarm-based aperture synthesis radiometers to enable its use in Earth science.

8 REFERENCES

[1] C. Parkinson, "Satellite Passive-Microwave Measurements of Sea Ice," in *Encyclopedia of Ocean Sciences (Second Edition)*, Elsevier, 2008, pp. 80-90.

[2] K. McMullan, M. Brown, M. Martin-Neira, W. Rits, J. Ekholm, J. Marti and L. J., "SMOS: The Payload," *IEEE Transactions on Geoscience and Remote Sensing,* vol. 46, no. 3, pp. 594 - 605, March 2008.

[3] European Space Agency, "SMOS Data Products Brochure," November 2017.

[4] CESBIO, "SMOS-Next: User's Group Meeting," Toulouse, 2014.

[5] L. Hall, "SpiderFab," NASA, 7 August 2017. [Online]. Available: https://www.nasa.gov/content/spiderfab. [Accessed 13 August 2020].

[6] N. Rodriguez-Fernandez, Kerr, Y. and E. Anterrieu, "A Follow-up for the Soil Moisture and Ocean Salinity Mission," EGU General Assembly 2021, 19-30 April 2021. [Online]. Available: https://meetingorganizer.copernicus.org/EGU21/EGU21-4796.html. [Accessed 27 September 2021].

[7] A. Maghraby, A. Grubisic, C. Colombo and A. Tatnall, "A Novel Interferometric Microwave Radiometer Concept Using Satellite Formation Flight for Geostationary Atmospheric Sounding," *IEEE Transactions on Geoscience and Remote Sensing Vol. 56,* pp. 3487-3498, June 2018.

[8] F. Hadaegh, C. S.-J. Chung and H. Manohara, "On Development of 100-Gram-Class Spacecraft for Swarm Applications," *IEEE Systems Journal,* vol. 10, no. 2, pp. 673-684, 26 March 2016.

[9] B. Schwarz, "Coastal Salinity Measurement Using a Doppler Radiometer," *Advances in Space Research,* vol. 50, no. 8, pp. 1138-1149, 6 February October 2012.

[10] S. Mecklenburg, "ESA's Soil Moisture and Ocean Salinity Mission: From Science to Operational Applications Users," *Remote Sensing of Environment,* vol. 180, pp. 3-18, July 2016.

[11] J. Wigneron, A. Chanzy, P. Waldteufel and O. Marloie, "Retrieval Capabilities of L-Band 2D Interferometric Radiometry Over Land Surfaces (SMOS Mission)," VSP, Netherlands, January 2000.

[12] D. Entekhabi, "The Soil Moisture Active Passive (SMAP) Mission," *Proceedings of the IEEE,* vol. 98.5, no. 5, pp. 704-716, May 2010.

[13] J. Arnold, "Nasa Earth Science Office," NASA, 30 December 1999. [Online]. Available: https://weather.msfc.nasa.gov/landprocess/. [Accessed 30 August 2020].

[14] F. Ulaby, Microwave Radar and Radiometric Remote Sensing, Ann Arbor: The Unversity of Michigan Press, 2014.

[15] L. Keafer and R. Harrington, "Radiometer Requirements for Earth-Observation Systems Using Large Space Antennas," NASA Reference Publication 1101, Langley Research Center, 1983.

[16] C. Pațilea, "Sea ice Thickness Retrieval Using Microwave Satellite Observations From SMAP and SMOS," Meereisportal, 12 April 2019. [Online]. Available: https://www.meereisportal.de/en/archive/2019-kurzmeldungen-gesamttexte/sea-ice-thickness-retrieval-using-microwave-satellite-observations-from-smap-and-smos/. [Accessed 11 12 2020].

[17] L. Kaleschke, M. N., H. C., Hendricks, H. G. and T. R., "A Sea-ice Thickness Retrieval Model for 1.4 GHz Radiometry and Application to Airborne

Measurements Over Low Salinity Sea-ice," *The Cryosphere,* vol. 4, pp. 583 - 592, 2010.

[18] European Space Agency, "SMOS: the Global Success Story Continues," 22 02 2013. [Online]. Available: https://www.esa.int/Applications/Observing_the_Earth/SMOS/SMOS_the_global_success_story_continues. [Accessed 31 12 2020].

[19] National Aeronautics and Space Administration, "Aquarius/SAC-D Launch Press Kit," June 2011. [Online]. Available: https://www.google.com/url?sa=t&rct=j&q=&esrc=s&source=web&cd=&cad=rja&uact=8&ved=2ahUKEwiBrsSMsaLrAhULNOwKHc2MAZwQFjAAegQIBBAB&url=https%3A%2F%2Fspaceflightnow.com%2Fdelta%2Fd354%2Fimages%2Fpresskit.pdf&usg=AOvVaw0xaJPQl5LB99smkPNXwpA9. [Accessed 17 August 2020].

[20] X. Wu, J. Walker, N. Das, R. Panciera and C. Rüdiger, "Evaluation of the SMAP Brightness Temperature Downscaling Algorithm Using Active–Passive Microwave Observations," *Remote Sensing of Environment,* vol. 155, pp. 210 - 221, 2014.

[21] National Aeronautics and Space Administration, "SMAP Handbook Soil Moisture Active Passive," 2014. [Online]. Available: https://smap.jpl.nasa.gov/system/internal_resources/details/original/178_SMAP_Handbook_FINAL_1_JULY_2014_We. [Accessed 18 August 2020].

[22] Copernicus Imaging Microwave Radiometer - Mission Requirements Document, "CIMR Mission Requirements Document v3," 2 October 2019. [Online]. Available: https://cimr.eu/documents. [Accessed 18 August 2020].

[23] C. Gruhier, P. de Rosnay, S. Hasenauer, T. Holmes, d. Jeu, R., Y. Kerr, E. Mougin, E. Njoku, F. Timouk and W. Wagner, "Soil Moisture Active and Passive Microwave Products: Intercomparison and Evaluation Over a Sahelian Site," *Hydrology and Earth System Sciences,* vol. 14, no. 1, 2010.

[24] G. Bonin, N. Roth, S. Armitage, J. Newman, B. Risi and R. Zee, "CanX-4 and CanX-5 Precision Formation Flight: Mission Accomplished!," in *29th Annual AIAA/USU Conference on Small Satellites*, 2015.

[25] S. Wu, W. Chen and C. Chao, "The STU-2 CubeSat Mission and In-Orbit Test Results," in *30th Annual AIAA/USU Conference on Small Satellites*, Logan, Utah, 2016.

[26] D. Rowen, B. Hardy, C. Coffman, D. Hinkley, R. Welle and S. Janson, "The NASA Optical Communications and Sensor Demonstration Program: Proximity Operations," 2018.

[27] European Space Agency, "AAReST (Autonomous Assembly Reconfigurable Space Telescope Flight Demonstrator)," [Online]. Available: https://directory.eoportal.org/web/eoportal/satellite-missions/a/aarest. [Accessed 19 August 2020].

[28] H. Linz, B. Divya, L. Buinhas, M. Lezius, E. Ferrer, R. Förstner, K. Frankl and M. Philips-Blum, "InfraRed Astronomy Satellite Swarm Interferometry (IRASSI): Overview and Study Results," *Advances in Space Research,* vol. 65, no. 2, pp. 831-849, 2019.

[29] M. Aung, A. Ahmed, M. Wette, D. Scharf, J. Tien, G. Purcell, M. Regehr and B. Landin, "An Overview of Formation Flying Technology Development for the Terrestrial Planet Funder Mission," in *IEEE Aerospace Conference Proceedings*, Pasadena, 2004.

[30] National Aeronautics and Space Administration, "Terrestrial Planet Finder Interferometer Science Working Group Report," Pasadena, California, 2007.

[31] S. Engelen and C. Verhoeven, "Olfar, a Radio Telescope Based on Nano-satellites in Moon Orbit," 2010.

[32] European Space Agency, "SMOS System Requirements Document," 2005.

[33] D. Morgan and C. Soon-Jo, "Model Predictive Control of Swarms of Spacecraft Using Sequential Convex Programming," *Journal of Guidance, Control, and Dynamics,* vol. 37, no. 6, pp. 1725 - 1739, 2014.

[34] A. Camps and C. Swift, "Observation, A Two-Dimensional Doppler-Radiometer for Earth," *IEEE Transactions on Geoscience and Remote Sensing,* vol. 39, no. 7, pp. 1566 - 1572, July 2001.

[35] W. Dorigo, W. Wagner, C. Albergel, F. Albrecht, G. Balsamo, L. Brocca, D. Chung and M. Ertl, "ESA CCI Soil Moisture for Improved Earth System Understanding: State-of-the-art and Future Directions," *Remote Sensing of the Environment,* vol. 203, pp. 185-215, 2017.

[36] Y. Kerr, N. Rodriguez-Fernandez, D. Entekhabi, R. Bindlish, T. Lee, S. Yueh and G. Lagerloef, "Present and Future of L-band Radiometry," in *IGARSS 2018*, Valencia, 2018.

[37] Y. Monjid, "Fourier Correlation Imaging Concept for Passive Earth Observation to the SMOS-Next Mission, PhD Thesis," Université Toulouse, Toulouse, 2017.

[38] VACCO Industries, "Reaction Control Propulsion Module," 2020. [Online]. Available: https://www.vacco.com/space/chems-overview. [Accessed 20 Juni 2020].

[39] F. Pranajaya and R. Zee, "The Generic Nanosatellite Bus," in *2009 First Internatinoal Conference on Advances in Satellite and Space Communications*, 2009.

[40] S. D'Amico, "Proximity Operations of Formation-Flying Spacecraft Using an Eccentricity/Inclination Vector Seperation," *Journal of Guidance Control and Dynamics,* vol. 29, no. 3, pp. 554-562, 2006.

[41] ALMA, "10 Things to Understand ALMA," [Online]. Available: https://alma-telescope.jp/en/about. [Accessed 15 2 2021].

[42] E. Schreiber, Vollelektronisches Abbildungsverfahren für die Mikrowellenradiometrie durch Frequenzvariation und Apertursynthese, Ph.D dissertation, Köln: Karlsruhe Institut für Technologie (KIT), 2014.

[43] R. A. Thompson, J. Moran and G. Swenson, Interferometry and Synthesis in Radio Astronomy, Switzerland: Springer Open, 2017.

[44] M. Peichl, "Theoretische und Experimentelle Untersuchungen des Apertursynthese-Verfahrens bei 37 GHz," Universität Fridericiana Karlsruhe, Karlsruhe, 1994.

[45] M. Jirousek, M. Peichl, V. A. and S. H., "A Multi-frequency Microwave Aperture Synthesis Radiometer for High-Resolution Imaging," in *2004 IEEE International Geoscience and Remote Sensing Symposium*, Anchorage, AK, USA, 2004.

[46] M. Jirousek, "Abbildendes Mikrowellen-Spektrometer mit Apertursynthese," Fakultät für Elektrotechnik und Informationstechnik, des Karlsruher Instituts für technologie (KIT), Karlsruhe, 2011.

[47] E. Schreiber, M. Peichl and H. Süss, "First Design Investigations on a Fully-electronic Microwave Imaging Radiometer System," in *2009 German Microwave Conference*, Munich, 2009.

[48] A. Camps, "Application of Interferometric Radiometry to Earth Observation PhD thesis," Caltech Submillimeter Observatory, Barcelona, 1996.

[49] C. Ruf, C. Swift, A. B. Tanner and D. M. Le Vine, "Interferometric Synthetic Aperture Microwave Radiometry for the Remote Sensing of the Earth," *IEEE Transactions on Geoscience and Remote Sensing,* vol. 26, no. 5, pp. 597-611, 1988.

[50] K. Komiyama, "High Resolution Imaging by Supersynthesis Radiometers (SSR) for the Passive Microwave Remote Sensing of the Earth," *Electronic Letters,* vol. 27, no. 4, pp. 389-390, 1991.

[51] T. Carr, M. Lynch, M. Paul, G. Brown, J. May, N. Six, V. Robinson and W. Block, "Very Long Baseline Interferometry of Jupiter at 18 MHz," *Radio Science,* vol. 5, pp. 1223-1226, 1970.

[52] European Space Agency, "SMOS (Soil Moisture and Ocean Salinity) Mission," eoPortal Directory, [Online]. Available: https://directory.eoportal.org/web/eoportal/satellite-missions/s/smos. [Accessed 20 July 2020].

[53] H. Park and K. Yong-Hoon, "Improvement of a Doppler-Radiometer Using a Sparse Array," *IEEE Geoscience and Remote Sensing Letters,* vol. 6, no. 2, pp. 229 - 233 , April 2009.

[54] J. Wrobel and R. Walker, "Sensitivity," in *Synthesis Imaging in Radio Astronomy 11 ASP Conference Series, Vol. 180*, 1999, pp. 171-186.

[55] H. Park, "Radiometric Resolution of Motion Induced Synthetic Aperture Radiometer," *IEEE Geoscience and Remote Sensing Letters, Vol. 8, No. 4,* July 2011.

[56] W. Clohessy and R. Wiltshire, "Terminal Guidance System for Satellite Rendezvous," *Journal of Aerospace Sciences,* vol. 27, no. 9, pp. 653-658, 1960.

[57] University of Austin Texas, "The Clohessy Wiltshire Model," [Online]. Available: https://www.google.com/url?sa=t&rct=j&q=&esrc=s&source=web&cd=&ved=2ahUKEwj1hrOHhKfzAhXzg_0HHQEHBrEQFnoECAIQAQ&url=http%3A%2F%2Fwww.ae.utexas.edu%2Fcourses%2Fase366k%2Fcw_equations.pdf&usg=AOvVaw1uBF9oAZlCmL87lzE2UdSJ. [Accessed 4 August 2020].

[58] S. D'Amico, "Autonomous Formation Flying in Low Earth Orbit," Technische Universität Delft, Delft, 2010.

[59] D. Brouwer, "Solution of the Problem of Artiflcial Satellite Theory Without Drag," *The Astronomical Journal,* vol. 64, pp. 378-397, 1959.

[60] G. Krieger, A. Moreira, H. Fiedler, I. Hajnsek, M. Werner, M. Younis and M. Zink, "TanDEM-X: A satellite Formation for High-Resolution SAR Interferometry.," *IEEE Transactions on Geoscience and Remote Sensing,* vol. 45, no. 11, pp. 3317-3341, 2007.

[61] A. Moreira, G. Krieger and J. Mittermayer, "Satellite Configuration for Interferometric and/or Tomographic Remote Sensing by Means of Synthetic Aperture Radar (SAR).". USA Patent U.S. Patent No. 6,677,884, 13 January 2004.

[62] L. H. Sentman, "Comparison of the Exact and Approximate Methods for Predicting Free-Molecular Aerodynamic Coefficients," *American Rocket Society Journal,* vol. 31, pp. 1576-1579, 1961.

[63] J. Sullivan, S. Grimberg and D. Simone, "Comprehensive Survey and Assessment of Spacecraft Relative Motion Dynamics Models," *Journal of Guidance, Control, and Dynamics,* vol. 40, no. 8, pp. 1837-1859, 2017.

[64] J. A. Kechichian, "Motion in General Elliptic Orbit with Respect to a Dragging and Precessing Coordinate Frame," *Journal of the Astronautical Sciences,* vol. 46, no. 1, pp. 25 -45, 1998.

[65] S. A. Schweighart and R. J. Sedwick, "High-Fidelity Linearized J2 Model for Satellite Formation Flight," *Journal of Guidance, Control and Dynamics,* vol. 25, no. 6, pp. 1073-1080, 2002.

[66] D. Morgan and S.-J. Chung, "Swarm-Keeping Strategies for Spacecraft Under J2 and Atmospheric Drag Perturbation," *Journal of Guidance Control and Dynamics,* vol. 35, no. 5, August 2012.

[67] G. Xu and D. Wang, "Nonlinear Dynamic Equations of Satellite Relative Motion Around an Oblate Earth," *Journal of Guidance Control and Dynamics,* vol. 31, no. 5, pp. 1521-1524, September 2008.

[68] D. Wang, B. Wu and P. E. K. Poh, Satellite Formation Flying, Singapore: Springer Verlag, 2017.

[69] K. Alfriend, Spacecraft Formation Flying, Elsevier Astrodynamics Series, 2010.

[70] J. Eyer, A Dynamics and Control Algorithm for Low Earth Orbit Precision Formation Flying Satellites, PhD Thesis, Toronto: University of Toronto, 2009.

[71] M. D'Errico, "Distributed Space Missions for Earth System Monitoring," Springer, 2013, p. 623.

[72] W. Arnold and A. Laub, "Generalized Eigenproblem Algorithms and Software for Algebraic Riccati Equations," *Proceedings of the IEEE,* vol. 72, no. 12, pp. 1746 - 1754, 1984.

[73] D. Vallado, "A Critical Assessment of Satellite Drag and Atmospheric Density Modeling," *Acta Astronautica,* vol. 95, pp. 141-165, 2014.

[74] L. Greenland and J.-Y. Lee, "Accelerating the Nonuniform Fast Fourier Transform," *SIAM Review,* vol. 46, no. 3, pp. 443-454, 2004.

[75] R. Patera, "General Method for Calculating Satellite Collision Probability," *Journal of Guidance Control and Dynamics,* vol. 24, no. 4, pp. 716-722, July 2001.

[76] Y. He, M. Xu, X. Jia and R. Armellin, "High-Precision Repeat-Groundtrack Orbit Design and Maintenance for Earth Observation Missions," *Celestial Mechanics and Dynamical Astronomy,* vol. 128, pp. 275-294, 2017.

[77] G. Krieger, H. Fiedler and J. Mittermayer, "Analysis of Multistatic Configurations for Spaceborne SAR Interferometry.," *IEEE Proceedings-Radar, Sonar and Navigation,* vol. 150, no. 3, pp. 87-96, 2003.

[78] T. Reid and A. Misra, "Formation Flight of Satellites in the Presence of Atmoshperic Drag," *Journal of Aerospace Engineering, Sciences and Applications,* vol. 3, no. 1, pp. 64-91, 2011.

[79] J. Hamel and J. Lafontaine, "Linearized Dynamics of Formation Flying Spacecraft on a J2-Perturbed Elliptical Orbit," *Journal of Guidance, Control and Dynamics,* vol. 30, no. 6, pp. 1649-1658, 2007.

[80] F. Boone, "Interferometric Array Design: Optimizing the Locations of the Antenna Pads," *Astronomy & Astrophysics,* vol. 377, no. 1, pp. 268-376, October 2001.

[81] E. Keto, "The Shapes of Cross-Correlation Interferometers," *The Astrophysical Journal,* vol. 475, pp. 843-852, 1997.

[82] Y. Su, "Optimization of Interferometric Array Configurations by "Sieving" u-v Points," *Astronomy and Astrophysics,* vol. 414, no. 1, pp. 389-397, January 2004.

[83] C.-H. Jang, F. Hu, F. He, M.-H. Jong and D. Zhu, "Circular Hexagonal Lattice Array and its Optimization in Aperture Synthesis Radiometers," *IEEE Antennas and Wireless Propagation Letters,* vol. 16, pp. 685 - 688, 2017.

[84] D. Woody, "Radio Interferometer Array Point Spread Functions, I. Theory and Statistics," *ALMA MEMO 389,* August 2001.

[85] N. Jin, "Analysis and Particle Swarm Optimization of Correlator Antenna Arrays for Radio Astronomy Applications," *IEEE Transactions on Antennas and Propagation,* vol. 56, no. 5, pp. 1269 - 1279, May May 2008.

[86] L. Kogan, "Optimizing a Large Array Configuration to Minimize the Sidelobes," *IEEE Transactions on Antennas and Propagation,* vol. 48, no. 7, pp. 1075-1077, 2000.

[87] S. Kiehbadroudinezhad, "Optimization af an Antenna Array Using Genetic Algorithms," *The Astronomical Journal,* vol. 147, 2014.

[88] R. Lewis and V. Torczon, "Pattern Search Methods for Linearly Constrained Minimization," *SIAM Journal on Optimization,* vol. 10, no. 3, pp. 917-941, 2000.

[89] R. Lewis and V. Torczon, "A Globally Convergent Augmented Lagrangian Pattern Search Algorithm for Optimization with General Constraints and Simple Bounds," *SIAM Journal on Optimization,* vol. 12, no. 4, pp. 1075-1089, 2002.

[90] D. Briggs, "High Fidelity Deconvolution of Moderately Resolved Sources PhD Thesis," The new Mexico Institute of Mining and Technology, Socorro, New Mexico, March 1995.

[91] A. Camps, "Radiometric Sensitivity Computation in Aperture Synthesis Interferometric Radiometry," *IEEE Transactions on Geoscience and Remote Sensing,* vol. 36, no. 2, pp. 680 - 685, 1998.

[92] V. Industries, "Reaction Control Propulsion Module," 2020. [Online]. Available: https://www.vacco.com/space/chems-overview. [Accessed 20 Juni 2020].

[93] N. Prasad, "An Overview of GPS Receivers for Small Satellites," Satsearch, September 2021. [Online]. Available: https://blog.satsearch.co/2019-11-12-an-overview-of-gps-receivers-for-small-satellites. [Accessed 6 September 2021].

[94] A. Cervone, B. Zandbergen and D. C. e. S. M. Guerrieri, "Green Micro-resistojet Research at Delft University of Technology new Options for Cubesat Propulsion," *CEAS Space Journal volume,* vol. 9, pp. 111-125, July 2017.

[95] H. Henninger, S. Stefan and E. Diedrich, "Analysis and Comparison of new Downlink Technologies for Earth Observation Satellites," *Radioengineering,* vol. 25, no. 1, pp. 1-10, 2016.

[96] European Space Agency, "Sentinel Online Mission Summary," [Online]. Available: https://sentinel.esa.int/web/sentinel/missions/sentinel-1/overview/mission-summary. [Accessed 21 12 2020].

[97] J. B. Hagen and D. T. Farley, "Digital-Correlation Techniques in Radio Science," *Radio Science,* vol. 8, no. 8-9, pp. 775-784, 1973.

[98] SAIT Ltd, "Cubesat X-band Transmitter," SAIT Ltd, Russia, 2021.

[99] M. Weiß, "Synchronisation of Bistatic Radar Systems," in *2004 IEEE International Geoscience and Remote Sensing Symposium*, Anchorage, AK, USA, 2004.

[100] G. Krieger and M. Younis, "Impact of Oscillator Noise in Bistatic and Multistatic SAR," *IEEE Geoscience and Remote Sensing Letters,* vol. 3, no. 3, pp. 424-428, 2006.

[101] M. Younis, R. Metzig and G. Krieger, "Performance Prediction of a Phase Synchronization Link for Bistatic SAR," *IEE Geoscience and remote sensing letters,* vol. 3, no. 3, pp. 429-433, 2006.

[102] L. D'Addario, "Time Synchronization in Orbiting VLBI," *IEEE Transactions on instrumentation and measurement,* vol. 40, no. 3, pp. 584-590, 1991.

[103] NASA, "State of the art of Small Spacecraft Technology - Communications," NASA, 4 May 2020. [Online]. Available: https://www.nasa.gov/smallsat-institute/sst-soa/communications. [Accessed 11 Juli 2020].

[104] N. Roth, Navigation and Control Design for the CanX-45 Satellite Formation Flying Mission, Toronto: University of Toronto, 2010.

A 1. ANNEX

A 1.1. Simulator validation

The core modules of the system simulator have been validated by comparing test case results with literature. The following sections will discuss the validation of the Orbit Propagation Module and the Image Processing Module.

The validation of the Orbit Propagation Module was conducted in two steps: Firstly, representative uncontrolled relative validation orbits were propagated and compared with results from the numerical STK High Precision Orbit Propagator (HPOP). This ensures that the basic relative orbit model, the orbit perturbations, and the coordinate transformations are implemented correctly. Secondly, controlled flight, i.e., the orbit control algorithm, is validated by comparing simulation results with results from literature. In particular, the results that are compared between the simulation and literature are the rate of fuel consumption and the accuracy of position control.

As a validation case a simple close-proximity two-satellite formation has been investigated under orbital perturbations. Firstly, orbital simulations were run with two different relative orbits, taking into account J_2 perturbations only. A circular chief orbit was chosen with the following orbital elements: $a = 750\ km, i = 97.3°$ and $\Omega = 54.95°$. Figure A.1-1 shows the relative orbital motion of a deputy satellite in the Hill frame, with relative orbital elements set at $\Delta\boldsymbol{i} = [10,0]^T$ and $\Delta\boldsymbol{e} = [10,0]^T$ as given by STK and the present system simulator. This orbit does not adhere to the condition given in equation (3-19) and is thus subject to a gradual shift in its inclination. The green trajectory belongs to the STK solution while the purple trajectory belongs to the SSBSAR simulator. From the image it can be seen that the two trajectories are almost identical.

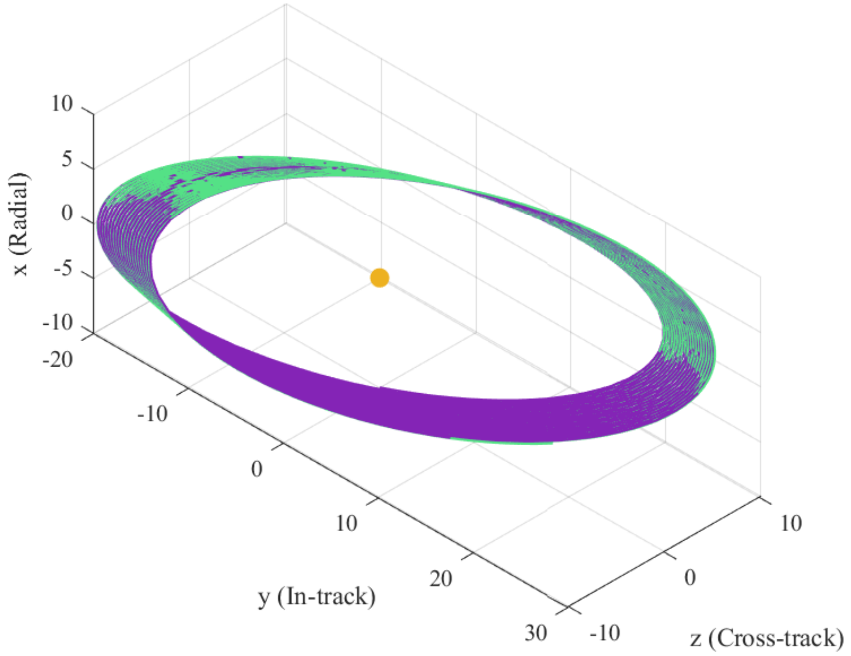

Figure A.1-1 Relative orbital motion of a deputy satellite in the Hill frame, with relative orbital elements set to $\Delta i = [10,0]^T$ and $\Delta e = [10,0]^T$ as given by STK (green) and the SSBSAR (purple).

A quantitative comparison of the modelling discrepancies between the two orbital solutions is shown in Figure A.1-2. The image compares the deviations in all three Hill directions. The deviations can be seen to not exceed 10 cm even over 20 orbits. The residual discrepancies could have many reasons, from discrepancies in the exact used numerical equations to the type of solver used to solve the differential equations. Small inaccuracies in defining initial orbit conditions could also be the cause for the discrepancy.

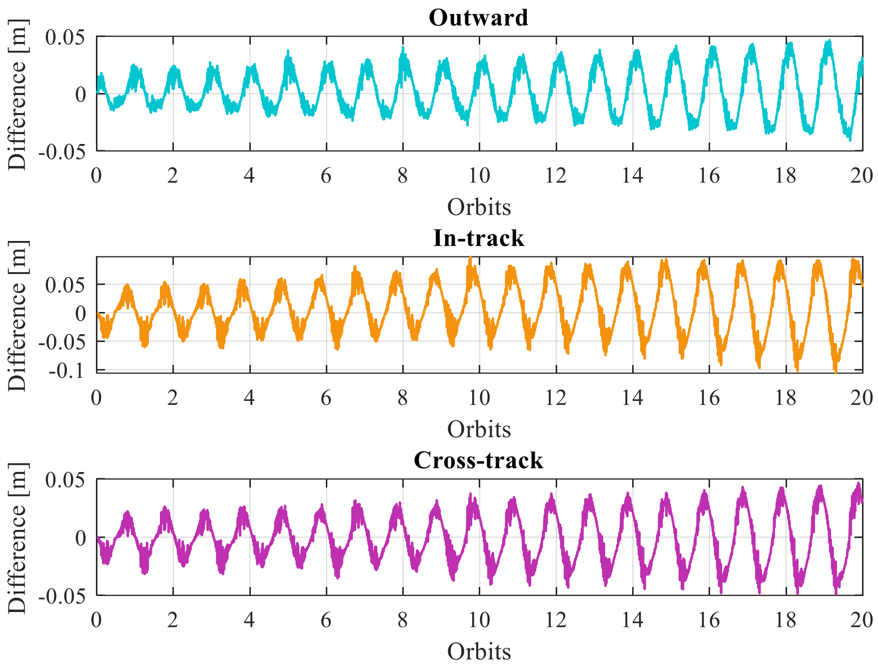

Figure A.1-2 Discrepancies between the STK and SSBSAR orbital simulations for the relative orbital motion of a deputy satellite, with relative orbital elements set to $\Delta i = [10,0]^T$ and $\Delta e = [10,0]^T$ under J_2 perturbations only.

Figure A.1-3 shows the discrepancies between the STK and the SSBSAR simulations, with relative orbital elements set to $\Delta \boldsymbol{i} = [0,10]^T$ and $\Delta \boldsymbol{e} = [0,10]^T$. This relative orbit thus adheres to the condition given in equation (3-19). While the in-track discrepancies are slightly larger than the discrepancies from the orbit shown in Figure A.1-2, they still do not exceed 20 cm. The larger discrepancies are likely caused by errors in the linearization of the initial conditions.

Figure A.1-4 and Figure A.1-5 show the orbit and the discrepancies under the added influence of aerodynamic drag for relative orbital elements set to $\Delta \boldsymbol{i} = [0,10]^T$ and $\Delta \boldsymbol{e} = [0,10]^T$. This case assumes two 100 kg satellites with slight differences of aerodynamic areas ($A_c = 2\,m^2, A_d = 1.5\,m^2$) and drag coefficients ($C_{D,c} = 2.2, C_{D,d} = 1.5$) between the chief and the deputy satellites. In this case the outward and in-track deviations between the two simulations grow rather strongly (< 2 m over 20 orbits). This is because the magnitude of aerodynamic drag is slightly different in both cases, and the resulting gradual deceleration influences the orbit height and the in-track position. The magnitude of aerodynamic drag very likely results from a difference in the assumed density model of the atmosphere. Very small differences in density modelling will have a large result on the satellite trajectory.

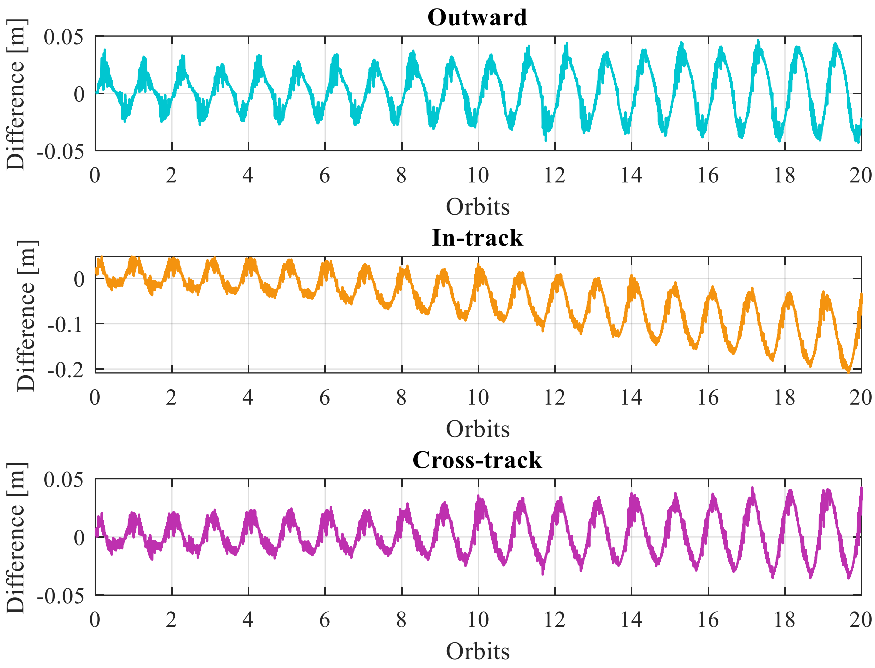

Figure A.1-3 Discrepancies between the STK and SSBSAR orbital simulations for the relative orbital motion of a deputy satellite, with relative orbital elements set at $\Delta i = [0,10]^T$ and $\Delta e = [0,10]^T$ under J_2 perturbations only.

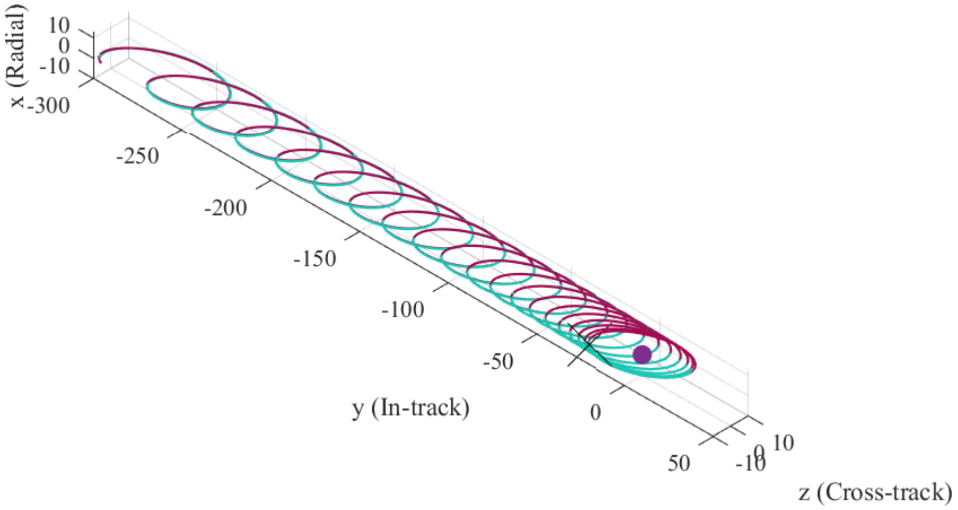

Figure A.1-4 Relative orbital motion of a deputy satellite in the Hill frame, with relative orbital elements set at $\Delta i = [0,10]^T$ and $\Delta e = [0,10]^T$ as given by STK (red) and the SSBSAR (turquoise) under J_2 and aerodynamic perturbations.

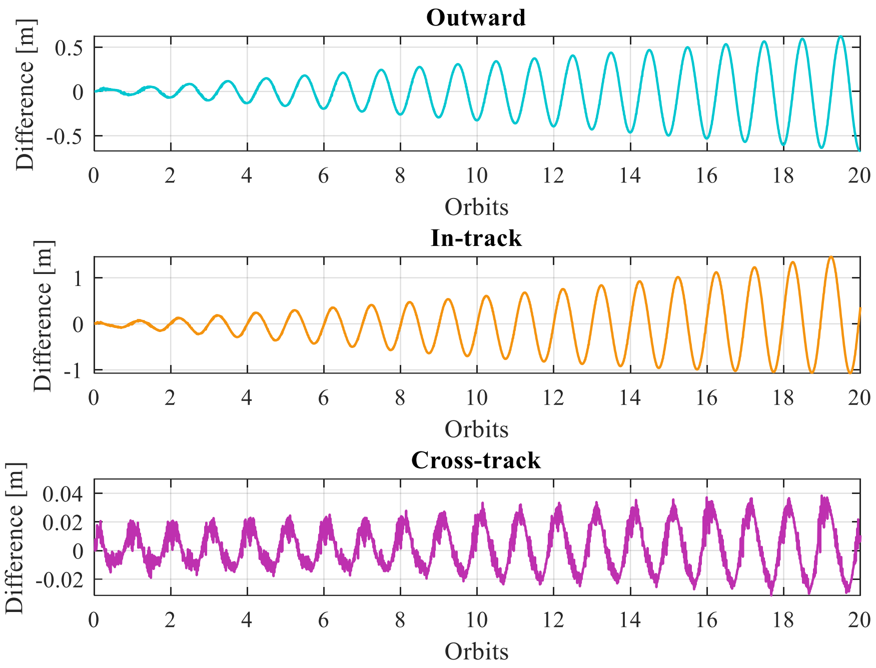

Figure A.1-5 Discrepancies between the STK and SSBSAR orbital simulations for the relative orbital motion of a deputy satellite, with relative orbital elements set at $\Delta i = [0{,}10]^T$ and $\Delta e = [0{,}10]^T$ under J_2 and aerodynamic perturbations.

Since orbit corrections by the orbital control system will need to be conducted frequently during one orbit, the propagation time will only have to encompass a fraction of one orbit at a time. Overall, the relatively small magnitude of the deviations between the validation STK case and the SSBSAR shows that the orbital propagator accuracy is sufficient to propagate for the short propagation periods that are relevant for the current simulations.

Ultimately the purpose of simulating controlled flight within the SSBSAR is to extract realistic values for fuel consumption and control accuracy that could be used to gauge the feasibility of a specific orbit configuration. The validation of the orbit control algorithm can thus be performed by comparing the fuel consumption and control accuracy values from the SSBSAR with those given in existing studies. As the orbit control method was adopted from the CanX-45 mission due to its similarity with the scenario investigated in this thesis, it is natural to use CanX-45 as a validation case. The significant difference between the SSBSAR and CanX-45 implementation of the orbit control method, is the simplified modelling of the DGNSS position and velocity errors by SSBSAR. While this simplifies the simulation, the modelling accuracy of the GNC state estimation should still be representative enough for the purposes of this thesis.

The results of two simulations have been published for CanX-45 that will be used as a benchmark, one by Eyer [70] in 2007 and one by Roth [104] in 2010. Both of these publications assume slightly different formation flying scenarios.

Table A.1-1 Scenario settings for validation of scenario Eyer [70]. Values denoted with an asterisk are assumed, as they are not explicitly listed in the source.

Simulation setting	*Values*
Chief orbit	$a = 7105\ km, i = 97.6°, e = 0.025, \omega = 0°, \Omega = 99.56°, M = 0°$
Deputy orbit	$\Delta\boldsymbol{e} = [0{,}25]^T, \Delta\boldsymbol{i} = [-50{,}0]^T$
Nominal thrust (Deputy)	$u_N = 5\ mN$
GNC Accuracies (Deputy)	$GNC_{Pos} = 5\ cm, GNC_{Vel} = 0.07\ mm/s$
Thrust errors (Deputy)	$\alpha_e = 2°, b_e = 0.05\ (5\%)$
Control period	$T_{pwm} = 300\ s$
Spacecraft masses	$m_{s,d} = 6.85\ kg$

Using the scenario settings from Eyer given in Table A.1-2, a simulation was run for 50 orbits and the fuel consumption and the mean control accuracy was extracted. The results are given in Table A.1-2. It can be seen that the deviation of the SSBSAR does not exceed 1.42 % for the fuel consumption and 2.4 % on the 3D RMSE. Considering that the exact accuracies of the GNC state estimation were not known, the deviation is remarkably small.

Table A.1-2 Values for the mean fuel consumption in Δv $[\frac{m}{s \cdot orbit}]$ and the 3D RMS control accuracy [m] for the scenario settings given in Eyer [70].

	Fuel consumption [m/(s·orbit)]	*3D RMS control accuracy [m]*
Eyer	*0.0140*	*0.185*
SSBSAR	*0.0142*	*0.181*
Deviation	*1.42 %*	*- 2.4 %*

The scenario settings for the validation of the scenario simulated by Roth are given in Table A.1-3. The control period, the average nominal thrust and the GNC state estimation accuracies represent estimates for the simulation conducted by Roth. The satellite orbits are identical.

Table A.1-3 Scenario settings for validation of scenario Roth [104]. Values denoted with an asterisk are assumed, as they are not explicitly listed in the source.

Simulation setting	*Values*
Chief orbit	$a = 7105\ km, i = 97.6°, e = 0.025, \omega = 0°, \Omega = 99.56°, M = 0°$
Deputy orbit	$\Delta\boldsymbol{e} = [0,25]^T, \Delta\boldsymbol{i} = [-50,0]^T$
Nominal thrust (Deputy)	$u_N = 15\ mN$
GNC Accuracies (Deputy)	$GNC_{Pos} = 2.6\ cm, GNC_{Vel} = 0.1\ cm/s$
Thrust errors (Deputy)	$\alpha_e = 1.7°, b_e = 0.1\ (10\%)$
Control period	$T_{pwm} = 215s$
Spacecraft masses	$m_{s,d} = 6.85\ kg$

Based on the scenario given by Roth a simulation was run with SSBSAR. The results are given in Table A.1-4. The higher fuel consumption and lower control accuracy can be attributed to the lower accuracy of the GNC state estimate. In comparison with the Eyer validation case, the deviation of the SSBSAR results from those given by Roth, is slightly larger.

Table A.1-4 Values for the mean fuel consumption in Δv $[\frac{m}{s \cdot orbit}]$ and the 3D RMS control accuracy [m] for the scenario settings given in Roth [104].

	Fuel consumption [m/(s·orbit)]	*3D RMS control accuracy [m]*
Roth	*0.051*	*0.64*
SSBSAR	*0.059*	*0.66*
Deviation	*15.7 %*	*3.12 %*

While the validation of the satellite controller yielded some discrepancies with former studies, the deviations are likely attributable to the uncertainty with the exact input parameters. Nevertheless, the small deviation in the scenario assumed by Eyer, show that the control algorithm has been implemented correctly and fuel consumption and accuracy results are generally reliable.

A 1.2. Validation of Image Processing Module

The Image Processing Module generates the PSF and determines the array performance parameters that characterize a specific array configuration, such as the MBE and the angular resolution. Within the course of this thesis the SSBSAR Image Processing Module has been validated against the array snapshot configuration and known array performance parameters given by Camps [48]. Figure A.1-6 shows the Y-configuration antenna array used in the analyses by Camps, which carries 43 antennas per beam. The PSF of the shown configuration without windowing can be seen in Figure A.1-7.

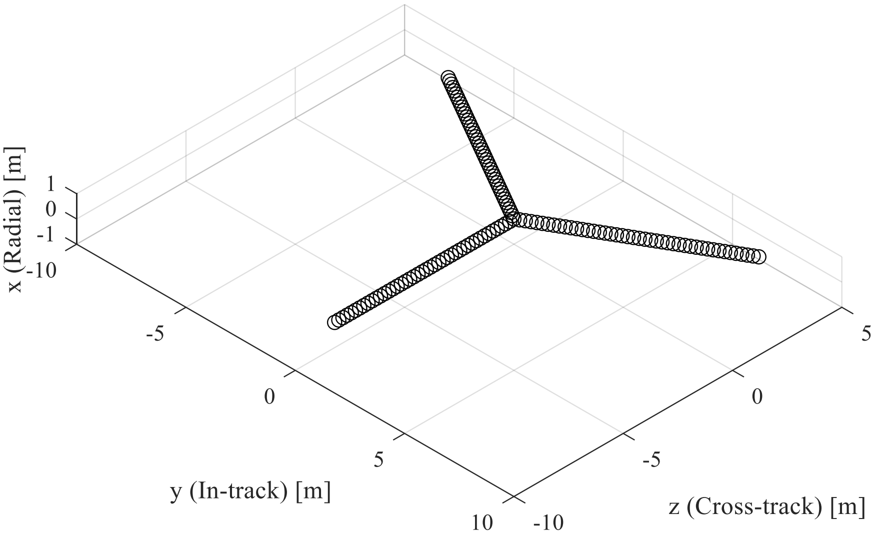

Figure A.1-6 Antenna configuration as investigated by Camps [48].

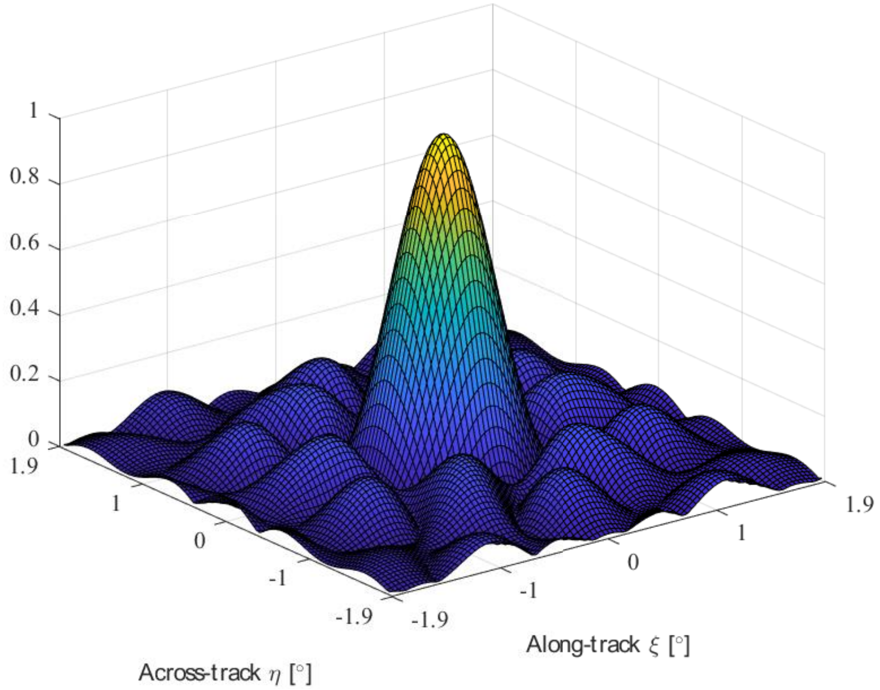

Figure A.1-7 PSF of antenna configuration investigated by Camps [48] generated with the SSBSAR.

For validation of the SSBSAR the angular resolution and the MBE were calculated for the given array configuration. The resulting angular resolutions and MBE are compared to those given by Camps in Table A.1-5. Overall, there is very little deviation between the results. Slight deviations in the MBE can stem from the numeric integration of the PSF surface inside and outside the main lobe. Despite the discretization, the error in surface integration should not exceed 1%. Errors of this magnitude are insignificant for the analyses conducted within this thesis.

Table A.1-5 Angular resolution, θ_w and Main Beam Efficiency (MBE) of validation configuration compared with [48] for snapshots tapered by rectangular and Blackman windows.

Window	*Rect. (Camps)*	*Rect. (SSBSAR)*	*Blackman (Camps)*	*Blackman (SSBSAR)*
θ_w *@ -3 dB*	*0.77°*	*0.77°*	*1.1°*	*1.1°*
θ_w *@ -10 dB*	*1.21°*	*1.21°*	*1.81°*	*1.83°*
MBE @ -3 dB	*27 %*	*28 %*	*52.9 %*	*51,7 %*
MBE @ -10 dB	-	-	*85.7 %*	*86,4 %*